Universitat Autònoma de Barcelona

Doctoral Thesis

Characterization of a Pixel CdTe Detector for Nuclear Medicine Imaging

Author:
Gerard Ariño Estrada

Supervisor:
Prof. Mokhtar Chmeissani Raad
Tutor:
Prof. Enrique Fernández Sánchez

A thesis submitted in fulfilment of the requirements
for the degree of

in the

Institut de Física d'Altes Energies,
Departament de Física

March 2015

"A person can spend his whole life between four walls. If he doesn't think or feel that he's a prisoner, then he's not a prisoner. But then there are people for whom the whole planet is a prison, who see the infinite expanse of the universe, the millions of stars and galaxies that remain forever inaccessible to them. And that awareness makes them the greatest prisoners of time and space."

Vladimir Bartol, *Alamut*

Acknowledgements

These pages contain the work of more than four years. A work I have done thanks to the strong support of my supervisor, Mokhtar, *shukran* for giving me this opportunity, it has been the best PhD I could ever do. It has been awesome to work, learn and enjoy next to a postdoc like Gianluca, *grazie mile*, è stato un piacere. *Bedankt* Machiel, for all your helpful advises. Thanks a lot to the members of the VIP team: Carles, Dilber, Jorge, Katya, Ricardo and Yónatan. *Many thanks* as well to the IFAE colleagues, for the lunches, coffees and good moments we have shared. I also acknowledge the support received by the grant ERC-AdG-#250207, and from the MINECO, through the program of PhD fellowships for Severo Ochoa institutes.

Moltes gràcies als que, desde crios, heu confiat en mi. *Moltes gràcies* als que, junts, ens hem fet grans. *Muchas gracias* a aquellos de los que he aprendido tanto como me he reído. *Grazie mile* a quelli che sono lontani, ma saranno sempre vicino. *Teşekkür edirim* to Dilber, that never lets me to give up. Finalment, *moltes gràcies* a la meua família, especialment a Jordi i ma mare, pel seu suport.

Contents

Acknowledgements ii

List of Figures vii

List of Tables xiv

Abbreviations xv

1 Principles and Techniques of Photon Interaction and Detection 4
1.1 Positron Interaction with Matter . . . 4
1.2 Photon Interaction With Matter . . . 6
1.2.1 Photoelectric absorption . . . 6
1.2.2 Compton scattering . . . 8
1.3 Scintillation Detectors . . . 10
1.3.1 Scintillation Mechanism . . . 10
1.3.2 Characteristics of Scintillators . . . 11
1.3.3 Scintillator Crystals for PET . . . 12
1.4 Photodetectors . . . 12
1.4.1 Photomultiplier Tubes . . . 14
1.4.1.1 Principle of Operation . . . 15
1.4.1.2 PMT Characteristics . . . 15
1.4.2 Avalanche Photodiodes . . . 16
1.4.2.1 Principle of Operation . . . 16
1.4.2.2 APD Properties . . . 17
1.4.2.3 Geiger Mode APD . . . 18
1.4.3 Silicon Photomultipliers . . . 19
1.4.3.1 Principle of Operation . . . 19
1.4.3.2 SiPM Properties . . . 20
1.5 Semiconductor Detectors . . . 24
1.5.1 Semiconductor Band Structure . . . 24
1.5.2 Semiconductor Detector Structure . . . 25
1.5.3 Principle of Operation . . . 25
1.5.3.1 Fano Factor . . . 26
1.5.4 Charge Carrier Drift . . . 27
1.5.5 Signal Induction . . . 27
1.5.6 Charge Trapping . . . 28
1.5.7 Small Pixel Effect . . . 29

1.5.8 Charge Sharing . . . 29
1.5.9 Energy Resolution . . . 30

2 Nuclear Medicine **32**
2.1 Nuclear Medicine for Diagnostic Purposes . . . 32
2.2 PET . . . 33
2.2.1 Positron Emitter Radiotracers . . . 33
2.2.2 Coincidence Detection . . . 34
2.2.3 Time-of-Flight Measurement . . . 35
2.2.4 Photon Interaction Position . . . 35
2.2.5 Parallax Error . . . 36
2.2.6 Energy Resolution . . . 37
2.2.7 State-of-the-art PET Scanners . . . 37
2.2.8 PET Applications . . . 39
2.2.8.1 Tumor Diagnosis and Treatment . . . 39
2.2.8.2 Brain Diseases . . . 39
2.2.8.3 Cardiovascular Pathologies . . . 40
2.2.8.4 Quality Assurance in Hadron Therapy . . . 41
2.2.9 New PET Generation . . . 41
2.2.9.1 ToF-PET . . . 41
2.2.9.2 Hybrid Imaging . . . 42
2.2.9.3 PET with Semiconductor Detectors . . . 42
2.3 PEM . . . 43
2.3.1 State-of-the-Art PEM Scanners . . . 43
2.4 SPECT . . . 44
2.4.1 Compton Camera . . . 47
2.5 Reconstruction Algorithms in Nuclear Medicine . . . 48
2.5.1 FBP . . . 50
2.5.2 ML-EM and OSEM . . . 51
2.5.3 LM-OSEM . . . 52
2.5.4 OE . . . 52

3 VIP Project **54**
3.1 The VIP Module . . . 55
3.2 The VIP-PIX . . . 56
3.2.1 Readout ASIC Architecture . . . 57
3.2.2 Readout Pixel Architecture . . . 58
3.2.3 Analog Front-End and ADC Characterization . . . 59
3.2.4 TDC Characterization . . . 60
3.2.5 Temperature Sensor Characterization . . . 61
3.3 Performance Simulation of VIP Scanners . . . 62
3.3.1 VIP-PET . . . 62
3.3.2 VIP-PEM . . . 65
3.3.3 VIP-CC . . . 69

4 Single Pixel CdTe Characterization and Performance **73**
4.1 Setup Description . . . 73

4.1.1 Single Pixel CdTe Diode . . . 74
4.1.2 AMPTEK Front-End Electronics . . . 76
4.1.2.1 Preamplifier A250 . . . 76
4.1.2.2 Pulse Amplifier and Shaper A275 . . . 77
4.1.3 Pulse Amplitude Measurement . . . 78
4.1.4 Time Detection Measurement . . . 79
4.2 Data Acquisition . . . 79
4.2.1 Single Event Trigger System . . . 80
4.2.2 Coincidence Trigger System . . . 80
4.2.3 Single Event Data Acquisition . . . 82
4.2.4 Coincidence Data Acquisition . . . 84
4.2.5 Software Functionality Description . . . 85
4.3 Energy and Timing Resolution Measurements . . . 87
4.3.1 Deterioration of Energy Resolution in Time . . . 87
4.3.2 Energy Resolution . . . 88
4.3.2.1 Measurement with ^{57}Co . . . 89
4.3.2.2 Measurement with ^{22}Na . . . 89
4.3.3 Coincidence Time Resolution . . . 91
4.4 Discussion . . . 95

5 Pixel CdTe Performance with VATA Front-End Electronics 96
5.1 Setup . . . 96
5.1.1 Pixelated CdTe Diode . . . 97
5.1.2 VATAGP7.1 . . . 97
5.1.3 Detector Assembly . . . 98
5.1.4 Signal Conditioning Board . . . 102
5.1.5 FPGA . . . 102
5.1.6 Graphic User Interface (GUI) . . . 104
5.2 Results . . . 105
5.2.1 Calibration . . . 107
5.2.2 Measurements with ^{22}Na . . . 109
5.2.2.1 Negative Energy Induction on Neighbor Pixels . . . 111
5.2.2.2 Charge Sharing Evaluation . . . 112
5.2.2.3 Energy Resolution . . . 116
5.2.3 Measurements with ^{57}Co . . . 119
5.2.3.1 Charge Sharing Evaluation . . . 120
5.2.3.2 Energy Resolution . . . 122
5.3 Discussion . . . 124

6 VIP-Detector Characterization 125
6.1 VIP-Detector Setup Description . . . 125
6.1.1 VIP-Detector Assembly . . . 126
6.1.2 Mother Board PCB (MB) . . . 127
6.2 Chip Probing . . . 129
6.2.1 Probing Results . . . 130
6.3 Results with VIP-Detector . . . 133
6.3.1 VIP-PIX Response Characterization . . . 133

6.3.2 VIP-Detector Spectroscopy with ^{57}Co . . . 134
6.3.2.1 VIP-Detector Spectroscopy with ^{22}Na . . . 137
6.4 Discussion . . . 138

7 Conclusions **140**

A JB-2N Power Supply Specifications **143**

B Software Used in the VIP-PIX Setup **145**
B.1 FPGA . . . 145
B.2 GUI: VISCA . . . 147
B.2.1 Software Flow Diagram . . . 148

Bibliography **151**

List of Figures

1.1 Shape of a typical positron energy spectrum in a β^+ decay. Adapted from [1] p.67. . . . 5
1.2 Scheme of the momentum of photons emitted in a positronium decay (E_1 and E_2) and the positronium momentum ($P_\pm$). . . . 6
1.3 Linear attenuation coefficient and its contributions in CdTe. Data from [2]. 7
1.4 Compton scattering between a photon and an electron at rest. . . . 8
1.5 Klein-Nishina distribution in a polar plot for differed incoming energies. The θ direction gives the Compton angle and the radial axis indicates the probability of that angle to occur. . . . 9
1.6 Energy spectra of the outcoming photons. . . . 9
1.7 Energy band structure of an activated crystalline scintillator. From [3] p.232. . . . 10
1.8 Basic elements of a PM tube. From [4]. . . . 14
1.9 A configuration for an avalanche photodiode is sketched at the top of the figure. Below is a plot of the resulting electric field when a bias voltage is applied. From [3], p.291. . . . 17
1.10 Variation of energy and timing resolution as a function of APD bias. From [4]. . . . 18
1.11 Schematic of the equivalent circuit of a SiPM with 6 cells. . . . 20
1.12 Effects of non-linear SiPM operation on identification as a function of photon energy and for different bias voltages. Data was taken with a SiPM with a 3×3 mm^2 cross-sectional area from Hamamatsu (50 μm micro-cell size). The scintillator used was a 3×3×5 mm^3 LSO crystal element. From [5]. . . . 21
1.13 Dependence of SiPM gain on temperature. Data taken with a SiPM with a 1×1 mm^2 cross-sectional area from Hamamatsu (50 μm micro-cell size). All the temperature measurements were performed at a constant SiPM bias. From [5]. . . . 21
1.14 Dark rate vs. Bias voltage (T=25°) for a SiPM device. From [6]. . . . 22
1.15 Dark rate vs. Temperature (constant gain) for a SiPM device. From [6]. . 22
1.16 Coincidence time resolution for a Hamamatsu S10931-050P SiPM vs bias voltage for different trigger thresholds. The best value is achieved (220 ps FWHM) at 72.4 V. From [7]. . . . 23
1.17 The energy resolution measured with CsI(Tl) 3×3×3 mm^3 coupled to the MPPC 025C (for two bias voltages) and in comparison with PMT XP2020Q. Errors bars are within size of the points. From [8]. . . . 23
1.18 Band structure for electron energies in insulators and semiconductors. From [3] p.354. . . . 24
1.19 Structure of a semiconductor detector and sketch of its funtionality. . . . 25

1.20 The upper plot shows an ideal case of electron and hole currents flowing in a semiconductor following the creation of N_0 electron-hole pairs. In the lower plot, t_1 represents the collection time for the carrier type (either electrons or holes) that is collected first, and t_2 is the collection time for the other carrier. If both are fully collected, a charge of eN_0 is induced to form the signal, where e is the electronic charge. From [3], p.378. . . . 28
1.21 Weighting potential for detections with different pixel pitch to detector thickness ratio, a/d. . . . 29
1.22 Definition of energy resolution. For peaks whose shape is Gaussian with standard deviation σ, the FWHM is given by 2.35σ. . . . 31

2.1 Time-of-Flight Principle . . . 35
2.2 Sketch of the parallax error effect in a LOR in a PET scanner. . . . 36
2.3 (left) LOR of a true PET event, (middle) LOR of a scattered event, and (right) LOR caused by a random coincidence. Where the LOR is indicated b the dotted line whereas the real photon paths are given by the solid lines. 37
2.4 Typical geometry of modern PET system detectors. . . . 38
2.5 A) PMT assigned in 4 quadrants separately. B) Each PMT shares 4 quadrants of 4 block detectors and improves the spatial resolution. From [9]. . . . 38
2.6 FDG cerebral glucose metabolism parametric maps (upper panel) of a normal and an Alzheimer's disease patient. The lower panel shows minimal ^{11}C-PIB updake in the normal individual, but marked with widespread uptake in the cortex and striatum of the same Alzheimer's disease patient, indicating deposition of amyloid plaques. From [10]. . . . 40
2.7 Reconstructed image of the Derenzo phantom obtained by the PEM Flex Solo II (left) and whole body PET (right). From [11]. . . . 44
2.8 The PEM Flex Solo II scanner. From [12]. . . . 44
2.9 Schematic of a SPECT Anger camera. . . . 46
2.10 Schematic representation of four collimator types. Top left and right represent converging and diverging collimators respectively. Bottom left and right represent pinhole and parallel hole collimators. From [13]. . . . 46
2.11 A picture of the Symbia E, a SPECT commercialized by SIEMENS. . . . 47
2.12 Schematic of two Compton cones of two events for photons originated in the same point. . . . 48
2.13 A LOR defined as detection coordinates (x_1,x_2,y_1,y_2) and polar coordinates (s,ϕ). From [14]. . . . 49
2.14 Sinogram for a point source. Each row display corresponds to an individual projection for a ϕ value. From [15]. . . . 50
2.15 The concept of FBP reconstruction algorithm. From [16]. . . . 50
2.16 The concept of ML-EM reconstruction algorithm. From [16]. . . . 51

3.1 The VIP module. . . . 55
3.2 The VIP-PET geometry. . . . 55
3.3 VIP-PIX picture. . . . 56
3.4 Assembly of a CdTe diode and a VIP-PIX. . . . 57
3.5 Architecture of the VIP-PIX. From [17]. . . . 58
3.6 Architecture of on single pixel in the VIP-PIX. From [17]. . . . 58
3.7 Architecture of the proposed pixel readout electronics. From [17]. . . . 59

3.8 Measured output waveforms of the shaper (Ch2) and the discriminator (Ch4) with the waveform of the injected test pulse (Ch3). From [17]. . . . 59
3.9 Measured output waveform of the peak and hold circuit (solid line) with the waveform of the injected test pulse (dashed line). From [17]. 59
3.10 Measured linearity of the TDC. From [17]. 61
3.11 Measured resolution FWHM of the TDC. From [18]. 61
3.12 Measured response of the temperature sensor. From [18]. 62
3.13 NEMA NU 4-2008 VIP scanner counting rates as a function of effective activity concentration and total source activity of a line source for the mouse-size phantom. From [19]. 63
3.14 VIP radial, tangential, and axial spatial resolution (FWHM) as a function of radial offset. From [19]. 64
3.15 Transverse images of the image quality phantom reconstructed using FBP with $1.5{\cdot}10^6$ coincidences. Top row: the phantom is in air; bottom row: phantom is in a water sphere; left: hot rods; middle: cold inserts; right: uniform region. From [19]. 65
3.16 Basic unit detector (A) and full detector (B) geometrical specifications. From [20]. 65
3.17 Values of sensitivity for a ^{22}Na point-like source in different positions along the z-axis (axial scan). From [21]. 66
3.18 Values of coincidence rate as a function of activity concentration in the rat-like phantom as defined in the NEMA NU 4-2008 report [22]. Rate values for true, random, and scatter events are shown separately for comparison. From [21]. 67
3.19 NEMA NU4-2008 phantom is aligned along the Y axis, reconstructed using the LM-OSEM algorithm with five iterations and twenty subsets. Top-left: cold inserts region; top-middle: uniform region; top-right: hot rods. Bottom-left: activity line profiles of cold inserts region; bottom-middle: activity line profiles of uniform region; bottom-right: activity line profiles along the 1 mm and 2 mm hot rods. From [20]. 68
3.20 NEMA NU4-2008 phantom is aligned along the Z axis, reconstructed using the LM-OSEM algorithm with five iterations and twenty sub-sects. Top-left: cold inserts region; top-middle: uniform region; top-right: hot rods. Bottom-left: activity line profiles of cold inserts region; bottom-middle: activity line profiles of uniform region; bottom-right: activity line profiles along the 1 mm and 2 mm hot rods. From [20]. 68
3.21 Schematic of the VIP Compton camera. From [23]. 69
3.22 Sensitivity of the Compton gamma camera, as a function of source activity for ^{18}F. 70
3.23 Sensitivity of the Compton gamma camera, as a function of source activity for ^{99m}Tc. 71
3.24 (Left) Depiction of the Derenzo phantom in the XY plane. (Middle) LM-OSEM result on 70 M Compton coincidences with a Derenzo phantom after applying a 3D median filter. (Right) Line-profile through the rods with 1.5 mm diameter. With the phantom at a distance of 100 mm from the scatterer and an activity of $2{\times}10^8$ Bq, the Compton camera sensitivity is 3.3 cps/kBq and it would take 1.8 min to get the 70 M coincidences used for this image. 71

4.1 Shown the setup to operate the two CdTe detectors in coincidence mode. 74
4.2 Schematic of the CdTe diode structure. 75
4.3 Schematic of the pixel electrode pattern. 75
4.4 A275 input/output waveforms. *Upper:* input pulse. *Bottom: First output (A),* 3 pole configuration. *Second output (B),* 5 pole configuration. 77
4.5 Peak sensing time flow of the input signal, GATE and PEAK section OUTPUT. 78
4.6 Timing diagram of the Trigger Matching Mode of the TDC CAEN 1290N 79
4.7 Waveforms of the preamplifier output (Ch1), shaper output (Ch2) and ENABLE GATE signal of the CAEN V785(Ch4). 81
4.8 Coincidence diagram scheme. Two identical CdTe diodes with identical readouts are operated in coincidence mode. The diodes have been coupled to the preamplifier A250 that is mounted on the test board PC250 and the signal is duplicated. One branch is amplified by a factor of 2 and is connected to the pulse amplitude shaper A275, which is mounted on a test board PC275. The other branch is amplified by a factor of 9 and is connected to the discriminator input. The discriminator output for each CdTe diode is duplicated. One is connected to the AND logic unit and one is connected to one of the input channels of the TDC to measure the relative timestamp, which will take place only if the AND logic is TRUE. For each coincidence trigger the setup delivers the energy and the timestamps of both detectors. 81
4.9 Single event acquisition flow diagram. 83
4.10 Coincidence acquisition flow diagram. 83
4.11 Snapshot of the Graziella GUI. 85
4.12 Scheme of the hierarchy of the devices in the setup. 86
4.13 Spectroscopies of ^{57}Co for events acquired during the minutes 0-3 and 7-9 after biasing the CdTe diode. 88
4.14 Spectroscopy of ^{57}Co at 500 V/mm and room temperature. 89
4.15 Spectroscopy of ^{22}Na at 500 V/mm and room temperature. 90
4.16 Spectroscopy of ^{22}Na at 500 V/mm and room temperature. 91
4.17 Coincidence time difference distribution of two CdTe diodes operated at -1000 V/mm and at -8°C. 92
4.18 FWHM and window with for 70% and 90% of the events for different minimum acceptance energies. 92
4.19 Scatter plot of the energy spectroscopy of both detectors. The events in Fig. 4.17 are enclosed in the pink rectangle. The events in Fig. 4.20 are enclosed in the blue rectangle. 93
4.20 Coincidence time difference distribution of two CdTe diodes operated at -1000 V/mm and at -8°C. Only coincidences with both photons with energy above 500 keV accepted. 94
4.21 Fraction of events of the data sample above different threshold acceptance energies, relative to the energy cut of 25 keV. 94

5.1 Green color: electrode, red circles: passivation holes, white color: isolation lines. 97
5.2 Sketch of the electronic components of one channel of the VATAGP7.1 readout ASIC. 98

5.3 Time sequence of the input/output signals of the VATA serial readout mode. . . . 99
5.4 Layout of the VATAGP7.1 ASIC. . . . 100
5.5 Sketch of the glass substrate design employed. . . . 101
5.6 Picture of the edge view of the CdTe diode assembled on the glass substrate. 101
5.7 Picture of the rigiflex PCB. . . . 102
5.8 Signal conditioning board (left) and rigiflex PCB (right). . . . 103
5.9 Sketch of the funcionalities of the FPGA. . . . 104
5.10 DLL functions used to connect the PC with the FPGA. . . . 105
5.11 Scheme of the relation between the software and the devices in the setup. 106
5.12 Map of the channels connected to the pixels for each diode. Diode 1 in left and diode 2 in the right. The pixels have been colored according to their position in the diode: *corner* pixels in red, *long edge* pixels in orange, *short edge* pixels in green, and *inner* pixels in blue. . . . 106
5.13 Setup response for test pulses with different amplitudes for channel 22. The input pulse with maximum amplitude has 22.25 fC, which corresponds to 618 keV in CdTe. . . . 107
5.14 Calibration of ADC counts vs energy for channel 22. Three points at 59.5 keV, 122 keV, and 511 keV have been used for the fit. The fit offset is in agrement with the measurement of the pedestal. . . . 108
5.15 Noise distribution, in keV and for channel by channel, at 500 V/mm at room temperature in keV. Markers colored according to the colors used in Fig. 5.12 for the position of the pixels. . . . 108
5.16 Scatter plot of the energy values of channel 22 (x axis) and channel 17 (y axis) for any channel triggering. Spectroscopy acquired at 500 V/mm bias voltage and at room temperature. . . . 109
5.17 Scatter plot of the energy values of channel 22 (x axis) and channel 12 (y axis) for any channel triggering. Spectroscopy acquired at 500 V/mm bias voltage and at room temperature. . . . 111
5.18 Charge induction efficiency versus lateral direction of the impact point with z=1 mm, for 500 V/mm in a diode of 2 mm thickness and after 900 ns. 112
5.19 Percentage of events with energy above 2σ per channel compared to the total events triggered in channel 22. . . . 113
5.20 Energy spectroscopy of the 4 pixels surrounding pixel 22. The relative positions of each pixel with respect to the trigger pixel according to Fig. 5.12 are 17 top, 27 bottom, 21 right and 23 left. . . . 114
5.21 Fraction of events undergoing charge sharing normalized to the total events triggered by that pixel. The pixels have been differentiated according to their position in the diode. The average for inner, edge and corner pixels has been drawn with a line. The colors used correspond to those shown in Fig. 5.12. . . . 115
5.22 Spectroscopies of ^{22}Na at 500 V/mm and at room temperature for channel 22. The four distributions corresponds to four cuts on the same data sample. (Blue) raw data, (red) charge sharing events above 2σ rejected, (yellow) charge sharing events above 1σ rejected and (magenta) negative events below 2σ rejected. . . . 116
5.23 Zoom of the plot shown in Fig. 5.22 between 400 keV and 550 keV. . . . 117

5.24 Energy resolution of the four distributions shown in Fig. 5.22 for all the channels in both diodes. The average value for each distribution is drawn with a straight line. . . . 118
5.25 Scatter plot of the energy values of channel 22 (x axis) and channel 12 (y axis) for any channel triggering. Spectroscopy acquired at 500 V/mm bias voltage and at room temperature. . . . 119
5.26 Percentage of events with energy above 2σ per channel compared to the total events triggered in channel 22. . . . 120
5.27 Fraction of events undergoing charge sharing normalized to the total events triggered by that pixel. The pixels have been differentiated according to their position in the diode. The average for inner, edge and corner pixels has been drawn with a line. . . . 121
5.28 Spectroscopies of ^{57}Co at 500 V/mm and at room temperature for channel 22. The four distributions corresponds to four cuts on the same data sample. (Blue) raw data, (red) charge sharing events above 2σ rejected, (yellow) charge sharing events above 1σ rejected and (magenta) negative events below 2σ rejected. . . . 122
5.29 Energy resolution of the four distributions shown in Fig. 5.28 for all the channels in both diodes. The average value for each distribution is drawn with a straight line. . . . 123

6.1 VIP-Detector assembly. A CdTe diode of 10.4 mm × 10.5 mm surface is mounted on a VIP-PIX chip. One ball of 250 μm diameter of BiSn is deposited in each pixel pad of the VIP-PIX. Later the balls are melted on the CdTe diode electrodes through flip chip process. . . . 126
6.2 Baby-board for the VIP-PIX ASIC. The VIP-PIX is attached to the BB with conductive glue. The big pad in the center is a ground plate for the VIP-PIX. . . . 127
6.3 Baby board with a VIP-Detector assembly mounted on top. . . . 127
6.4 Motherboard PCB. . . . 128
6.5 Picture of the setup used for the chip probing. . . . 130
6.6 Probe card used for the probing of the VIP-PIX. . . . 131
6.7 Example of the results shown after a probing process. . . . 131
6.8 Classification of the chips in one wafer. . . . 132
6.9 ADC response for test pulse with amplitudes from 10 mV up to 540 mV. 133
6.10 TDC response for signals sent after delays of 0 ns, 12.5 ns, 25 ns, 37.5 ns, 50 ns, 62.5 ns, 75 ns and 87.5 ns. The error bars grow when the value of the measurements is higher. . . . 134
6.11 TDC measurement for pulses sent after 0 ns, 12.5 ns, 25 ns, 37.5 ns, 50 ns, 62.5 ns, 75 ns and 82.5 ns. 100 measurements have been taken for each point. The error bars are inside the markers. . . . 135
6.12 ^{57}Co spectroscopy for pixel 68 of the VIP-Detector 02E03 at 500 V/mm and at room temperature. . . . 135
6.13 Energy resolution in %, at 122 keV for every pixel of the sample detector with ID 02E03. The pixels have been placed according to their position in the detector matrix. Pixels with no results are switched off either because of bad ADC or high leakage current. A white pixels means a none operational pixel due to bad ADC, or high leakage current, or bad contact with the BiSn solder bump. . . . 136

6.14 The energy resolution presented as FWHM normalized to the peak energy of 122 keV for all the pixels in the sample 02E03. The average of all the pixels is shown with a straight line. . . . 137
6.15 Spectroscopy of ^{22}Na for pixel 68 acquired at 500 V/mm bias voltage and at room temperature. . . . 137
6.16 Energy resolution [%] of the pixels in sample 02E03 at 511 keV at 500 V/mm bias voltage and at room temperature. A white pixels means a none operational pixel due to bad ADC, or high leakage current, or bad contact with the BiSn solder bump. . . . 138
6.17 The energy resolution presented as FWHM normalized to the peak energy of 511keV for all the pixels in the sample 02E03. The average of all the pixels is shown with a straight line. . . . 139

A.1 Datasheet of the JB-2N power supply from Hivolt. . . . 144

B.1 Sketch of the processes carried out by the FPGA. The intermediate stages between the FPGA and the VIP-PIX, the MB and the BB, have been ommited for simplicity. . . . 146
B.2 Five of the pads of the chip ID for one VIP-PIX chip with two of the pads connected. If the two pads are not connected then this bit =0, otherwise =1. . . . 146
B.3 Hierarchy of the devices included in the setup and VISCA. . . . 148
B.4 Screenshot of VISCA front panel . . . 149

List of Tables

1.1 Properties of common inorganic scintillators. From [3] p.235 and [5, 24]. . 13
1.2 Comparative of the three types of photo-detectors typically used with scintillators. Data compiled from [4, 5, 25, 26]. 14
1.3 Characteristic of dynodes. From [27]. 15
1.4 Energy resolution in % of $4 \times 4 \times 10$ mm^3 scintillators at 662 keV (^{137}Cs). From [28]. 18
1.5 Properties of different semiconductor materials at room temperature. Data from [3, 29, 30]. 26

2.1 Some positron-emitting radionuclides used for in vivo imaging with the tracers they are attached to and their applications. Information from [31]. 33
2.2 Current PEM systems with their geometries and detectors employed. . . . 45
2.3 Some single photon emission radionuclides used for in vivo imaging with the tracers they are attached to and their applications. Information from [13]. 45

3.1 Specifications of CdTe Detector and Pixel Electronics. From [17]. 57
3.2 Measured performance of the Analog Front-End plus ADC. From [17]. . . 60

4.1 Basic specifications of the preamplifier AMPTEK A250 and the requirements of the setup. 76

6.1 Classification of chips per wafer and total. 132

Abbreviations

ADC	Analog-to-Digital Converter
ASIC	Application-Specific Integrated Circuit
APD	Avalanche Photodiode
CC	Compton Camera
CT	Computed Tomography
DAC	Digital-to-Analog Converter
DAQ	Data Acquisition
DLL	Dynamic Link Library
DOI	Depth Of Interaction
Eq.	Equation
Eqs.	Equations
FBP	Filtered Backprojection
FIFO	First-In First-Out
Fig.	Figure
FOV	Field-of-View
FPGA	Field Programmable Gate Array
FT	Fourier Transform
FWHM	Full Width at Half Maximum
GAMOS	GEANT4-based Architecture for Medicine-Oriented Simulations
GM-APD	Geiger-Mode APD
HV	High Voltage
i.e.	id est
LM-OSEM	List-Mode Ordered Subset Expectation Maximization
LOR	Line Of Response
LSB	Less Significant Bit

LV	Low Voltage
ML-EM	Maximum-Likelihood Expectation-Maximization
MRI	Magnetic Ressonance Imaging
NEC	Noise Equivalent Count
OSEM	ordered subset expectationmaximization
PCB	Printed Circuit Board
PDE	Photon Detection Efficiency
PEM	Positron Emission Mammography
PMT	Photomultiplier Tube
QA	Quality Assurance
QE	Quantum Efficiency
RMS	Root Mean Square
SF	Scatter Fraction
SI	International System of Units
SiPM	Silicon Photomultiplier
SNR	Signal-to-Noise Ratio
SPAD	Single Photon Avalanche Photodiode
SPECT	Single Photon Emission Computed Tomography
SSRB	Single-Slice Re-Binning technique
Tab.	Table
TDC	Time-to-Digital Converter
THM	traveling heater method
ToF-PET	Time-of-Flight PET
VIP	Voxel Imaging PET
WB-PET	Whole-Body PET

Introduction

Nuclear medicine is a branch of medicine that employs radioactive substances for either the diagnostic or treatment of human diseases. Nuclear medicine can provide a map of the physiologic activity in a human body with diagnostic techniques such as *Positron Emission Tomography (PET)*. In this technique, a biochemical substance with a radionuclide attached to it, a *radiotracer*, is injected into the patient and gets distributed throughout the body. The radiation coming from the patient body is detected by a scanner and the data is processed to obtain an image.

The functional activity information is very useful to detect anomalies in regions with similar density where anatomic diagnostic techniques cannot spot them. PET is a very useful diagnostic tool given that changes in the physiology of a human body appear usually earlier than anatomic changes. PET is usually used to diagnose most type of tumors [32]. PET is also employed for the staging of cancer treatments and to study the response of the patient to such treatments [33]. Apart from its use in oncology, PET is an indispensable tool in the study and diagnostic of brain diseases such as Parkinson [34], Alzheimer or epilepsy.

The principle of PET is based on the detection of two photons created in a positron-electron annihilation. The radiotracer emits a positron which annihilates with an electron of the surrounding media after traveling a short distance of a few millimeters in the body. In this annihilation, two photons, each with an energy of 511 keV, are emitted in opposite directions. The detection of these two photons allows to define a *Line Of Response (LOR)* between the two detection points. By acquiring many of these LORs and applying reconstruction algorithms, the position of the origin of the annihilations can be estimated. The map of the annihilations is an estimation of where the most active regions of the biochemical substance are located inside the body.

State-of-the-art PET scanners are made of scintillation detectors coupled to photodetectors [35–37]. Scintillation detectors offer a very good stopping power for photons of 511 keV and very good timing resolution. For these reasons scintillation crystals are still the main choice for PET detectors. However, scintillation detectors have some intrinsic limitations like poor energy resolution and a segmentation into high granular 3D voxels [4]. Therefore, only a moderate signal purity can be achieved and a poor spatial resolution is obtained, which causes a displacement of the measured LOR from its correct value, called *parallax error*. Devices to obtain the depth-of-interaction (DOI) position along the radial axis are under development but they rarely obtain a spatial resolution better than 1.5 mm FWHM [38].

Semiconductor detectors can overcome the intrinsic limitations of scintillation detectors. Such detectors can provide an alternative solution and lead the new generation of nuclear medicine imaging scanners. Devices employing semiconductor detectors for nuclear medicine applications have already been built [39, 40]. Semiconductor detectors can be segmented into 3D voxels down to a few tens of micrometers pixel pitch and with a thickness from a few hundreds of micrometers to a few centimeters. Hence, they can be designed to achieve a submillimeter spatial resolution in the radial direction without employing any DOI reconstruction algorithms. They also offer a very good energy resolution that allows to discern between good and bad events and increase the signal-to-noise ratio (SNR). Finally, they are compatible with high magnetic fields when they are oriented properly so they can be employed simultaneously with magnetic resonance imaging (MRI) scanners.

The *Voxel Imaging PET (VIP)* Pathfinder project proposes a novel PET scanner design based on pixelated CdTe detectors [41]. The purpose of this design is to solve the problems of scintillation crystals in PET. The excellent energy resolution achieved by CdTe detectors allows to apply an excellent rejection of scattered events and, therefore, to increase significantly the purity of the data sample. The 3D design gives a precision on the impact point in the radial direction of, at least, 1 mm, which reduces the parallax error. Finally, the design is made in such a way that an MRI scanner would not affect the PET performance given that the electric field of the detectors and the magnetic field of the MR device are parallel.

This thesis describes the characterization of the CdTe detectors at different stages: single pixel detector, pixel detector with commercial readout and pixel detector with the VIP developed readout. The theoretical overview describes the interaction mechanisms of positrons and photons with matter, the functionality of scintillation detectors, the photo-detectors used for scintillation detectors readout, and semiconductor detectors with special focus to pixel and CdTe detectors. In the nuclear medicine chapter, a complete overview of such techniques and the state-of-the-art of the scanners are presented. The details of the VIP project are described in the third chapter with special focus to the VIP-PIX chip. Chapters four, five and six present the work on the single pixel diode, the pixelated diode, and the VIP-Detector, respectively. The setups employed for the measurements are described and the results are presented for each of the analyses. Finally, the results obtained are discussed in the conclusions and are put in the context of the state-of-the-art devices for radiation detection in nuclear medicine applications.

Chapter 1

Principles and Techniques of Photon Interaction and Detection

Good comprehension of the physics in nuclear medicine techniques is crucial to understand the behavior, problems and potential improvements of the nuclear medicine scanners. This chapter makes emphasis on the physics concepts behind such techniques. It explains the properties of the radiation processes and the main interaction mechanisms of the particles emitted with matter.

This chapter covers the radiation detectors that are used in nuclear medicine. In particular the scintillator detectors, different types and characteristics, and the photo-sensors used with such scintillator crystals. Finally the chapter touch down on the semiconductor detectors and their mode of operations.

1.1 Positron Interaction with Matter

Positron is usually emitted by a nucleous through a $beta^+$ *decay*. The radionuclide in the radiotracer for PET undergoes a $beta^+$ *decay* and emit a positron. A proton, p, of the nucleus is transformed into a neutron, n, and emits a positron, e^+, and a neutrino, ν, as shown in Eq. 1.1.

$$p \rightarrow n + e^+ + \nu. \tag{1.1}$$

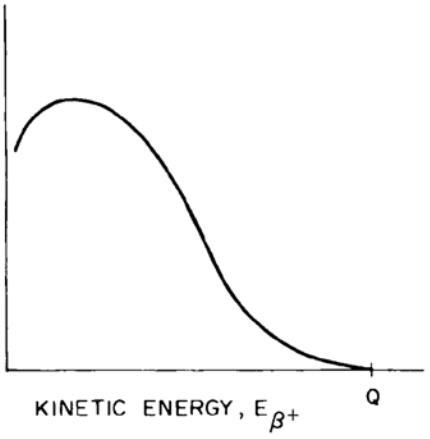

FIGURE 1.1: Shape of a typical positron energy spectrum in a β^+ decay. Adapted from [1] p.67.

Given the extremely low interaction probability of the neutrino with matter, the only effective out-coming radiation from the nucleus is that of the positron. In each decay transition, the energy released by the nucleus is shared by the positron and the neutrino and the energy of the positron, E_{e^+}, follows a continuous distribution of probability with $0<E_{e^+}<Q$ as shown in Fig. 1.1.

Free positrons travel in the media with a velocity according to the kinetic energy they have received. When positrons have lost most of their energy and travel at low velocity, they form a bounded system with an electron of the surrounding media. This system is called a *positronium*. The average distance the positron travels before it forms a positronium with an electron is proportional to its energy.

The positronium is a very similar state to that of the hydrogen atom, but instead of an electron with an orbit around a proton, now both the electron and the positron move in orbits around their center of mass. The positronium decays by means of a positron-electron annihilation. If the positronium is assumed to have, ideally, zero momentum, a pair of two back-to-back gammas of 511 keV will be emitted in completely opposite directions. However, the positronium normally has a slight momentum due to the kinetic energy of either the electron or the positron. In such case the angle between the two photons is slightly less than 180°. The higher the momentum of the positron, the bigger Ψ, the deviation from 180°, is. The process is sketched in Fig. 1.2.

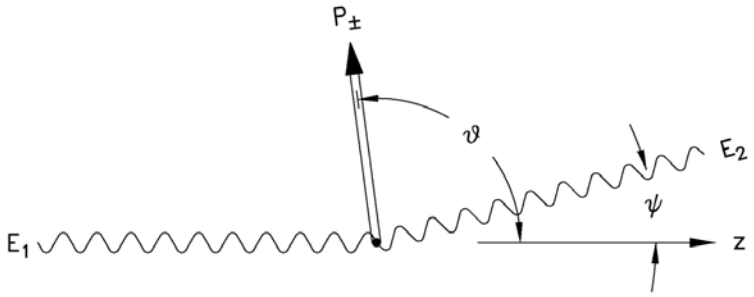

FIGURE 1.2: Scheme of the momentum of photons emitted in a positronium decay (E_1 and E_2) and the positronium momentum ($P_\pm$).

1.2 Photon Interaction With Matter

Photons interact with matter by means of Rayleigh scattering, Compton scattering, photoelectric absorption or pair creation. The probability of each mechanism to occur depends on the energy of the photon and some properties of the material like its density or its effective atomic number, Z. In Fig. 1.3 the partial cross section of these mechanisms for photons interacting in lead as a function of the photon energy is shown.

The photons of interest in this work are those within a range of few keV up to 511 keV. At this energy and for scintillation crystals and semiconductor materials, the dominant process are Compton scattering and the photoelectric effect, described in further detail in the next sections.

1.2.1 Photoelectric absorption

In a photoelectric absorption a photon interacts with electrons bound to the atoms of the media and disappears. This interaction does not take place between photons and free electrons. The photon transfers all its energy to an electron bound to an atom and, in case the photon is energetic enough, the electron becomes free and is called *photoelectron*. This photoelectron usually comes from a low energy shell of the atom and has an energy of

$$E_{e^-} = E_i - E_b, \tag{1.2}$$

where E_i is the incident photon energy and E_b the binding energy of the electron in its original shell. The probability of a photon to undergo a photoelectric absorption is proportional to Z^4 of the material.

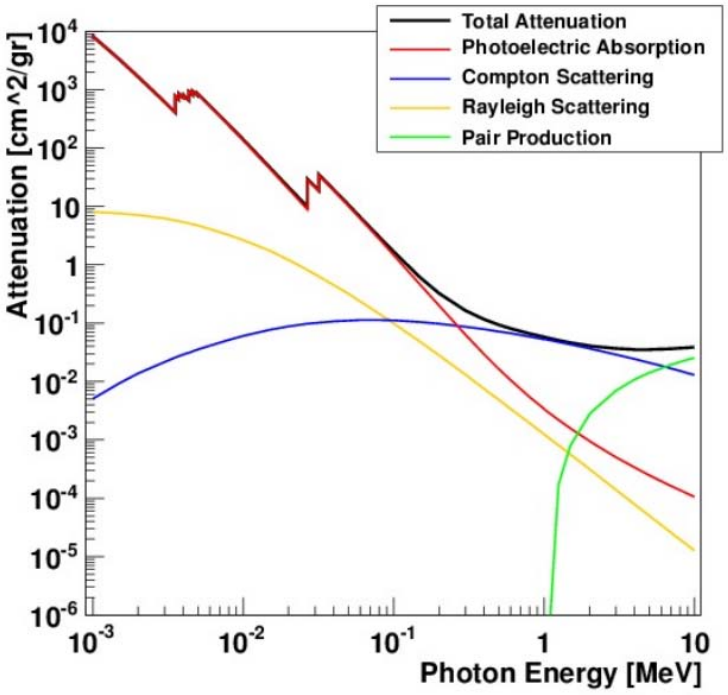

FIGURE 1.3: Linear attenuation coefficient and its contributions in CdTe. Data from [2].

The photoelectron leaves a vacancy in a lower shell of the atom. This vacancy will very likely be filled by an electron from a higher shell, which at the same time could leave a vacancy and produce the same effect. Every time an electron jumps to a lower shell a characteristic X-ray photon is emitted. This photon has an energy of

$$E_X = E_{b'} - E_b, \tag{1.3}$$

where $E_{b'}$ is the energy of the electron in the higher shell. If the electron de-excites to the K shell coming from the L the photon is called K_α, if it comes from the M shell it is called K_β, and so on.

These characteristic x-ray photons have energies of the order of a few tens of keV and are usually reabsorbed quickly in the media. For radiation detectors with small size, the x-ray can escape without interacting with the material, and small peaks corresponding to each transition can be observed next to the main photo-emission peak.

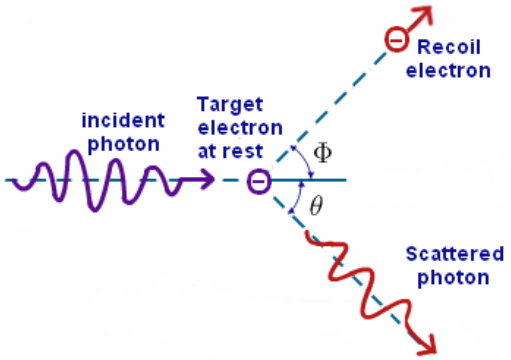

FIGURE 1.4: Compton scattering between a photon and an electron at rest.

1.2.2 Compton scattering

The Compton effect is the process of inelastic scattering of an incident photon with an electron in the absorbing material. In this process, the photon undergoes a change of direction with an angle θ with respect to the incident direction, as sketched in Fig. 1.4. The photon transfers part of its energy to the electron which is then called *recoil electron*.

Applying the conservation of the four-vector energy-momentum and assuming the electron to be initially at rest, one can express the energy of the out-coming photon, E_f, in terms of the energy of the incident photon, E_i, the electron rest mass, m_e, and the scatter angle, θ:

$$E_f = \frac{1}{\frac{1}{E_i} + \frac{1-cos\theta}{m_e c^2}}. \tag{1.4}$$

The probability of a photon to have a Compton interaction with a material depends linearly with Z. The differential cross-section per solid angle of the Compton interaction for an incident photon of energy E_i is predicted by the *Klein-Nishina* formula (from [3] p.51)

$$\frac{d\sigma}{d\Omega} = Z r_0^2 \left(\frac{1}{1+\alpha(1-cos\theta)}\right)\left(\frac{1+cos^2\theta}{2}\right)\left(1+\frac{\alpha^2(1-cos\theta)}{(1+cos^2\theta)[1+\theta(1-cos\theta)]}\right), \tag{1.5}$$

where $\alpha = E_i/(m_e c^2)$ and r_0 is the classical electron radius. Eq. 1.5 is plotted in Fig. 1.5 for different values of photon energy. For incident photons with a few eV energy, all the scattering angles are likely to be produced while for higher values of the order of MeV forward directions are much more likely to occur than backward directions.

In reality the electron is not initially at rest and has a slight momentum. This momentum produces a smearing of the energy of the scattered photon with respect to the prediction

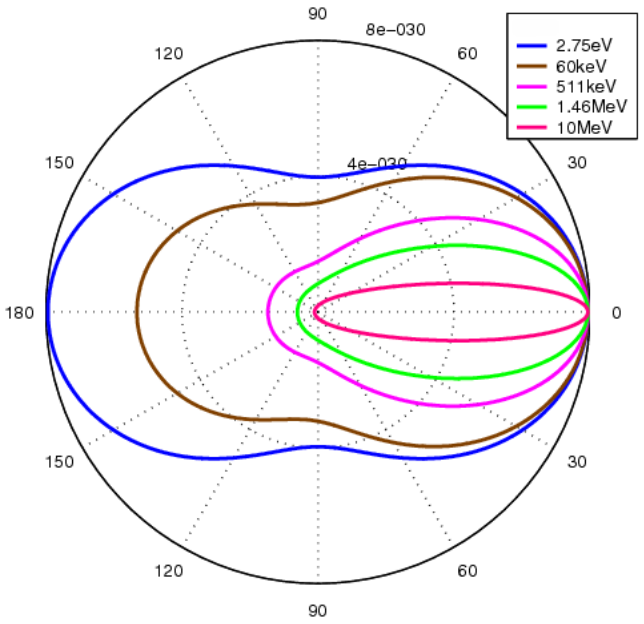

FIGURE 1.5: Klein-Nishina distribution in a polar plot for differed incoming energies. The θ direction gives the Compton angle and the radial axis indicates the probability of that angle to occur.

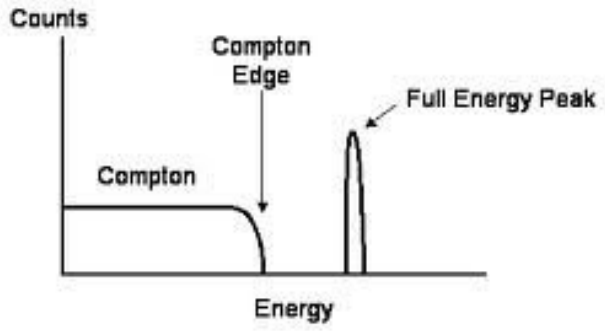

FIGURE 1.6: Energy spectra of the outcoming photons.

in Eq. 1.4. This effect is known as *Doppler Broadening*.

The energy spectra of the out-coming photons for a fixed incident energy is shown in Fig. 1.6. One can see three effects. First, the single peak corresponding to the photons that have not undergone a Compton interaction, the full energy peak. Second, the forbidden region between the Compton edge and the full energy peak. And finally, the

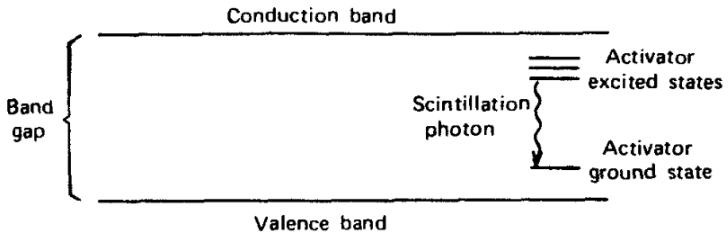

FIGURE 1.7: Energy band structure of an activated crystalline scintillator. From [3] p.232.

Compton distribution, that goes from the Compton edge, where photons deposit the maximum energy and produce *back-scattering* ($\theta = \pi$), down to 0, where the scattering angle is almost 0.

1.3 Scintillation Detectors

Scintillation detectors absorb ionizing radiation and convert part of the absorbed energy into visible light. Scintillation materials can be found in either solid or liquid state and they can be crystalline or non-crystalline, and organic or inorganic. The widespread type of scintillation materials allows to choose which to use according to their properties.

Inorganic scintillation crystals are very appropriate for photon detection and energy measurement. The scintillator produces light with an intensity proportional to the deposited energy. For the particular case of PET, inorganic scintillator crystals are useful because their high density and atomic number gives them a high stopping power for gammas with energies of a few hundreds of keV. In this case a photodetector is needed to transform the light pulse into an electric signal.

1.3.1 Scintillation Mechanism

Inorganic scintillator materials are doped with activator materials in which the band gap is smaller than in the rest of the lattice, see Fig. 1.7. When ionizing radiation interacts with the crystal an amount of free electron-hole pairs are produced. These particles move along the crystal until they get trapped into the activation centers due to their lower energy state. In the decay to the ground state of the activator center, visible light is emitted. The frequency of the visible photons and the decay rate strictly depends

on the properties of the activation center. The overall efficiency of the conversion of deposited energy into visible light is, according to [42]

$$\eta = \beta S Q, \tag{1.6}$$

where β is the conversion efficiency of the photon to electron-hole pairs, S is the transfer efficiency to the energy held by the electron-hole pairs to the luminescence centers, and Q is the quantum efficiency of the luminescence centers themselves.

Scintillator crystals are the main choice for gamma spectroscopy in such different applications as astronomy, homeland security or medical imaging [36, 43, 44] due to their good stopping power for gammas given their high density and Z. This increases the detecting efficiency of the device and reduces the probability of generating Compton interactions in the material, which is an undesirable source of noise for nuclear medicine imaging scanners.

1.3.2 Characteristics of Scintillators

Scintillation detectors have good timing properties. The decay time is relatively short and they also have a small time jitter. This allows to measure the detection time with very good precision and to achieve high count rates.

Some scintillators are hygroscopic, i.e., they absorb water from the environment and their performance is affected. This creates extra problems in the packaging problems that may be added to the possible fragility of the crystal.

The photon yield is defined as the average number of photons created per unit of energy. With a higher photon yield more photons will be emitted and there will be less fluctuation in the number of photons. The statistical fluctuation is therefore reduced and the energy resolution improves.

The coupling between the crystal and the photodetector is also important. The transmission of the light pulses into the photodetector coupled to the scintillator is better when both have similar refractive indices. The desired refractive index for a photodetector in this case is around 1.5.

The properties of different scintillator crystals are summarized in Tab. 1.1.

1.3.3 Scintillator Crystals for PET

The scintillation crystals used in commercial PET scanners are LSO [36], LYSO [35] and BGO [37]. Other scintillators like BrF_2 (fast component) and plastic offer excellent timing properties, but the low photon yield in the first case and the low density in the second make them less efficient than other candidates to capture the gamma photons and measure their energy. On the other hand, the $CdWO_4$ has very similar density, Z and photon yield than LSO or BGO and could be a good choice to capture gamma photons and measure their energy but due the low decay time it is not a good choice for PET.

1.4 Photodetectors

The intensity of the light emitted by a scintillator is usually measured by means of a photodetector. Photodetectors are radiation detectors able to measure light intensity by transforming the light pulse into an electric pulse with an amplitude proportional to the intensity. When a photodetector is coupled to a scintillation crystal new bounds are added to the overall detector performance.

The main characteristics of a photodetector coupled to a scintillation crystal are the *quantum efficiency (QE)*, the gain and the response time jitter. The QE is the ratio of the detected photons over the total emitted by the crystal. A low quantum efficiency of a photodetector results in an effective reduction of the detected scintillation light and so, a degradation of the energy resolution of the overall detector. A photodetector with high gain can deliver a signal to be directly processed whereas a photodetector with low gain might require extra amplification steps that might add extra noise. A good timing response of the photodetector is also important if the full detector is desired to achieve high count rates.

The three main types of photodetectors for scintillation crystals are the *Photomultiplier Tubes, (PMT)*, the *Avalanche Photodiodes, (APD)* and the *Silicon Photomultipliers, (SiPM)*. The quantum efficiency, time performance and other interesting features of

Crystal	**Density** $[g/cm^3]$	**Effective** Z	**Hygroscopic**	**Decay time** $[\mu s]$	**Photon Yield** Photon/keV	**Refractive** Index
$CdWO_4$	7.90	64	No	1.1-14.5	15	2.3
Lu_2SiO_5(Ce) (LSO)	7.40	65	No	0.047	25	1.82
LYSO	∼LSO	∼LSO	No	∼LSO	∼LSO	1.82
$Bi_4Ge_3O_{12}$ BGO	7.13	75	No	0.30	8.2	2.15
Gd_2SiO_5 GSO	6.71	59	No	0.056-0.4	15	2.3
$LaBr_3$(Ce)	5.29	46	Yes	0.026	63	2.05-2.10
BaF_2 (slow)	4.89	53	No	0.63	9.5	
BaF_2 (fast)	4.89	53	No	0.0006	1.4	1.56
CsI(Na)	4.51	54	Yes	0.46-4.18	39	1.84
CsI(Tl)	4.51	54	Slightly	0.68-3.34	65	1.80
NaI(Tl)	3.67	51	Yes	0.23	38	1.85
CaF_2	3.18	17	No	0.9	24	1.47
Plastic	1.03	12	No	0.002	10	1.58

TABLE 1.1: Properties of common inorganic scintillators. From [3] p.235 and [5, 24].

	PMT	**APD**	**SiPM**
Gain	10^5-10^7	50-100	10^5-10^6
Time jitter [ns]	0.3	>1	0.1
QE @ 420nm [%]	~25%	~70%	10-40 (PDE)
Bias [V]	≥1000	100-1500	15-100
Temperature coefficient [%/°C]	¡1	2-3	3-5
Magnetic field sensitivity	Yes	No	No
Active area	1-2000 cm^2	1-100 mm^2	1-10 mm^2

TABLE 1.2: Comparative of the three types of photo-detectors typically used with scintillators. Data compiled from [4, 5, 25, 26].

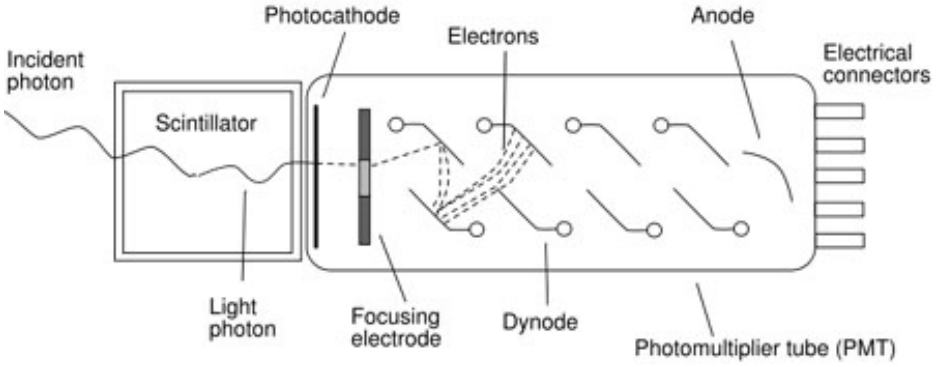

FIGURE 1.8: Basic elements of a PM tube. From [4].

these different devices are summarized in Tab. 1.2. The three photodetectors will be further explained in the next sections.

1.4.1 Photomultiplier Tubes

PMTs are photo-detectors commonly used in medical imaging for the readout of scintillation crystals. More than 80 years after its development they are still the most employed photo-detectors to convert scintillation photons into an electric signal. They offer high gain and very good timing properties. Because of their excellent time resolution of less than 1 ns, they are be very well appreciated in PET applications, specially in *Time-of-Flight PET (ToF-PET)* [45–48].

The main structure of a PMT is shown in Fig. 1.8. Although they can be designed in many different shapes, the same working principle applies. A PMT consists of a vacuum tube in which there is a photocathode, several electrodes called dynodes and an anode.

Dynode	Collection Efficiency	Features
circular-cage	good	compact, high speed
box-and-grid	very good	high collection efficiency
linear-focused	good	high speed, high linearity
venetian blind	poor	large input window
fine mesh	poor	for use in high magnetic field, high linearity
MCP	poor	ultra-high speed

TABLE 1.3: Characteristic of dynodes. From [27].

1.4.1.1 Principle of Operation

Photons interact with the photocathode by means of the photoelectric effect, in which photoelectron is produced. The probability of the photocathode to interact with the light photons is given by the quantum efficiency. A bias voltage is applied between the dynodes in such a way that when the photoelectron appears in the photocathode it drifts towards the first dynode. The photoelectron collides with the first dynode and generates more photoelectrons which will drift towards the next dynode. The shape of the dynode is important in order to focus the electrons to the next dynode and avoid a large spread in transit path lengths. In every dynode the number of electrons produced is multiplied. For n dynodes with an average electron gain N, the overall gain is $G = N^n$. Different structures of dynodes lead to different characteristics. An overview of these characteristics for each structure is shown in Tab. 1.3. The last electrode is the anode, where the final signal is induced.

1.4.1.2 PMT Characteristics

PMTs usually have from 10 to 15 dynodes with an electrical potential difference of 100 V to 150 V each. The total bias voltage to apply to the PMT is between 1000 and 2000 V. The drift time of electrons inside the PMT does not depend on the amount of photoelectrons produced in the photocathode, i.e., the timing response of the detector does not depend on the deposited energy. This leads to a reduced time jitter as mentioned before.

The QE is of extreme importance in the very first dynodes because their fluctuation affects more to the overall statistical fluctuation of the PMT, and therefore, the energy resolution of the detector. Moreover, the electric field inside the PMT has many different

orientations. Unlike semiconductor detectors, a PMT cannot be operated under strong magnetic fields.

1.4.2 Avalanche Photodiodes

In an APD, the photon interacts with the semiconductor bulk and creates an electron-hole pair by means of the photoelectric effect. This electron is later multiplied due to the avalanche process that takes place in a semiconductor diode when a big bias voltage is applied. APDs offer a high QE and good energy resolution. Moreover, they can be operated under strong magnetic fields without a deterioration on their performance when the electric and magnetic field are parallel.

Among their drawbacks there is the limited gain, that usually requires extra amplification steps in the readout process, response time jitter over 1 ns and a performance very sensitive to the bias voltage.

1.4.2.1 Principle of Operation

The gain of the APDs depends on the bias voltage applied and the temperature of the diode. For this reason, very stable conditions are required to achieve a good energy resolution of the device.

The most common configuration used to fabricate APDs, among others, is the reach-through configuration, which is shown in Fig. 1.9. It consists of four regions: the bulk region, π, the two electrodes, which are p^+ and n^+ doped, and a p doped region between the bulk and the n^+ electrode.

Light photons cross the p^+ layer and interact in the bulk, π. Light photons usually interact through the photoelectric effect given their reduced energy, <4 eV, and produce an electron-hole pair. Electrons and holes drift towards opposite anodes, n^+ and p^+ respectively, due to the bias voltage applied. Holes reach the electrode and get trapped. When electrons reach the p region, called *multiplication region*, additional electron-hole pairs are created in a cascade process due to the higher electric field. The extra electrons produced drift towards the n^+ electrode and induce a current signal.

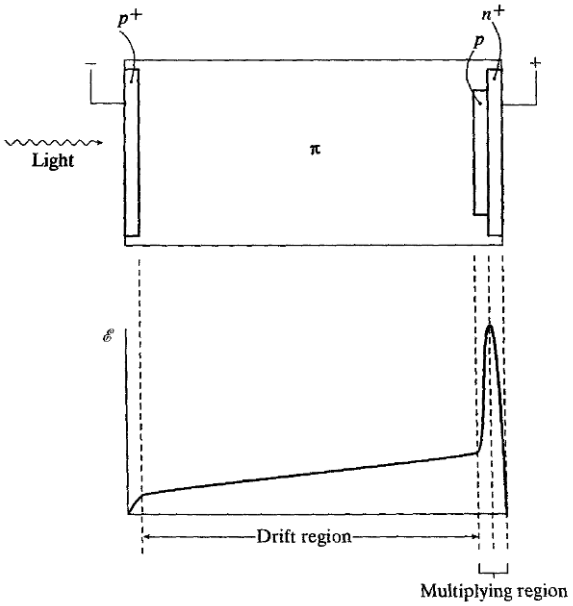

FIGURE 1.9: A configuration for an avalanche photodiode is sketched at the top of the figure. Below is a plot of the resulting electric field when a bias voltage is applied. From [3], p.291.

1.4.2.2 APD Properties

The typical gain achieved by this kind of devices is of the order of a few hundreds [49, 50]. The magnitude of the signal is not enough to apply signal processing, therefore an amplifier has to be coupled to the APD output. Another inconvenience is the noise created in the avalanche process due to the fluctuation of charge carriers. The relative noise to the total signal increases depending on the multiplication factor [51]. This effect is known as *excess noise* and is evaluated quantitatively as the *excess noise factor*.

Anti-reflective coating is used around the surface of the semiconductor to achieve a good QE. The QE of these devices, which depends on the photon wavelength can reach 90% [52]. Another attractive feature of APDs is their compatibility with strong magnetic fields. Since the typical thickness of APD is of a few hundreds of micrometers, the electron drift is not affected by the magnetic field.

The main disadvantage of APDs is their timing response. The timing response depends on the impact point along the drift direction and, hence, the time jitter is big compared to that of PMTs.

The timing and energy resolution performance of a scintillator detector coupled to an APD for different bias voltages is shown in Fig. 1.10. The timing resolution does not

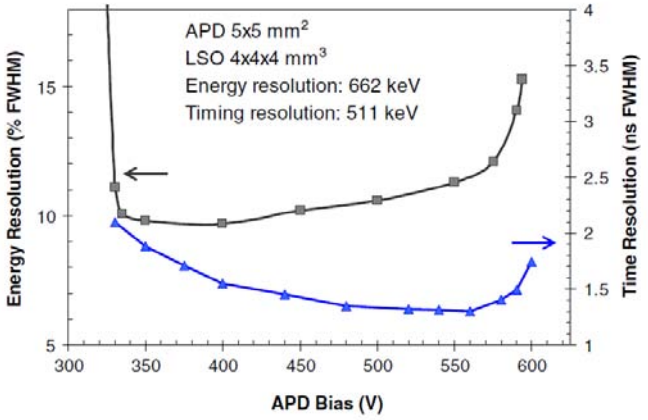

FIGURE 1.10: Variation of energy and timing resolution as a function of APD bias. From [4].

Scintillators	PMT	APD
LSO_{ref}	12.4	9.5
LSO_A	11.8	10.4
LSO_B	11.2	9.8
LSO_g	12±1	10.2±0.1
$LYSO_g$	13±1	10.2±0.3
GSO	13.7	7.5
BGO	20.9	10.5

TABLE 1.4: Energy resolution in % of 4 × 4 × 10 mm^3 scintillators at 662 keV (^{137}Cs). From [28].

reach in any case values less than <1 ns, like PMTs, but the energy resolution is slightly better. A comparison of the energy resolution for PMTs and APDs coupled to different scintillator crystals is shown in Tab. 1.4. In all cases the APD has clearly a better energy resolution than PMT.

1.4.2.3 Geiger Mode APD

The increase of the bias voltage in an APD increases the gain. This is due to the fact that when electrons are accelerated they are more likely of ionizing other atoms in the lattice and multiply themselves. The *breakdown voltage* is that voltage at which the rate of multiplication of electrons is equal to the rate of the "extraction" of the electrons from the diode. When an APD is operated above the breakdown voltage the current produced in a single photon detection grows exponentially with time. The current will increase as much as allowed by the power supply applied to the diode. This behavior is comparable to that of the *Geiger counter* in gas detectors.

Geiger-Mode APDs (GM-APDs) or *Single Photon ADPs (SPADs)* are APDs operated at a bias above the breakdown voltage. Once a single photon is detected and the diode enters in a Geiger mode, the current flowing through the diode is continuous and has to be stopped by means of an electronic circuit. The process of stopping the continuous discharge after a particle detection to make the diode stable and ready do detect another particle again is called *quenching*. The simplest way to obtain a quenching circuit is to place a resistor between the voltage supply and the photodiode.

GM-APDs show timing properties comparable to PMTs with high timing resolutions of a few tens of nanoseconds [53–55]. They are also capable of working in high magnetic fields. They are excellent as photon counters but they cannot measure the energy and they have a relatively large dead-time after each photon detection.

1.4.3 Silicon Photomultipliers

SiPMs are arrays of small GM-APDs of reduced size connected in parallel and delivering a single output signal. SiPMs are, essentially, APD detectors. However, they offer a gain comparable to that of PMTs of the order of $\sim 10^5$-10^6 and a response time jitter below a nanosecond. Like the APDs, SiPM can work in the presence of high magnetic fields. For these reasons SiPM is becoming a preferred choice for the readout of scintillator crystals.

1.4.3.1 Principle of Operation

Each of the cells of the SiPM behaves as explained in Sec. 1.4.2.3. The typical size of each cell is from $\sim 20\times 20$ μm^2 to $\sim 100\times 100$ μm^2 and each SiPM has of the order of 10^3-10^4 cells. All cells are connected in parallel through a quenching resistor and the full array delivers a single output. An electronic schematic of a SiPM is shown in Fig. 1.11. Each cell needs to recharge after a detection and is inoperative for a dead time that depends on the quenching resistor and the capacitance of the cell, i.e., the cell size. The single cell dead time lasts typically from tens to hundreds of ns but due to after-pulse effects like cross talks between neighbor cells or delayed release it can go up to the order of μs.

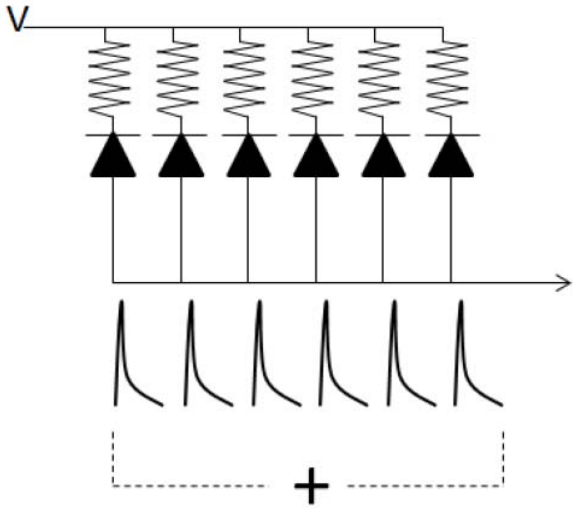

FIGURE 1.11: Schematic of the equivalent circuit of a SiPM with 6 cells.

The probability to detect a photon with a SiPM device is measured by the *photon detection efficiency (PDE)*, which depends on the QE of the active area, the ratio of the sensitive to total area ($\epsilon_{geometry}$) and the probability of a carrier in the active cell to initiate a Geiger discharge (ϵ_{Geiger}) as follows

$$PDE = QE \times \epsilon_{geometry} \times \epsilon_{Geiger}. \tag{1.7}$$

1.4.3.2 SiPM Properties

The bias voltages applied to the SiPM cells are usually less than 100 V. Given their extremely thin shape, such voltages are enough to exceed the breakdown voltage. The performance of SiPMs is extremely depending on the bias voltage. The gain is very sensitive to variations of the bias voltage as it is shown in Fig. 1.12. One can see that not only the gain of the device gets affected but also its linearity. At 71.1 V the system is fairly linear whereas for 72.5 V (an increase of $< 2\%$ of the absolute bias voltage) the behavior is far from being linear.

As other semiconductor detectors, SiPM are also sensitive to temperature. In Fig. 1.13 the relative gain of a SiPM device as a function of the temperature is shown. The detector gain decreases almost 25% with an increase of temperature of 10°C. Furthermore, in the case that the device employs a quenching resistor, the change of the resistivity due to

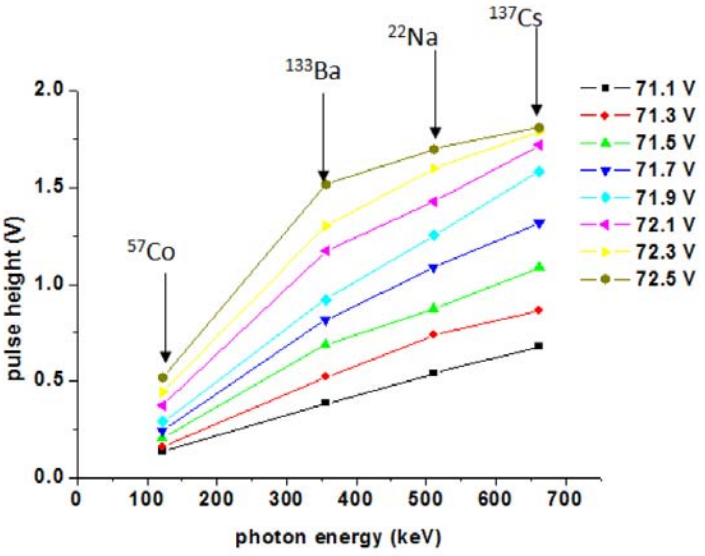

FIGURE 1.12: Effects of non-linear SiPM operation on identification as a function of photon energy and for different bias voltages. Data was taken with a SiPM with a 3×3 mm^2 cross-sectional area from Hamamatsu (50 μm micro-cell size). The scintillator used was a 3×3×5 mm^3 LSO crystal element. From [5].

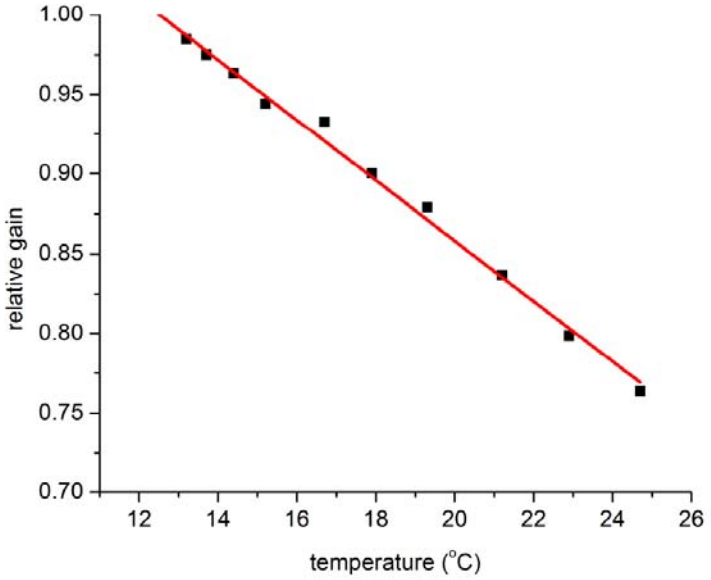

FIGURE 1.13: Dependence of SiPM gain on temperature. Data taken with a SiPM with a 1×1 mm^2 cross-sectional area from Hamamatsu (50 μm micro-cell size). All the temperature measurements were performed at a constant SiPM bias. From [5].

temperature variations can lead to changes on the pulse shape with other implications not only in the gain but also on recovery time and timing performance.

SiPMs show high dark count rate. Dark counts are signals created in the cells by other reasons than the incoming photons, like thermal excitation or after-pulsing effects. The dark count rate depends on the bias voltage and on the temperature, as shown in Figs. 1.14 and 1.15 respectively, and can reach values of up to several MHz.

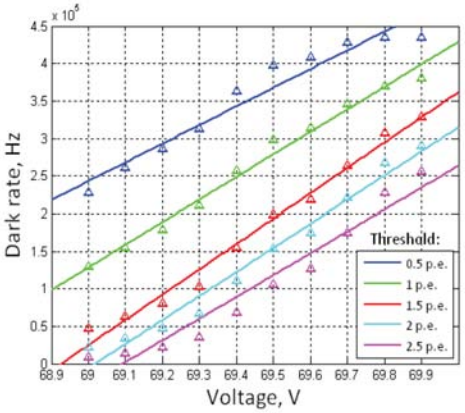

FIGURE 1.14: Dark rate vs. Bias voltage (T=25°) for a SiPM device. From [6].

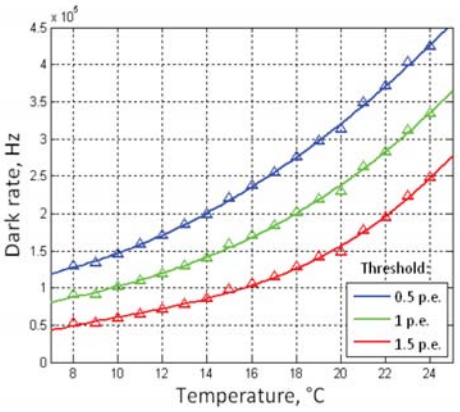

FIGURE 1.15: Dark rate vs. Temperature (constant gain) for a SiPM device. From [6].

The time resolution of SiPMs depends on the trigger threshold at which the output signal is compared to a predetermined DC level: the closer the threshold is to the noise baseline, the better time resolution is achieved. The bias voltage affects the breakdown timing properties and, hence, the time resolution of the device. A plot of the coincidence time resolution for two SiPMs of 50 μm pitch vs the bias voltage and at different trigger threshold values is shown in Fig. 1.16. One can see that the best timing resolution (220 ps) is achieved for the lowest trigger threshold (50 mV) and for a relatively large bias voltage (72.4 V).

The intensity of light that interacts with a SiPM is proportional to the amount of cells that undergo a breakdown discharge. Given that all the output signals of all the cells are summed, the height of the pulse is a measure of the deposited energy on the scintillation crystal. SiPMs offer an energy resolution comparable to that of PMTs, as shown in Fig. 1.17. A small increase in bias voltage will improve the energy resolution of a SiPM.

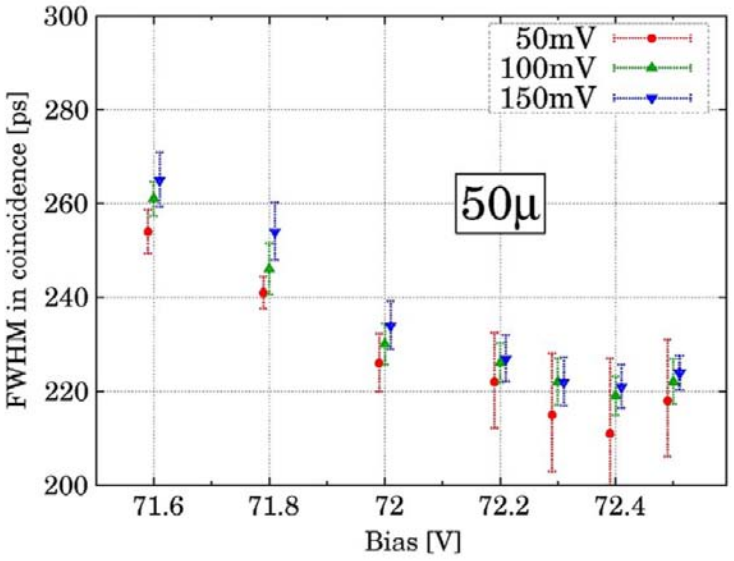

FIGURE 1.16: Coincidence time resolution for a Hamamatsu S10931-050P SiPM vs bias voltage for different trigger thresholds. The best value is achieved (220 ps FWHM) at 72.4 V. From [7].

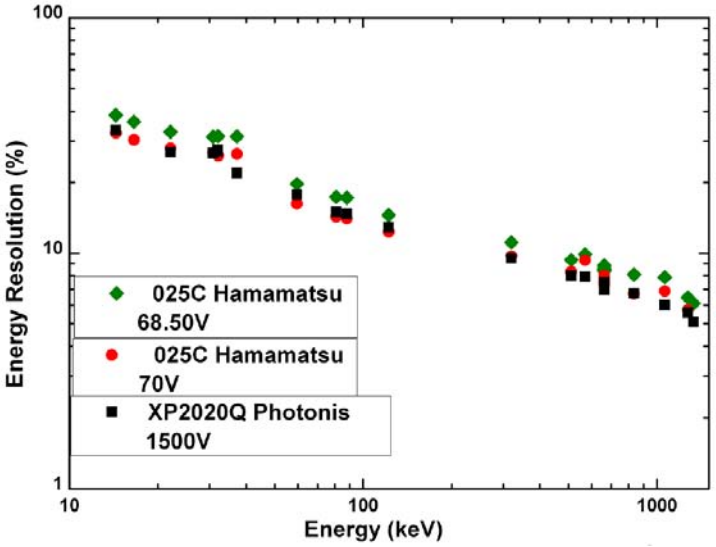

FIGURE 1.17: The energy resolution measured with CsI(Tl) 3×3×3 mm^3 coupled to the MPPC 025C (for two bias voltages) and in comparison with PMT XP2020Q. Errors bars are within size of the points. From [8].

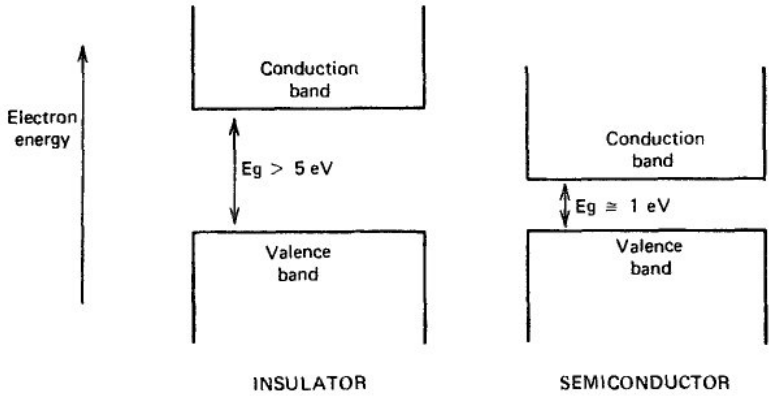

FIGURE 1.18: Band structure for electron energies in insulators and semiconductors. From [3] p.354.

1.5 Semiconductor Detectors

Semiconductor materials offer very good properties as radiation detectors. Their small pixel pitch, detector thickness, large bandgap, and high yield of e^-/keV makes them suitable for different applications. They achieve an excellent energy resolution due to the lower statistical fluctuation compared to other radiation detectors such as scintillator crystals and they can be operated under strong magnetic fields.

Among their drawbacks there are the large jitter in the trigger time stamp, the high manufacturing cost, and the complexity on the readout electronics, which require low noise and compact size.

The most commonly used semiconductor detectors are silicon (Si), germanium (Ge), cadmium telluride (CdTe), cadmium zinc telluride (CZT) and gallium arsenide (GaAs).

1.5.1 Semiconductor Band Structure

Semiconductor materials have periodic crystalline lattices with allowed energy bands where the electron can travel along all the bulk, called *conduction bands*. *Valence bands* which keep the electron bound to one single atom. Depending on the energy gap between the conduction and valence band, the material is considered an *insulator* or a *semiconductor*, as shown in Fig. 1.18

For energy gaps of about 5 eV or more, thermal excitation of electrons, at reasonable temperatures, is very unlikely to happen and the conduction band remains empty. For a

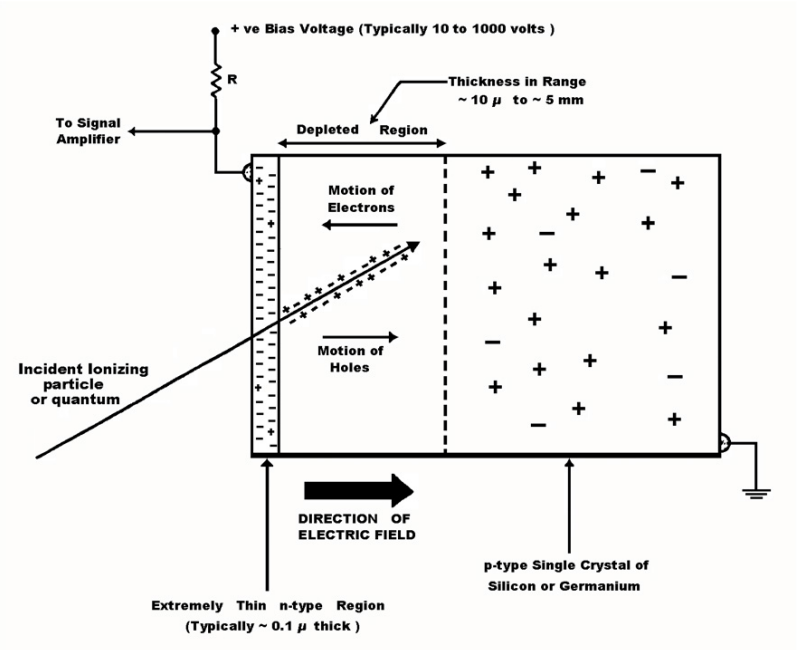

FIGURE 1.19: Structure of a semiconductor detector and sketch of its funtionality.

bandgap of 1 eV, thermal excitation becomes feasible and some electrons can populate the conduction band. The higher the number of electrons in the conduction band, the more conductor the material becomes.

Semiconductor materials become more conductive with temperature increase due to higher rate of valence-to-conduction band transitions of electrons.

1.5.2 Semiconductor Detector Structure

A coplanar semiconductor detector consists of a bulk semiconductor material sandwiched by two electrodes. A bias voltage is applied between the electrodes to create a *depletion region* in the semiconductor. A depletion region is the part of the material from where, due to the electric field, all the free charges have drifted towards a region closer to the electrodes. In Fig. 1.19 the electrodes and the depletion region of a semiconductor detector are sketched.

1.5.3 Principle of Operation

When a particle ionizes an atom of the semiconductor, an electron in the valence band obtains energy to jump to the conduction band. The vacancy left by the electron in the

	Si	**Ge(77 K)**	**CdTe**	**CZT**	**GaAs**
Z	14	32	48/52	48/30/52	31/33
Density [g/cm^3]	2.33	5.32	6.06	6	5.32
Band-gap [eV]	1.12	0.72	1.52	1.64	1.43
Ionization Energy [eV/e-h pair]	3.61	2.98	4.43	4.64	4.2
Fano factor ($\sim$100 keV)	0.06	0.06	0.06	0.1	0.14
$\mu_e \left[cm^2/(V \cdot s)\right]$	1350	3900	1000-1100	1000-1300	8500
$\mu_h \left[cm^2/(V \cdot s)\right]$	480	1900	100	50-80	400
$(\mu\tau)_e \left[cm^2/V\right]$	>1	>1	$3{\cdot}10^{-3}$	$4{\cdot}10^{-3}$	$8{\cdot}10^{-5}$
$(\mu\tau)_e \left[cm^2/V\right]$	$\sim$1	>1	$2{\cdot}10^{-4}$	$1.2{\cdot}10^{-4}$	$4{\cdot}10^{-6}$

TABLE 1.5: Properties of different semiconductor materials at room temperature. Data from [3, 29, 30].

atom is called a *hole* or *vacancy* and behaves as a charge carrier with the same amount of charge as the electron but with opposite sign, usually represented as h^+. The pair of both charge carriers is called an *electron-hole pair*.

The depletion region is the only active part of the semiconductor able to detect particles. If a particle ionizes atoms in a non-depleted region of the semiconductors, the electron-hole pairs created would be rapidly recombined with other free electron or holes and no signal would be obtained.

1.5.3.1 Fano Factor

Assuming that the ionizing energy needed to create an electron-hole pair is ϵ, the amount of created pairs should be E/ϵ. This is valid for independent processes that obey a Poisson distribution but a slight difference from this value is observed in semiconductor detectors.

The *Fano Factor, F*, is defined to correct the statistical distribution predicted for a Poisson distribution

$$F \equiv \frac{\text{observed statistical variance}}{E/\epsilon}. \tag{1.8}$$

The value of the Fano factor depends on the material and the deposited energy, the values for some semiconductor materials are shown in Tab. 1.5. Small values of the Fano factor mean small statistical fluctuation and therefore, good energy resolution.

1.5.4 Charge Carrier Drift

Electrons and holes created in the ionization process drift towards opposite directions due to the electric field. The motion of a hole can be understood as an electron from a neighbour atom filling the vacancy. The vacancy has effectively moved to the neighbor atom and the process is repeated successively until the vacancy reaches an atom of the electrode. The drift velocity of both charge carriers depends on the bias voltage. The mobility, μ, for each charge carrier can be defined as

$$v_h = \frac{\mu_h V}{D} \tag{1.9}$$

$$v_e = \frac{\mu_e V}{D}, \tag{1.10}$$

where V is the bias voltage and D is the detector thickness. Mobilities of electrons and hole are characteristic of each material, the values for some semiconductor materials are summarized in Tab. 1.5. Eqs. 1.9 and 1.10 do not hold for high bias voltages. At a given bias voltage the velocity will not increase linear with it and a saturation velocity will be reached.

Charge carriers can interact with other free particles and suffer dispersion. They can also be trapped by impurities in the crystal lattice or recombine with thermally generated electron-hole pairs. The *lifetime*, τ, is defined as the average time that takes for a charge carrier to be trapped in a material. The *mobility-lifetime product*, $\mu\tau$, is the average distance a charge carrier can travel along the material normalized to the bias voltage.

1.5.5 Signal Induction

Charge carriers induce a current signal on the electrodes due to their motion along the material. The total induced charge has the contributions of both charge carriers. Each charge carrier induces signal on the electrode during its drift time. Depending on the impact position the ratio of the contributions of charge carriers will change as it is shown in Fig. 1.20top.

The total induced charge vs time is shown in Fig. 1.20 bottom. One can see two different slopes corresponding to both charge carrier drifting (0,t_1) and to one charge carrier in the last phase (t_1,t_2).

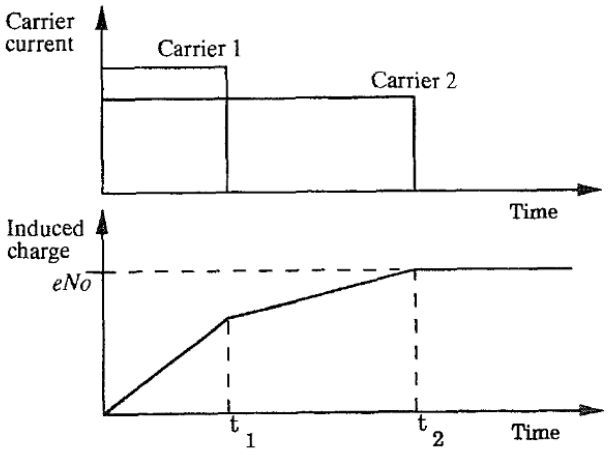

FIGURE 1.20: The upper plot shows an ideal case of electron and hole currents flowing in a semiconductor following the creation of N_0 electron-hole pairs. In the lower plot, t_1 represents the collection time for the carrier type (either electrons or holes) that is collected first, and t_2 is the collection time for the other carrier. If both are fully collected, a charge of eN_0 is induced to form the signal, where e is the electronic charge. From [3], p.378.

1.5.6 Charge Trapping

The fraction of charge carriers suffering trapping effect is predicted by the Hecht relation [56], which can be expressed as [57, 58]

$$\frac{Q^*}{Q_0} = \frac{v_h \tau_h}{W}\left(1 - exp\left[\frac{-x_i}{v_h \tau_h}\right]\right) + \frac{v_e \tau_e}{W}\left(1 - exp\left[\frac{x_i - W}{v_e \tau_e}\right]\right), \tag{1.11}$$

where Q^* is the total charge reaching the electrodes, Q_0 the initial charge created by the ionization, v is the charge carrier velocity, W the detector thickness, x_i the interaction point position along the drift direction measured from the cathode and τ is the charge carrier lifetime. The product $v\tau$ is the mean free path of the charge carrier and is an indication of the average distance than can travel along the detector before being trapped.

Charge trapping creates a blurring in the low energy direction and deteriorates energy resolution. Short $v\tau$ for either charge carrier or huge detector thickness leads to big fraction of charge lost due to trapping. A strategy to reduce the charge trapping effect and obtain a good energy resolution is to operate thin detectors at high bias voltage like it is shown in [59].

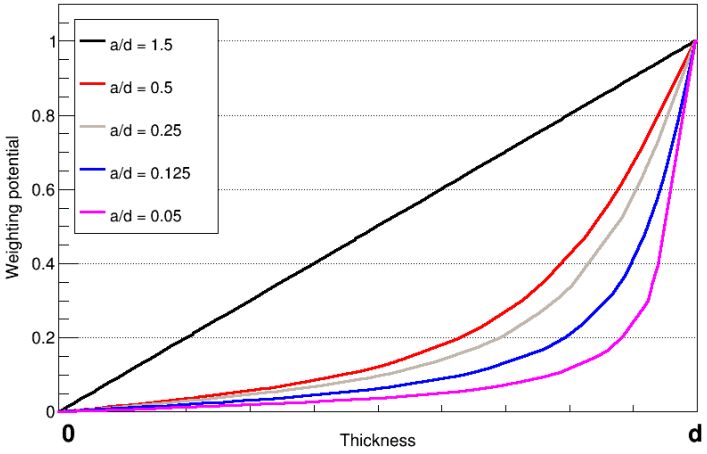

FIGURE 1.21: Weighting potential for detections with different pixel pitch to detector thickness ratio, a/d.

1.5.7 Small Pixel Effect

The charge induction on the electrodes is linear with time (or charge carrier position) for each charge carrier when a planar electrode is used, i.e., an electrode with approximately a pixel pitch, a, bigger than twice the detector thickness, d, $a \gtrsim 2d$.

The method to evaluate the signal induced in a material by the motion of an electronic charge is to use the Shockley-Ramo theorem [60, 61]. This theorem defines a *weighting potential* dependent on the drift direction position according to which the charge is induced in a certain point. This concept is used [62] to obtain a numeric expression to evaluate the weighting potential, this expression has been used to evaluate the weighting potential for CdTe detector with different a/d ratios, it is shown in Fig. 1.21. For a a/d ratio of $\sim$1.5 the charge induction is linear with time whereas for values below 0.5 the curve becomes more pronounced, with a smaller slope at the beginning and bigger and the end.

1.5.8 Charge Sharing

It is common to find pixel detectors with a very low a/d ratio where a could be around tens of micrometers while d around millimeters. With such small pixels a single energy deposition can induce charge in more than one pixel, this effect is known as *charge sharing*.

The energy of an event undergoing charge sharing is shared between, at least, two pixels. To reduce the charge sharing between pixels, one can merge the energies measured by those pixels. By the summing process, the associated error increases and a deterioration of the energy resolution is unavoidable. This kind of events can be also rejected in order to not affect the energy resolution and to avoid extra offline corrections. Algorithms to reduce the effect of charge sharing in pixel semiconductor performance are presented in [63, 64].

1.5.9 Energy Resolution

The response of a semiconductor detector for ionizing radiation is a current pulse characterized by its height and called pulse height $PH(E)$, where E is the deposited energy of the particle. The response function $\rho(E', E)$ gives the energy measured in the detector E' when the deposited energy by the particle is E. Ideally, the response of a detector to particles with energy E should be a Dirac delta distribution $\delta(E' - E)$. In the reality, this distribution frequently becomes Gaussian. Assuming a theoretical energy spectrum $S(E)$, the $PH(E)$ spectra will be the result of the following convolution:

$$PH(E) = \int S(E')\rho(E', E)dE'. \tag{1.12}$$

The energy resolution of a detector is defined as the ratio

$$R = \frac{\Delta E}{E_0}, \tag{1.13}$$

being ΔE the FWHM[1] of the Gauss distribution corresponding to a mono-energetic peak of energy E_0, see Fig. 1.22. The contribution to the FWHM can come from different sources: the statistical fluctuation of the charge carriers produced in the ionization process, the noise introduced by the electronics in the readout process, the dark current due to thermally generated electron-hole pairs, escaped energy, and charge sharing. For a number n of contributions that are assumed to be independent the total noise can be expressed as

$$FWHM_{Total} = \left(\sum_{i=0}^{i=n} FWHM_i^2\right)^{1/2} \tag{1.14}$$

[1]From English *Full Width at Half Maximum*. It is the width of a curve at a height equal to half the value of the highest point. For a Gaussian distribution $FWHM = 2.35\sigma$.

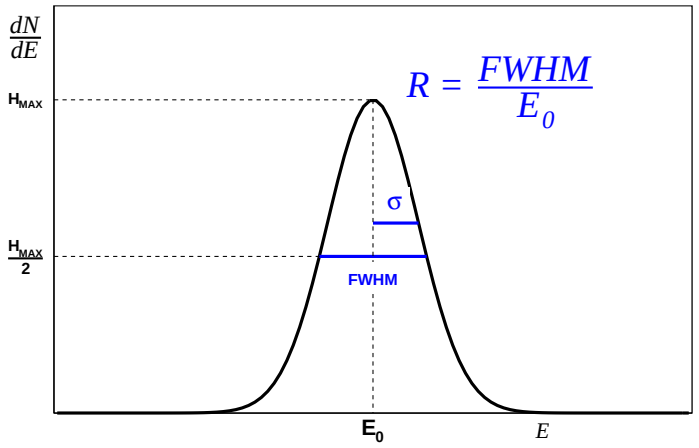

FIGURE 1.22: Definition of energy resolution. For peaks whose shape is Gaussian with standard deviation σ, the FWHM is given by 2.35σ.

Chapter 2

Nuclear Medicine

This chapter focuses on Positron Emission Tomography (PET), single photon emission computed tomography (SPECT), and Positron Emission Mammography(PEM) and the state-of-the-art devices in the market and under development. Though Compton Camera is not yet a viable nuclear medicine device, some attention to this emerging concept is brought.

The chapter includes as well an overview of the specific detectors being used and their intrinsic limitations. Finally it make brief introduction to the reconstruction algorithms that are commonly used.

2.1 Nuclear Medicine for Diagnostic Purposes

Nuclear Medicine is the branch of medicine that employs compounds labeled with radioactive nuclei (*radionuclides*) for the treatment or the diagnostic of human diseases. This chapter will focus on the diagnostic techniques in nuclear medicine.

The techniques consist of the administration of a substance with a radionuclide, called *radiotracer*, to the patient and the detection of the radiation that it emits. When the radiotracer is injected into the patient, the substance spreads throughout the body according to the metabolic process characteristic of the substance. The amount of radiation emitted in a region is a measure of the density of the radiotracer in-situ and, hence, of the metabolic activity. The information of substance density inside the body

Radionuclide	**Half-Life [min]**	**Maximum Energy**	**Tracer**	**Diagnostic Imaging**
^{18}F	110	635 keV	18F-FDG 18F-DOPA 18F-FLT 18-NaF 18F-FMISO	Tumors Neuroendocrine tumors Lymphoma Bone metastasis Solid tumors
^{11}C	20.4	960 keV	11C-Choline 11C-Methionine 11C-Acetate	Prostate cancer Brain tumors Prostate cancer
^{68}Ga	68.3	1.9 MeV	68Ga-DOTA-peptides	Neuroendocrine tumors

TABLE 2.1: Some positron-emitting radionuclides used for in vivo imaging with the tracers they are attached to and their applications. Information from [31].

can be used to create a map of metabolic activity. A map of metabolic activity can show abnormalities due to an excess or lack of uptake of the substance compared to what is expected.

The radiotracer emits a positron or a single photon from one to another. The geometry of the scanner devices and their detector requirements differ depending on the type and the energy of the particle used in the technique. Other aspects like the collimation principle used also restrict the requirements.

2.2 PET

PET uses positron-emitting radiotracers. The positron travels along the media until it annihilates with an electron as explained in Sec. 1.1 and a pair of back-to-back photons are created. Both photons are detected by two independent pixels and the energy and the time of detection is recorded. The detection of the two photons determines a LOR along which the annihilation has taken place. The acquisition of many pairs of photons gives place to many of those lines. The superposition and processing of these lines by means of reconstruction algorithms allows to obtain an image.

2.2.1 Positron Emitter Radiotracers

The maximum energy, half-life, molecules they are attached to, and applications of some radionuclides are listed in Tab. 2.1.

The most commonly used radiotracer in PET is ^{18}*F-Fludeoxyglucose (*^{18}*F-FDG).* It is a general purpose radiotracer because it follows the metabolic routine of the glucose, which is processed in most cells of the body. A higher consumption of glucose than expected in one region indicates the possible presence of tumors, whereas regions with lower consumptions indicate damaged or dead tissues. For the particular case of the brain, it can show the presence of long term diseases such as Alzheimer or Parkinson in stages before the patient is showing any symptom yet. Other radiotracers follow more specific metabolic routines and their usage is reduced to a limited number of applications.

Another reason why ^{18}F-FDG is the most commonly used radiotracer in nuclear medicine is its relatively long decay time compared to other radiotracers, which gives more time to prepare the patient for the test. To use shorter half-life radiotracers implies that the production facility for such radiotracers should be in situ.

The range of the positron is proportional to its kinetic energy. Because the distribution of the kinetic energy of the positron is continuous between 0 and the maximum energy, the range of the positron will vary from 0 to a few millimeters. Moreover, since the positron does not follow a straight path, its range and distance from the emission point are not strongly correlated. This leads to an intrinsic and unavoidable blurring of the image that can only be reduced by employing a radionuclide emitting positrons at lower energy that travel less distance along the surrounding media.

2.2.2 Coincidence Detection

Each coincidence detection event consists of two photons, each with 511 keV energy. The line described by the positions of the two photon detection points is called LOR. Two photons are considered to belong to the same positron-electron annihilation when they are detected within a window of time called *coincidence time window*. The jitter on the detection time depends on the path difference of the photons and on the timing resolution of the detectors. Therefore, the width of the coincidence time window has to be set according to the timing resolution of the detector in order to achieve an acceptable efficiency and avoid the presence of multiple events (events with more than two detected photons), which are usually rejected.

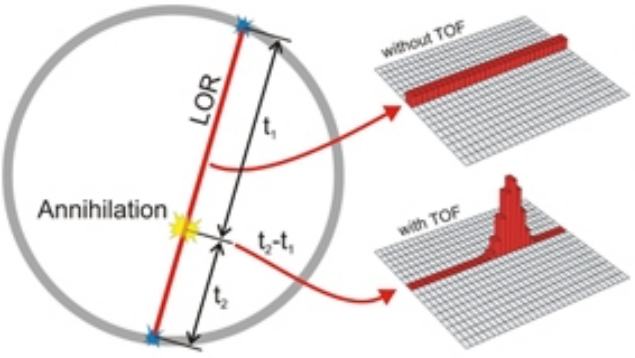

FIGURE 2.1: Time-of-Flight Principle

2.2.3 Time-of-Flight Measurement

The annihilation point along the LOR can be obtained by measuring the difference in time at which both photons are detected, Δt. For a particular Δt and with c being the speed of light, the distance of the annihilation with respect to the center of the line of response is shown in Eq. 2.1.

$$\Delta d = \frac{\Delta t \times c}{2} \tag{2.1}$$

The precision on the Δt measure is the *coincidence time resolution*. Time-of-flight measurements are usually used in PET scanners to determine a non-flat distribution of probability of where the annihilation has taken place along the LOR. The comparison between the distributions of probability for standard PET and ToF-PET are shown in Fig. 2.1.

Excellent timing properties are required for ToF-PET. However, efficiency and energy resolution criteria have to be kept within acceptable values. For this reason commercial ToF-PET scanners can achieve a resolution not better than 500 ps [36], which corresponds to 7.5 cm spatial resolution.

2.2.4 Photon Interaction Position

A good precision on the position of the photon interaction is needed to reconstruct the LOR of a coincidence. The pixel size is an upper bound of the precision on the interaction position measurement of the photon. State-of-the-art PET scanners employ

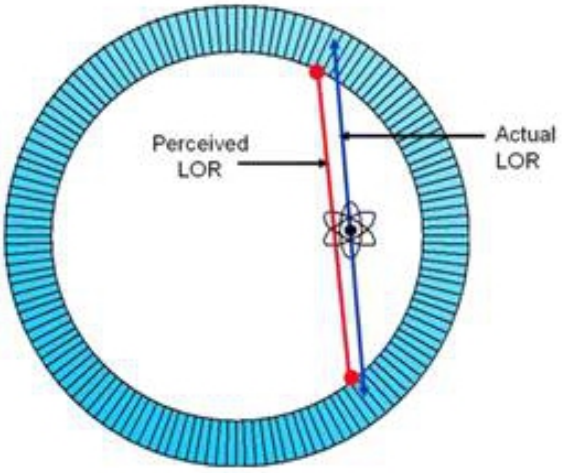

FIGURE 2.2: Sketch of the parallax error effect in a LOR in a PET scanner.

scintillation crystals segmented in a 2D array of pixels along the plane facing the photons that give a precision of a few millimeters.

Scintillation crystals are usually readout through the backside of the block using a photodetector. For this reason they cannot be segmented along this direction. The crystal could be made thinner but then it would compromise the sensitivity of the device. Hence, the scintillation thickness is of a few centimeters and the precision along the depth direction becomes as big as the thickness size.

2.2.5 Parallax Error

The *parallax error* is the angular displacement of the perceived LOR compared to the actual one due an big uncertainty on the DOI measurement as depicted in Fig. 2.2.

One way to reduce this effect is to segment the detector in the depth direction to obtain a better precision of the DOI measurement. Unfortunately, scintillation crystal detectors cannot be segmented in such a way, and other strategies have to be taken to solve this problem.

Different approaches can be found to estimate the DOI in scintillator crystal detectors such as multi-layer crystals with different offsets [65], light sharing in multi-layer crystals [66], monolithic detectors [67, 68] or employing APD coupled to the crystals in the edge-on side [69]. The dual-ended designs [70–72] is a promising method given the good

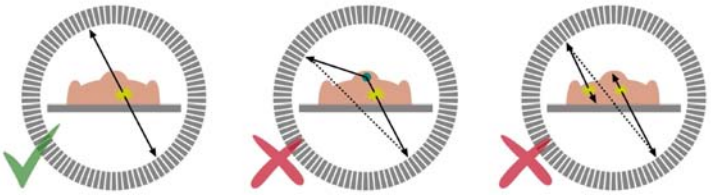

FIGURE 2.3: (left) LOR of a true PET event, (middle) LOR of a scattered event, and (right) LOR caused by a random coincidence. Where the LOR is indicated b the dotted line whereas the real photon paths are given by the solid lines.

resolution it provides but adds complexity in the readout electronics and the packaging of the device.

Semiconductor detectors offer different possibilities to diminish this effect due to the possibilities of finer 3D segmentation of the material [73–75].

2.2.6 Energy Resolution

In PET the photon energy is measured in order to classify events and increase the signal purity. Both photons produced in an annihilation have 511 keV, but they might undergo scattering in the body of the patient or in the detector. Scattered photons change their direction and loose energy giving rise to *scattered events*. Two photons can be detected within the coincidence time window and be physically uncorrelated, these are called *random events*. Sketches of true, scatter and random events are shown in Fig. 2.3.

Scattered photons have lower energy than 511 keV. A good energy resolution detection allows to distinguish the scattered events and reject them. Good energy resolution measurement is crucial to achieve a high SNR ratio and to obtain images with high contrast.

2.2.7 State-of-the-art PET Scanners

Inorganic scintillator crystals are the most commonly used, as building block detectors, for PET scanner because of their good stopping power, low cost, relatively good energy resolution and good timing properties. Scintillator crystals in PET are often readout by PMTs. Scintillator crystals and PMTs are coupled to form detector units called *Detector Block* as shown in Fig. 2.4.

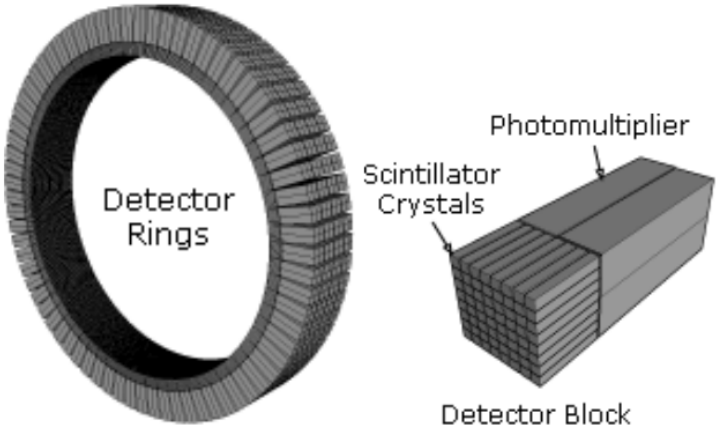

FIGURE 2.4: Typical geometry of modern PET system detectors.

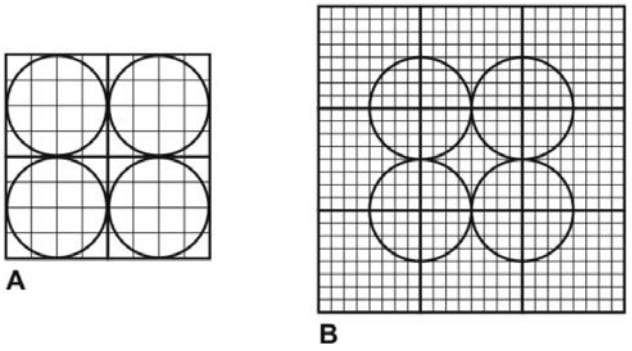

FIGURE 2.5: A) PMT assigned in 4 quadrants separately. B) Each PMT shares 4 quadrants of 4 block detectors and improves the spatial resolution. From [9].

The classic way to couple the PMTs to the scintillator crystals is shown in Fig. 2.5 A. An improvement of this configuration is shown by the quadrant sharing technique [76] shown in Fig. 2.5 B. This design improves the spatial resolution compared to the previous configuration at the cost of increasing the dead time of the device due to the need to analyze signals from bigger areas.

APD is an alternative to PMT as photo-detector to readout scintillator crystal [77, 78]. They offer compact design, good energy resolution, high QE, and compatibility to operate in high magnetic fields, which makes a simultaneous PET-MRI scanner feasible [79]. However, APDs are very sensitive to temperature changes and bias voltage and have poor timing response properties. This can add some complications to maintain the stability of the full scanner.

SiPM are becoming a popular choice to readout scintillator crystals in many applications as well as in PET [80, 81]. They combine most of the good features of APDs and PMTs.

SiPMs have good energy and timing resolution, can operate under strong magnetic fields, do not need complicated readout electronics and require low bias voltage.

2.2.8 PET Applications

2.2.8.1 Tumor Diagnosis and Treatment

A tumor is an abnormal mass of tissue created by uncontrollably grown cells. If a tumor is *malignant*, i.e., made of cancerous cells, it can grow dangerously, damaging neighboring tissues and expanding to other organs in the body. Cancerous cells can enter into the bloodstream and form new tumors in another part of the body. This process is called *metastasis.*

Because of the fast growth of tumor tissues compared to healthy ones, they consume a significantly higher amount of glucose. FDG radiotracers are used to spot these abnormally high rates of glucose consumptions in the body. Many different tumors can be diagnosed through PET: lung, breast, brain, neck, colorectal, lymphoma and melanoma [10]. An important feature of PET is that it can detect physiological anomalies before anatomic changes take place, which allows to diagnose diseases in earlier stages than with *Computed Tomography (CT)* or MRI.

PET has a very important role in conventional radiation therapy treatments. PET screenings allow to precisely adjust the radiation treatment schedule and to monitor the treatment response [82, 83]. The dose distribution can be optimized so that a major part reaches the tumor and the neighbor tissues receive a minimum impact [84–86].

2.2.8.2 Brain Diseases

The most common brain diseases that can be diagnosed with PET are brain tumors, Alzheimer's disease, Parkinson disease and epilepsy. Whereas, brain tumors are one of the most dangerous types of cancer and with more difficult treatment, the rest of the aforementioned diseases have, nowadays, no cure and only a reduction of the symptoms is reachable. For these reasons the diagnostic of these diseases in early stages is of crucial importance to control their development inside the patient brain as much as possible.

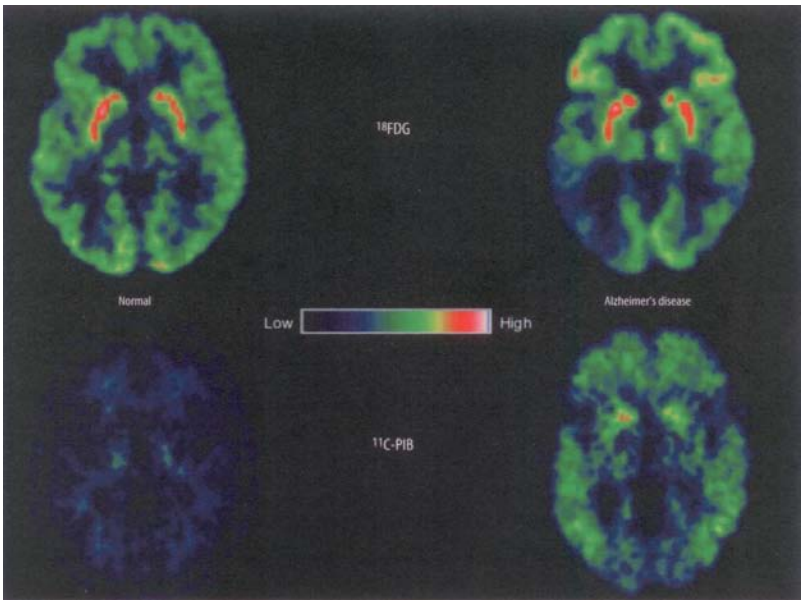

FIGURE 2.6: FDG cerebral glucose metabolism parametric maps (upper panel) of a normal and an Alzheimer's disease patient. The lower panel shows minimal ^{11}C-PIB updake in the normal individual, but marked with widespread uptake in the cortex and striatum of the same Alzheimer's disease patient, indicating deposition of amyloid plaques. From [10].

It is a challenging task to do imaging of a Brain disease because of the high background activity of the brain. In the case of Alzheimer disease and Parkinson disease, the result of imaging with ^{18}F-FDG is the appearance of regions with low activity. More specific radiotracers such as ^{11}C-PIB are required to obtain a better diagnostic and distinguish one disease from the other. Fig. 2.6 shows the comparison between a healthy brain and a brain suffering Alzheimer's disease for ^{18}FDG and ^{11}C-PIB.

The main use of PET in epilepsy is to localize epileptogenic focuses in patients with focal epilepsy in order to perform further surgery. The metabolism of glucose of such focuses increases during the seizure period [87].

2.2.8.3 Cardiovascular Pathologies

PET is used in cardiovascular studies to determine the damaged tissue of the heart after a heart attack. Dead tissue does not consume glucose, and therefore as with Alzheimer disease and Parkinson disease in brain diseases, regions with low activity will show the impact of the disease [88, 89].

The blood circulation in the heart arteries can be imaged with the radionuclide ^{82}Rb to find *coronary artery disease* [90]. The coronary artery disease often causes an increased possibility of having a myocardial infarction.

2.2.8.4 Quality Assurance in Hadron Therapy

Hadron therapy is an alternative to the standard radiation therapy that employs photons and electrons [91]. Particles used in hadron therapy are protons and ^{12}C ions [92]. The effect of hadron therapy on the tissues is more localized than with the standard therapies due to the higher probability of interaction in a shorter range. In order to ensure that the radiation is applied on the desired tissue, a *quality assurance (QA)* process has to be done simultaneously with the hadron therapy session to monitoring the effect of the beam.

Hadron therapy produces residual positron emitters with a concentration proportional to the intensity of the beam. PET is used to obtain, in vivo, measurement of both the position where the beam is damaging more tissue and the intensity of the beam at the point of interaction [93–95], by detecting the photons from these residual positrons.

2.2.9 New PET Generation

The major trends in PET development are, nowadays: the ToF-PETs, simultaneous PET/CT and PET/MRI systems, and PETs based on semiconductor detectors.

2.2.9.1 ToF-PET

ToF-PET scanners use the TOF measurement, as explained in Sec. 2.2.3, to determine with more precision the point of annihilation of the positron. ToF-PET scanners obtain images with significantly better quality than conventional PET scanners [96]. First detector devices for ToF-PET scanners were based on the fastest scintillation crystals such as BaF_2 and CsF [97, 98].

The main advantage of ToF-PET is the higher SNR obtained in the acquired image. However, the scintillations aforementioned have a low efficiency and, hence, a trade-off problem between the sensitivity and the TOF measurement arises. TOF technique has

been already proposed with LSO crystals [99, 100] to solve this problem and already has been implemented in a commercial device [35].

2.2.9.2 Hybrid Imaging

The current spatial resolution of a typical PET scanner is of the order of millimeters and gives *functional* information whereas the resolution of CT and MRI is of the order of micrometers and gives *anatomical* information. The combination of both results by merging both images, provides valuable information of both the location and the nature of the anomalies. PET/CT in particular has become a popular image modality [101, 102].

Apart from the combination of anatomical and functional information, PET/CT also allows to perform a correction for the photon attenuation in PET using the CT information. Therefore, PET/CT provides better image quality than PET and adds the anatomical information. First commercially available PET/CT scanners were the Biograph (CTI PET Systems, currently part of Siemens Medical Solutions) [103], the Discovery (GE Healthcare) [37], and the Gemini (Philips Medical Systems) [35].

PET/MRI scanners are desired for the study in medical fields such as neurology, oncology, and cardiology [104–106] because they offer many advantages with respect to PET/CT. MRI shows an improved soft tissue contrast compared to CT, does not require ionizing radiation, can have a true simultaneous acquisition, instead of the sequential acquisition of CT and, finally, real-time MRI can be used to account for the patient motion during the PET acquisition.

However, the main drawback of PET/MRI systems is the incompatibility of the PMTs of PET scanners with strong magnetic fields. The proposed solutions are either to place the PET PMTs outside the MRI magnetic field ring [107–109] or to use APDs or SiPMs instead of PMTs [79, 110].

2.2.9.3 PET with Semiconductor Detectors

Semiconductor materials such as CdTe or CZT for PET are becoming popular. Although the stopping power of these materials for 511 keV photons is lower than some scintillator

crystals and, therefore have a lower detection sensitivity for the same thickness, semiconductor detector devices offer an excellent energy resolution that allows to perform a highly efficient scatter event rejection. Moreover, since they can be segmented into small 3D voxels, they can provide a very good DOI information and can also distinguish from multiple interactions inside the detectors.

Among the drawbacks of employing semiconductor detectors for PET are the huge number of electronic channels and the higher cost.

Semiconductor detectors are promising for hybrid PET/MRI systems because of their compatibility with strong magnetic fields. However, one cannot perform TOF measurements due to the big spread in the timing response created by the different mobilities of electrons and holes in the semiconductor.

Developing CdTe and CZT detectors for PET is a big challenge because of the difficulty in growing large pieces of material. Despite these drawbacks, a number of CdTe and CZT based detectors have already been tested and show good results [39, 40, 74, 75, 111].

2.3 PEM

A PEM scanner is an organ dedicated PET for breast screening [112]. The main advantage of PEM compared to PET is the reduced size of the apparatus given the smaller field of view (FOV) that it has to cover. This leads to an important reduction of the cost and a significant improvement of the sensitivity of the device [11]. Fig. 2.7 shows a comparison of the image quality for a PEM scanner and a *whole body PET (WB-PET)* scanner, where clearly the PEM has a much better contrast than the WB-PET.

PEM devices with different FOV configuration around the imaged breast are under development [113]. The most commonly available commercial devices consist of two parallel paddles with arrays of scintillator crystals coupled to PMTs [114]. Recent clinical trials show the huge potential of PEM devices in improving breast cancer treatment [115].

2.3.1 State-of-the-Art PEM Scanners

A commercially available PEM scanner is the Naviscan PEM Flex Solo II [114], which is shown in Fig. 2.8. It employs scintillation crystals coupled to PMTs and has a par-

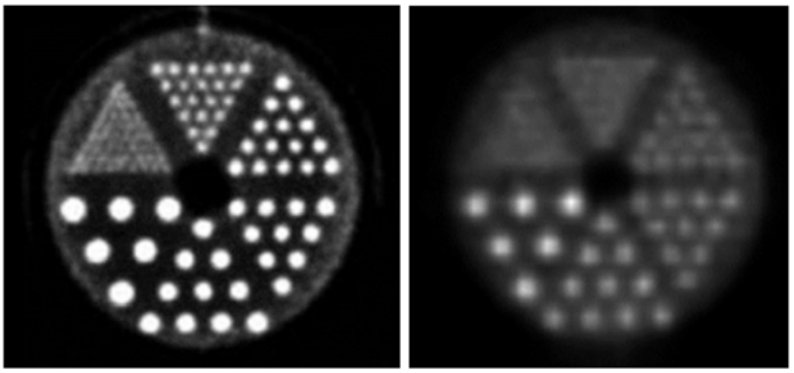

FIGURE 2.7: Reconstructed image of the Derenzo phantom obtained by the PEM Flex Solo II (left) and whole body PET (right). From [11].

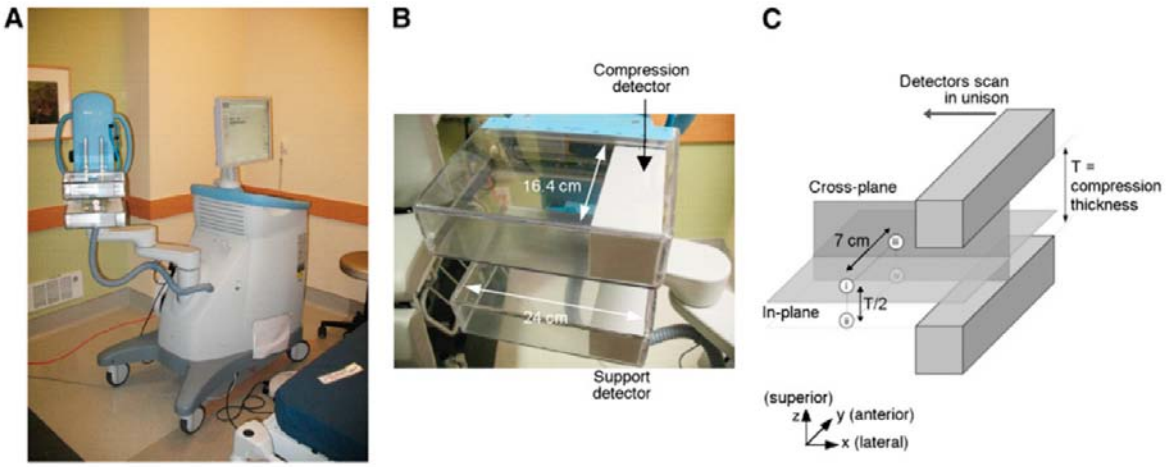

FIGURE 2.8: The PEM Flex Solo II scanner. From [12].

allel plane geometry. Although the parallel plane geometry is the most common, other geometries like a C shape or a ring are also used [116–118]. Different PEM scanners are listed in Tab. 2.2.

All the devices shown in Tab. 2.2 use scintillation crystals as the main detection material. This leads to a limited energy resolution and, in case of the parallel plane geometry, a huge parallax error that causes a poor spatial resolution in the direction between the paddles.

2.4 SPECT

SPECT produces images of the activity of radioactive tracers. Unlike PET, the principle of operation is not the detection of two photons coming from a positron-electron

Name	Geometry	Detectors
PEM-1 [112]	Planar	BGO+PMT
PEM Flex Solo II [12]	Planar	LYSO+PMT
BPET [118]	Split-ring	NaI(Tl)+PMT
maxPET [119]	Planar	LSO+PMT
LBNL-PEM [120]	Rec. Box	LSO+SiAPD+PMT
YAP PEM [113]	Planar	YAP:Ce+PMT
ClearPEM [121]	Planar	LuAP:Ce+APD
MDA PEM [122]	Planar	LYSO+PMT
C PEM [116]	C-Shape	LGSO+PMT
West Virginia PEM [123]	Planar	GSO+PSPMT
MAMMI PEM [117]	Ring	LYSO+PSPMT

TABLE 2.2: Current PEM systems with their geometries and detectors employed.

Radionuclide	Half-Life [h]	Maximum Energy	Tracer	Diagnostic Imaging
^{99m}Tc	6.02	141 keV	TlCl Sestamibi MDP HMPAO RBCs Sulfur colloid	Brain lymphoma Myocardial perfusion Metastases Brain perfusion Liver hemangioma Spleen imaging
^{67}Ga	3.26	141 keV	Citrate	Lymphoma
^{111}In	2.80	171,241 keV	Capromab pendetide	Prostate cancer

TABLE 2.3: Some single photon emission radionuclides used for in vivo imaging with the tracers they are attached to and their applications. Information from [13].

annihilation but the detection of a single photon.

Radiotracers employed in SPECT are single gamma emitters. Tab. 2.3 shows the most commonly used radiotracers for SPECT together with their properties and applications. All the radionuclides in Tab. 2.3 have longer half-life than those used in PET, which facilitates the production, transport, and the administration of the radiotracer to the patient. Moreover, the energy of the photon emitted is not restricted to 511 keV like in PET but can have many different values. The energy of the photons emitted in SPECT are lower than those emitted in PET so the photons usually interact with the detector through photoelectric effect. Hence, the noise due to scatter events is reduced.

SPECT requires a collimation of the photons in order to obtain information about the direction of the photon, so an image can be reconstructed. The collimator is made of thick material with apertures which allow only photons with a certain direction to pass and absorb the rest. The most used approach for SPECT is the Anger camera, shown

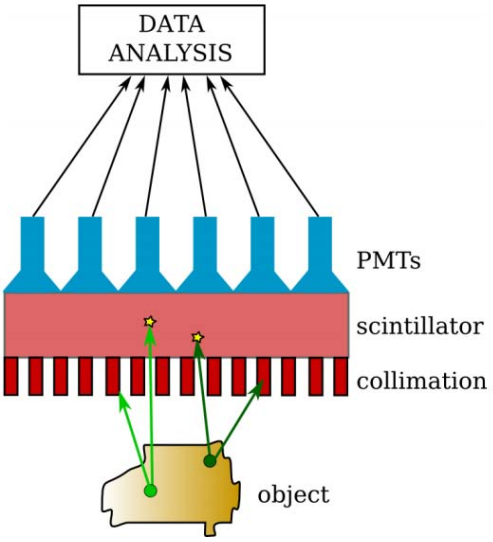

FIGURE 2.9: Schematic of a SPECT Anger camera.

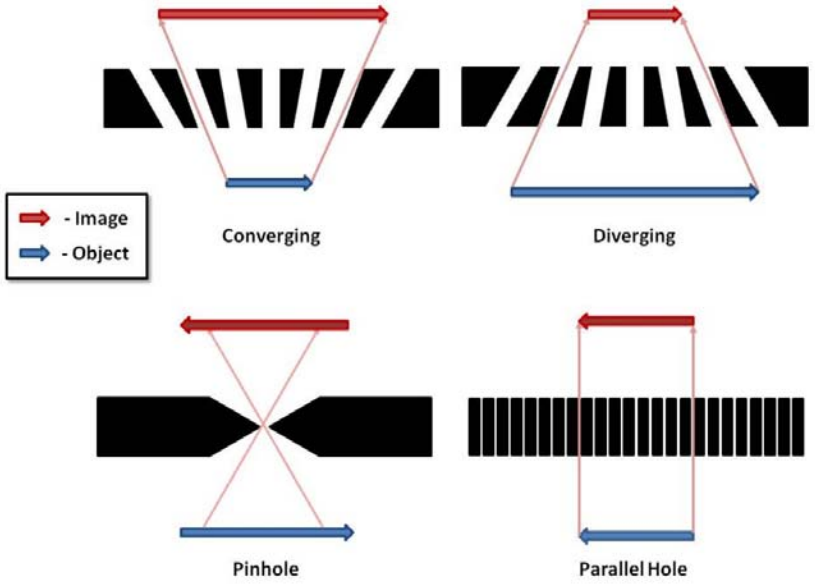

FIGURE 2.10: Schematic representation of four collimator types. Top left and right represent converging and diverging collimators respectively. Bottom left and right represent pinhole and parallel hole collimators. From [13].

in Fig. 2.9, which uses a parallel collimator and scintillation crystals coupled to PMTs to detect the photons. Other type of collimators are shown in Fig. 2.10. Collimators can converge, diverge or invert the image compared to the real object. The energy of the detected photons is compared to the known original energy of the emitted photons so the events that pass the collimator undergoing scattering can be rejected.

The image obtained by a SPECT scanner is a 2D projection of the object. Images

FIGURE 2.11: A picture of the Symbia E, a SPECT commercialized by SIEMENS.

of the same object obtained from different points of view can be merged to obtain a 3D image. Multi-head cameras as the one shown in Fig. 2.11 can be used for such a purpose. Another choice is to rotate the camera and take images from different point of views. The advantage of multi-head cameras is the bigger FOV coverage, whereas rotating scanners have lower cost.

2.4.1 Compton Camera

The application of Compton cameras for nuclear medicine was first proposed in 1974 [124] and it is, still nowadays, a pending issue. Compton gamma camera uses kinematic collimation, based on the Compton effect, of the photon emitted by the radiotracer. The schematic of the detection principle of a Compton camera is shown in Fig. 2.12. A photon undergoes a Compton scattering with a first detector, the scatterer, with an angle θ and deposits an energy E_1. Afterwards it deposits all its remaining energy, E_2, in the second detector, the absorber. The scattering angle, θ, defines a Compton cone, which is the equivalent to a LOR in PET. The value of θ can be obtained from Eq. 2.2.

$$cos(\theta) = 1 - m_e c^2 \left(\frac{1}{E_\gamma - E_1} - \frac{1}{E_\gamma} \right), \tag{2.2}$$

where E_γ is the known energy of the original gamma.

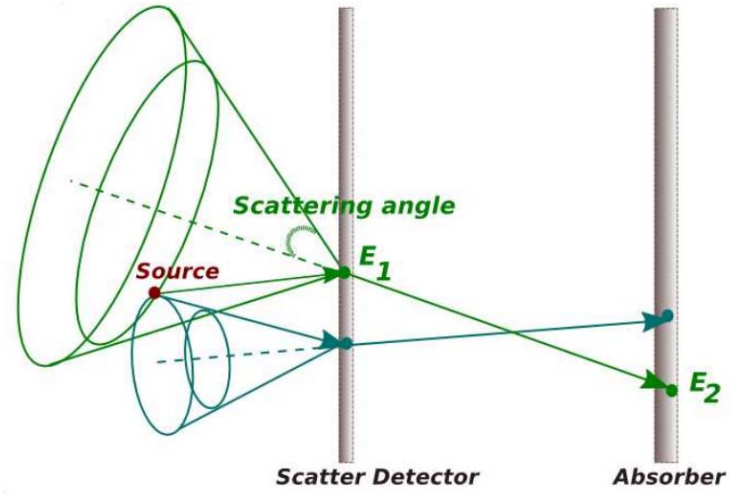

FIGURE 2.12: Schematic of two Compton cones of two events for photons originated in the same point.

One big advantage of the Compton camera compared to SPECT scanners is the high sensitivity, which allows to either reduce the scanning time or the dose injected to the patient. Another advantage is the possibility of using higher energy sources without the need of using thicker collimators. Finally, with a Compton camera it is possible to reconstruct the 3D position of the source and there is no need to rotate the camera or use multiple head scanners to obtain a 3D image.

Some serious challenges are still pending to be solved for Compton cameras. One big drawback is the effect of Doppler broadening on the energy resolution. due to the initial momentum of the recoil electron. Because of the Doppler broadening effect, Eq. 2.2 is only approximately true since it does not take the initial momentum of the recoil electron into account, hence introducing an additional smearing on θ.

Another challenge is the correct reconstruction of a scattered-absorbed event, which can lead to wrong Compton cones if not done properly. Finally, an important challenge is the reconstruction algorithm to be used for Compton gamma cameras, which is a whole field under development [125–127].

2.5 Reconstruction Algorithms in Nuclear Medicine

For each pair of detected photons from the same positron-electron annihilation a LOR is obtained. The information of this LOR is calculated using the locations of the two

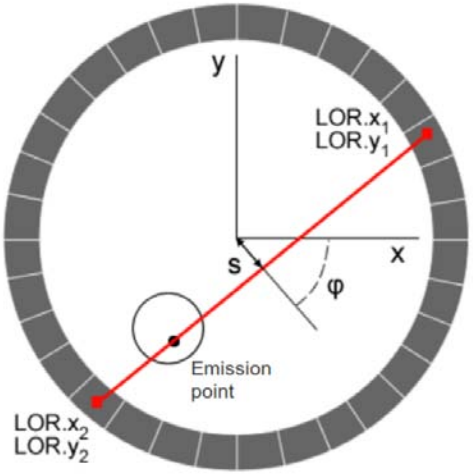

FIGURE 2.13: A LOR defined as detection coordinates (x_1,x_2,y_1,y_2) and polar coordinates (s,ϕ). From [14].

detection points in the detector. The LOR is usually expressed in terms of polar coordinates as shown in Fig. 2.13. Hence, each LOR can be represented with a single value for s and ϕ.

The projections from all angles of the LORs can be arranged in a matrix called *sinogram*. A sinogram is a 2D matrix in ϕ-s space where each point is evaluated as shown in Eq. 2.3, where $f(x, y)$ is a representation of the activity distribution and y_r is the transverse direction coordinate perpendicular to the s axis direction.

$$p_{s,\phi} = \int_{-\infty}^{\infty} f(x, y) dy_r \tag{2.3}$$

Fig. 2.14 shows a sinogram for a point source and sketches the projections on the s direction for different ϕ values. The coincidence events in PET are stored as sinograms and most image reconstruction algorithms are based on them.

The majority of nuclear medicine scans are acquired in 3D mode, which is more complex to handle than 2D data. The 3D data is often re-binned into a 2D format, such that the reconstructed 3D image is a stack of 2D reconstructed layers of structures lying within a selected plane of the 3D object. This approach of getting images is called *tomographic imaging*.

The most commonly used methods for reconstruction in nuclear imaging are the *filtered*

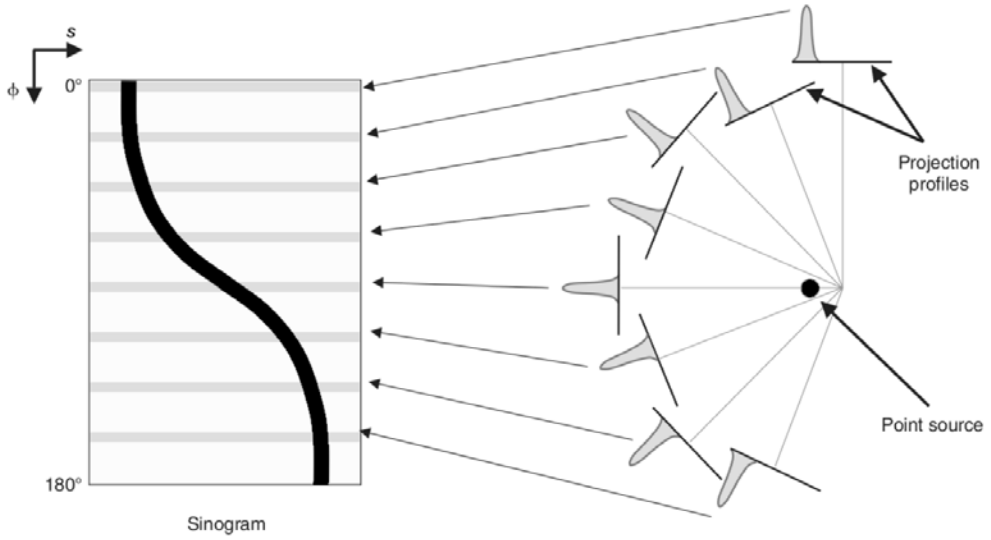

FIGURE 2.14: Sinogram for a point source. Each row display corresponds to an individual projection for a ϕ value. From [15].

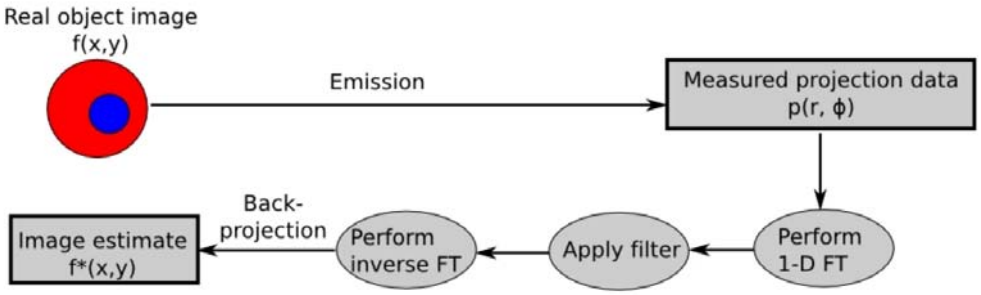

FIGURE 2.15: The concept of FBP reconstruction algorithm. From [16].

backprojection (FBP) algorithm, *maximum-likelihood expectation-maximization (ML-EM)* algorithm, the speeded up version of ML-EM which is the *ordered subset expectation maximization (OSEM)*, the *list-mode OSEM (LM-OSEM)* and the *origin ensemble (OE)* algorithm.

2.5.1 FBP

The 2D FBP reconstruction algorithm is an analytic method and, hence, very fast. The steps of the FBP algorithm are illustrated in Fig. 2.15. The projection profiles acquired at N projection angles in the spatial domain are expressed in terms of a Fourier series in the frequency domain as the sum of a series of sinusoidal waves of different amplitudes, spatial frequencies and phase shifts running across the image. The 1D Fourier transform (FT) of the image profile is necessary to apply a filter to each FT profile. After the

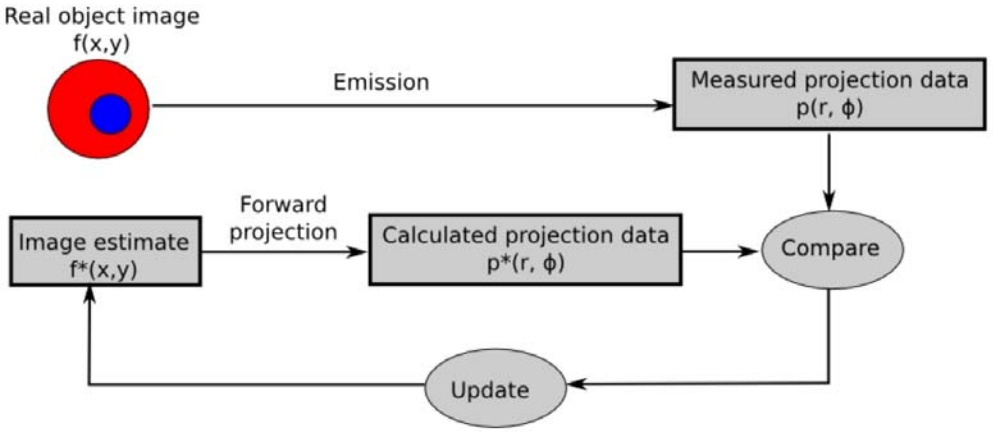

FIGURE 2.16: The concept of ML-EM reconstruction algorithm. From [16].

filtering, the inverse FT of each FT profile is computed. This way one gets filtered projection profiles. Finally, backprojection [128] is performed using the filtered profiles to obtain an estimate of the image.

The main drawback of FBP is that it requires a complete angular coverage around the object. For this reason it is an excellent choice for PET. In the case of PEM devices with a ring or C-shape it works also good but it shows problems for parallel geometries. Finally, in the case of SPECT, its usability depends on with how many different views, with different angles data, are taken.

2.5.2 ML-EM and OSEM

ML-EM [129] and OSEM [130] are iterative image reconstruction algorithms. Iterative methods require more computational power than analytic ones but are less sensitive to the imperfections of the detectors or the data set. In such algorithms, an estimation of an image is made and its forward-projections are computed. Afterwards, these projections are compared with the measured data and, if there is a difference between the estimated and measured sets of projections, the image is corrected (i.e. the error is back projected) to reduce such difference and a new iteration is performed. Iterations continue until a minimum agreement between the two sets is reached.

The concept of the ML-EM algorithm is shown in Fig. 2.16. The ML-EM method uses statistical considerations to compute the most likely distribution that would create the

measured observation data. It assigns a greater weight to high-count elements of a profile and less weight to low-count regions.

In the case of OSEM, the projection views are grouped in different sets (subsets). The algorithm goes through the subsets in a specified order, and the image is updated after each subset is considered. Increasing the number of subsets accelerates the convergence but may increase the noise as well.

ML-EM and OSEM offer good results on image quality for detectors with much less sensitivity to the detector geometry than FBP. However, they require high computational power, especially in the case the scanner is divided into high number of channels.

2.5.3 LM-OSEM

LM-OSEM [131] is an iterative algorithm where the input consists of detected events that are presented in list-mode. Normally, the maximum-likelihood algorithms pre-process the data by binning it into evenly-spaced angular sinograms. LM-OSEM, however, acts on the raw data as it was recorded by the scanner. Therefore, the list-mode data can be streamed from disk storage and be processed event-by-event. With this approach it is not needed to keep a system matrix in memory and the required computational power is reduced.

This algorithm is particularly useful for scanners with a high amount of channels, where LM-EM and OSEM become too slow, and with a partial angular coverage, where FBP does not perform properly. This is the case of SPECT scanners or the PEM scanners with parallel paddle geometries.

2.5.4 OE

OE [132] is a stochastic and relatively fast converging technique. The main advantages of OE are that its convergence speed does not depend on the number of detector voxels, it does not require forward/backward operations or voxelization of the image space. It is suitable for any scanner geometry and it accepts raw list-mode data from scanners (instead of sinograms or data binned in detector bins).

The reconstruction algorithm can be described as follows. For each coincidence a random position is assigned along the LOR and the event density matrix D stores the number of entries in each FOV voxel location L. The randomized positions (origins) along the LORs must be all inside the FOV. Then, the algorithm randomly changes the event origins along the corresponding LORs, generating system state transitions governed by acceptance probabilities. The steps for each event and iteration are:

- A new random location L_{i+1} is selected on the corresponding LOR inside the FOV.
- The new location is accepted with a probability P, that compares the event density $D_{L_{i+1}}$ at the new location with the density D_{L_i} at the old location for this event like in Eq. 2.4.

$$P(L_i \rightarrow L_{i+1}) = min\left[1, \frac{D_{L_{i+1}} + 1}{D_{L_i}}\right] \tag{2.4}$$

- If the new location is accepted, the matrix D is immediately updated.

The convergence criteria of the algorithm are still under study, since too many iterations can produce an undesired effect where the final solution for the image converges into one point.

Chapter 3

VIP Project

The VIP project proposes a novel design of detector module, the VIP module, which is based on pixelated CdTe detectors to build a full seamless PET scanner. The VIP module can also be shaped with a rectangular geometry. This allows to construct VIP modules for parallelepiped scanners for PEM or Compton Camera (CC) used as a SPECT scanner.

The VIP research work has been grouped into three main tasks. One is the simulation of the expected performance of medical imaging scanners based on the VIP module: VIP-PET, VIP-PEM and VIP-CC. The image reconstruction techniques have been studied, individually for each scanner, taking into account the different characteristics of each device. Another task is the development of the VIP-PIX ASIC, which includes a fully integrated and independent readout per pixel and delivers energy and time information of the detected events. Finally, the characterization of the CdTe in stages of a single pixel, an array of pixels, and a pixelated detector using the VIP-PIX for the readout.

This chapter is an overview of the VIP project. The core of the project, the VIP module, will be fully explained and the main funcionalities of the VIP-PIX ASIC will be described. The specifications and some simulation results achieved with the three VIP-based scanners will be shown as well.

3.1 The VIP Module

The VIP module is a CdTe based detector divided into small pixels, each with its own independent readout channel. As shown in Fig. 3.1, it is divided into subunits, 4 in this example. Each subunit consists of 2 CdTe diodes of dimensions 10 mm × 10 mm × 2 mm. Each CdTe diode is divided into 100 pixels with a pitch of 1 mm × 1 mm. The VIP-PIX ASIC is placed on the backside of each CdTe diode via bump-bonding such that each pixel becomes a fully independent detector with signal processing and digitization performed in situ. The VIP-PIX is mounted on an extra thin kapton pcb of 250 μm that connects all the VIP-PIXs with an FPGA that further processes the data acquired.

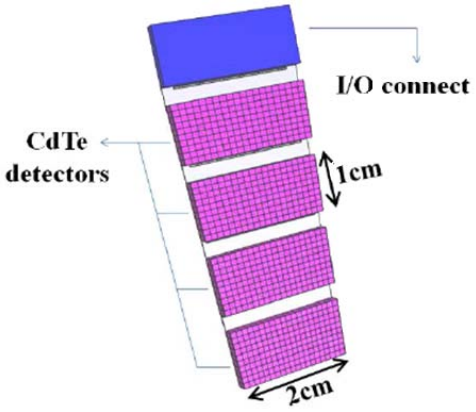

FIGURE 3.1: The VIP module.

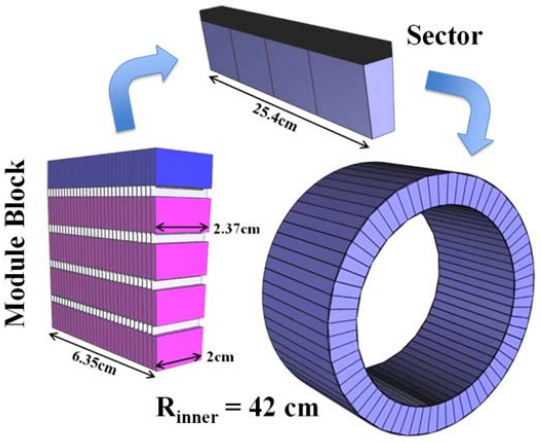

FIGURE 3.2: The VIP-PET geometry.

The VIP module will be used to build the VIP-PET scanner as shown in Fig. 3.2. A stack of 30 detector modules forms a module block. A sector consists of 4 blocks and the full ring has 66 sectors. The dimensions of this ring are 42 cm inner radius and 25.4 cm width in z (perpendicular to the $r-\theta$ plane). With this geometry the VIP-PET will have a total of 7920 VIP modules and more than 6 million voxels, which leads to a volumetric density of 450 voxels per cm^3.

The VIP-PET scanner offers a solution for problems that arise in scintillator based PET scanners. The VIP-PET is segmented into pixels of 1 mm in the radial direction and this provides a precision better than 300 μm[1] This is better than the 1.5 mm precision achieved by scintillation crystals after DOI reconstruction algorithms [38]. Therefore,

[1]The Root Mean Square (RMS) for a distribution of points from 0 to L with the expected value $\mu = \frac{L}{2}$ is $\sqrt{\frac{L^2}{12}}$. For a pixel of 1 mm it is $\sqrt{\frac{1\ mm^2}{12}} = 0.289$ mm.

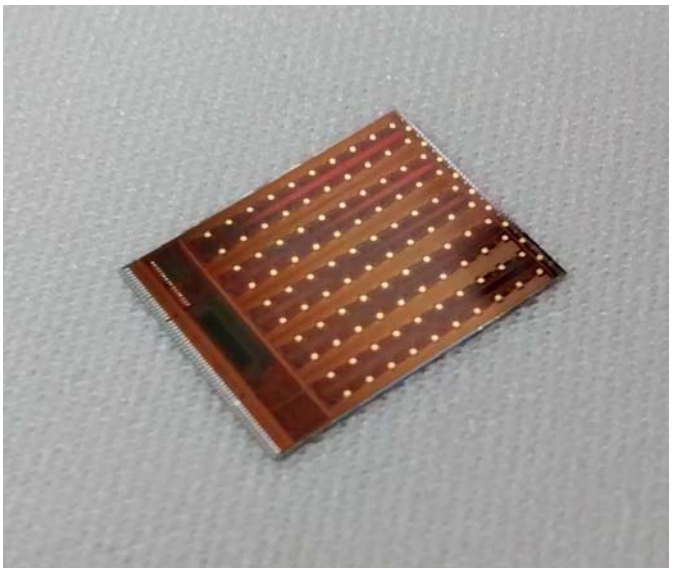

FIGURE 3.3: VIP-PIX picture.

parallax error is reduced and the LORs are more precise, which improves spatial resolution.

With an energy resolution of 1% at 511 keV it is possible to discern events that have undergone a Compton interaction from those who have not. By rejecting Compton events the signal quality improves significantly and hence the SNR increases.

The electric field applied on the CdTe diodes of the VIP-PET is parallel to the magnetic field of MR scanners with the same geometry and the detector performance is not affected, which makes a hybrid VIP-PET/MRI system possible.

The photons coming from positron-electron annihilations traverse 4 cm depth of CdTe, which has a stopping power of 80% for 511 keV photons [41]. The sensitivity achieved by this amount of material is comparable to state-of-the-art PET scanners [19].

3.2 The VIP-PIX

The VIP-PIX is a dedicated ASIC for the readout of semiconductor detectors. A picture of the VIP-PIX is shown in Fig. 3.3. It provides low noise and low power pixel readout with digital output. The size of the ASIC is 10 mm $\times$ 12 mm and the thickness is 50 μm. The VIP-PIX is connected to CdTe diodes of size 10 mm $\times$ 10 mm with 100 pixels of 1 mm $\times$ 1 mm by means of bump-bonding. An assembly of the VIP-PIX and a CdTe

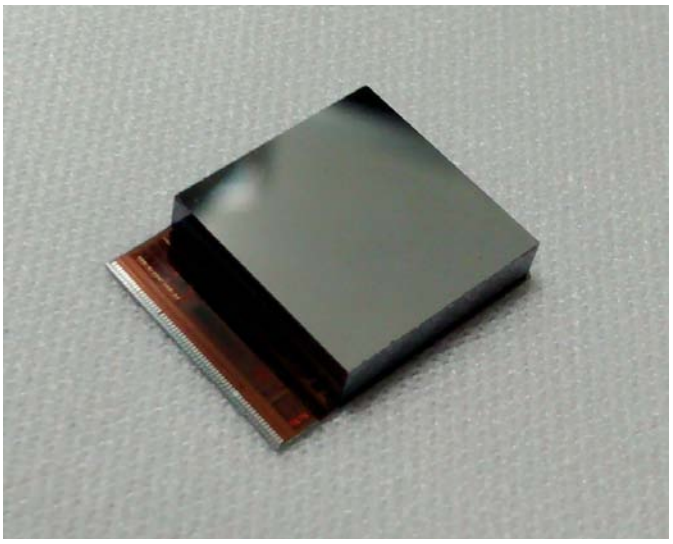

FIGURE 3.4: Assembly of a CdTe diode and a VIP-PIX.

Specification	**Value**
Detector Size	10 mm × 10 mm × 2 mm
Voxel Size	1 mm × 1 mm × 2 mm
Detector DC bias voltage	2000 V
Detector Leakage Current	250 pA/pixel
Electron/Hole Drift Time	18 ns/200 ns
Pixel Capacitance	80 fF
Energy Resolution of Pixel Electronics	10 bits for 511 keV
Maximum Jitter of time stamp	10 ns
Maximum Power Consumptions	200 μW/pixel

TABLE 3.1: Specifications of CdTe Detector and Pixel Electronics. From [17].

diode is shown in Fig. 3.4. Tab. 3.1 summarizes the specifications of the pixelated CdTe detector and the readout ASIC.

3.2.1 Readout ASIC Architecture

The architecture of the VIP-PIX is shown in Fig. 3.5. It is divided into two regions: the 2D matrix of pixels and the back-end. The matrix is placed on the left of the scheme and occupies an area of 10 mm × 10 mm. It contains 100 pixels in an array of 10 × 10. The back-end is on the right side of the ASIC and occupies a surface of 10 mm × 2 mm.

The ASIC back-end includes, among other circuits, a temperature sensor and a time-to-digital converter (TDC). A digital controller is also placed in the back-end. It sends the control signals to the pixels according to the operation mode. It is also responsible

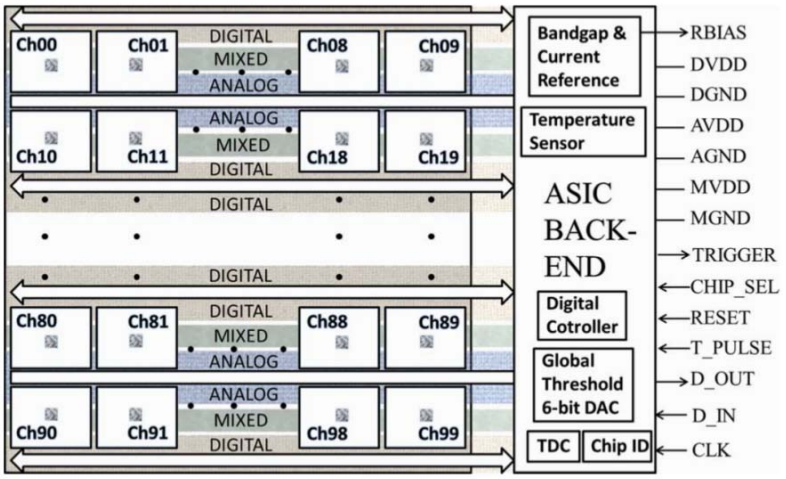

FIGURE 3.5: Architecture of the VIP-PIX. From [17].

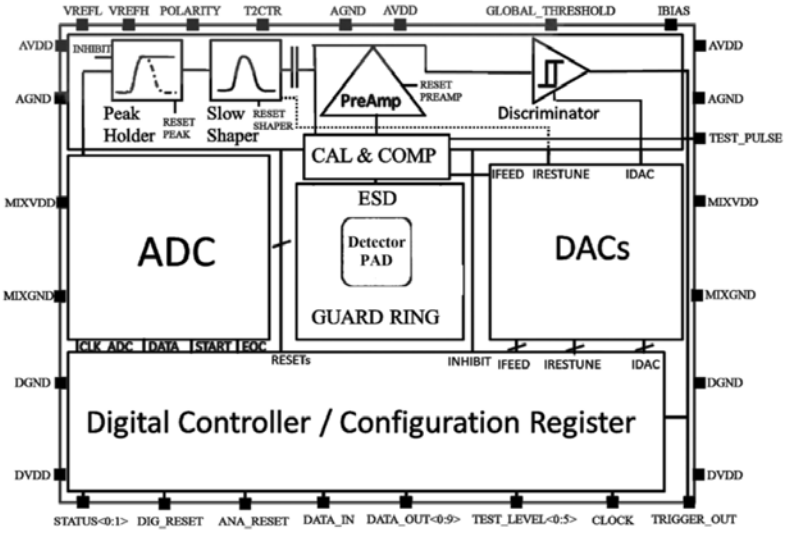

FIGURE 3.6: Architecture of on single pixel in the VIP-PIX. From [17].

to establish a communication with the PCB to either receive the configuration data or transmit the acquired data.

3.2.2 Readout Pixel Architecture

Each of the channels has an independent circuitry as the one shown in Fig. 3.6. The pixel readout structure has been divided into three regions. For the pixels in the odd rows the analog front-end is in the top region, the mixed signal circuits, like the analog-to-digital converter (ADC) and the digital-to-analog converters (DACs), are in the middle, and the digital part is at the bottom. For the pixels in the even rows, the top and bottom regions are flipped.

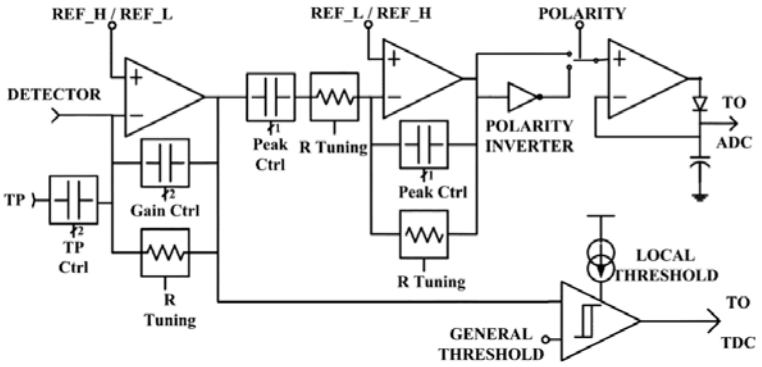

FIGURE 3.7: Architecture of the proposed pixel readout electronics. From [17].

The scheme of the analog front-end is shown in Fig. 3.7. It consists of a charge sensitive amplifier, a CR-RC shaper coupled to a peak-and-hold circuit, and a discriminator into which the preamplifier output is fed. A 10-bit ADC is used to digitize the peak-and-hold output before it is stored in a first-in first-out (FIFO) memory.

3.2.3 Analog Front-End and ADC Characterization

The functionality of the circuits in the pixel analog front-end are shown in Figs. 3.8 and 3.9.

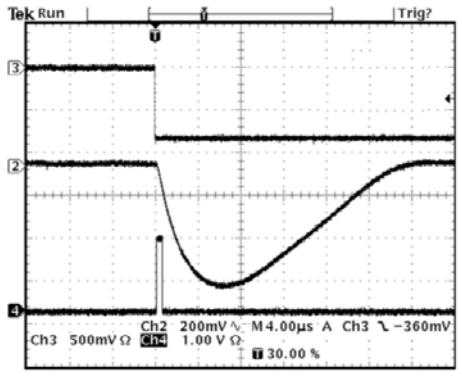

FIGURE 3.8: Measured output waveforms of the shaper (Ch2) and the discriminator (Ch4) with the waveform of the injected test pulse (Ch3). From [17].

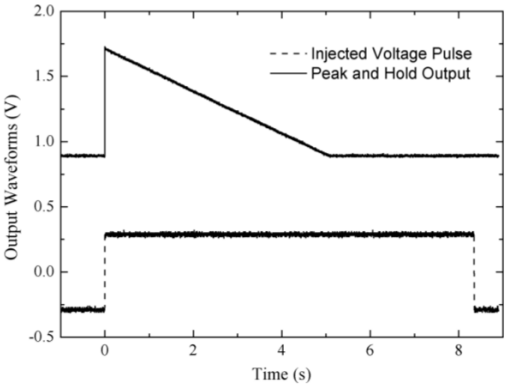

FIGURE 3.9: Measured output waveform of the peak and hold circuit (solid line) with the waveform of the injected test pulse (dashed line). From [17].

Fig. 3.8 shows the waveforms of an input pulse and the output of the discriminator and the shaper. The output of the shaper shows a peaking time of about 6 μs and it reaches the baseline after 24 μs approximately. Fig. 3.9 shows the output waveform of

Input charge dynamic range	± 17 fC to ± 70 fC
Gain for both polarities	10, 16, 20 and 40 mV/fC
Shaper peak time	4 to 16 μs
Detector Leakage Current	250 pA/pixel
Peak-and-hold circuit discharge rate	160 μs/ms
Detector leakage compensation	up to 10 nA per pixel
Minimum threshold	6 keV
ENC[a] @40 mV/fC (Pos/Neg polarity)	98 e^- RMS / 107 e^- RMS
Discriminator jitter	<10 ns for E>20 keV
Supply Voltage	2.5 V
Preamplifier/Shaper	75 μW/20 μW
Peak and Hold/Discriminator	20 μW/35 μW
ADC/Total Power Consumption	50 μW/200 μW
ADC conversion clock frequency	1 MHz
Analog front-end area	300 μm-400μm
ADC area	400 μm-400μm

[a]Equivalent Noise Charge

TABLE 3.2: Measured performance of the Analog Front-End plus ADC. From [17].

the peak-and-hold, which discharges 800 mV in 5 s if no reset is applied. Such a slow discharge rate allows to digitize the output with any delay required.

The ADC shows a linear behavior with a standard deviation of 0.2 less significant bit (LSB). Tab. 3.2 summarizes the complete characterization of the electronic path that includes the analog front-end and the ADC.

3.2.4 TDC Characterization

The characterization of the TDC, which is located in the backend of the VIP-PIX chip, is done by comparing its performance to a commercial TDC that has 25 ps time resolution. The linearity of the TDC is shown in Fig. 3.10. The slope of the linear fit is 10.6 ADC counts/ns, which corresponds to a sensitivity of 95 ps/ADC count.

Fig. 3.11 shows the resolution of the TDC with 100 measurements per point. One can observe that the resolution increases linearly with the pulse width. The resolution FWHM is 600 ps at full range, well below 1 ns.

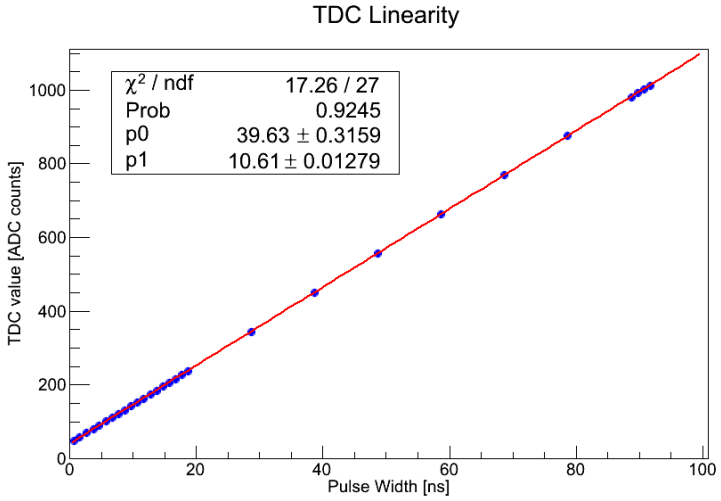

FIGURE 3.10: Measured linearity of the TDC. From [17].

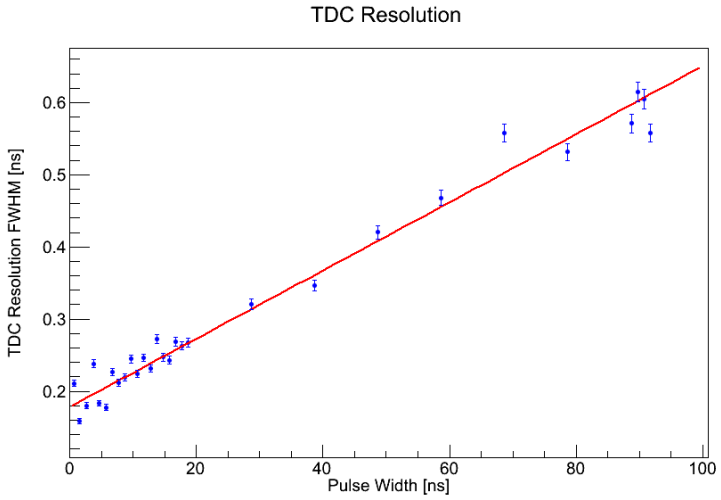

FIGURE 3.11: Measured resolution FWHM of the TDC. From [18].

3.2.5 Temperature Sensor Characterization

The CdTe leakage current and energy resolution is very sensitive to change of temperature. Therefore to insure the VIP CdTe is maintained at the right temperature, a temperature sensors has been included in the backend of the VIP-PIX. The response of the temperature sensor of the VIP-PIX has been characterized in an environment with a temperature known with 0.1 °C precision. Fig. 3.12 shows the response of the temperature sensor in the range from -20 °C to +25 °C. The slope is 2.9 ADC counts/°C, which is 0.34 °C/ADC count. With such resolution the temperature of the VIP scanner can be maintained within a precision of ±0.5°C.

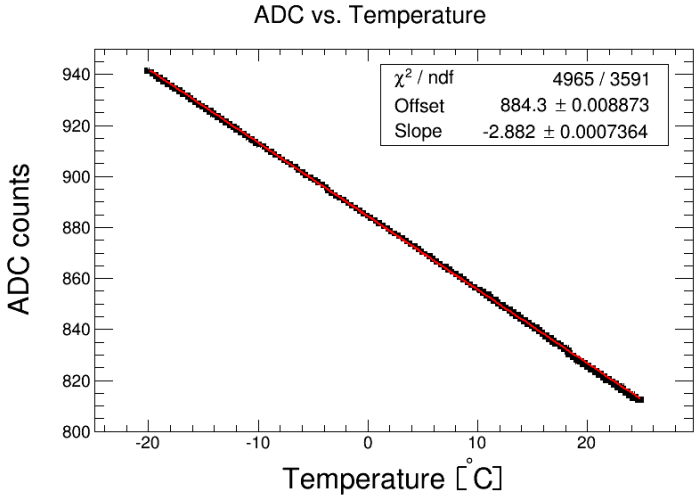

FIGURE 3.12: Measured response of the temperature sensor. From [18].

3.3 Performance Simulation of VIP Scanners

In order to quantify with precision the performance of VIP scanners, simulations of radiation matter interaction for each particular geometry and different radiation sources have been performed. The framework used for this purpose has been the GEANT4-based Architecture for Medicine-Oriented Simulations (GAMOS) [133].

Three different scanners have been simulated: the VIP-PET, the VIP-PEM scanner and the VIP-CC. The optimal reconstruction algorithm has been studied for each particular case given that the field of view, the amount of channels or the detection principle have to be taken into account to choose the appropriate algorithm.

3.3.1 VIP-PET

The aim of the VIP-PET simulation is to assess the performance and limitation of the design. The evaluation of the VIP-PET scanner performance, done with GAMOS, is described in more detail in [19].

The fraction of scatter events (SF) in the data sample of the VIP-PET has been evaluated according to the prescription of the NEMA NU 2-2001 standard [134]. The SF for the VIP-PET is found to be 3.95% while state-of-the-art brain PET scanners can hardly reach any value below 30%. The VIP-PET has also been compared to small animal PET scanners according to the NEMA NU 4-2008 protocol [22]. In this case the SF

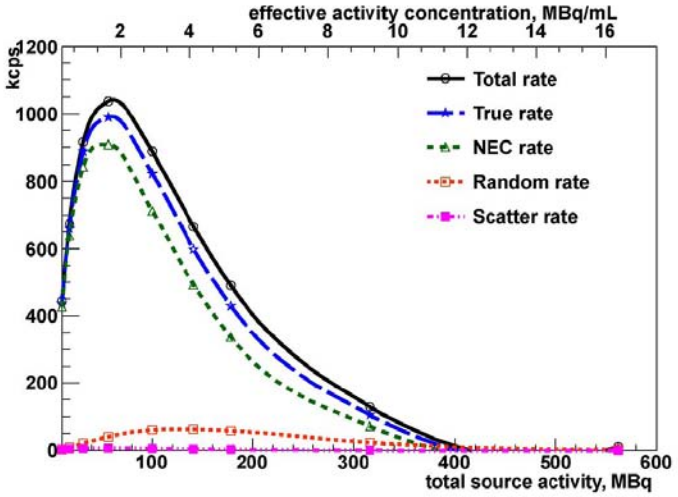

FIGURE 3.13: NEMA NU 4-2008 VIP scanner counting rates as a function of effective activity concentration and total source activity of a line source for the mouse-size phantom. From [19].

of the VIP-PET is 0.75% whereas for state-of-the-art small animal PET scanners it is more than 10% The significant reduction of scattered events in the data sample is due to the superior energy resolution of the VIP-module which allows to narrow the acceptance window of events to an energy of ±8 keV around the 511 keV peak and reject most of the scattered events.

The counting rate has been tested in order to measure the efficiency of the scanner as a function of the activity. The rate of true, scatter and random events as well as the noise equivalent count (NEC) rate are plotted as a function of the activity in Fig. 3.13. One can see that most of the total rate corresponds to true events whereas random or scatter events show little contribution. The decrease of the rates with increasing activity is due to multiple events. Multiple events are those in which, for a given window of time t_W, more than two photons are detected. This time window is set proportionally to the coincidence time resolution, hence a very good coincidence time resolution will allow t_W to be smaller and to operate at higher dose activities.

Better sensitivity is always desirable in order to increase the amount of data acquired without increasing the radiation dose in the patient. For the VIP-PET, the sensitivities according to the NEMA NU 2-2001 and NEMA NU 4-2008 protocol are 14.37 cps/kBq and 21 cps/kBq respectively. Both results are superior, when compared with the average performance of commercial PETs. Note, moreover, that since the VIP-PET has a better data sample purity, it can produce better images with less acquired data.

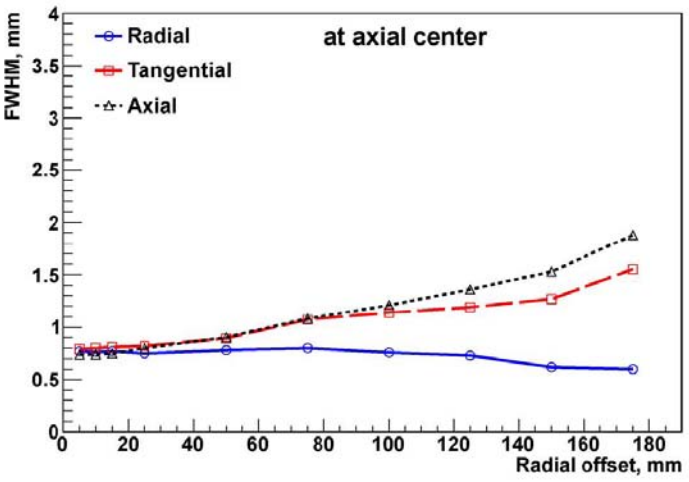

FIGURE 3.14: VIP radial, tangential, and axial spatial resolution (FWHM) as a function of radial offset. From [19].

A phantom with a known geometry and radiation activity is used to evaluate the image quality. Images are reconstructed using the single-slice re-binning technique (SSRB) and FBP reconstruction. The test has been performed following the NEMA NU 4-2008 prescriptions. The results of the radial, tangential and axial spatial resolution in terms of FWHM for different radial offsets are shown in Fig. 3.14. Results are not far from the 0.8 mm limit for a detector with ideal features [135] and thus proves the excellent performance of the VIP-PET.

Another test performed is to obtain an image of the phantom described in the NEMA NU 4-2008 standard which includes cylinders with high and low activity. The protocol requires to put the phantom in air but the same test has been repeated with the phantom in water to prove the VIP-PET behavior under more challenging conditions where more scattered events are present. Both images have been reconstructed using the FBP 2D algorithm. The results are shown in Fig. 3.15. The performance of the scanner is not significantly affected by the water surrounding the phantom because of the capability of the VIP-PET to reject almost all scattered events.

In conclusion, the VIP-PET is a very good spatial and energy resolution PET scanner, optimized for brain metabolism studies. The high sensitivity combined with the virtually noise-free data allows to reduce the time scan and decrease the blurring of the image due to the motion of the patient. Simulations show that 1 mm diameter rods can be detected without background activity and no deterioration of the image is observed

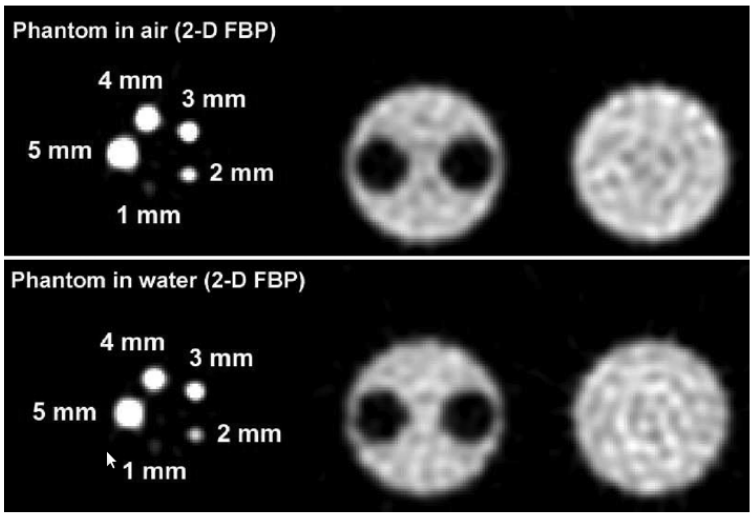

FIGURE 3.15: Transverse images of the image quality phantom reconstructed using FBP with $1.5{\cdot}10^6$ coincidences. Top row: the phantom is in air; bottom row: phantom is in a water sphere; left: hot rods; middle: cold inserts; right: uniform region. From [19].

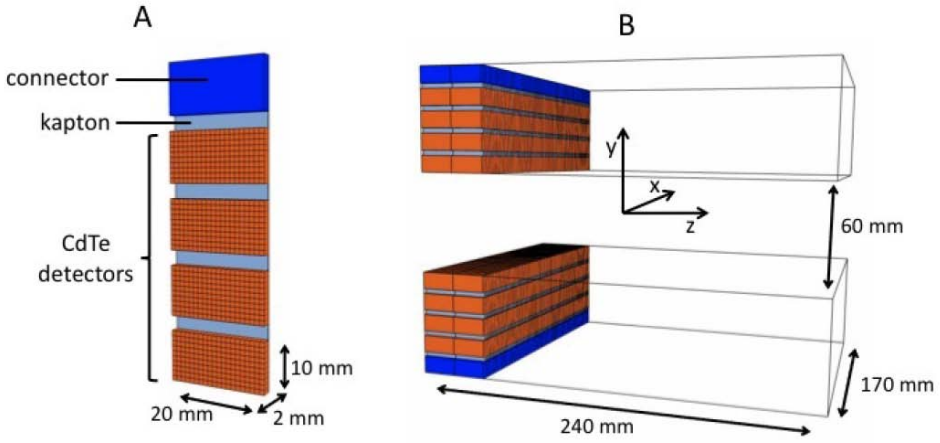

FIGURE 3.16: Basic unit detector (A) and full detector (B) geometrical specifications. From [20].

when a scattering volume is placed around the active region. According to the results presented, VIP-PET has all the capabilities needed to perform a main role in the next generation of PET scanners.

3.3.2 VIP-PEM

The VIP-PEM design has two parallelepiped shape heads based on VIP modules, see Fig. 3.16. Each head is made of 80 VIP modules arranged along two lines for a total

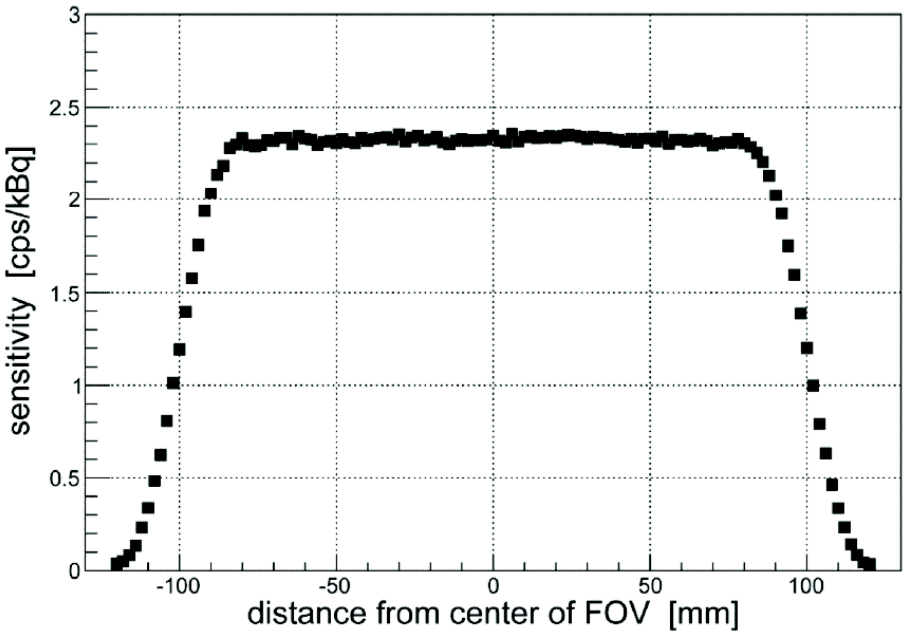

FIGURE 3.17: Values of sensitivity for a ^{22}Na point-like source in different positions along the z-axis (axial scan). From [21].

128000 channels per head. The results of the evaluation tests for the VIP-PEM are presented in more detail in [20, 21].

The VIP-PEM shows a good sensitivity that improves the performance of state-of-the-art PET scanners [12]. The sensitivity of the device for a point-like source in different positions along the Z-axis is shown in Fig. 3.17. As one can expect due to the geometry of the device, the distribution is flat along all the axes except for the edges, where the particles emitted cannot reach the detectors and the sensitivity drops quickly to 0.

The purity of the signal can be evaluated by the fraction of true events on the data sample. The VIP-PET achieves very high signal purity up to high activities, as shown in Fig. 3.18. The fraction of scattered events is negligible regardless of the activity due to the excellent rejection because the very good energy resolution allows a for tight window around the energies of the coincidence photons. The contribution of random events is moderated at low activity values and increases significantly from 10^7 Bq on. It achieves its maximum rate at 10^8 Bq, where the scatter rate is higher than the true rate. For higher values of the activity the multiple events dominate the data sample and the total count rate reaches 0 immediately.

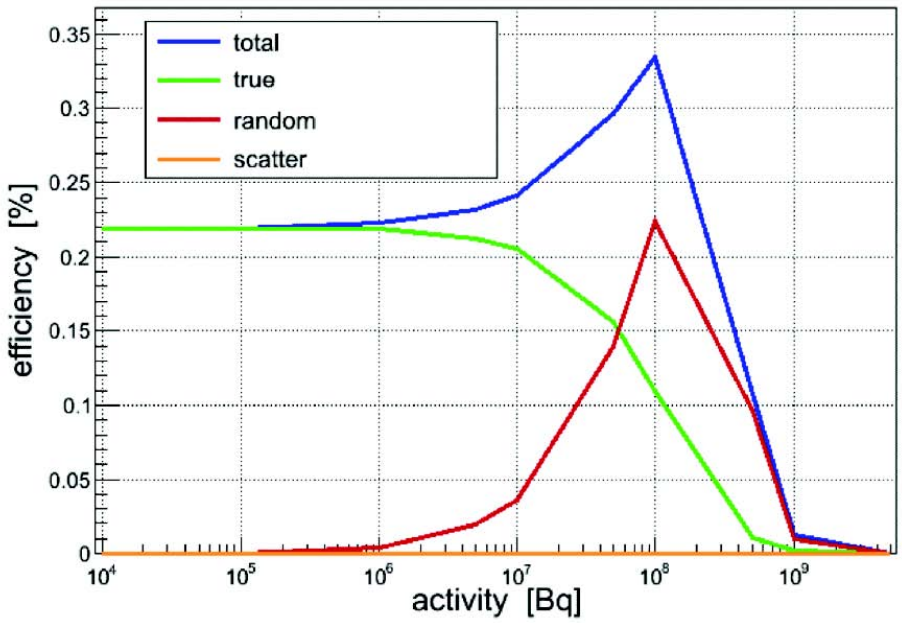

FIGURE 3.18: Values of coincidence rate as a function of activity concentration in the rat-like phantom as defined in the NEMA NU 4-2008 report [22]. Rate values for true, random, and scatter events are shown separately for comparison. From [21].

The reconstruction algorithm used to perform the quality tests with the VIP-PEM is LM-OSEM. OSEM gives a good result but consumes too much of CPU time whereas FBP is not appropriate because it requires a FOV of 180°, see Sec.2.5 for further details.

The small FOV and the parallelepiped shape of the scanner can cause very different values for the resolutions along different axes [12] due to the parallax error. The magnitude of this effect can be tested by taking an image with the same phantom aligned along the Y axis, first, and along the Z axis afterwards (using the same coordinates as in 3.16), as shown in Figs. 3.19 and 3.20. In the VIP-PEM, due to the 3D segmentation, the parallax error is dramatically reduced and practically no difference can be observed for the resolutions along the Y or the Z axis.

The VIP-PEM design has the potential to outperform the current state-of-the-art PEM scanners. VIP-PEM has a good sensitivity, excellent signal purity due to scatter event rejection, and superior spatial resolution, especially in the Z axis. Moreover, the smaller size detector of the VIP-PEM, compared to VIP-PET, reduces significantly the cost. For all these reasons VIP-PEM is a good candidate for future PEM choices in nuclear medicine.

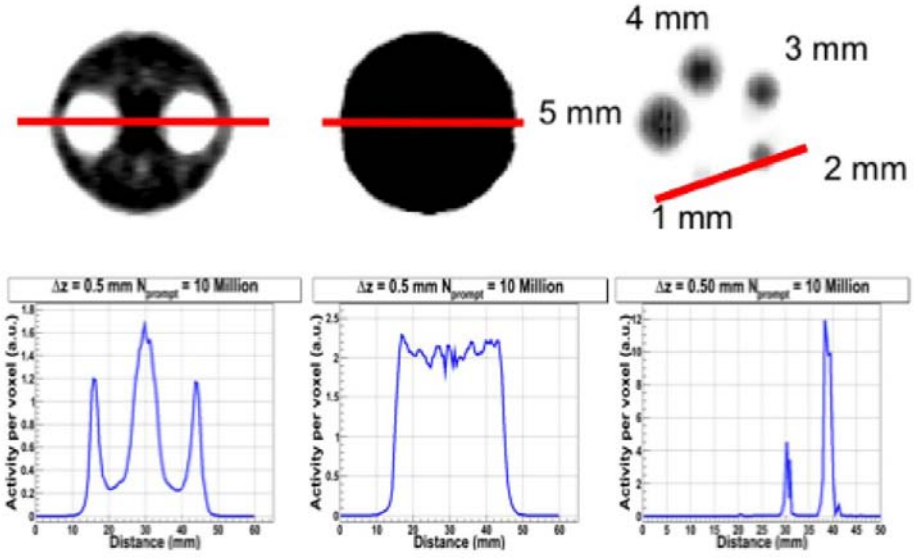

FIGURE 3.19: NEMA NU4-2008 phantom is aligned along the Y axis, reconstructed using the LM-OSEM algorithm with five iterations and twenty subsets. Top-left: cold inserts region; top-middle: uniform region; top-right: hot rods. Bottom-left: activity line profiles of cold inserts region; bottom-middle: activity line profiles of uniform region; bottom-right: activity line profiles along the 1 mm and 2 mm hot rods. From [20].

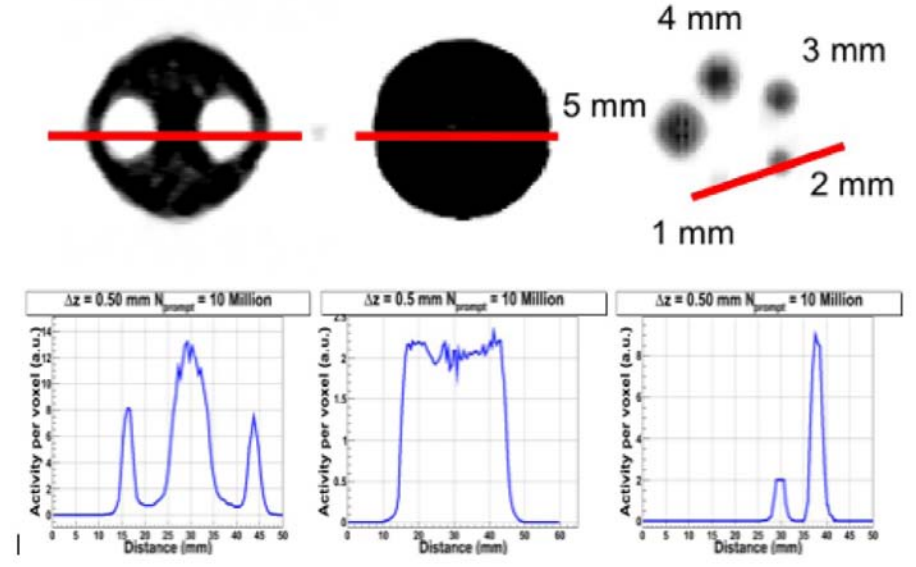

FIGURE 3.20: NEMA NU4-2008 phantom is aligned along the Z axis, reconstructed using the LM-OSEM algorithm with five iterations and twenty sub-sects. Top-left: cold inserts region; top-middle: uniform region; top-right: hot rods. Bottom-left: activity line profiles of cold inserts region; bottom-middle: activity line profiles of uniform region; bottom-right: activity line profiles along the 1 mm and 2 mm hot rods. From [20].

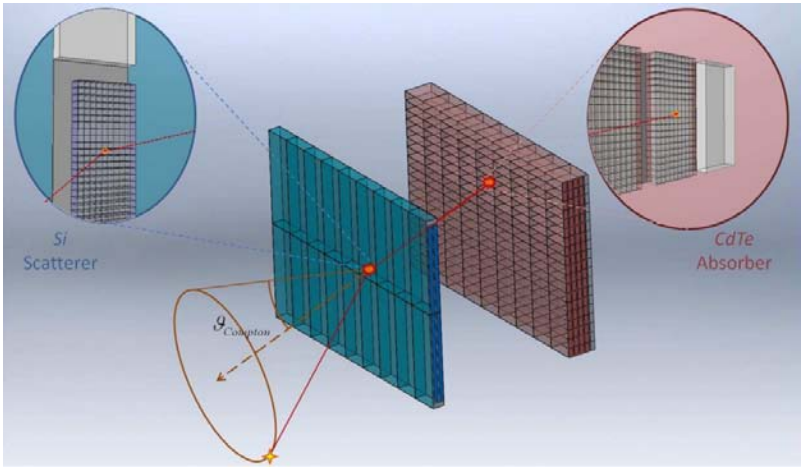

FIGURE 3.21: Schematic of the VIP Compton camera. From [23].

3.3.3 VIP-CC

The VIP design for a Compton camera scanner consists of a scatter detector made of Si and an absorber made of CdTe, as shown in Fig. 3.21. The scanner is made out of VIP modules, with Si diodes for the scatterer and with CdTe diodes for the absorber. The Si has relatively low Z and density compared with other semiconductor materials, which increases the probability of a Compton scattering. Moreover, the scatter detector is 2 cm thick to optimize the probability of having only one single Compton interaction per photon. The CdTe has significantly higher Z and density, hence photons transversing it have more probability to undergo a photoelectric effect. The absorber is 4 cm thick to optimize the amount of trapped photons at reasonable cost.

The main advantage of the VIP-CC is the use of pixelated semiconductor detectors for both the scatterer and the absorber. The high energy resolution achieved by the VIP module allows to recognize with higher accuracy the coincidences, and to obtain a precise estimation of the scattering angle. The small voxel size also allows to reconstruct the interaction points with smaller uncertainty and, hence, to obtain better spatial resolution.

As in the case of VIP-PET and VIP-PEM, the event count rate capability of the VIP-CC is crucial for its performance. Apart from the true coincidences, the background signals can be due to random events, scattered events or other physics (i.e. backscattering or Rayleigh). In this case, the random coincidences consist of two unrelated photons, one detected in the scatterer and another in the absorber. The scatter coincidences are those

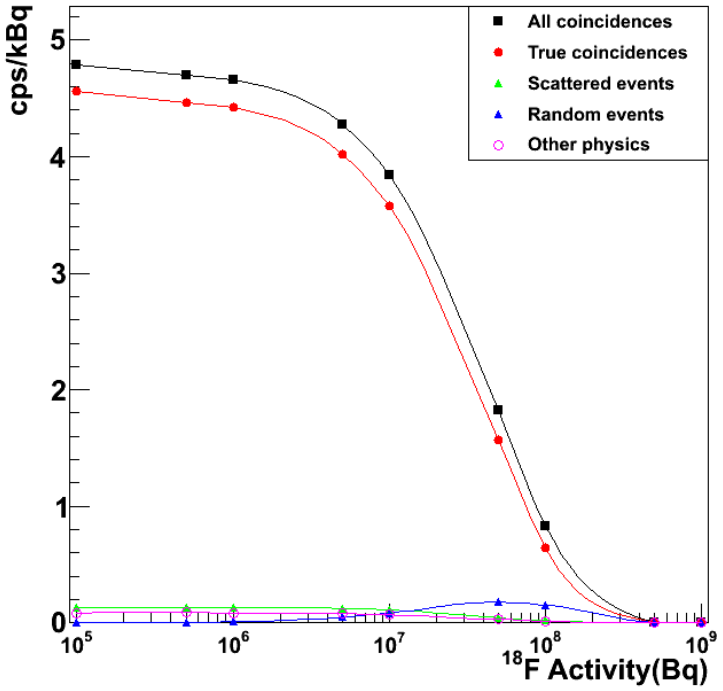

FIGURE 3.22: Sensitivity of the Compton gamma camera, as a function of source activity for ^{18}F.

in which the photon scatters somewhere else before Compton scattering in the scatterer and getting absorbed in the absorber. All coincidences have 1 hit in the scatterer and 1 in the absorber (otherwise they would not be selected). Figs. 3.22 and 3.23 show the count rate according to the protocol NEMA NU1 [136] for ^{18}F and ^{99m}Tc, respectively. In both cases the true event rate is dominant for activities up to 10^7 Bq. With ^{99m}Tc the random events peak is at 10^8 Bq where it has the same value as the true rate. This is caused by the lower energy peak of this source (140 keV). In the case of ^{18}F this effect is negligible due to the much higher energy of its main emission line, 511 keV.

The spatial resolution of the VIP-CC has been measured by simulating Derenzo phantom [137]. Details about the reconstruction algorithms used in the image quality test for the VIP-CC can be found in [23, 138, 139]. VIP-CC can clearly distinguish rods of 1.5 mm diameter spaced by 6 mm as shown in the line profile in Fig. 3.24 when using the LM-OSEM algorithm.

As with the other VIP devices for nuclear medicine, the VIP-CC shows a superior signal purity and excellent spatial resolution. Moreover, it significantly improves the sensitivity

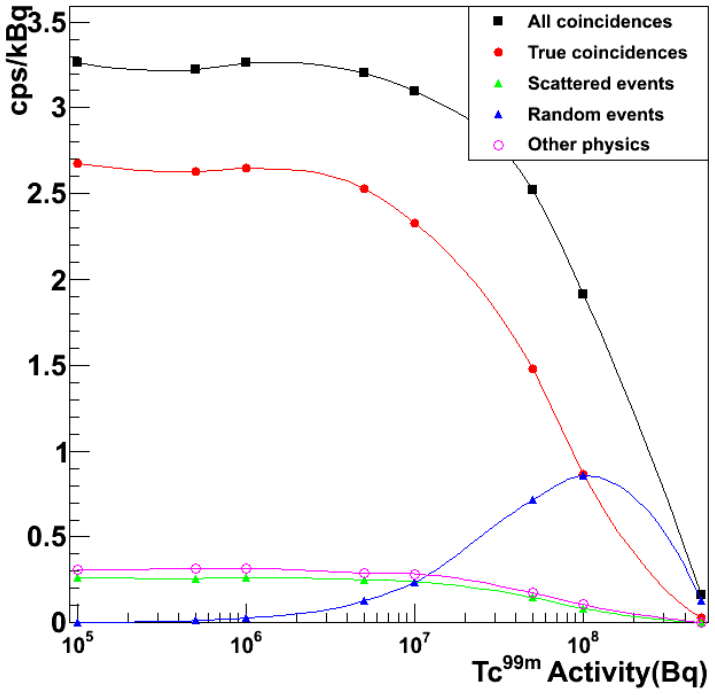

FIGURE 3.23: Sensitivity of the Compton gamma camera, as a function of source activity for ^{99m}Tc.

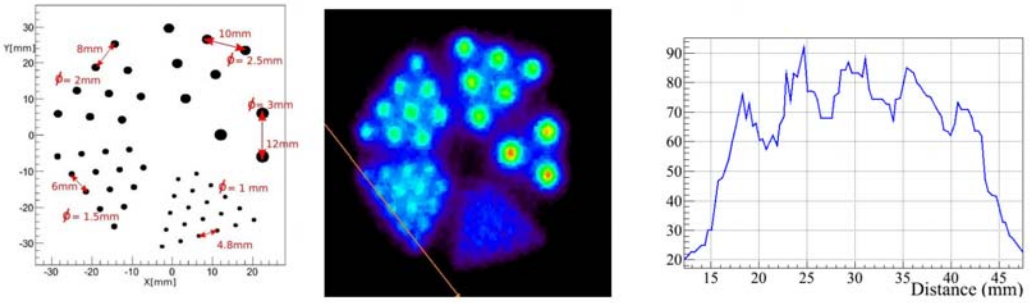

FIGURE 3.24: (Left) Depiction of the Derenzo phantom in the XY plane. (Middle) LM-OSEM result on 70 M Compton coincidences with a Derenzo phantom after applying a 3D median filter. (Right) Line-profile through the rods with 1.5 mm diameter. With the phantom at a distance of 100 mm from the scatterer and an activity of $2{\times}10^8$ Bq, the Compton camera sensitivity is 3.3 cps/kBq and it would take 1.8 min to get the 70 M coincidences used for this image.

which allows shortening the time scan and reduce contribution of the patient motion to the image blurring without increasing the dose injected to the patient.

Although some SPECT scanner with semiconductor detectors have been already commercialized [140], yet it is not the case for Compton Camera. The VIP-CC provides a viable concept to construct such camera and thus has the potential to make Compton Camera for medical imaging a reality.

Chapter 4

Single Pixel CdTe Characterization and Performance

At the start of the VIP project, the VIP chip and pixel CdTe detector were just specifications on paper and it was foreseen to test the VIP sensor (chip+CdTe) in the years to come. It was decided to start with basic tests to see the performance of only the the CdTe detector, with respect to timing of the trigger and the energy resolution. This chapter is about the performance of a single pixel CdTe diode coupled to commercial readout-out electronics. A dedicated *Graphic User Interface (GUI)* is used to control the relevant devices of the test setup and to collect data using different trigger modes. From the data sample that has been collected the detector energy resolution, at different X-ray photons energies, and coincidence time resolutions have been measured.

4.1 Setup Description

The setup described in this section has been designed to operate a single channel CdTe diode. The output of the diode was connected to the *AMPTEK*[1] A250 charge sensitive amplifier, also called preamplifier, to integrate and amplify the CdTe signal. The preamplifier has been coupled to the AMPTEK A275, a pulse amplifier, also called shaper,

[1] AMPTEK Inc, USA.

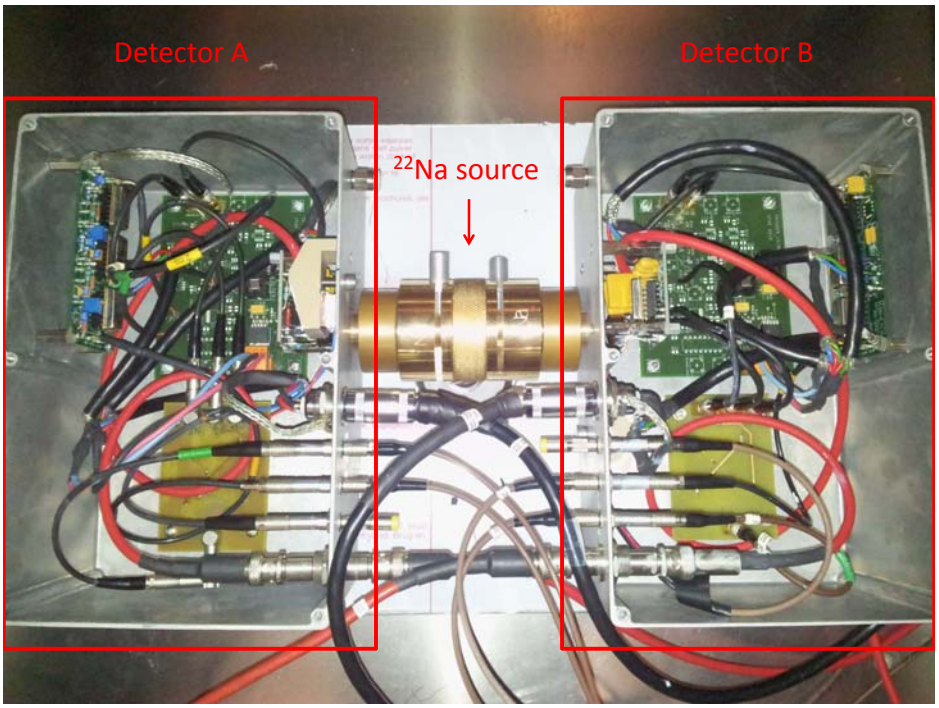

FIGURE 4.1: Shown the setup to operate the two CdTe detectors in coincidence mode.

to filter the preamplifier output signal. The shaper delivers a pulse with the amplitude proportional to the amplitude of the preamplifier output signal. The amplitude of the shaper output has been measured with a peak sensing ADC CAEN V785.

A discriminator with pre-defined threshold has been used to trigger on the preamplifier output signal. The discriminator output trigger has been connected to the TDC CAEN V1290N to measure the timestamp at which the preamplifier signal crossed the predefined threshold.

Two identical CdTe detectors, each using the same readout electronics, have been put face-to-face and have been operated simultaneously to measure the coincidence time resolution. A picture of the setup is shown in Fig. 4.1.

4.1.1 Single Pixel CdTe Diode

The CdTe diode used in this test setup was manufactured by *ACRORAD*[2]. At ACRORAD, the CdTe crystal is grown by the traveling heater method (THM) [141]. After the crystal is cut and polished, and the metal electrodes are deposited, the detector area is 4.1 mm × 4.1 mm and the thickness is 2 mm. The CdTe diode is mounted on a ceramic

[2]ACRORAD LTD, Japan.

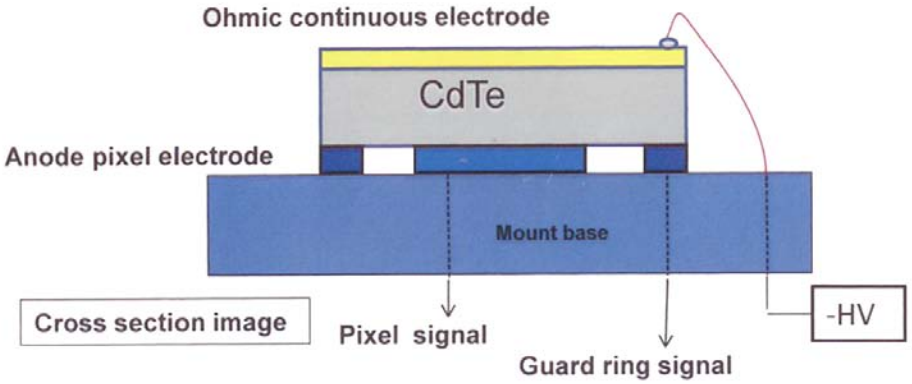

FIGURE 4.2: Schematic of the CdTe diode structure.

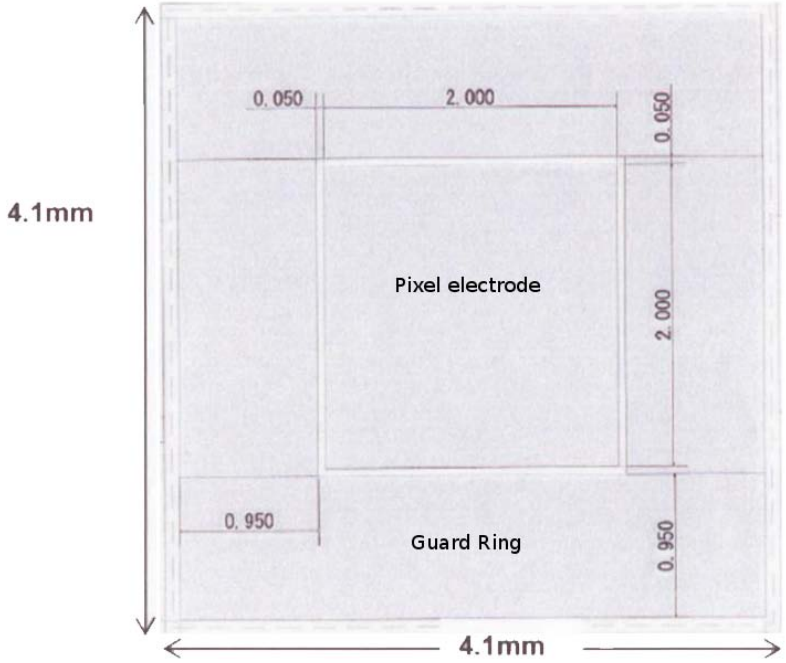

FIGURE 4.3: Schematic of the pixel electrode pattern.

substrate as shown in the cross-section schematic view of Fig. 4.2. The configuration of the electrode is: pixel-Au/Ti/Al/CdTe/Pt-continous. The bias voltage is applied on the ohmic continuous electrode.

The electrode on the bottom side of the detector is divided into two regions: the *pixel electrode* and the *guard ring*. as shown in Fig. 4.3. The pixel region occupies a surface of 2 mm $\times$ 2 mm in the center of the electrode. This region is the active part of the

	AMPTEK A250	Required
Sensitivity for CdTe	36 mV/MeV	-
Rise Time [ns]	2.5 @ 0 pF	<35
Decay Time Constant [μs]	300	>100
Operating Temperature [°C]	-55,+125	-10,+25

TABLE 4.1: Basic specifications of the preamplifier AMPTEK A250 and the requirements of the setup.

diode. The guard ring is separated by 50 μm from the pixel region.

4.1.2 AMPTEK Front-End Electronics

4.1.2.1 Preamplifier A250

The CdTe diode is a current source and since the signal coming from the pixel electrode is very small, it needs to be amplified to make it possible to process it. For this reason the AMPTEK A250 has been used as a first stage amplifier, because of its high band width and excellent linearity. The total induced charge, or the integrated current, is proportional to the energy deposited by the photon in the bulk of the CdTe diode. The specifications of the preamplifier and the requirements for the measurements done are shown in Tab. 4.1.

An energy of 1 MeV deposited in the CdTe detector will generate a voltage output of 36 mV. Since the response of the preamplifier is linear, one can expect 18 mV amplitude pulse for a 511 keV deposition.

The peak time for an event with full contribution of electrons at -2000 V bias voltage in a CdTe diode with 2 mm thickness is 20 ns, where the saturation value of the mobility considered is μ_e=2000 cm^2/(V·s) [142]. The preamplifier A250 has a rise-time of 2.5 ns, which is faster than the diode signal and thus fulfills this requirement.

The decay constant of the preamplifier has to be long enough to avoid the decrease of the preamplifier peak value during the window peak time of pulse shaping. A decay time of 1% of the signal after 10 μs has been considered as a safe value to operate the preamplifier. In this case, the decay constant RC is set to 100 μs. The preamplifier has a decay constant RC=300 μs. This amount of time is enough for the circuit to reach the baseline level and avoid the overlap of signal processing of two events. The expected

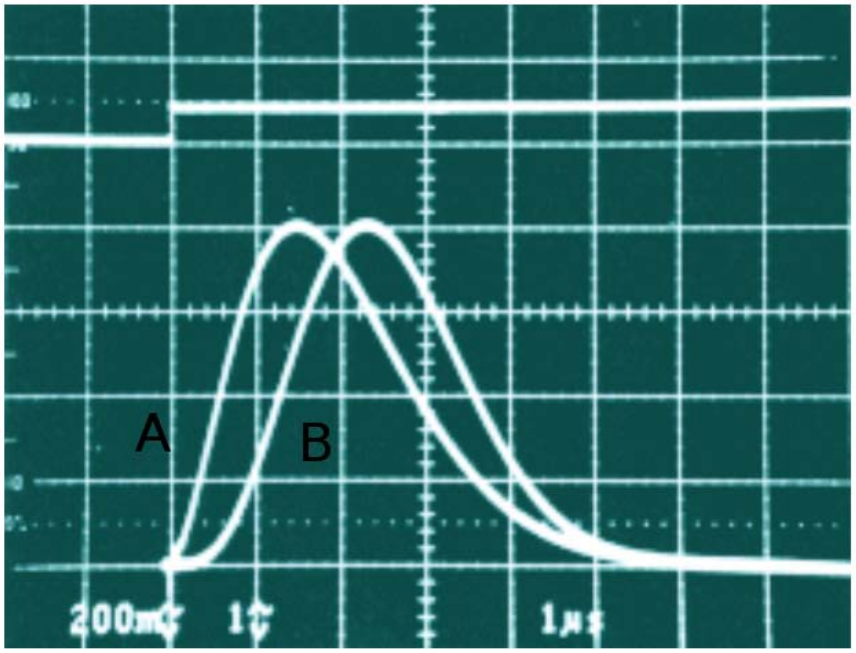

FIGURE 4.4: A275 input/output waveforms. *Upper:* input pulse. *Bottom: First output (A),* 3 pole configuration. *Second output (B),* 5 pole configuration.

rate of detection is less than 50 cps so one could expect an average of 20 ms between each detection.

The test setup is to be operated between room temperature and -10°C.

4.1.2.2 Pulse Amplifier and Shaper A275

The gain of the A250 is relatively small, 36mV/MeV because the intention is to be used as a first stage amplifier, i.e., as preamplifier. Its output signal is very fast but at the same time it has a high level of noise and this limits the precision of the energy measurements.

A pulse shaper, a second stage filter and amplification, is needed to reduce the noise and to further amplify the signal. The shaper transforms the step-function like signal of the A250 into a pulse of limited duration, around 5 μs, with an amplitude proportional to its input. An example of the shaper output is shown in Fig. 4.4. The peaking time is the time it takes for the shaper output to reach the maximum amplitude. The peaking time is characteristic of the shaper circuit and independent of the amplitude of the input signal.

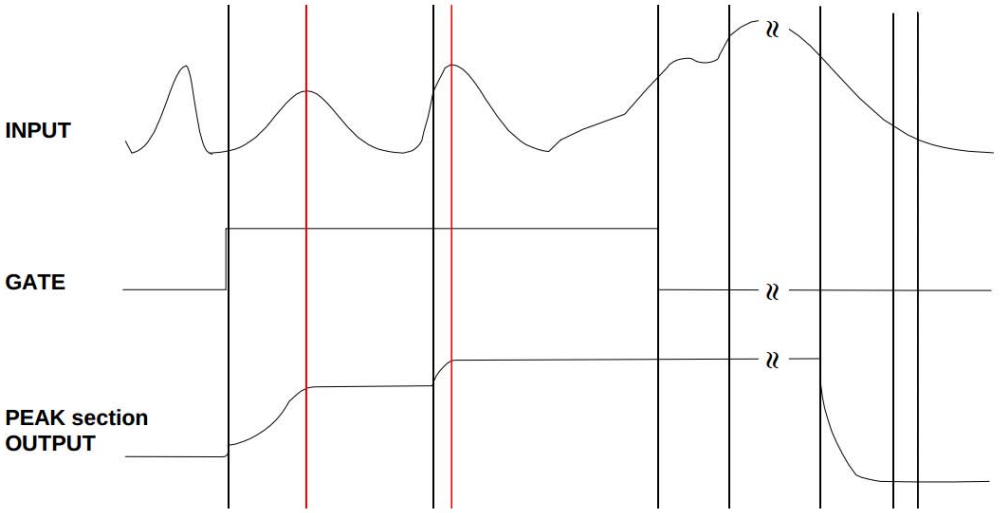

FIGURE 4.5: Peak sensing time flow of the input signal, GATE and PEAK section OUTPUT.

The maximum rise time for the preamplifier output is of 1.1 μs for a mobility of the holes of μ_h=70 cm^2/(V·s) [143] and a bias voltage of -500 V/mm. This value is well below the 2.3 μs peaking time of the A275 so no charge is likely to be lost at -500 V bias voltage, which means that all the charge will be integrated without problems.

The required operating temperature is the same as in the case of the preamplifier A250.

4.1.3 Pulse Amplitude Measurement

The amplitude of the A275, the shaper, output pulse has been measured with the peak sensing ADC CAEN V785. The ADC records the maximum input signal received within an adjustable time window as shown in Fig. 4.5

The *PEAK section OUTPUT* is constant while the GATE is down, regardless of the behavior of the input signal. When the *GATE* goes up the *PEAK section OUTPUT* starts to hold the higher value of the *INPUT* signal. When the *GATE* signal goes back down, the analog value of *PEAK section OUTPUT* is digitized and stored in the buffer memory. The peak sensing ADC has 12 bit precision and is configured in a range of 4 V, which corresponds to 1 mV per ADC count.

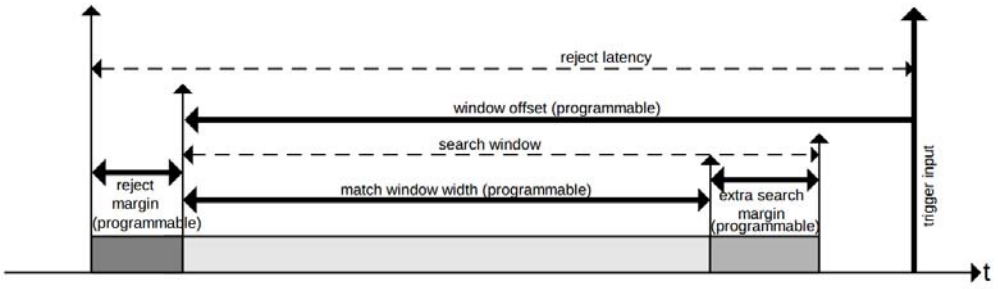

FIGURE 4.6: Timing diagram of the Trigger Matching Mode of the TDC CAEN 1290N

4.1.4 Time Detection Measurement

The timestamp of the trigger signals have been measured with the TDC CAEN V1290N. The TDC has been used in the *Trigger Matching Mode*, which is sketched in Fig. 4.6. A resolution of 25 ps is achieved with this operation mode, which is enough for our purpose.

The time diagram of each acquisition sequence is relative to the time of arrival of the *trigger input* as shown in Fig. 4.6. The *search window* starts after a period *window offset* with respect to the *trigger input*. The window offset can be negative and, hence, signals can be recorded before the *trigger input* arrives. However, for safety, the signals have been delayed to ensure that they are always detected after the trigger input. Rise edges that arrive to the TDC during the *search window* time will be registered.

4.2 Data Acquisition

Two types of data sets have been acquired: single events and coincidence events. Single events consist of the measurement of the energy of one detected photon. Coincidence events consist of the measurement of the energy and the timestamps of two detected photons. With the GUI the user can use either trigger system to collect the corresponding data sample.

4.2.1 Single Event Trigger System

The single event acquisition is meant to detect a particle, using the discriminator signal, in one single detector and soon after to start the readout of the pulse height, which is proportional to the energy deposited. To collect such a data sample, one can use either the output of the preamplifier or that of the shaper to generate the trigger signal. In the case of the preamplifier output the trigger has faster rise-time which helps to minimize the jitter of the detection timestamp. However, the preamplifier has relatively small gain and high noise, which makes it difficult to set the trigger for an photon with small energy. The shaper output allows to set the threshold at lower energy values due to its high gain and significantly lower noise but has a bigger jitter on the timestamp measurement. Since one of the aims of this setup is to measure the coincidence time resolution between two detectors, the preamplifier output has been used to generate the trigger signal.

The discriminator used in this setup is a LeCroy 821 which provides the trigger output signal with adjustable width. For the needs of this test, the width has been set to 5 μs. A snapshot for an event detected by the CdTe and acquired by the oscilloscope (see Fig. 4.7) shows a pulse shape and the timing of the preamplifier, shaper and the GATE signals. One can see that the maximum amplitude of the shaper output is within the GATE width and this will secure that the peak sensing ADC acquires the correct amplitude of the shaper output and, therefore measures the deposited energy correctly.

4.2.2 Coincidence Trigger System

The coincidence trigger system generates a trigger signal when both discriminators, one for each CdTe detector, trigger simultaneously (within a time-window of 150 ns).

The scheme of the coincidence detection system is shown in Fig. 4.8. It consists of two identical setups, each with a CdTe diode, a preamplifier and a shaper. Each preamplifier has a fan-out of 2, one output is amplified by a factor of 2 and is used to measure the pulse amplitude and the other one is amplified by a factor of 9 and is used to generate the trigger signal. Both trigger thresholds are set to a value equivalent of 25 keV. The amplification step of gain 9 right, after the A250 (preamplifier) has been introduced in order to adjust the trigger threshold with better precision.

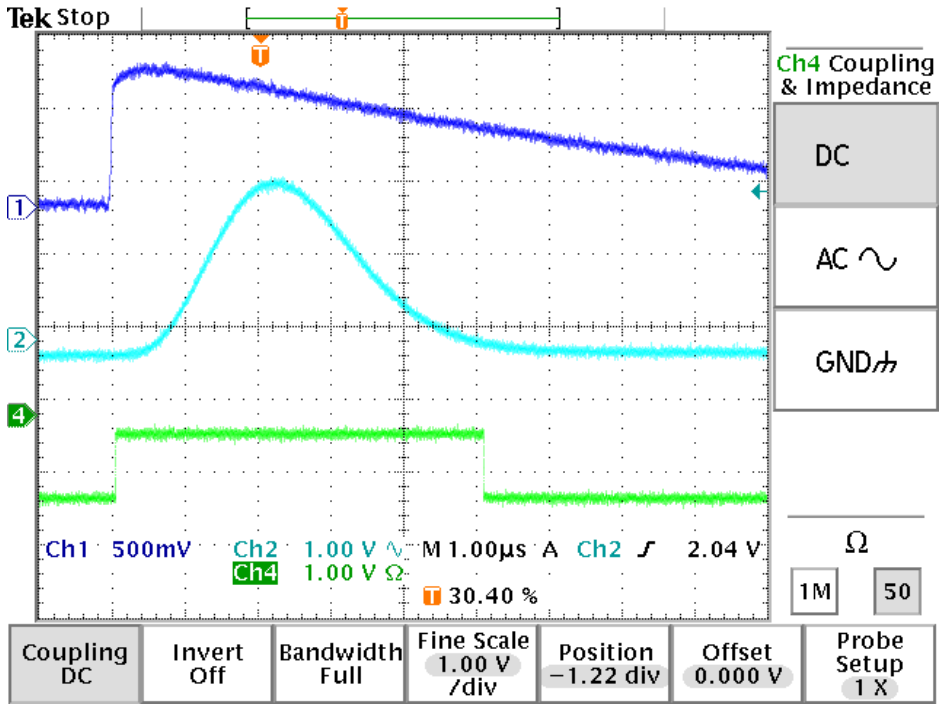

FIGURE 4.7: Waveforms of the preamplifier output (Ch1), shaper output (Ch2) and ENABLE GATE signal of the CAEN V785(Ch4).

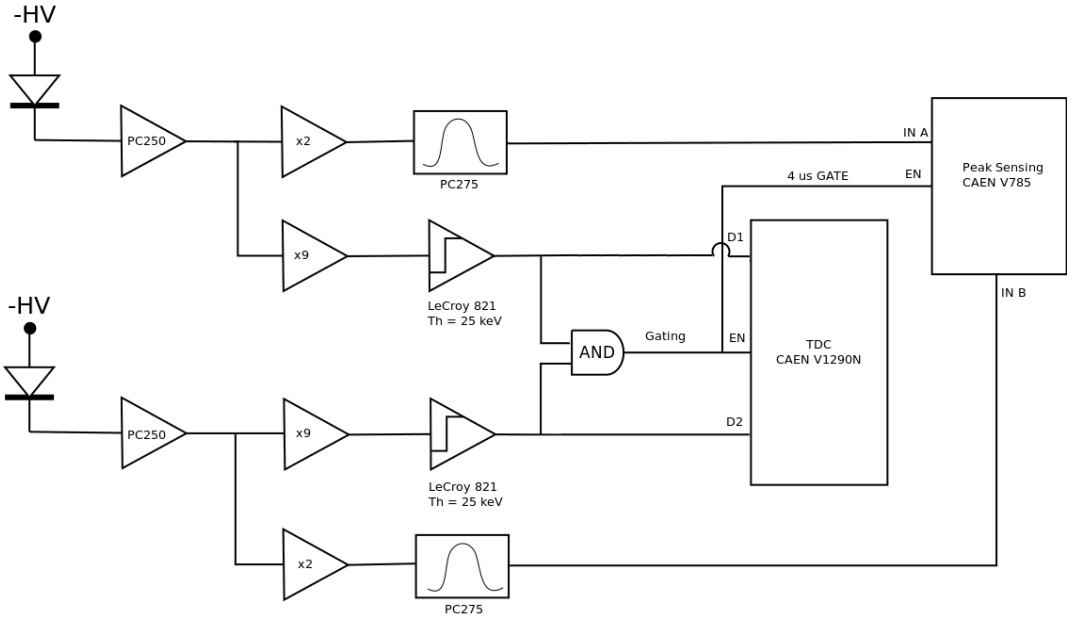

FIGURE 4.8: Coincidence diagram scheme. Two identical CdTe diodes with identical readouts are operated in coincidence mode. The diodes have been coupled to the preamplifier A250 that is mounted on the test board PC250 and the signal is duplicated. One branch is amplified by a factor of 2 and is connected to the pulse amplitude shaper A275, which is mounted on a test board PC275. The other branch is amplified by a factor of 9 and is connected to the discriminator input. The discriminator output for each CdTe diode is duplicated. One is connected to the AND logic unit and one is connected to one of the input channels of the TDC to measure the relative timestamp, which will take place only if the AND logic is TRUE. For each coincidence trigger the setup delivers the energy and the timestamps of both detectors.

The discriminators have a fan-out of 2. One output is used for the AND logic module that enables the TDC when both triggers overlap within predefined window. The other output is recorded in the TDC in case the AND signal is TRUE. The output of the AND logic also acts as a gate of 5 μs for the peak sensing ADC for the measurement of the pulse amplitude.

4.2.3 Single Event Data Acquisition

The single event data acquisition mode is used to perform energy spectroscopy. Using the same trigger mode, a random trigger (i.e. a trigger completely uncorrelated with the detector output) is generated to sample the distribution of background noise of the detector. The flow diagram of the algorithm used in both cases is shown in Fig. 4.9.

At the start, the user has to introduce the values for the test run: *Bias_voltage, Voltage_step, Ramp_time Max_events, Max_sets* and *waiting_time*. Next the software creates automatically the file where the data will be stored.

Then the detector is ramped up in steps of *Voltage_step* during a time *Ramp_time* until it reach the final bias voltage *Bias_voltage*. The system waits a time *Stabilization_time* before starting the data acquisition processes. For the capacitor, used to filter the Hight Voltage bias, to be completely charged up and hence the CdTe is properly biased.

When the CdTe detector is properly biased the event counter is set to 0. The data buffer or the peak sensing ADC is cleared in order to remove any data that could have been registered in an earlier run. The ENABLE_GATE is set up to allow the recording of events. At this point, when an event is detected the trigger will automatically generate the GATE for the peak sensing ADC and the event will be recorded as explained in Sec. 4.2.1. In parallel, the status of the buffer of the peak sensing is checked continuously. When it finds the buffer in a not empty state, ENABLE_GATE is set down.

The data words are read and stored in the buffer. In case the word is an event, the software checks if it belongs to the channel that is being analyzed and in case it does, the value of the amplitude is stored in the data array. Otherwise it is rejected.

Once a good event has been recorded, the rest of the words are not read and the buffer is cleared. The buffer status is checked every 20 ms. Therefore, the probability that two good events are recorded consecutively before the buffer status is checked is very low.

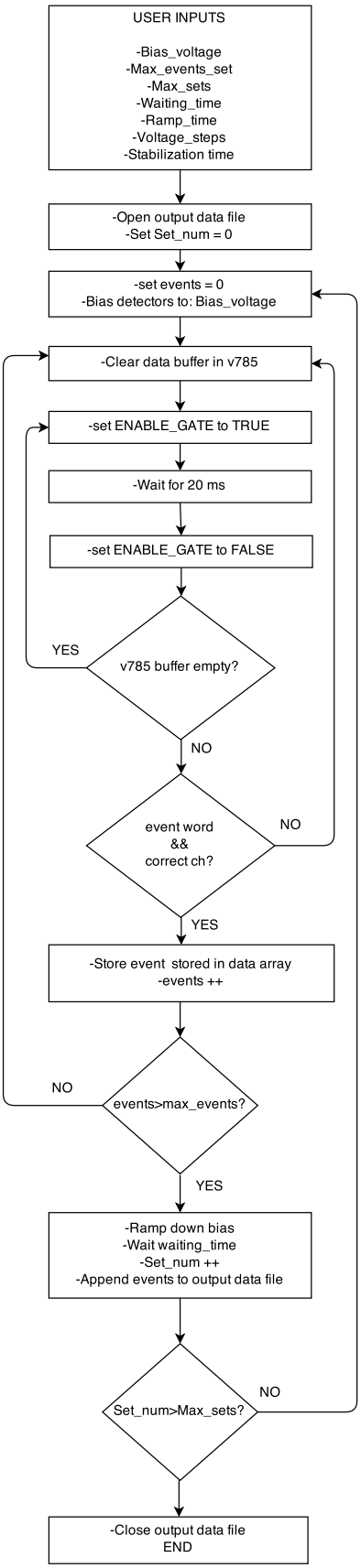

FIGURE 4.9: Single event acquisition flow diagram.

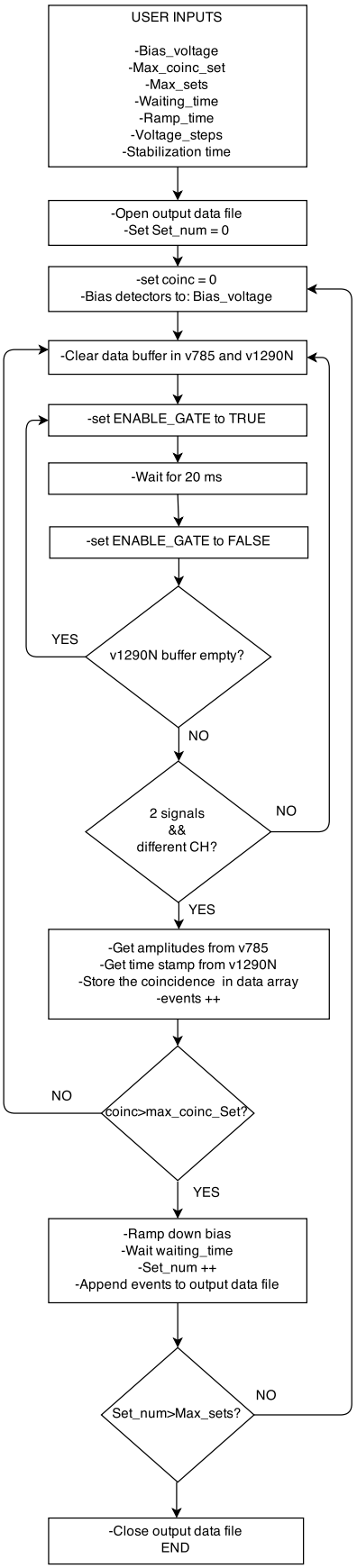

FIGURE 4.10: Coincidence acquisition flow diagram.

The event counter, *events*, is then updated. In the case that the amount of events acquired is bigger or equal to *Max_events* the detectors are ramped down. The ramp down process is completed with a duration of time *Ramp_time* and with a decrease of voltage of *Voltage_step* per step until it reaches 0 V. Then the software appends the array of events into the output data file.

If the maximum number of sets introduced by the user is reached, the software closes the output data file and the process finishes.

4.2.4 Coincidence Data Acquisition

The coincidence data acquisition mode is used to acquire the measurement of two photons created in the same positron-electron annihilation. This mode requires the operation of two detectors. Each coincidence consists of the energy of the photon detected by each detector, and the difference between their timestamps. The flow diagram of the algorithm for the acquisition of coincidences is shown in Fig. 4.10.

The user has to set the input parameters as explained in Sec. 4.2.3. The variable *Max_coinc_set* is equivalent to *Max_events_set* of the single event acquisition mode. Once the user has introduced the value of the variables, the software creates the output data file. Next, the set counter, *Set_num*, and the coincidence counter *coinc*, are set to 0. The bias voltage ramp up process is done as explained in Sec. 4.2.3.

The data buffers of both the peak sensing ADC and the TDC are cleared. Immediately after, the ENABLE_GATE signal is set up. The logic AND output is connected to the *trigger input* of the TDC. At the same time, it gates the peak sensing ADC to measure of the signal amplitudes for the two photons. From this moment on, events on both modules can be acquired. The software waits for 20 ms and sets the ENABLE_GATE signal back down to veto extra acquisitions. The data buffer of the TDC is checked and, in case it is empty the software sets the ENABLE_GATE again up. If the data buffer of the TDC is not empty, then it is read.

The coincidence event is considered good if the buffer of the TDC contains exactly 2 events coming from 2 different channels. In this case it is stored in the data array. Following this, the events stored in the peak sensing ADC are read and stored.

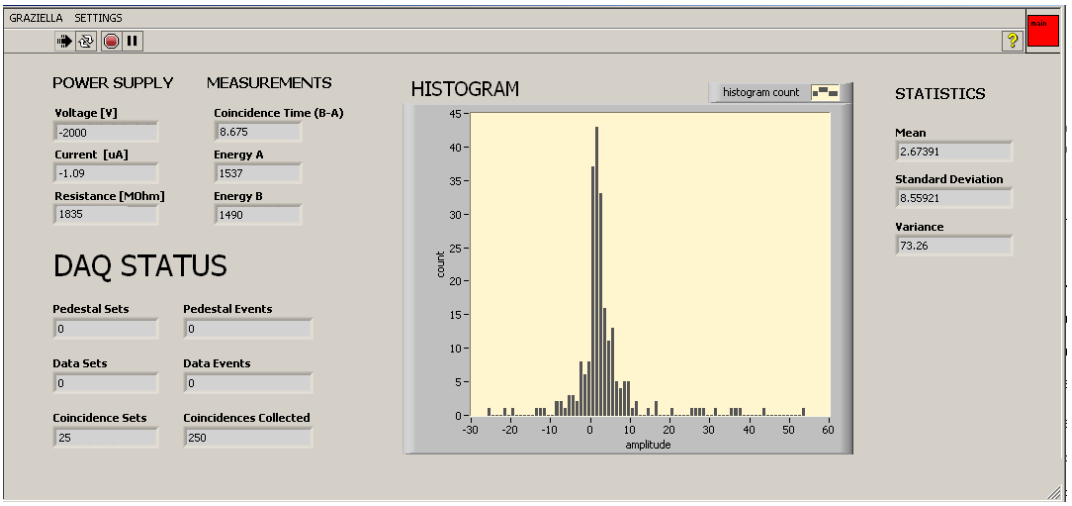

FIGURE 4.11: Snapshot of the Graziella GUI.

Each coincidence event consists of 4 values: photon energy in detector A, photon energy in detector B, timestamp of trigger A and timestamp of trigger B. However, the absolute timestamps of triggers A and B are meaningless for our setup. The difference between the two values is the only magnitude of interest, so the difference is computed immediately after reading the signals and the final coincidence consists of 3 values: the 2 shaper output amplitudes and the time difference.

At this point the coincidence counter is updated. In case the amount of collected coincidences reaches *Max_coinc*, the bias voltage is ramped down as previously described in Sec. 4.2.3 and the coincidences in the memory are appended to the output data file. When the number of coincidence sets is *Max_sets*, the output file is closed and the process finishes.

4.2.5 Software Functionality Description

The data acquisition (DAQ) software used for these measurements has been called *GRAZIELLA*. GRAZIELLA is an executable GUI developed with the *Labview*[3] software. It has been particularly designed to perform the data acquisition algorithms described in Secs. 4.2.3 and 4.2.4.

It is a friendly GUI with easy controls. A snapshot of the main control window is shown in Fig. 4.11. It monitors continuously the voltage and the leakage current when the

[3]Labview is an environment for the development of measurement and control systems supplied by National Instruments. http://www.ni.com/labview/esa/.

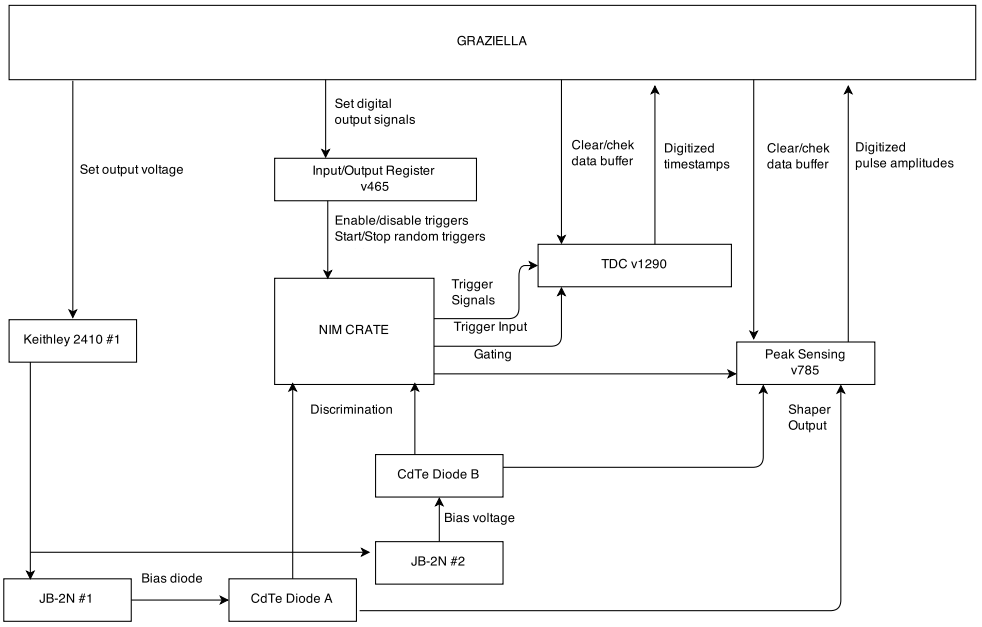

FIGURE 4.12: Scheme of the hierarchy of the devices in the setup.

bias voltage is directly set with the Keithley 2410 power supply. The current set and amount of statistics acquired are shown independently for the pedestal, single event and coincidence acquisition modes. Finally, it shows an histogram of the distribution of the last bench of data obtained. In the case of the pedestal and single event this corresponds to an energy spectrum, whereas for the coincidence mode it is the distribution of the difference in detection time. It shows the mean, RMS and the variance of the distribution shown.

The hierarchy of GRAZIELLA with the devices involved in the setup is shown in Fig. 4.12. It controls one power supply Keithley 2410, which is used in the setup as a low voltage DAC to control two power supplies JB-2N. See App. A for further details about this device. Each power supply JB-2N biases one CdTe diode. GRAZIELLA handles the ramp up/down processes, it computes the waiting time between steps and sets the voltage increase per step. It also reads the voltage, current and resistance of the Keithley 2410 if the diode is biased with this power supply. This can only be done in the single event acquisition mode and with a bias voltage up to -1100 V.

The trigger of the detectors are enabled or disabled using the input/output register CAEN V465 which sends a signal to enable/disable the AND logic of the trigger outputs.

In the case of the pedestal run the input/output register is used to start or stop a NIM clock generator module. This module sends a pulse with a given frequency and pulse width. This clock is used as a trigger to sample the distribution of the pedestal noise.

Meanwhile, GRAZIELLA checks continuously the status of the buffer of the TDC. When the buffer is not empty it registers the timestamp and clears the data from the buffer. Next, it registers the data from the peak sensing ADC buffer and clears it. If it is operating in the single event acquisition mode, only the peak sensing ADC buffer is checked.

4.3 Energy and Timing Resolution Measurements

The data analysis is divided into two samples. One sample is related to the energy spectrum measurements and the data is collected with the single event acquisition mode, from which one can obtain the energy spectrum for both detectors.

The other data sample is collected with the coincidence acquisition mode, from which one can obtain the energy spectrum and the time difference of the two photons. This data sample allows to establish a relation between the expected coincidence time resolution for different energy ranges of the two photons.

4.3.1 Deterioration of Energy Resolution in Time

The CdTe with Schottky contacts suffers from polarization when it is biased [144] for long period of time. Polarization affects the measured energy and creates a shift on the peak position. Fig. 4.13 shows two spectroscopies of ^{57}Co for the data sets acquired during the minutes 0-3 and 7-9 after biasing the CdTe. One can see clearly a small shift between the two distributions. In order to avoid a degradation of the energy resolution due to this effect, the bias voltage has been recycled every, at least, 180 s in all the measurements taken with the CdTe.

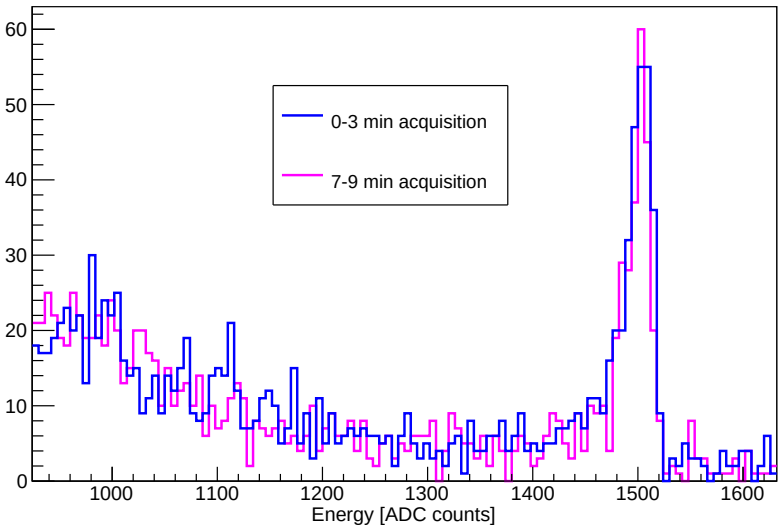

FIGURE 4.13: Spectroscopies of ^{57}Co for events acquired during the minutes 0-3 and 7-9 after biasing the CdTe diode.

4.3.2 Energy Resolution

To measure the energy resolution, two radioactive sources ^{57}Co and ^{22}Na have been used. ^{57}Co has its two lines of emission above 100 keV, at 122 keV and 136 keV with 88% and 12% emission probabilities[4], respectively.

^{22}Na disintegrates predominantly to ^{22}Ne. Only a very small fraction disintegrates to the ground state of the ^{22}Ne. The probability of disintegration through β^+ decay is 90%[5]. Right after the positron emission the ^{22}Ne decays into its ground state and emits a gamma of 1275 keV.

The positron eventually annihilates with an electron of the surrounding media and two 511 keV photons are emitted. Hence, for each positron emission three photons will effectively be created, two with 511 keV energy and one with 1275 keV.

The rate of photons with 511 keV is twice that of those with 1275 keV. However, the difference of energy is large and the probability of the 1275 keV photon to be absorbed by the detector is much less than that of 511 keV. Moreover, the electronics have been adjusted to the range of energy up to 1 MeV. All the events with higher energy than this will appear as overflow events with no information about their energies.

[4]Data from http://www.nucleide.org/DDEP_WG/Nuclides/Co-57_tables.pdf
[5]Data from http://www.nucleide.org/DDEP_WG/Nuclides/Na-22_tables.pdf

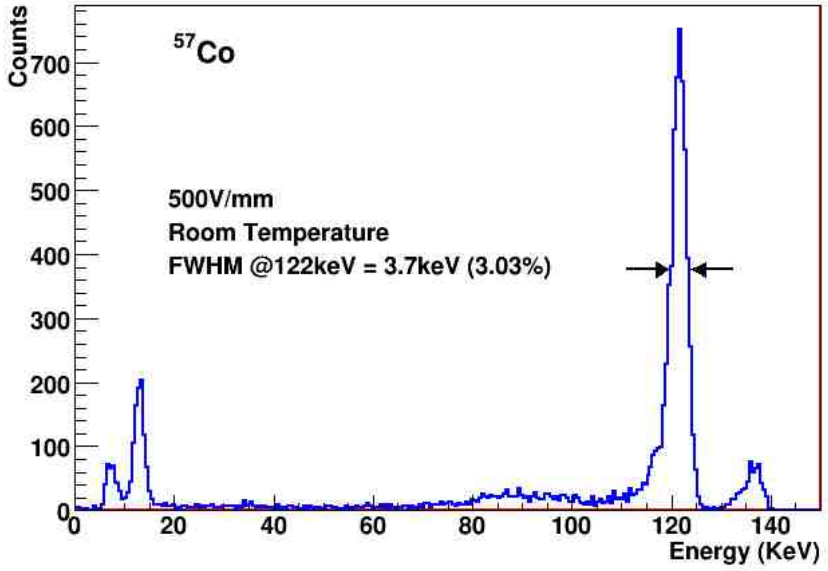

FIGURE 4.14: Spectroscopy of ^{57}Co at 500 V/mm and room temperature.

4.3.2.1 Measurement with ^{57}Co

The energy resolution has been measured at 122 keV with the CdTe at a bias voltage of 500 V/mm and at room temperature. The results can be seen in Fig. 4.14. One can distinguish clearly the two peaks at the decay lines 122 keV and 136 keV. In the lower energy range one can see the 14.4 keV peak of ^{57}Co and the 7.3 keV that corresponds to the most probable electron emission of the ^{57}Fe radionuclide[6]. The FWHM at 122 keV is 3.7 keV. This represents a resolution of 3.03%.

The 122 keV peak shows a clear asymmetry on the low energy side. There is a low energy tail of events that should be in the peak. These events have undergone the effect of charge trapping and have lost part of the energy. Between 80 keV and 100 keV one can see an excess of events above the background level and this is due the scattering process. Indeed this region corresponds to the range with maximum probability of scattering.

4.3.2.2 Measurement with ^{22}Na

^{22}Na is an ideal radioactive to evaluate detectors for the use in PET because it emits two photons, each with 511 KeV, as the FDG18, and thus providing an excellent environment for detector evaluation when it comes to both energy and time-coincidence resolution.

[6]Data from http://www.nucleide.org/DDEP_WG/Nuclides/Co-57_tables.pdf

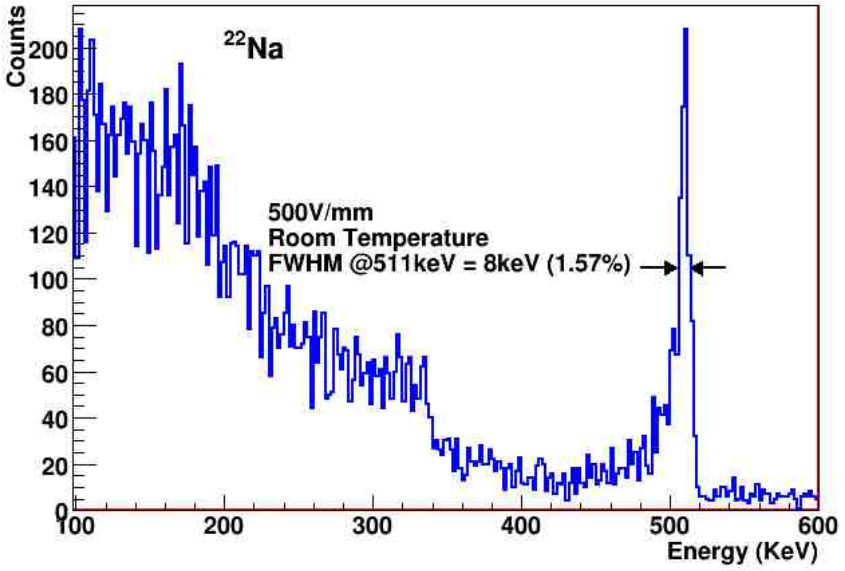

FIGURE 4.15: Spectroscopy of ^{22}Na at 500 V/mm and room temperature.

The spectroscopy of ^{22}Na acquired at 500 V/mm and at room temperature is shown in Fig. 4.15. One can see one peak which corresponds to the 511 keV photons created at the positron-electron annihilation. The FWHM is 8 keV which represents a resolution of 1.57%.

The Compton edge for events of 511 keV is 340 keV. The spectroscopy should follow a distribution similar to what is shown in Fig. 1.6, with the photopeak at 511 keV. Both the Compton edge and the photopeak are clear in the spectroscopy in Fig. 4.15. The region between the Compton edge and the 511 keV peak should be, theoretically, empty. However, Fig. 4.15 shows it is not. These events are due to background activity of photons with originally 1275 keV.

Increasing the bias voltage of a semiconductor detector increases the velocity of the charge carriers and, hence, reduces the drift time. With a shorter drift time, the probability of the charge carriers to be trapped by the material lattice is reduced. However, high bias voltages cause high noise on the detector because of the leakage current. One way to reduce the leakage current is to decrease the temperature. For these reasons the bias voltage has been doubled and, at the same time, the temperature has been reduced from room temperature down to -8°C. Fig. 4.16 shows the distribution of ^{22}Na spectroscopy at 1000 V/mm and at -8°C.

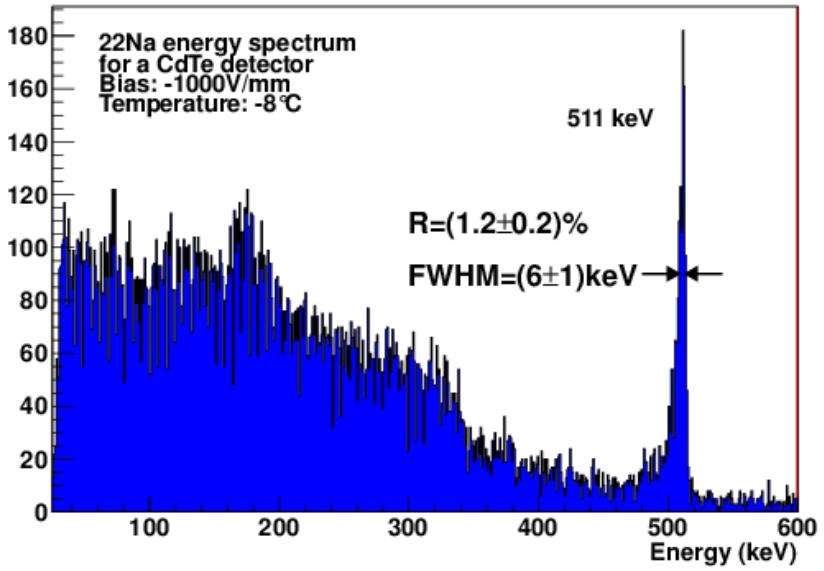

FIGURE 4.16: Spectroscopy of ^{22}Na at 500 V/mm and room temperature.

The FWHM of the 511 keV peak in Fig. 4.16 is 6 keV and this represents a 1.2% resolution. The improvement with respect to the resolution at room temperature is due to the reduction of the noise spread and the decrease of charge trapping. One can see, quantitatively, that the low energy tail of the 511keV peak is less pronounced.

4.3.3 Coincidence Time Resolution

The coincidence time resolution is obtained by evaluating the FWHM of the time difference distribution from the two 511keV photons, using the data sample obtained with the coincidence acquisition mode, as shown in Fig. 4.17. The trigger threshold of the setup has been placed at 25 keV. Only the coincidences with both photon energies above 25 keV have been included in the distribution.

The mean value of the distribution is around 10 ns which corresponds to the offset and is irrelevant for our investigation. The FWHM of the distribution is 12.5 ns. The fraction of the events within the FWHM window changes for distributions with different minimum acceptance energy. In order to compare fairly the different distributions, the time window containing a precise fraction of the coincidence events has been evaluated. In Fig. 4.17 the red colored region containing 70% of the coincidence events corresponds to a coincidence time window of 20 ns. The time window containing 90% of the coincidence events, colored in green, corresponds to a time window of 53.5 ns.

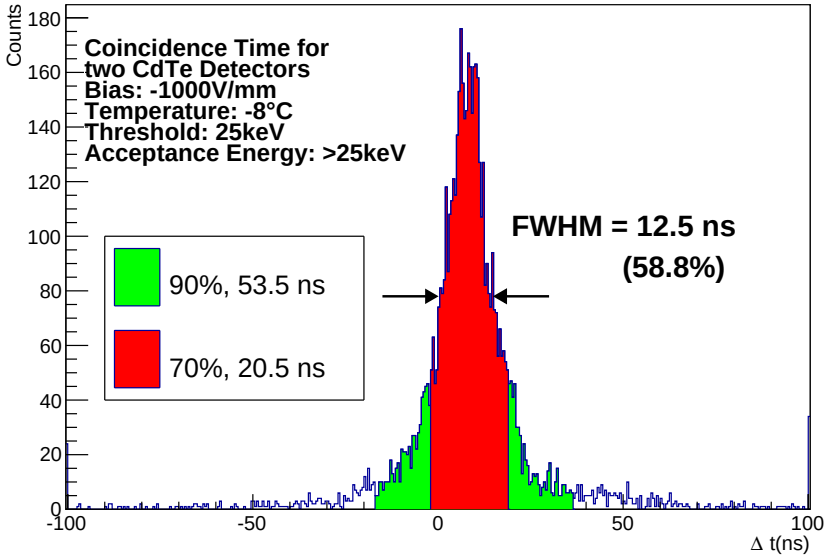

FIGURE 4.17: Coincidence time difference distribution of two CdTe diodes operated at -1000 V/mm and at -8°C.

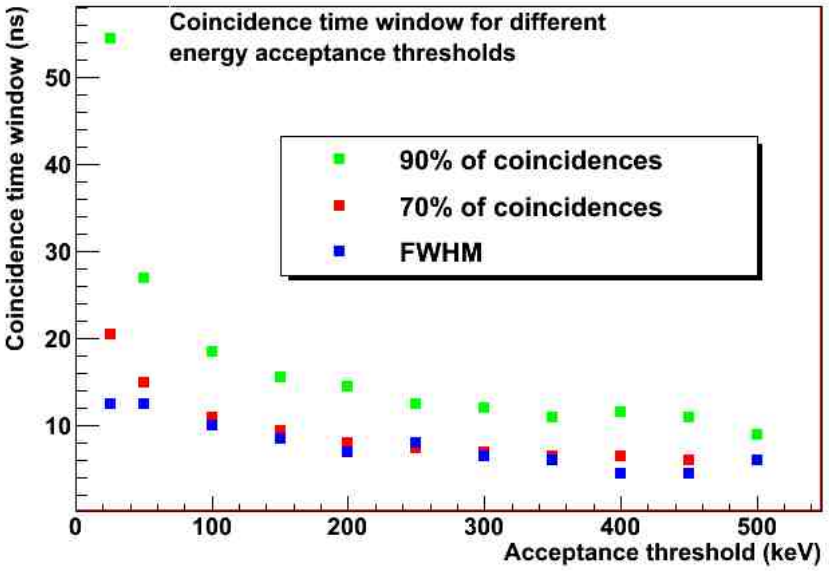

FIGURE 4.18: FWHM and window with for 70% and 90% of the events for different minimum acceptance energies.

The measurements showed on Fig. 4.17 have been applied on distributions with different minimum acceptance energy. A summary of the FWHM, and window widths for 70% and 90% of the events is shown in Fig. 4.18. The higher is placed the minimum acceptance energy, the smallest FWHM and the narrower the widths 70% and 90% of the events becomes.

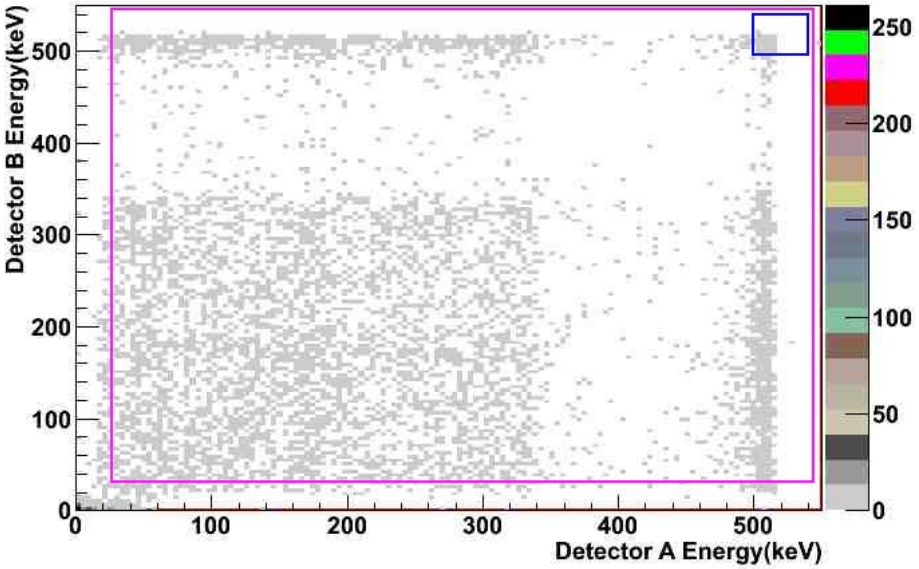

FIGURE 4.19: Scatter plot of the energy spectroscopy of both detectors. The events in Fig. 4.17 are enclosed in the pink rectangle. The events in Fig. 4.20 are enclosed in the blue rectangle.

Fig. 4.19 shows the scatter plot of the energy spectroscopies of both detectors. One can observe clearly the rectangle below the Compton edges of both detectors and the corner for both 511 keV events. The coincidence time difference distribution for events in the *511-511* corner is plotted in Fig. 4.20. The FWHM is reduced from 12.5 ns, where all events with energies above 25 keV are accepted, down to 6 ns with the new energy cut of 500 keV. In the cases that the time window contains 70% and 90% of the events, the reduction is even more significant. The time window containing 70% of the events is reduced from 20.5 ns to 6 ns, whereas for that containing 90% of the events is reduced from 53.5 ns down to 9 ns.

The improvement of the coincidence time resolution implies an increase of the offline energy threshold and, therefore, a reduction of the statistics. The trade-off between coincidence time resolution and detection efficiency is of crucial importance for the future performance of the VIP-module. Fig. 4.21 shows the fraction of events from the data sample above acceptance energies from 25 keV to 500 keV. One can see that barely 5% of the events have energies above 500 keV.

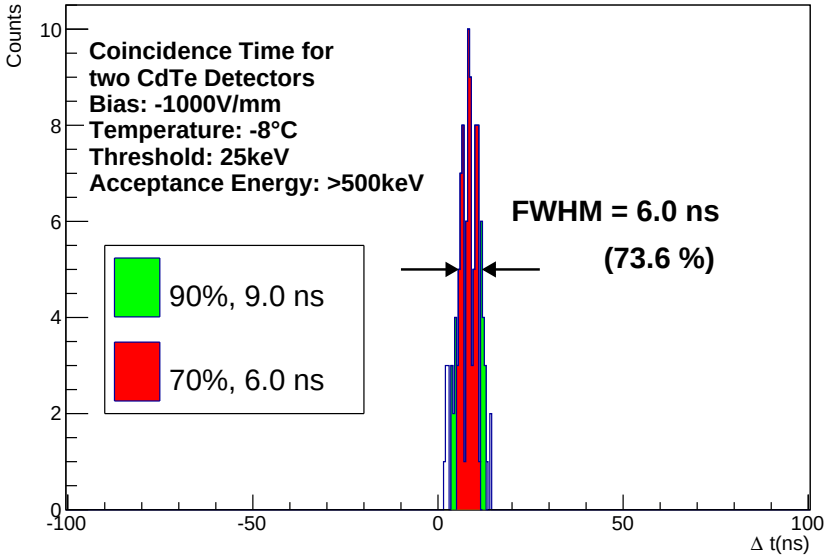

FIGURE 4.20: Coincidence time difference distribution of two CdTe diodes operated at -1000 V/mm and at -8°C. Only coincidences with both photons with energy above 500 keV accepted.

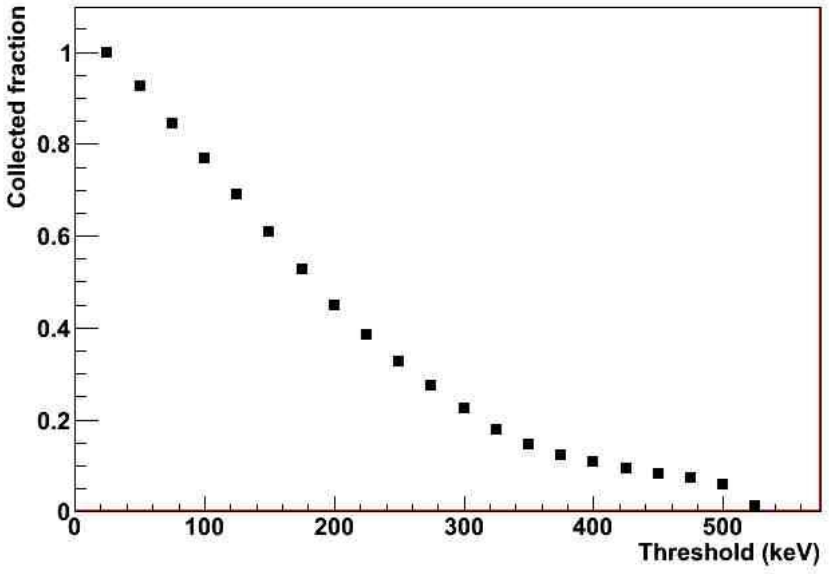

FIGURE 4.21: Fraction of events of the data sample above different threshold acceptance energies, relative to the energy cut of 25 keV.

4.4 Discussion

The single pixel CdTe detector operated at room temperature and 500 V/mm shows a resolution at 122 keV of 3.03%. Studies with CdTe/CZT detectors with slightly different thickness and operated at similar bias voltages show comparable resolutions [145–152]. The resolution achieved at the same conditions and at 511 keV is of 1.57%. For the same energy and a bias of 1000 V/mm and at -8°C the resolution at 511 keV improves to 1.2%. Again these results for high bias and low temperature are comparable with what has been already reported for this type of detectors [73, 151, 153, 154].

The results obtained for the coincidence time resolution show a strong dependence of this magnitude with the energy of the photons detected. A FWHM of 12.5 ns for events with energy above 25 keV has been measured. For events with an acceptance energy of 500 keV, the coincidence time resolution is 6.0 ns. Publications for similar detectors of CdTe and CZT report a coincidence time resolution between 9 ns and 25 ns [143, 154].

The excellent energy resolution of a CdTe diode with 2 mm thickness has been proved. The results achieved for the coincidence time resolution can be used to evaluate the maximum activity at which the VIP module can be operated without a significant pile-up effect. More than 50% of the events are acquired with a window width of 20 ns with the minimum acceptance energy threshold. By using this window width, the VIP-PET is expected to saturate at 5.3 kBq/mL [19]. This activity is relatively low compared to the 300 MBq that state-of-the-art PET scanners can achieve an activity concentration of 23.1 kBq/mL [155]. However, the VIP-PET achieves a scatter fraction of 3.95% [19] whereas the same state-of-the-art PET scanners achieve a scatter fraction of 37.9% [155]. A reduced scatter fraction means a high signal purity, which will allow the VIP-PET to ahieve a great performance regardless of the lower activity in which it can be operated.

Chapter 5

Pixel CdTe Performance with VATA Front-End Electronics

With 2 mm thick, and 4.1 mm x 4.1 mm single pixel CdTe detector it has been shown that one can achieve an energy resolution of 1.2 percent FWHM at 511 keV and a good timing resolution for coincidence events of 511 keV in a window time of 20 ns. However using small voxel CdTe detector of 1 mm $\times$ 1 mm $\times$ 2 mm, similar to those of VIP detector, might have impact on the result of measurements due to the small pixel effect and the charge sharing among neighboring pixels.

In this chapter, the results obtained using a pixel detector, an array of 10 $\times$ 10, will be discussed. The readout has been done by the VATAGP7.1 chip because the VIP chip was still under development.

5.1 Setup

The setup described in this section has been used to characterize the charge sharing between pixels. It consists of a pixelated CdTe diode readout by a commercial ASIC, the VATAGP7.1[1]. The VATAGP7.1 has been controlled by an FPGA and the PC controls the FPGA via USB port connection. A Labview executable has been developed to control the FPGA and the power supplies.

[1]VATAGP7.1 was developed by gamma medica-ideas. The manual of the VATAGP7.1 can be found in http://merlot.ijs.si/ studen/petProbe/schematics/VATAGP7.1-V0R8.pdf

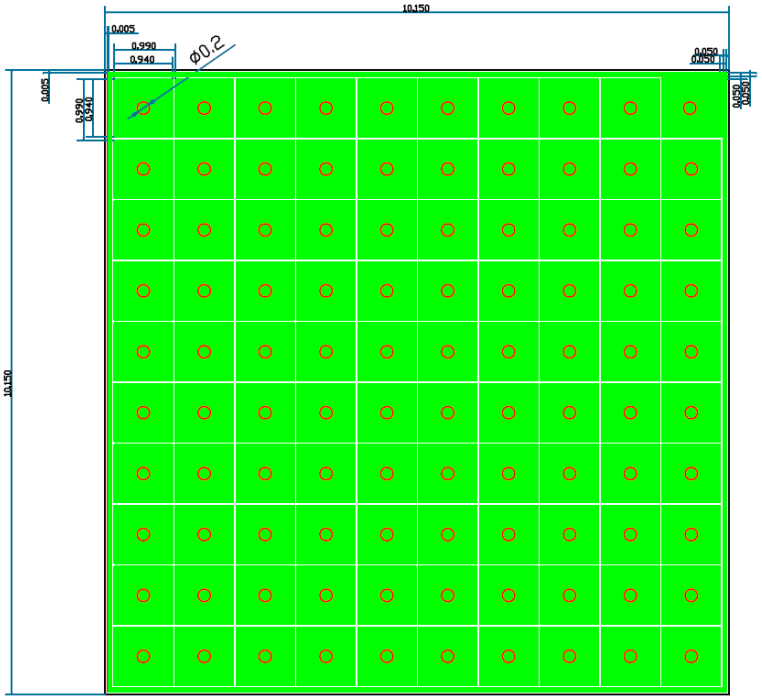

FIGURE 5.1: Green color: electrode, red circles: passivation holes, white color: isolation lines.

5.1.1 Pixelated CdTe Diode

The CdTe diode used in this setup has been manufactured by ACRORAD through the THM method. It has 10.15 mm × 10.15 mm surface and 2 mm thickness. It is a Schottky diode with the following electrode metal deposition: pixel/ALN/Au/Ni/Au/Al/CdTe/P-t/continuous. The pixel electrode is divided into 99 pixels as shown in Fig. 5.1, each with a pitch of 0.94 mm. Each pixel has a circular passivation hole in the center with 0.2 mm diameter. The pixels are separated each other by 50 μm. The 99 pixels are placed in a 10×10 distribution. One pixel electrode in the corner of the detector is connected to the guard ring. The guard ring itself, is 50 μm wide and it is separated from the outer pixels by a gap of 50 μm.

5.1.2 VATAGP7.1

VATAGP7.1 is an ASIC designed specifically for semiconductor detector and can ready 128 channels (strip detector). A conceptual sketch of the functionality for each channel is shown in Fig. 5.2. Each channel has a charge sensitive preamplifier and a sample/hold

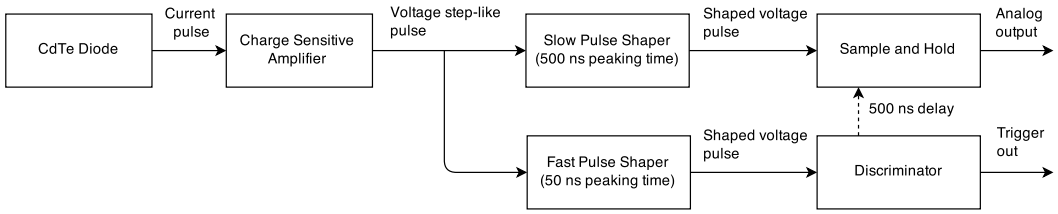

FIGURE 5.2: Sketch of the electronic components of one channel of the VATAGP7.1 readout ASIC.

multiplexed analogue readout. It also includes a fast shaper of 50 ns peaking time that gives a trigger signal with less time walk.

The VATAGP7 has 3 readout modes: the *Serial readout*, the *Sparse readout* and the *Sparse readout with neighbor channels*. In the *serial readout*, the values of the energy for all channels are acquired in every trigger. In the *sparse readout*, only the value of the energy of the trigger channel is acquired. Finally, in the *sparse readout with neighbor channels*, the value of the energy for the trigger channel and its neighbors are acquired.

The *serial readout* mode has been used to obtain the maximum information per each event. The sequence of the input signals required by the VATAGP7.1 for the readout of an event and the output signals are shown in Fig. 5.3. In this sketch, three physics events occur in channels 1, 124 and 100. The signals in channels 1 and 100 are large enough to create a trigger. The trigger signal corresponds to the signal *mgo and ta* in the diagram. The signal *mgo and ta* shows the two signals corresponding to the physics events of channels 1 and 100, represented in the diagram with the labels *a* and *b*, respectively.

After 500 ns of the trigger signal, the sample-and-hold signal, *sh* in the diagram, rises up and the readout process starts. Then a shift bit is clocked into the shift register by *shift_in_d* and *gck*. The analog value of channel 0 is enabled in *outp_d*. For each clock *gck*, the shift bit is clocked to the next channel. When the last channel is enabled, *shift_out_d* rises up to give a *shift_in* signal for the next chip in the chain. Finally, a reset is applied to the shift register. If all channels are clocked the reset is not needed.

5.1.3 Detector Assembly

The VATAGP7.1 is designed for the readout of strip detectors. For this reason it has all the connection pads placed on one side, see the layout of the VATAGP7.1 in Fig. 5.4.

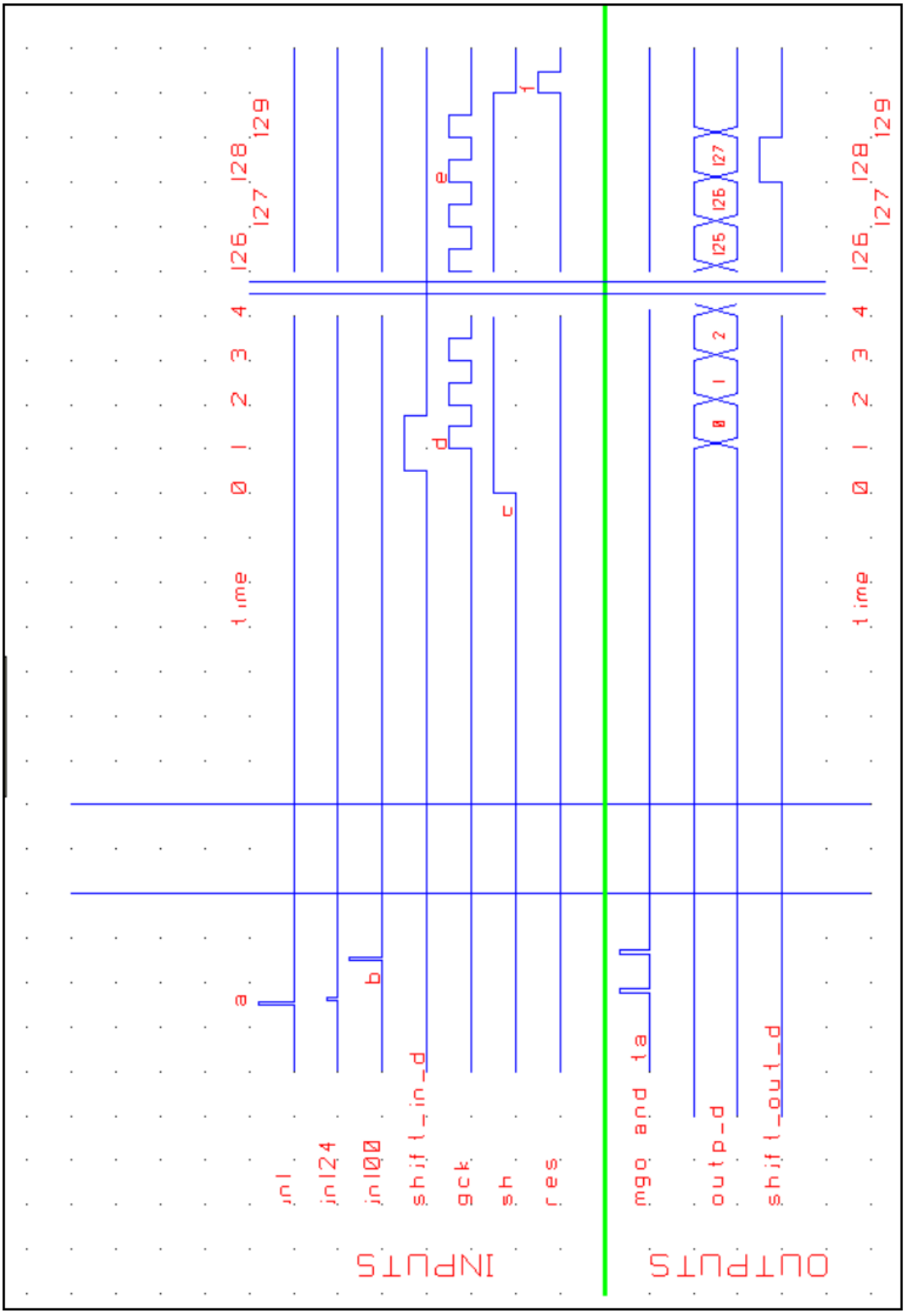

FIGURE 5.3: Time sequence of the input/output signals of the VATA serial readout mode.

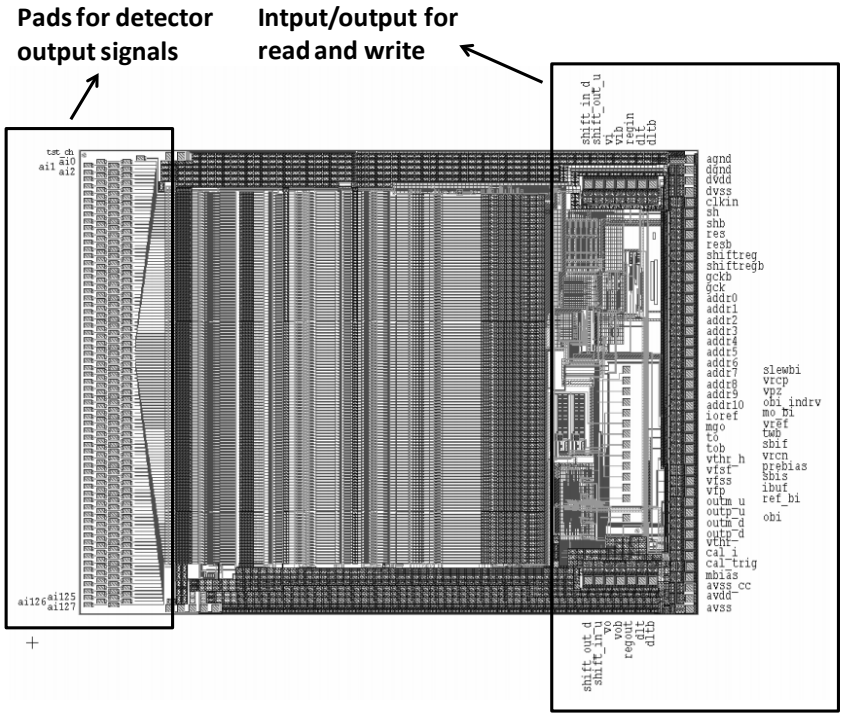

FIGURE 5.4: Layout of the VATAGP7.1 ASIC.

However, the CdTe diode used in the test setup has pixel electrode array. A glass substrate has been used as an adapter to convert the pixel matrix array of pads into linear array of pads to make it possible to be connected to the VATAGP7.1 inputs with wire bonds.

The glass substrate connection pattern is shown in Fig. 5.5. Each point represents the position for one bump-bond connection. The pixels have been grouped into pairs such that, effectively, the diode has 50 pixels. The pixels have a pixel electrode 2 mm × 1 mm, but one has 1 mm × 1 mm. A picture of the CdTe diode bonded to the glass substrate assembly is shown in Fig. 5.6. With such configuration, one single VATAGP7.1 can read 2 CdTe diodes.

The detector assembly and the VATAGP7.1 have been mounted on a rigidflex PCB. The picture of the rigiflex PCB with both the detector assembly and the ASIC mounted on it is shown in Fig. 5.7. The rigiflex PCB is designed to stack many identical layers and form a detector module with similar characteristics to the VIP module. The rigiflex PCBs have a flex part to be stacked without creating mechanical stress between layers.

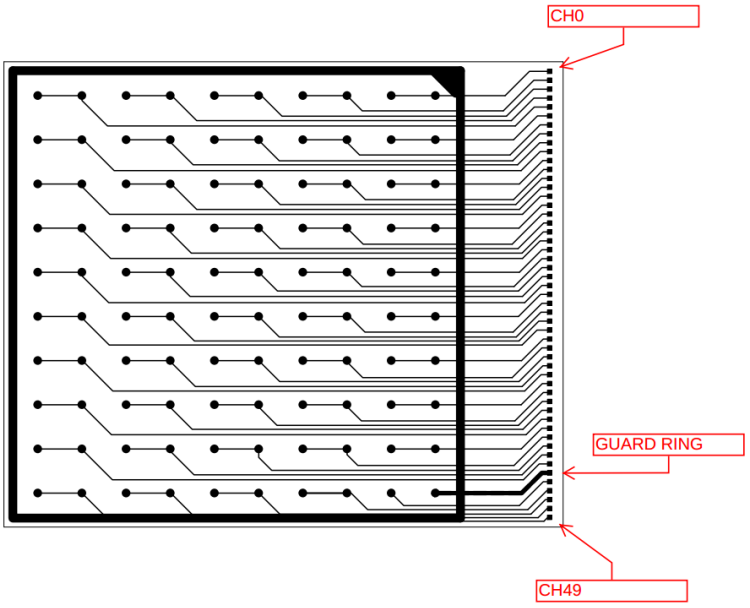

FIGURE 5.5: Sketch of the glass substrate design employed.

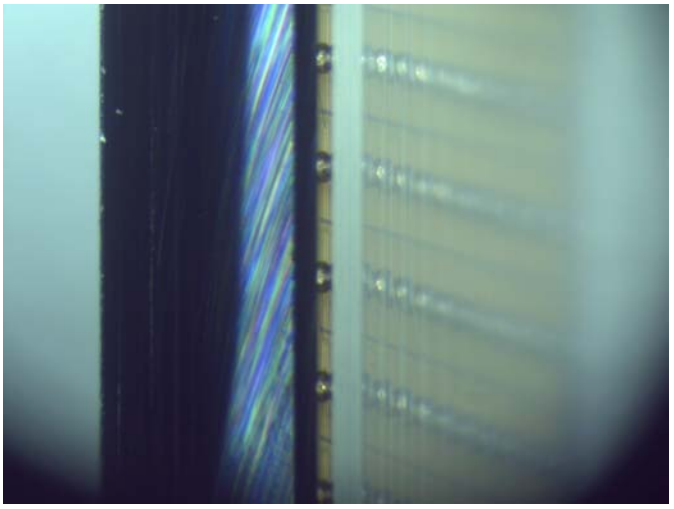

FIGURE 5.6: Picture of the edge view of the CdTe diode assembled on the glass substrate.

Each layer can hold 8 CdTe diodes and 4 VATAGP7.1. However, in this setup only 2 ASICs and 4 CdTe diodes have been mounted.

The glass substrates are attached to the PCB with glue. The glass substrate pads are connected to the lines in the PCB with wire bonds. The VATAGP7.1 chips are mounted on the glass substrate, which acts as signal fan-out, and fixed by glue. The ASICs are connected to the signal conditioning board through a connection HQCD-030 from *SAMTEC*.

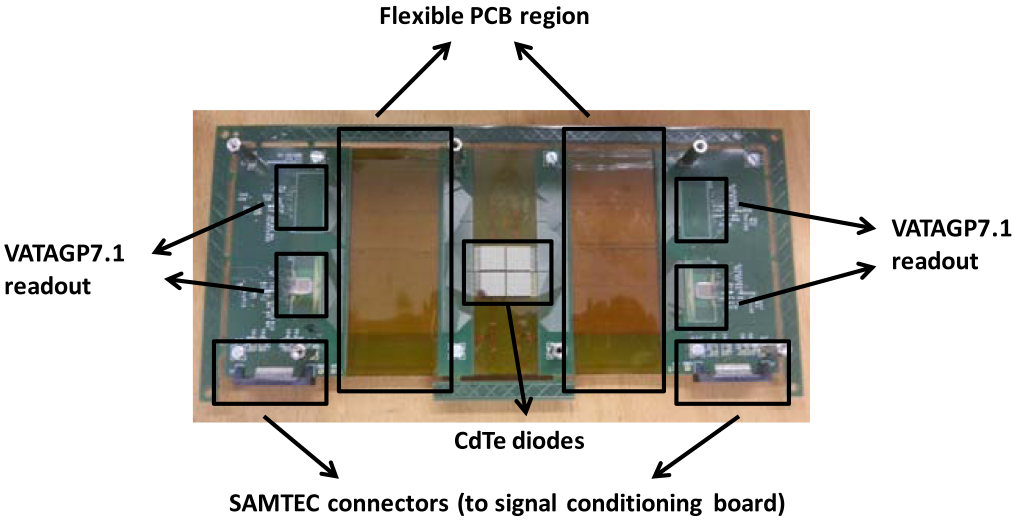

FIGURE 5.7: Picture of the rigiflex PCB.

5.1.4 Signal Conditioning Board

A signal conditioning board has been designed and manufactured to convert the current pulses into voltage pulses, amplify them for further signal processing, provide the LV and HV power, and adapt the FPGA NIM signal to the VATAGP7.1 required logical levels. The voltage levels of the digital signals of the VATAGP7.1 are not the standards and therefore, they need to be conditioned too. Moreover, it also provides voltage references for the VATAGP7.1. The signal conditioning board is shown in the picture in Fig. 5.8. It also includes the 14 bits ADC ADS6442 from *TI*[2]. The ADC digitizes the track and hold data outputs of the VATAGP7.1 ASIC and sends them to the FPGA. The conditioning board is designed to handle up to 4 VATAGP7.1 chips.

5.1.5 FPGA

An FPGA is an integrated circuit that can be configured for an unlimited limited number of times. The FPGA has been programmed to perform digital signal sequences such as the one shown in Fig. 5.3. The processes the FPGA carries out are *Program ASIC*, *Set Trigger Threshold*, and *Data acquisition*. The three processes are conceptually sketched in Fig. 5.9.

The *Program ASIC* process sends the control register to the ASIC. The control register consists of 926 bits and contains the configuration of all the settings in the ASIC.

[2]Texas Instruments, USA.

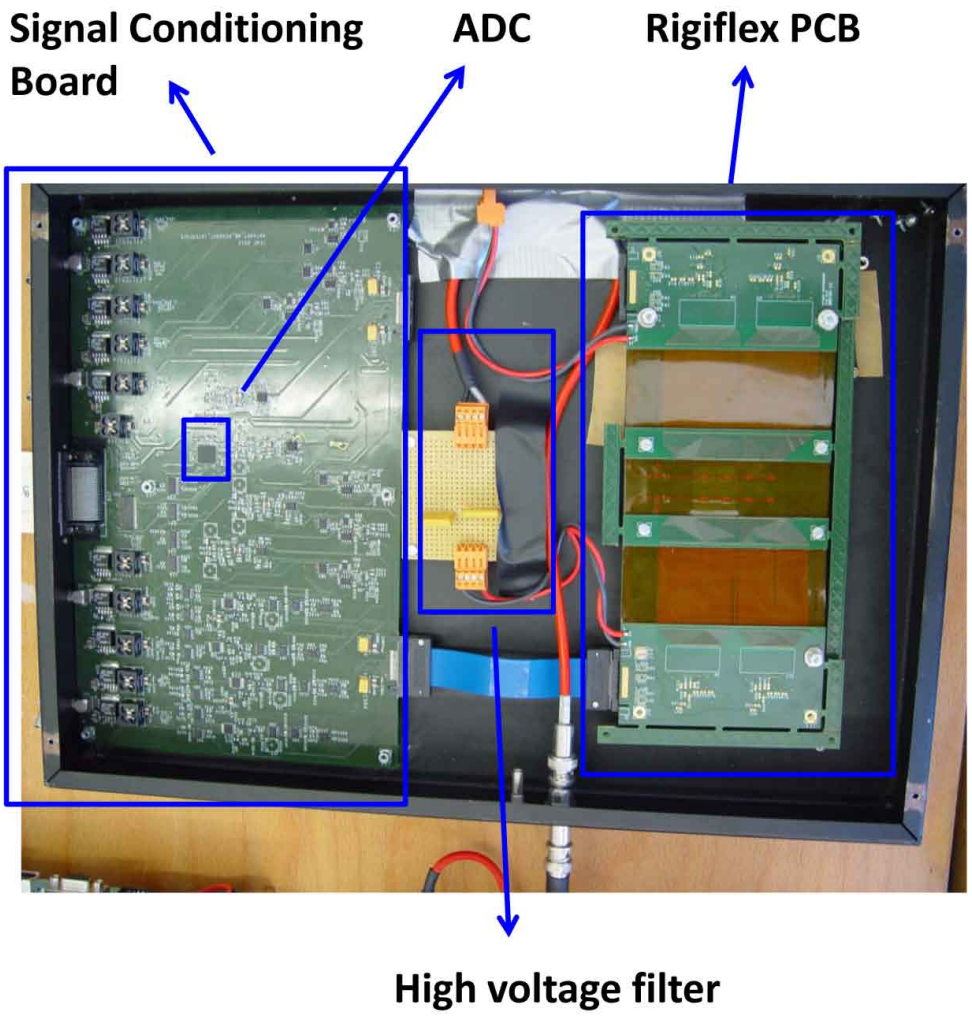

FIGURE 5.8: Signal conditioning board (left) and rigiflex PCB (right).

The trigger threshold of the VATAGP7.1 can be set either internally, through the control register, or externally, supplying a voltage reference. In this setup the trigger threshold is set externally The *Set Trigger Threshold* process sends the value *trigger threshold* to a DAC in the signal conditioning board and the DAC supplies the reference to the VATAGP7.1.

The *Data acquisition* process performs the readout sequence explained in Sec. 5.1.2 according to the parameters loaded in the FPGA. The *sample and hold time* is the time to sample the signal after the trigger and it is about 500ns. However, this delay has to be fine tuned to make sure one is sampling the peak of the slow shaper. The *number of events* and *timeout* set the maximum number of events and maximum acquisition time, respectively, in each acquisition process. The acquisition terminates when any of the two conditions is fulfilled. The *dead time* is the amount of time the trigger is vetoed after

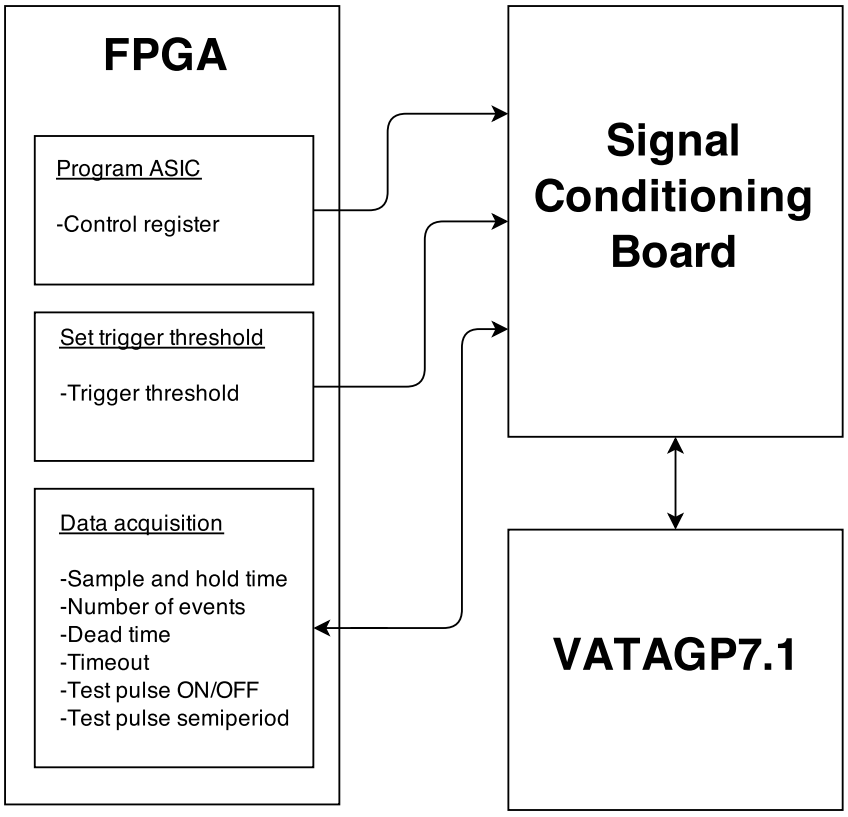

FIGURE 5.9: Sketch of the funcionalities of the FPGA.

one acquisition. *Test pulse ON/OFF* activates the test pulse mode. In the test pulse mode the FPGA sends digital pulses to generate the test pulses in the ASIC. Finally, the *Test pulse semi-period* sets the semi-period of the test pulse sending rate in the test pulse mode.

The FPGA is controlled by the DAQ software in the PC through a set of 5 functions implemented in a *dynamic-link library (DLL)*. A conceptual sketch of the 5 DLL functions is shown in Fig. 5.10.

5.1.6 Graphic User Interface (GUI)

VATA **C**ontrol (VAC) is a DAQ executable developed with Labview that allows the user to program the VATAGP7.1, control the bias voltage of the diode and collect data.

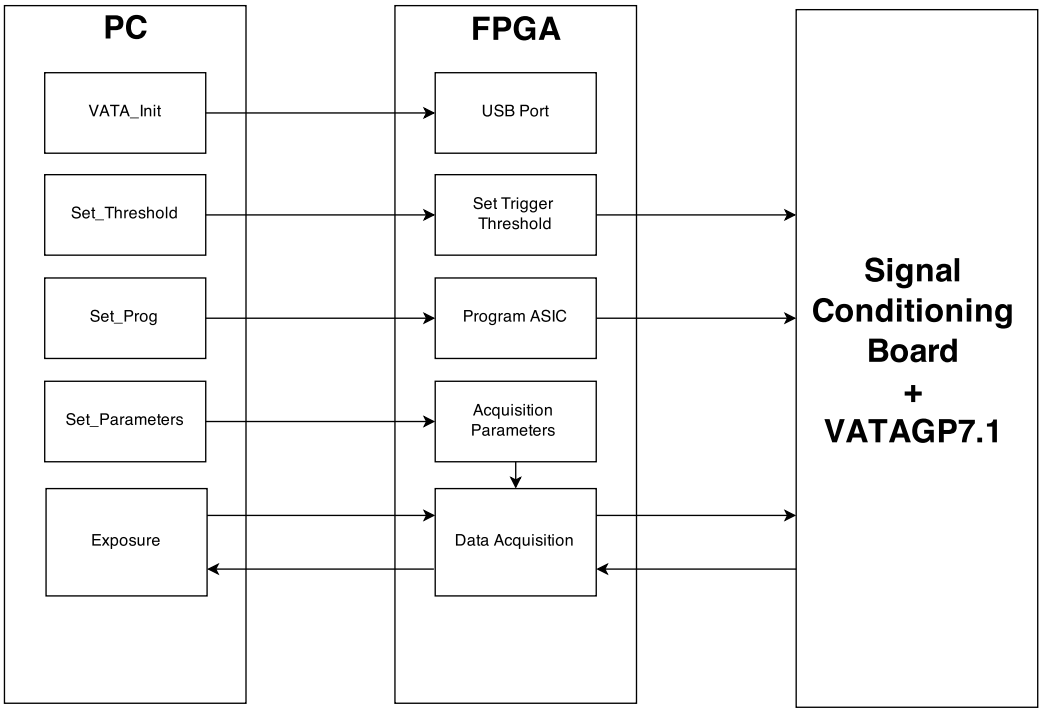

FIGURE 5.10: DLL functions used to connect the PC with the FPGA.

A sketch of the hierarchy of VAC and the rest of the devices in the setup is shown in Fig. 5.11. VAC has direct control of the Keithley 2410 power supply and the FPGA. The Keithley 2410 sets the bias voltage of the CdTe diode and takes measurements of the leakage current continuously. The FPGA is an interface between the software and the signal conditioning board and is used to control the VATAGP7.1 chip.

VAC obtains data corresponding to real physics, pedestal events or test pulses depending on the mode of operation. The user sets the trigger threshold and enables the channels to acquire real physics events. In order to acquire pedestal events, the FPGA sends the pulses that correspond to the triggers. The test pulses are generated by the FPGA as well. The VATAGP7.1 has to be set in the test pulse mode and, for every pulse sent by the FPGA, the VATAGP7.1 generates a test pulse with the amplitude set by the user.

5.2 Results

The pixels of 2 diodes have been connected to the input channels of the VATAGP7.1 as shown in Fig. 5.12. The behavior of pixels with size 2 mm $\times$ 1 mm has been characterized

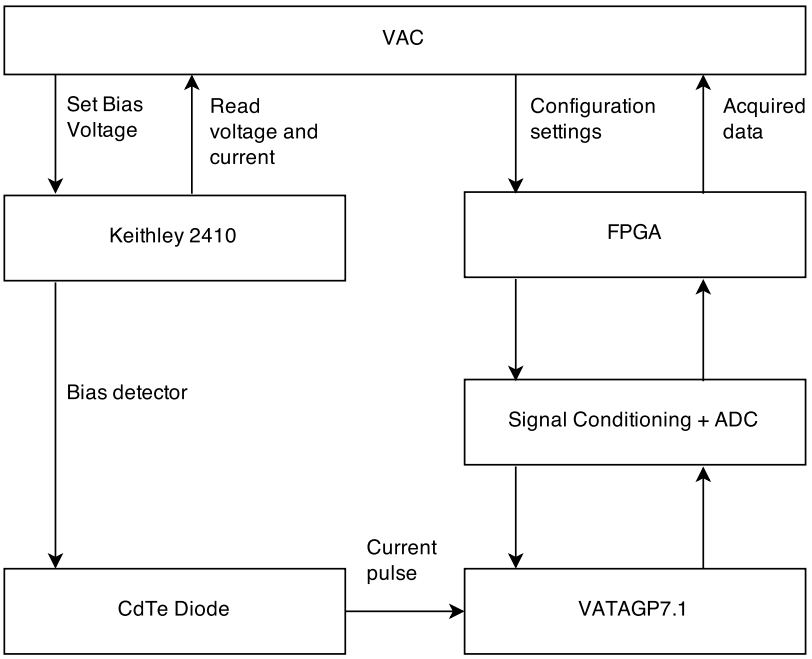

FIGURE 5.11: Scheme of the relation between the software and the devices in the setup.

4	3	2	1	0
9	8	7	6	5
14	13	12	11	10
19	18	17	16	15
24	23	22	21	20
29	28	27	26	25
34	33	32	31	30
39	38	37	36	35
44	43	42	41	40
49	48	47	46	45

54	53	52	51	50
59	58	57	56	55
64	63	62	61	60
69	68	67	66	65
74	73	72	71	70
79	78	77	76	75
84	83	82	81	80
89	88	87	86	85
94	93	92	91	90
99	98	97	96	95

FIGURE 5.12: Map of the channels connected to the pixels for each diode. Diode 1 in left and diode 2 in the right. The pixels have been colored according to their position in the diode: *corner* pixels in red, *long edge* pixels in orange, *short edge* pixels in green, and *inner* pixels in blue.

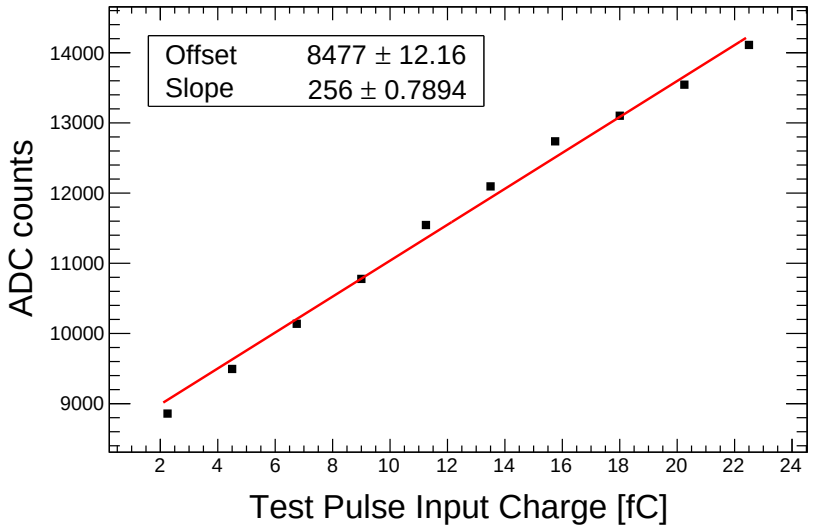

FIGURE 5.13: Setup response for test pulses with different amplitudes for channel 22. The input pulse with maximum amplitude has 22.25 fC, which corresponds to 618 keV in CdTe.

in terms of the charge sharing effect and the energy resolution for each pixel, both at different energy levels.

5.2.1 Calibration

The linearity of the setup has been checked by using test pulses with different amplitudes. The curve of the ADC measurements for different input charge values is shown in Fig. 5.13. The maximum input charge, 22 fC, corresponds to a deposition of 618 keV energy in CdTe, which has band-gap of 1.44 eV. One can see that the behavior of the device is fairly linear in this range.

The gain of the setup has been measured using three different radioactive sources: ^{241}Am, ^{57}Co and ^{22}Na. The main lines of emission for these radioactive sources are at 59.5 keV, 122 keV and 511 keV, respectively. The curve of the setup response for different energy depositions in the diode is shown in Fig. 5.14. The linear fit adjusts well to the data, with an offset of 7968 ADC counts, that corresponds to the measured pedestal mean, and a slope of 9.9 ADC counts per keV.

The distribution of the noise for each channel with the diodes biased at 500 V/mm and at room temperature has been measured. Fig. 5.15 shows the standard deviation, σ, of the noise distribution for all the pixels. The markers have been colored according to

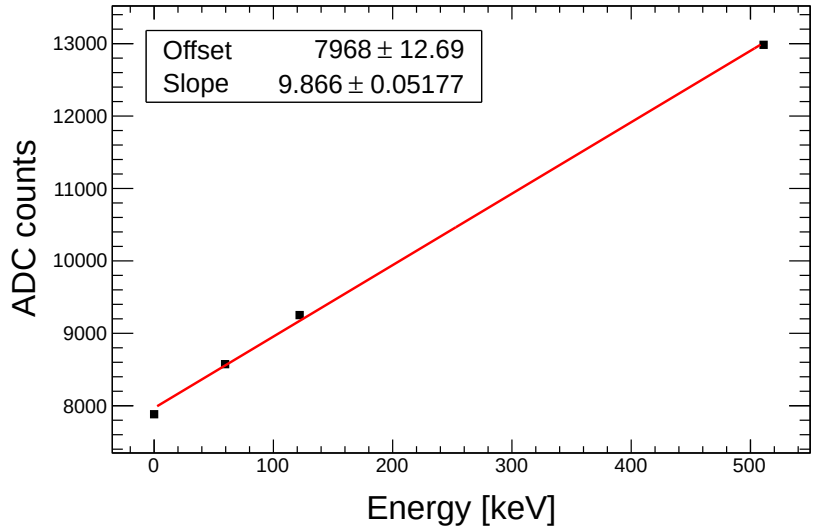

FIGURE 5.14: Calibration of ADC counts vs energy for channel 22. Three points at 59.5 keV, 122 keV, and 511 keV have been used for the fit. The fit offset is in agrement with the measurement of the pedestal.

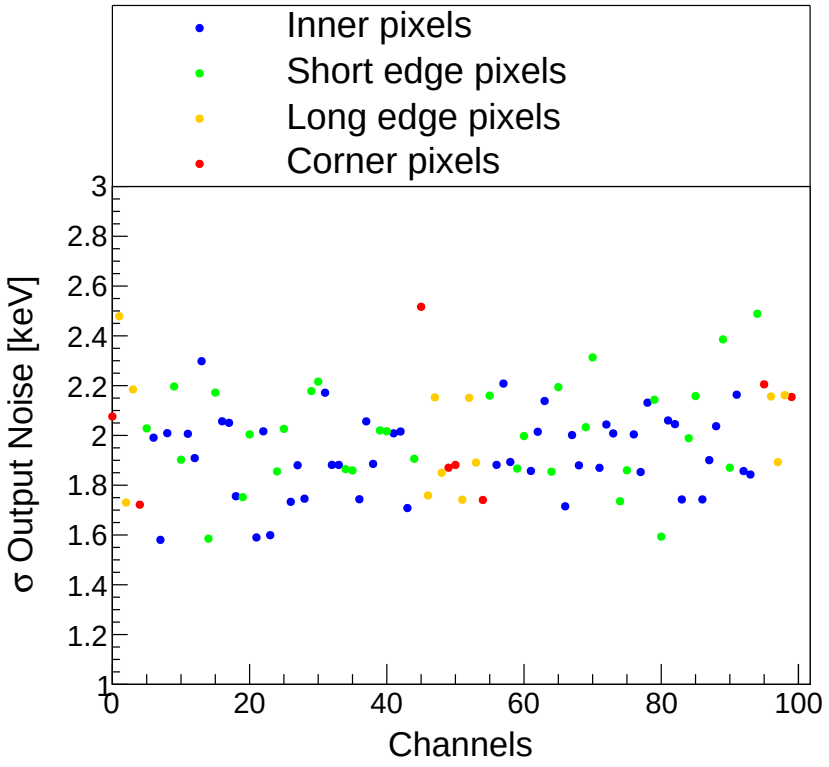

FIGURE 5.15: Noise distribution, in keV and for channel by channel, at 500 V/mm at room temperature in keV. Markers colored according to the colors used in Fig. 5.12 for the position of the pixels.

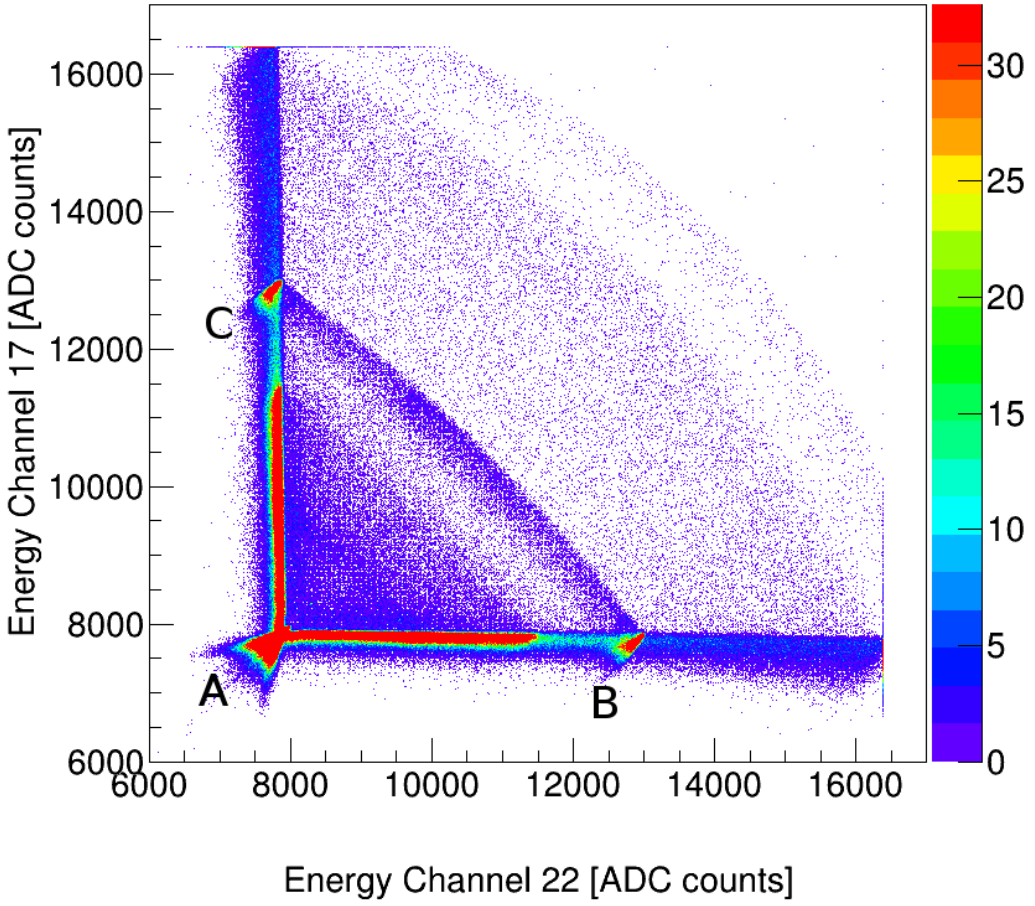

FIGURE 5.16: Scatter plot of the energy values of channel 22 (x axis) and channel 17 (y axis) for any channel triggering. Spectroscopy acquired at 500 V/mm bias voltage and at room temperature.

their position as in Fig. 5.12. No correlation with the noise spread and the pixel position is observed.

5.2.2 Measurements with ^{22}Na

The radioactive source ^{22}Na has been used to study the behavior of the device for the detection of photons with originally 511 keV energy. All the measurements have been acquired at bias voltage of 500 V/mm and at room temperature. Fig. 5.16 shows the scatter plot of the energy measured in two neighbor channels for the same trigger event. These channels are 22 and 17, and they share one side of the pixel which is 2 mm long.

One can identify 4 differentiated regions in the 2D spectra of events.

In the first place there is the Compton spectra of the 511 keV photon. This region extends from 0 keV up to 340 keV. In the second place one can observe a region of events that corresponds to the 511 keV photopeak. Along this region both channels together sum 511 keV energy. The third region is the Compton spectra caused by photons of 1.275 MeV. This region extends from 0 keV up to 1.06 MeV. Finally, the fourth region is that of the 1.275 MeV photopeak. The dynamic range has been optimized for the measurement of 511 keV photons and saturates at ∼1 MeV. For this reason the plot only shows a fraction of this region.

The energy sharing between pixels 17 and 22 is in most cases due to charge sharing which occurs when an energy deposition takes place in a point close to the electrode boundary.

Fig. 5.17 shows scatter plot for pixels 12 and 22 (not neighbors) for the same set of data shown in Fig. 5.16. In Fig. 5.17 there is a significant reduction of events with a positive energy on both pixels compared to Fig. 5.16. However, one can still distinguish the regions corresponding to the 511 keV spectra and, more clearly, the 511 keV photopeak region. In this case the positive energy on both pixels in the same event can be explained by Compton interactions, i.e., events that scatter in one pixel and create a second scattering or a photoelectric absorption in the second pixel. Two physically uncorrelated photons interacting with the detector within <500 ns time difference can explain part of this events as well. However, such events should not show a correlation between the energy of both pixels and should be spread homogeneously along the 2D space.

Fig. 5.16 also shows a fraction of events with an energy lower than the pedestal average energy, see region *A*. One can observe as well that these events have a more negative value for higher energies of the neighbor pixel, see regions *B* and *C*. The induction of negative energy on a pixel when a positive energy is induced in a neighbor pixel has been already reported [156, 157]. In this work such events have been referred to as *negative energy events*.

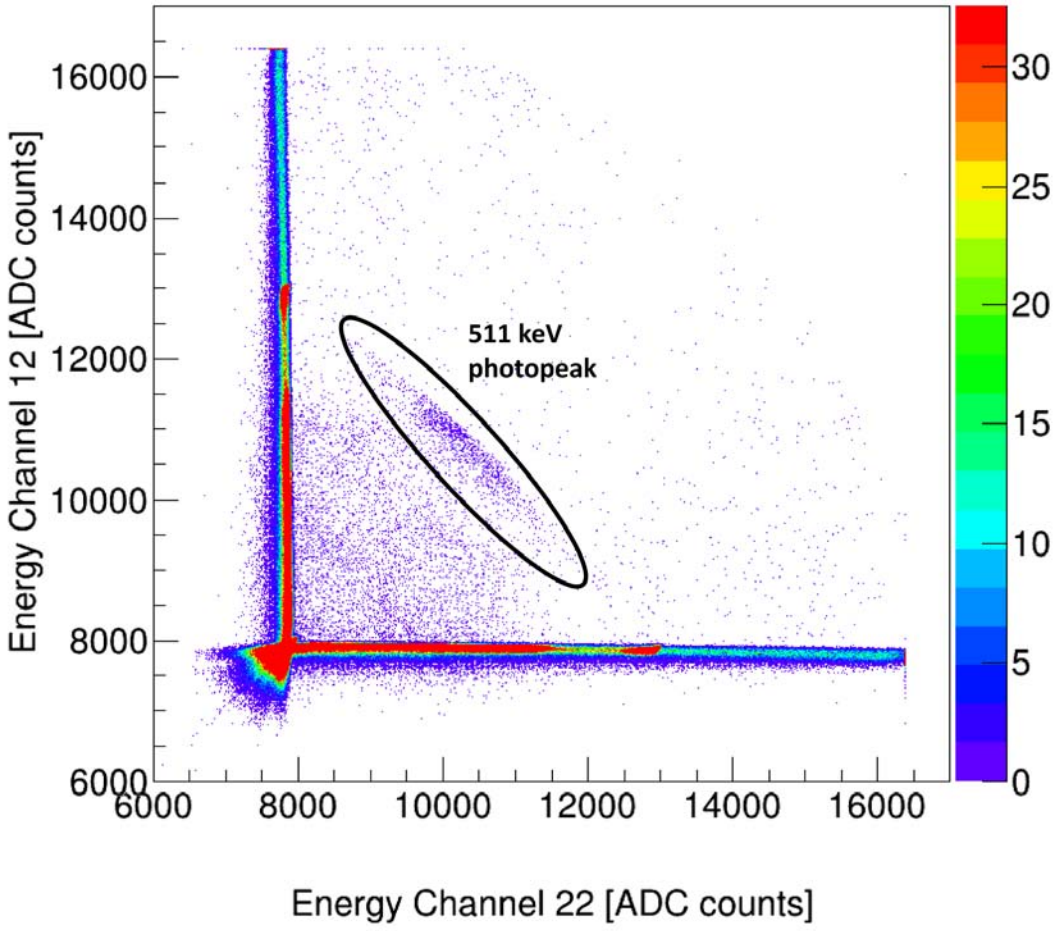

FIGURE 5.17: Scatter plot of the energy values of channel 22 (x axis) and channel 12 (y axis) for any channel triggering. Spectroscopy acquired at 500 V/mm bias voltage and at room temperature.

5.2.2.1 Negative Energy Induction on Neighbor Pixels

Fig. 5.18 shows the simulation results of the charge induction efficiency in a pixel for different impact points along the x-axis, which is perpendicular to the drift direction. The pixel is centered at x=0 and has a pitch of 1 mm. It shows the charge induction efficiency in the pixel for energy depositions between -1.5 mm and 1.5 mm. The contributions of electrons, holes, and their sum are shown.

One can see that, electrons can induce a negative charge on the neighboring pixel if the deposition has occurred in a position close to the pixel electrode in the x axis. The effect is more pronounced if the deposition takes place close to the pixel electrode in the z-axis (parallel to the drift direction) [156]. The signal induced by holes is positive,

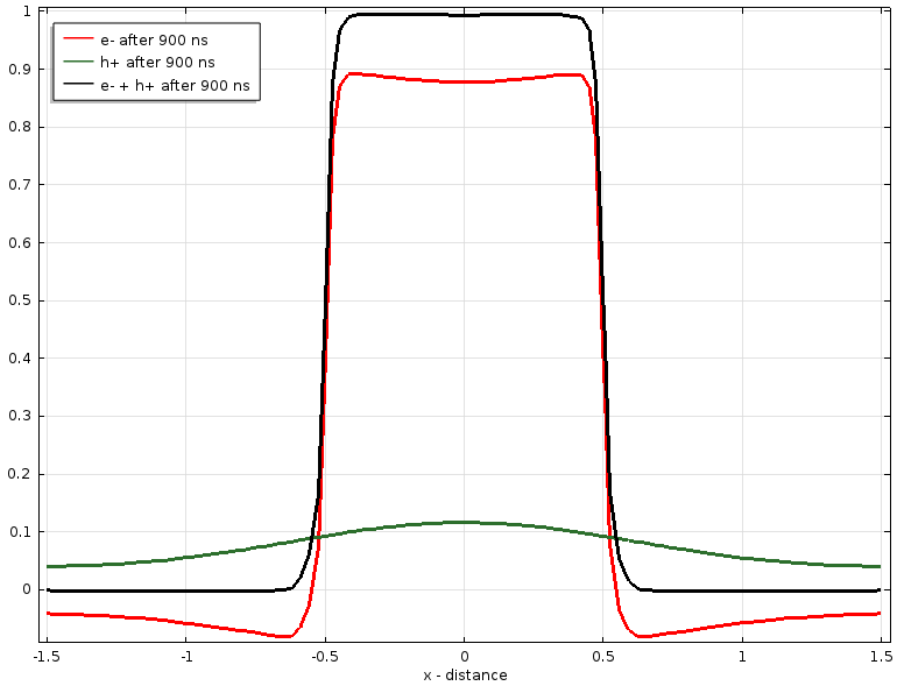

FIGURE 5.18: Charge induction efficiency versus lateral direction of the impact point with z=1 mm, for 500 V/mm in a diode of 2 mm thickness and after 900 ns.

therefore, it compensates the negative induction of the electrons and the sum of both contributions is 0 for depositions outside the pixel electrode.

The VATAGP7.1 shaper has a peaking time of 500 ns, which means that only the charge induced on the electrodes during the first 500 ns will be integrated. The drift time of holes for 2 mm, with the detector operated at 500 V/mm, is of the order of 800 ns[3]. In the case of electrons, such drift time is of the order of 80 ns[4]. Therefore, the contribution of electrons will be completely acquired for all events, whereas the contribution of holes will be partially lost depending on where the interaction takes place along the z-axis. The loss of charge may be enough such that the negative contribution of electrons cannot be compensated by the holes contribution and the final measurement of the energy is negative.

5.2.2.2 Charge Sharing Evaluation

The charge sharing effect for pixels with size 2 mm × 1 mm has been studied. A sample of events triggered by the same channel has been studied in first place. Fig. 5.19

[3]Assuming a mobility of holes of μ_h=100 cm^2/(V·s).
[4]Assuming a mobility of electrons of μ_e=1000 cm^2/(V·s).

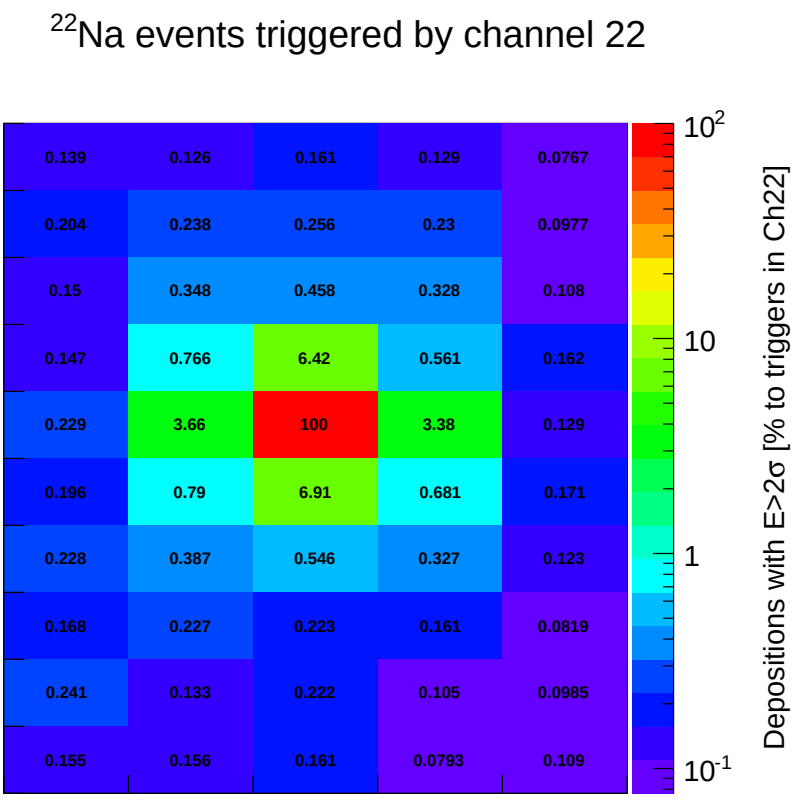

FIGURE 5.19: Percentage of events with energy above 2σ per channel compared to the total events triggered in channel 22.

shows the fraction of events with energy above 2σ of the pedestal distribution for each pixel in diode 1 triggered by a deposition in pixel 22. It also shows the correlation between number of events in each of the neighboring pixel and length of the electrode side each pixel shares with the triggered pixel. The measurements show a fairly linear proportionality between the fraction of events and the length of the side shared with the trigger channel.

The spectroscopy of the neighbor pixels to pixel 22 for events triggered by pixel 22 and also for events triggered by pixel 43 are shown in Fig. 5.20. The energy spectroscopies of pixels top, bottom, left and right around pixel 22 are shown. The statistics for the events triggered by pixel 22 is much more than those triggered by pixel 43, which is located relatively far away from pixels 17, 21, 23 and 27.

The amount of events undergoing charge sharing in every pixel has been evaluated. A charge sharing event is considered when at least one of the neighboring channels has

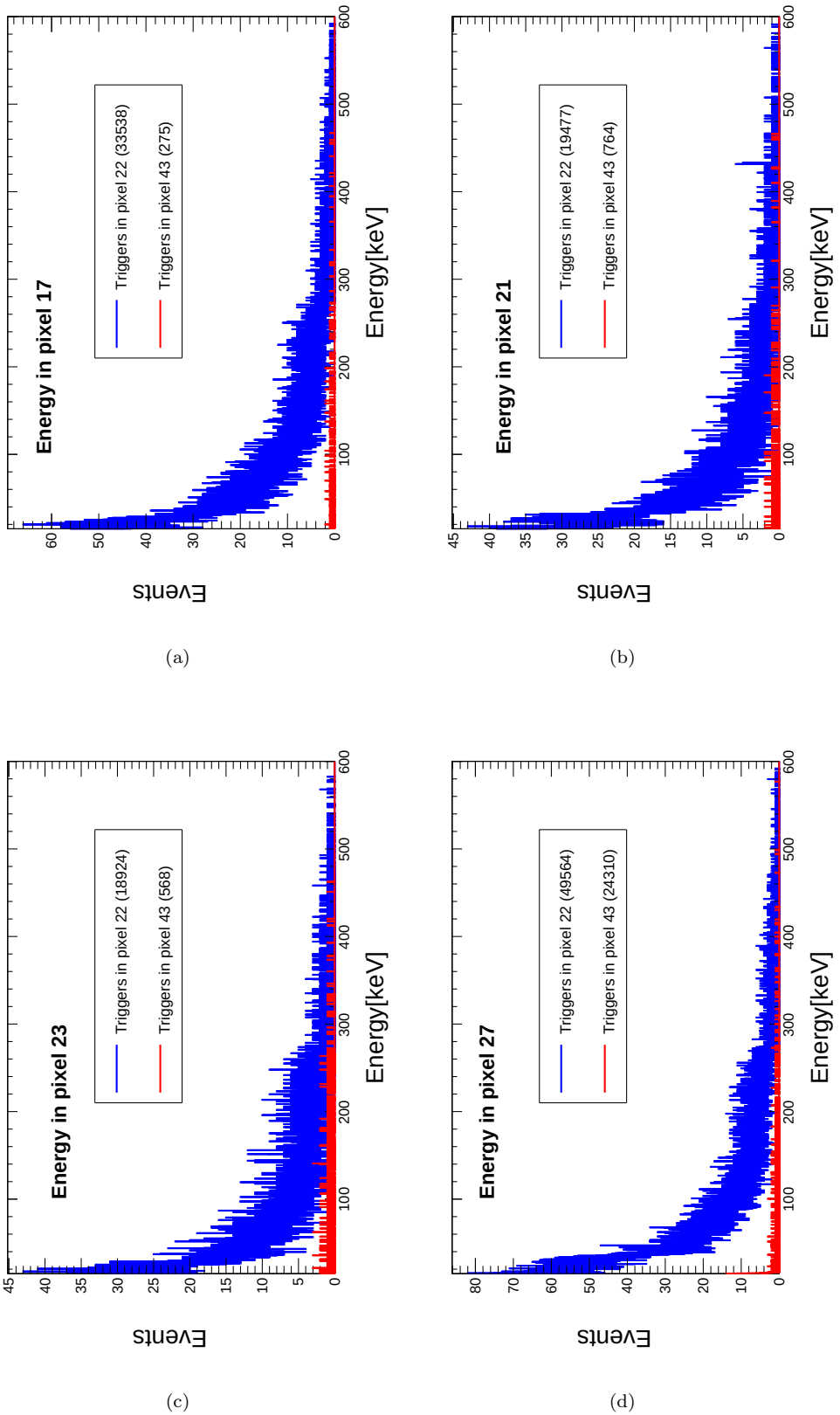

FIGURE 5.20: Energy spectroscopy of the 4 pixels surrounding pixel 22. The relative positions of each pixel with respect to the trigger pixel according to Fig. 5.12 are 17 top, 27 bottom, 21 right and 23 left.

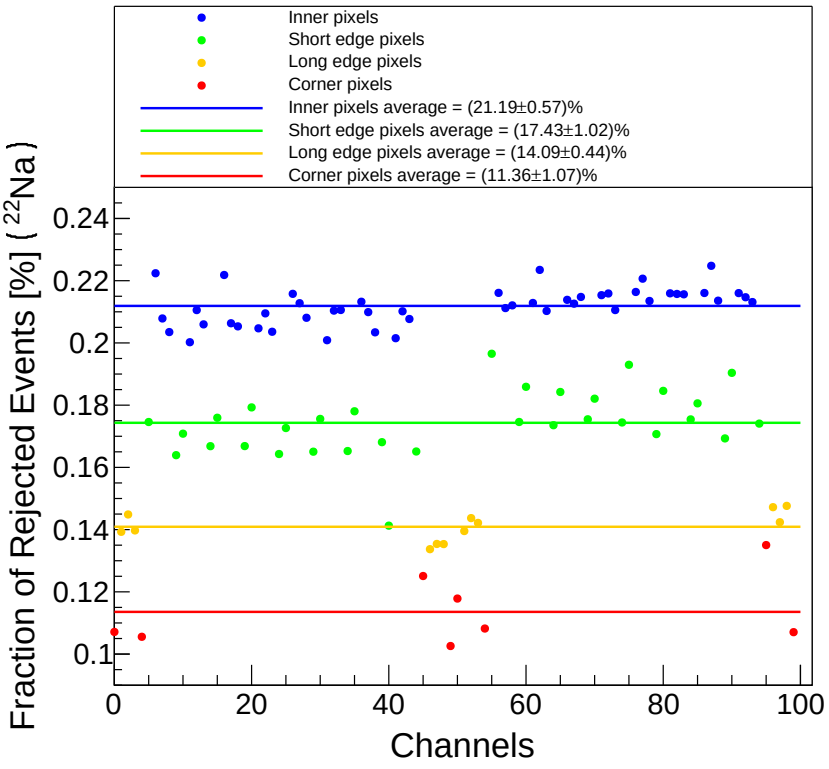

FIGURE 5.21: Fraction of events undergoing charge sharing normalized to the total events triggered by that pixel. The pixels have been differentiated according to their position in the diode. The average for inner, edge and corner pixels has been drawn with a line. The colors used correspond to those shown in Fig. 5.12.

an energy above 2σ of the pedestal distribution. Neighbor pixels have been considered those pixels surrounding the trigger pixel. For inner, short edge, long edge, and corner pixel, the number of neighboring pixels are 8, 5, 5, and 3 respectively.

Fig. 5.21 shows, for all the pixels, the percentage of events undergoing charge sharing normalized to the total number of events triggered by the central pixel. The fraction of events undergoing charge sharing is strongly correlated the position of the pixel among the diode. One can distinguish the behavior of the 4 categories of pixels: inner, short edge, long edge, and corner. They show a fraction of charge sharing events of 21.19%, 17.43%, 14.09% and 11.36% respectively.

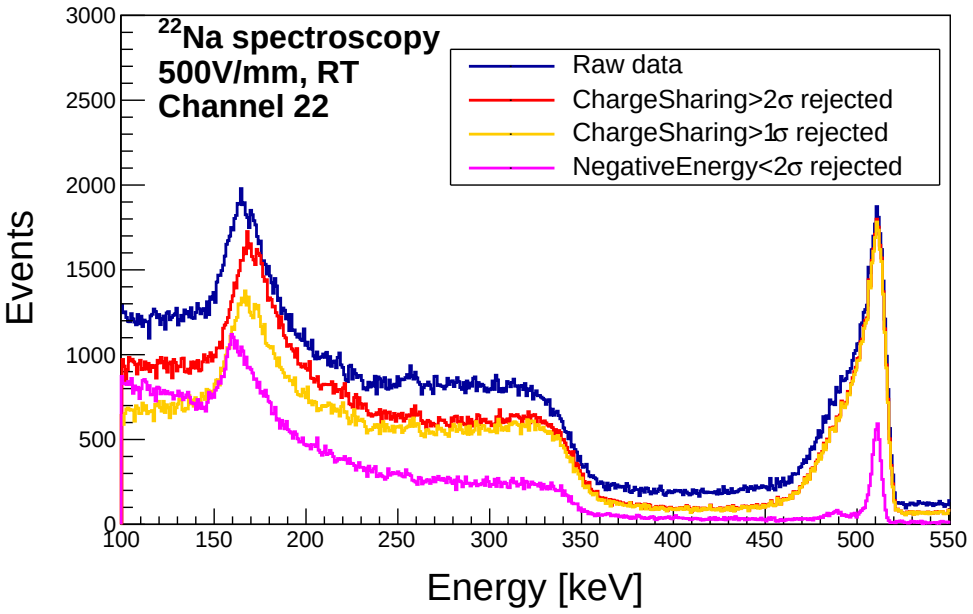

FIGURE 5.22: Spectroscopies of ^{22}Na at 500 V/mm and at room temperature for channel 22. The four distributions corresponds to four cuts on the same data sample. (Blue) raw data, (red) charge sharing events above 2σ rejected, (yellow) charge sharing events above 1σ rejected and (magenta) negative events below 2σ rejected.

5.2.2.3 Energy Resolution

The energy resolution of the device has been measured for a photon energy of 511 keV. A sample of data has been analyzed with different cuts at the pedestal level. The data has been taken at bias voltage of 500 V/mm and at room temperature. The results for pixel 22 can be seen in Fig. 5.22. The raw data histogram include all the events as measured but also calibrated for gain correction. The other histograms are done with cuts on positive energy deposition above 1 and 2 sigmas, in any of the neighboring pixel around pixel 22 to veto any of events that have undergone charge sharing. The last cut has been applied to eliminate those events that show negative pedestal in the neighboring pixels. This type of events are strongly correlated with events where the holes are the major carriers, that is events that deposit the energy close the anode of pixel 22.

Fig. 5.23 shows a zoom around the 511 keV peak shown in Fig. 5.22. One can see a long tail on the low energy side for the raw spectroscopy and those without the charge sharing events. The FWHM at 511 keV for the raw data is 3.46%. When the events with charge sharing for energy cut of 2 sigma are rejected, the FWHM improves to 3.19%. If

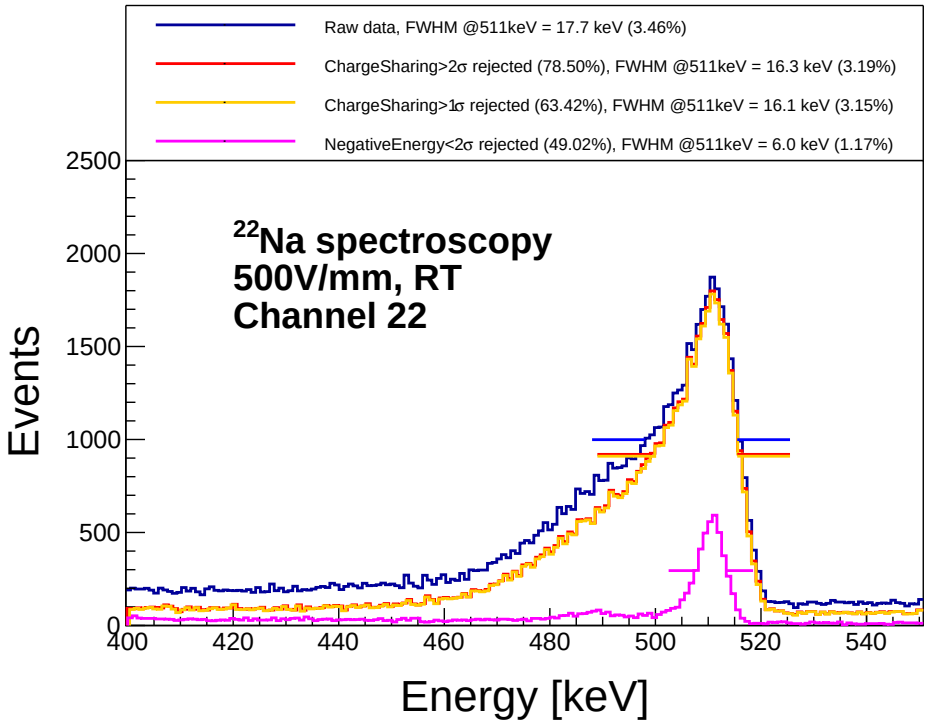

FIGURE 5.23: Zoom of the plot shown in Fig. 5.22 between 400 keV and 550 keV.

a 1 sigma cut is applied, the FWHM is 3.15%. The result is a little bit better but at the cost of statistics. The number of events in the data sample gets reduced from 78.5% to 63.4%. It is expected that with the 1 sigma cut good events are likely to be removed.

A dramatic improvement on the energy resolution is achieved by rejected the negative energy events. The 17.7 keV FWHM of the raw distribution decreases down to 6 keV, which represents a resolution of 1.17%. One can note that the peak of the distribution does not show the asymmetry on the low energy side created by the events dominated by holes. However, the reduction on the data sample is of 49.2%. This shows that the user must determine a trade-off between energy resolution and detection efficiency.

Fig. 5.24 shows the energy resolution of the four distributions for all the channels in the device. One can see an an increasing trend of the FWHM for the corner, long edge, and short edge pixels for the first three distributions. For corner and long edge pixels, which have more perimeter next to the guard ring, the trend is more intense. The voltage of the VATAGP7.1 preamplifier input is of ∼-1 V. The guard ring is connected to ground and the common electrode (opposite to the pixel electrode) is set to -1000 V. For energy depositions occurred close to the pixel electrode, part of the charge may leak to the guard

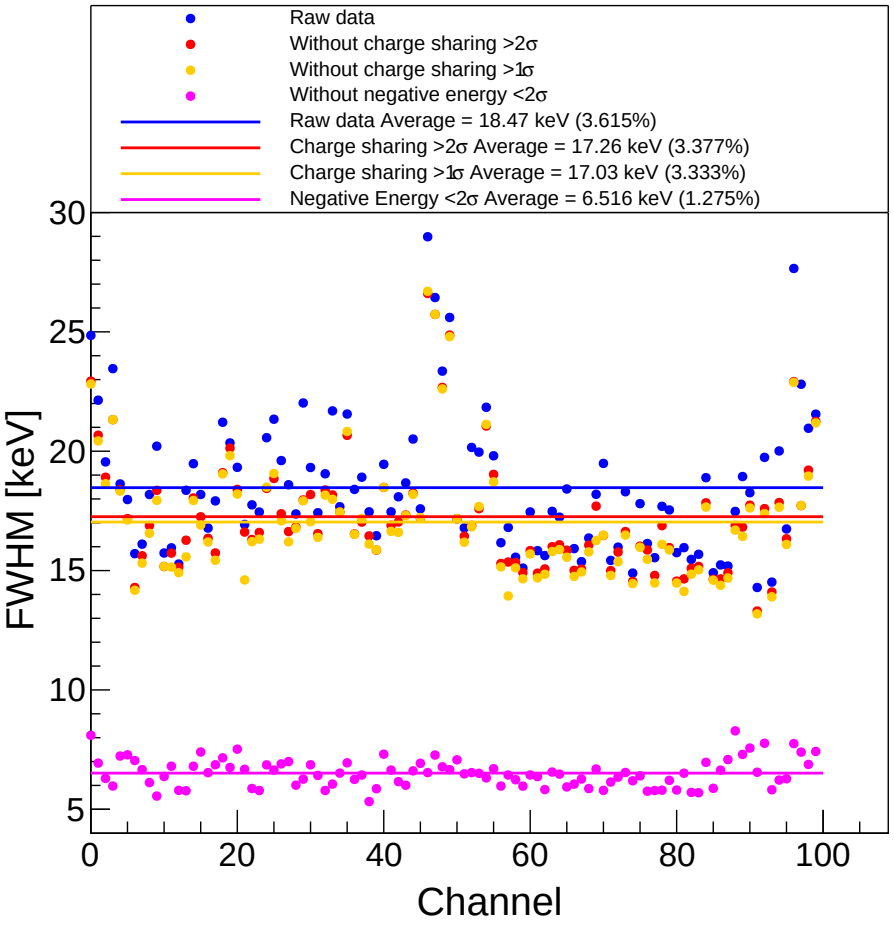

FIGURE 5.24: Energy resolution of the four distributions shown in Fig. 5.22 for all the channels in both diodes. The average value for each distribution is drawn with a straight line.

ring electrode and, therefore, there will be a loss of energy on the measurement. This trend disappears in the cut of the negative energy events because the events that occur close to the pixel electrode, which are potential responsible of this effect, are rejected.

The average resolutions for all the pixels show a slight improvement of energy resolution by rejecting charge sharing events above 2σ. The more restricting cut of events above 1σ does not improve, practically, the energy resolution, compared to the cut of charge sharing events above 2σ, from 3.377% to 3.333%. Finally, the dramatic improvement of the distribution without the low energy events is consistent in all the channels. The average resolution improves from the 3.615% of the raw spectroscopy down to a 1.275%.

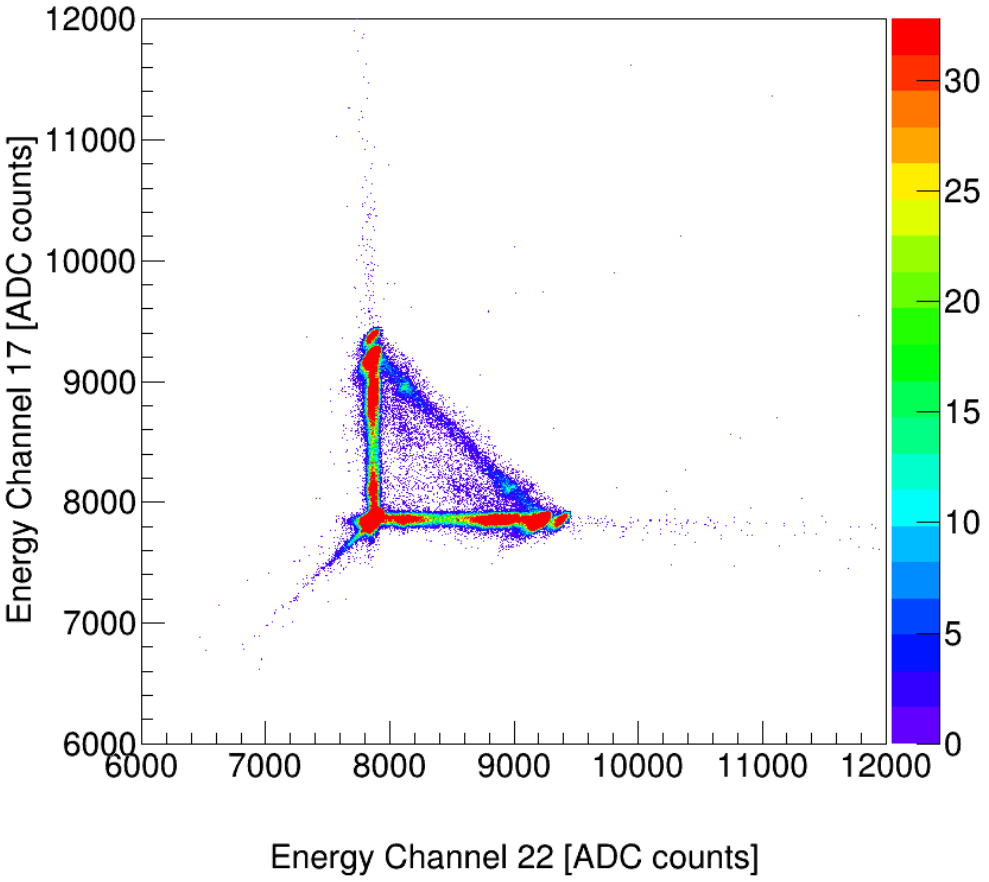

FIGURE 5.25: Scatter plot of the energy values of channel 22 (x axis) and channel 12 (y axis) for any channel triggering. Spectroscopy acquired at 500 V/mm bias voltage and at room temperature.

5.2.3 Measurements with ^{57}Co

The behavior of the detector for photons with 122 keV energy has been studied with a ^{57}Co radioactive source. All the measurements shown are acquired at 500 V/mm and at room temperature. Fig. 5.25 shows the plot of the energy measured in two neighbor channels for the same event for a data acquisition of ^{57}Co. One can observe the region corresponding to the photopeaks of 122 keV and 136 keV. In this case the negative events show smaller negative amplitude due to the lower energy of the ^{57}Co photopeaks (122 keV and 136 keV) compared to those of the ^{22}Na (511 keV and 1.275 MeV).

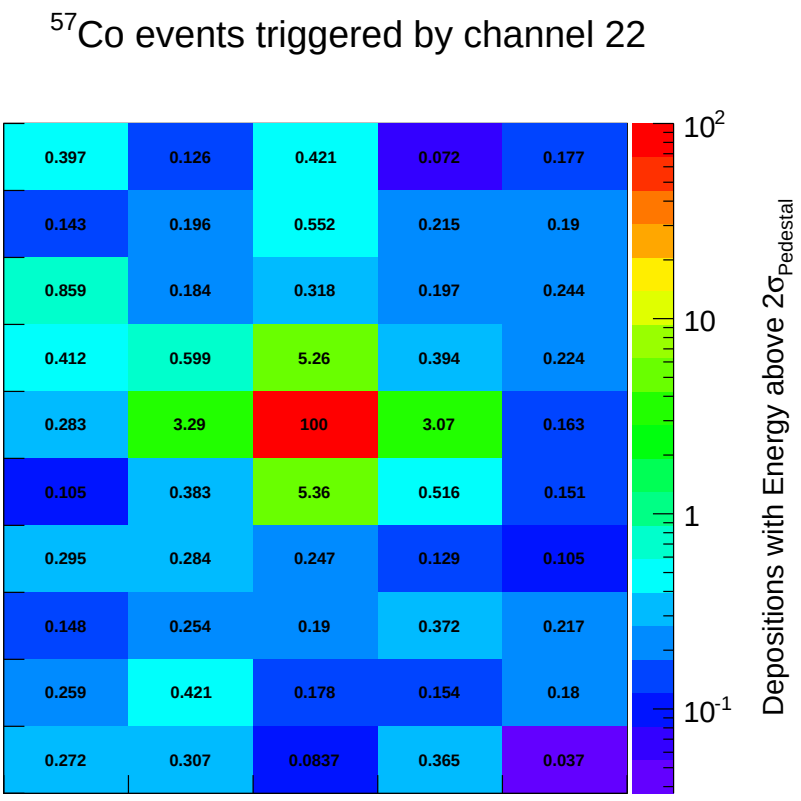

FIGURE 5.26: Percentage of events with energy above 2σ per channel compared to the total events triggered in channel 22.

5.2.3.1 Charge Sharing Evaluation

The effect of charge sharing for depositions of 122 keV has been studied. Fig. 5.26 shows the percentage of pixels with energy above 2σ of the pedestal distribution for each pixel in diode 1 for events triggered by pixel 22. The pixels neighbor to the trigger pixel show higher percentages. Although they also show a top-bottom and left-right geometry, the proportionality between the amount of statistics and the length of the side is not as linear for the results of the ^{22}Na.

One can observe that the fraction of events for pixels far from the triggered pixel is, in general terms, higher than those of ^{22}Na. They can be the result of Compton interactions. The probability of a 122 keV photon to create a Compton interaction is lower that that of a 511 keV photon. However, the photons created in Compton interactions of 122 keV photons have energies below 50 keV. Therefore, the absolute probability of such

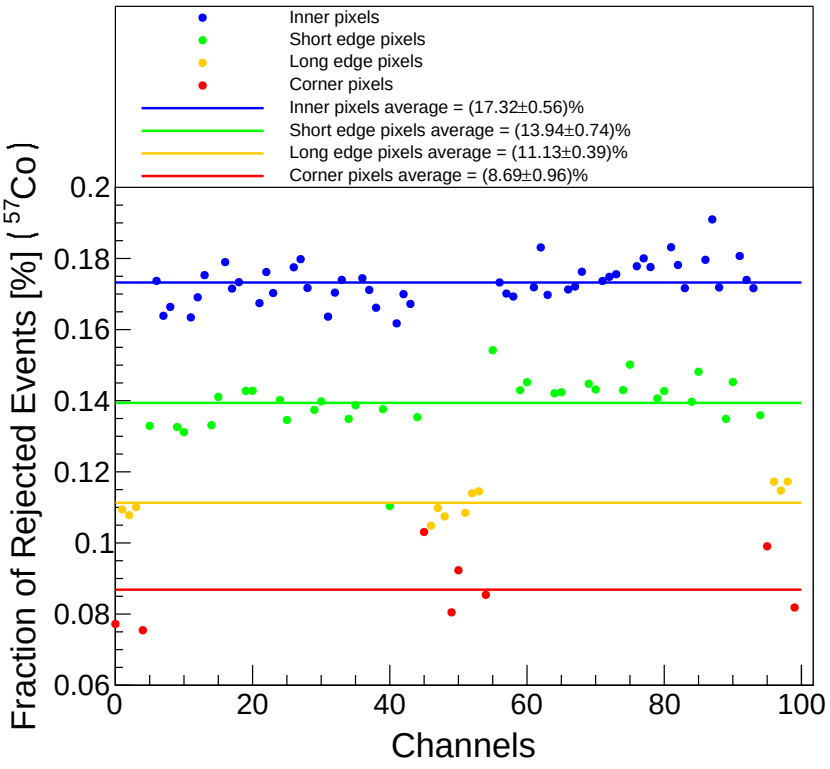

FIGURE 5.27: Fraction of events undergoing charge sharing normalized to the total events triggered by that pixel. The pixels have been differentiated according to their position in the diode. The average for inner, edge and corner pixels has been drawn with a line.

photons to interact with the diode, either by means of photoelectric effect or scattering, are higher.

Fig. 5.27 shows the percentage of events undergoing charge sharing on each pixel out of the total amount of events triggered in that pixel. As in the case of the ^{22}Na data, the pixels behave different according to their position in the diode. The average of events undergoing charge sharing for inner, short edge, long edge, and corner pixels are 17.32%, 13.94%, 11.13% and 8.69%, respectively. These values are lower than those obtained for the ^{22}Na data. The main photopeak of the ^{22}Na has 511 keV, whereas that of the ^{57}Co has 122 keV. The absolute charge shared per deposition is smaller in the case of the ^{57}Co and, therefore less charge sharing is observed.

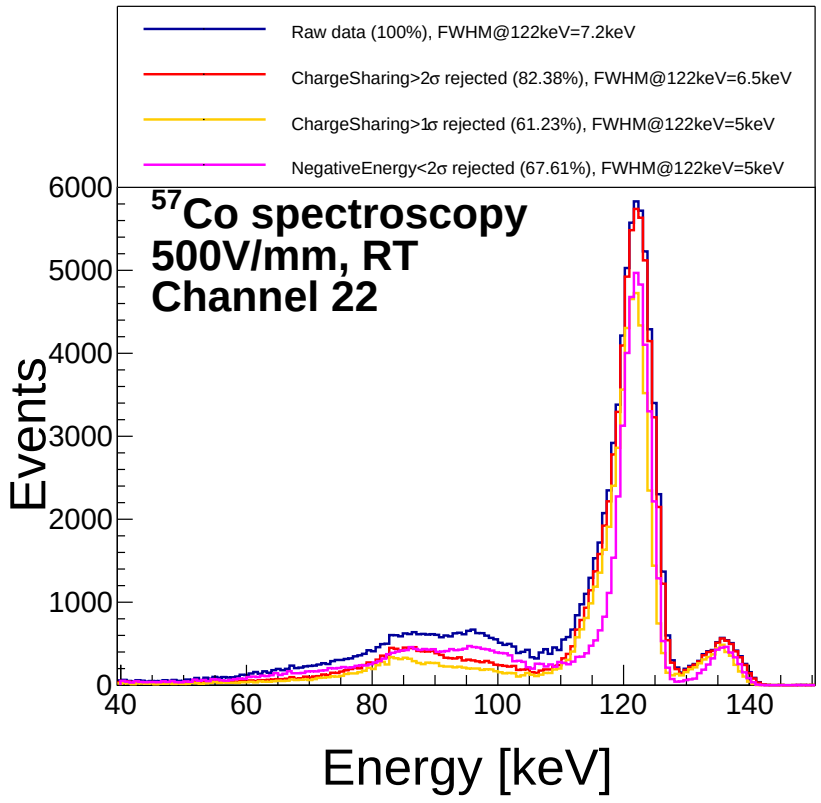

FIGURE 5.28: Spectroscopies of ^{57}Co at 500 V/mm and at room temperature for channel 22. The four distributions corresponds to four cuts on the same data sample. (Blue) raw data, (red) charge sharing events above 2σ rejected, (yellow) charge sharing events above 1σ rejected and (magenta) negative events below 2σ rejected.

5.2.3.2 Energy Resolution

The energy resolution has been studied for different energy cuts on the pixels surrounding the triggered pixel. Fig. 5.28 shows four cuts of the same data sample. The first cut corresponds to the raw distribution of events triggered by channel 22. In two of the distributions events undergoing charge sharing, with energy above 1 and 2 sigmas, have been rejected. In the fourth distribution, events with low energy below 2σ of the noise have been rejected.

The FWHM for the raw distribution is 7 keV, whereas for either the charge sharing rejection above 1σ and the negative energy below 2σ is 5 keV. The most restrictive cut is that of the charge sharing for 1σ, which leaves it with 61.3% of the statistics of the raw distribution. The FWHM does not improve much by applying cuts as in the case of

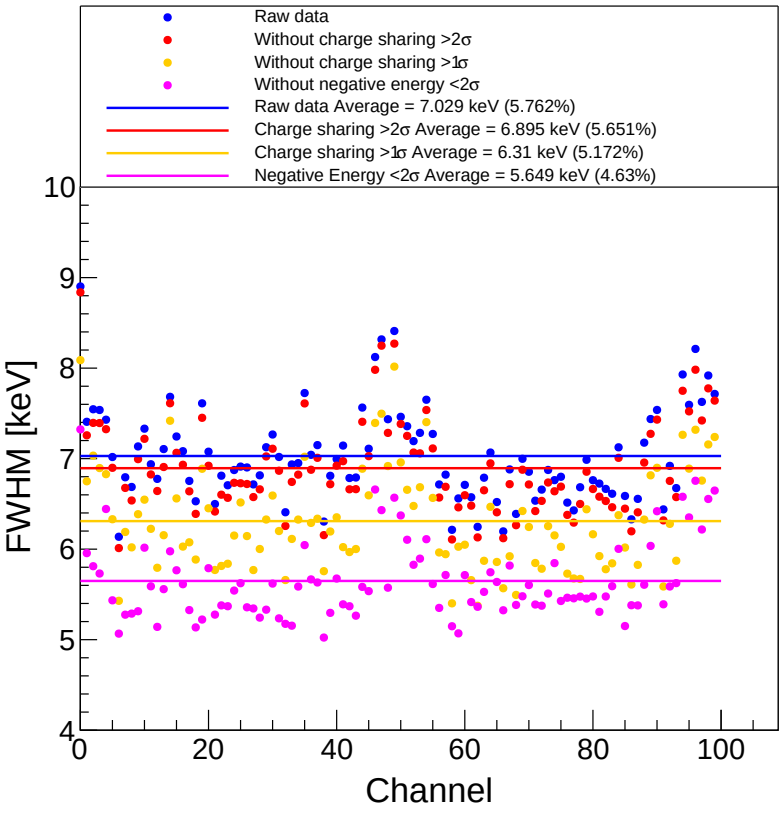

FIGURE 5.29: Energy resolution of the four distributions shown in Fig. 5.28 for all the channels in both diodes. The average value for each distribution is drawn with a straight line.

the ^{22}Na. This can be explained because the charge sharing is comparable to the noise of the pixel.

Fig. 5.29 shows the energy resolution of the distributions shown in Fig. 5.28 for all the pixels in the diode. Unlike the data shown for channel 22, the graph shows that in average, the best resolution is clearly achieved by the distribution with the negative energy rejection. The raw distributions show 7.03 keV FWHM in average versus a 4.63% of the distribution with the negative events rejection.

The results obtained with the ^{57}Co source show less charge sharing between pixels. They also show that the energy resolution cannot be improved as much as it has been done with the ^{22}Na measurements. Therefore, the trade-off between energy resolution and efficiency is, in this case, less crucial to find an optimum working point for the detector.

5.3 Discussion

The VATAGP7.1 has been used to build a pixelated detector of CdTe. Previous publications report of similar semiconductor devices employing this ASIC [145, 158]. Two CdTe diodes with effective pixels of 2 mm $\times$ 1 mm have been operated at 500 V/mm and at room temperature.

The charge sharing effect on the pixels has been measured for the spectroscopies of ^{22}Na and ^{57}Co. The percentage of events undergoing charge sharing out of the total triggers in that pixel is proportional to the perimeter of the pixel in contact with other pixels for both sources. For the data obtained with ^{22}Na, inner pixels, with 6 mm perimeter in contact with other pixels, show a charge sharing of 21.19%. This result can be reescaled to pixels of 1 mm $\times$ 1 mm. Such pixels would have a charge sharing of 28.26%.

The energy resolution when using raw data (no cut applied) at 511 keV is of 3.62% and is improved to 3.38% by rejecting the fraction of the charge sharing events. The energy resolution when using raw data (no cut applied) at 122 keV is of 5.90% and is improved to 5.33% by rejecting the fraction of the charge sharing events. The major improvement on the energy resolution has been achieved by rejecting the events with a dominant contribution of holes. Energy resolutions of 1.28% and 4.01% at 511 keV and 122 keV respectively have been achieved. Devices employing pixelated detectors have reported for similar results [159–163].

Chapter 6

VIP-Detector Characterization

This chapter is about the characterization of the smallest detector unit in the VIP design, the VIP-Detector. It consists of pixel CdTe attached to a VIP-PIX chip. The performance of the VIP-PIX is fundamental for the overall behavior of the VIP-Detector. For this reason, the VIP-PIX has been probed and tested to find the optimum working point to operate it.

The setup used to characterize both the VIP-PIX and the VIP-Detector is complex due to the abundant tests that have to be performed and their diversity. In terms of the detector characterization, the energy resolution at different energy levels has been studied for all the pixels in one VIP-Detector.

6.1 VIP-Detector Setup Description

The VIP-Detector consists of a pixelated CdTe diode attached to a VIP-PIX via bump-bonding. The hardware readout PCB has been split into two parts: a baby board PCB (BB), and a mother board PCB (MB). The BB contains a reduced amount of components and has small size. The MB is bigger and contains the rest of the components required for the readout of the VIP-Detector. Each VIP-Detector is mounted on an individual BB in order to test it and characterize it. The MB is connected to an FPGA to perform the digital signal sequences required by the VIP-PIX ASIC.

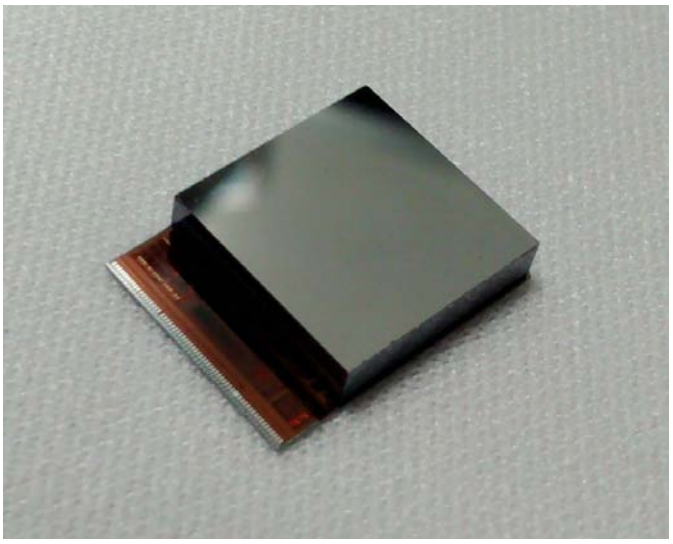

FIGURE 6.1: VIP-Detector assembly. A CdTe diode of 10.4 mm × 10.5 mm surface is mounted on a VIP-PIX chip. One ball of 250 μm diameter of BiSn is deposited in each pixel pad of the VIP-PIX. Later the balls are melted on the CdTe diode electrodes through flip chip process.

6.1.1 VIP-Detector Assembly

The CdTe sdiode has been developed by ACRORAD and has dimensions 10.4 mm × 10.5 mm with 2 mm thickness. The pixel electrode is divided into 100 pixels of 1 mm × 1 mm each and has an electrode configuration: pixel/ALN/Au/Ni/Au/Al/CdTe/Pt-continous. The CdTe diode is bump-bonded to the VIP-PIX with BiSn solder balls of 250 μm diameter such that each pixel electrode is connected to one readout channel. The VIP-Detector assembly has 100 pixels with independent readout, a picture is shown in Fig. 6.1.

The VIP-Detector assembly is mounted on a BB. The BB has dimensions of 45 mm × 45 mm and includes one of the stages of the high voltage filter. A picture of the naked BB is shown in Fig. 6.2. The VIP-Detector is attached to the BB with conductive glue. Each of the 64 I/O pads of the VIP-PIX is connected to the BB with wire boundings of aluminum of 25 μm diameter. A wire of aluminum of 80 μm diameter connects the continuous electrode of the diode to the HV pad.

The BB has two SAMTEC connectors on the bottom so it can be plugged in the MB. An aluminum box is mounted on the BB in order to protect the components mounted on it, specially the wire boundings of the ASIC pads and the high voltage wire. Fig. 6.3 shows the picture of one BB with one VIP-Detector assembly mounted on it.

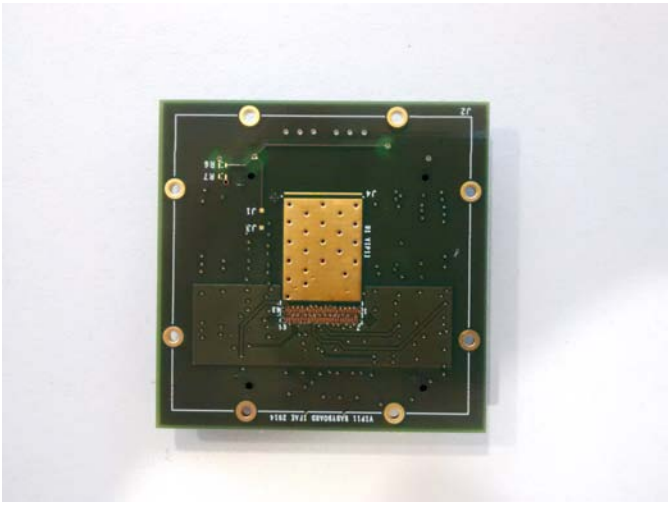

FIGURE 6.2: Baby-board for the VIP-PIX ASIC. The VIP-PIX is attached to the BB with conductive glue. The big pad in the center is a ground plate for the VIP-PIX.

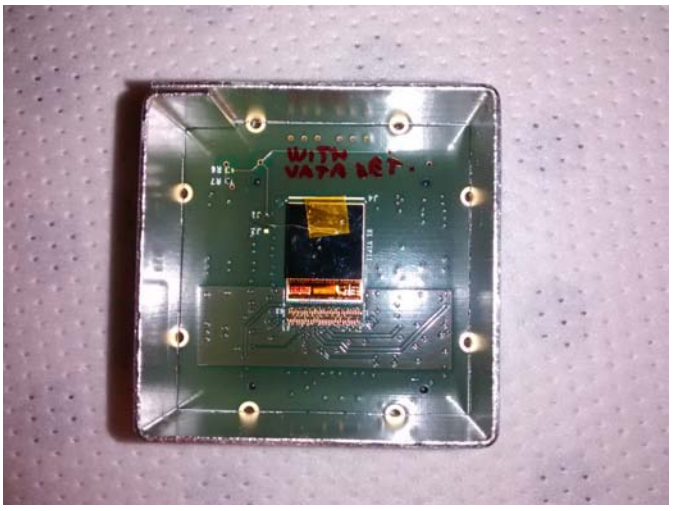

FIGURE 6.3: Baby board with a VIP-Detector assembly mounted on top.

6.1.2 Mother Board PCB (MB)

The MB used for the readout of the VIP-PIX chip is fixed inside an aluminum structure in order to protect the components and isolate them from electromagnetic interferences. A picture of the MB is shown in Fig. 6.4.

The DC power supply connectors provide the power to the MB. There are four connectors for 2.5 V and one for 3.3 V. Two flat connectors are placed to connect the MB with the FPGA. Two SAMTEC connectors are placed on the center to plug the BB.

One stage of the high voltage filter has been placed on the MB. One would expect for the high voltage filter to be physically as close as possible to the diode. However, given

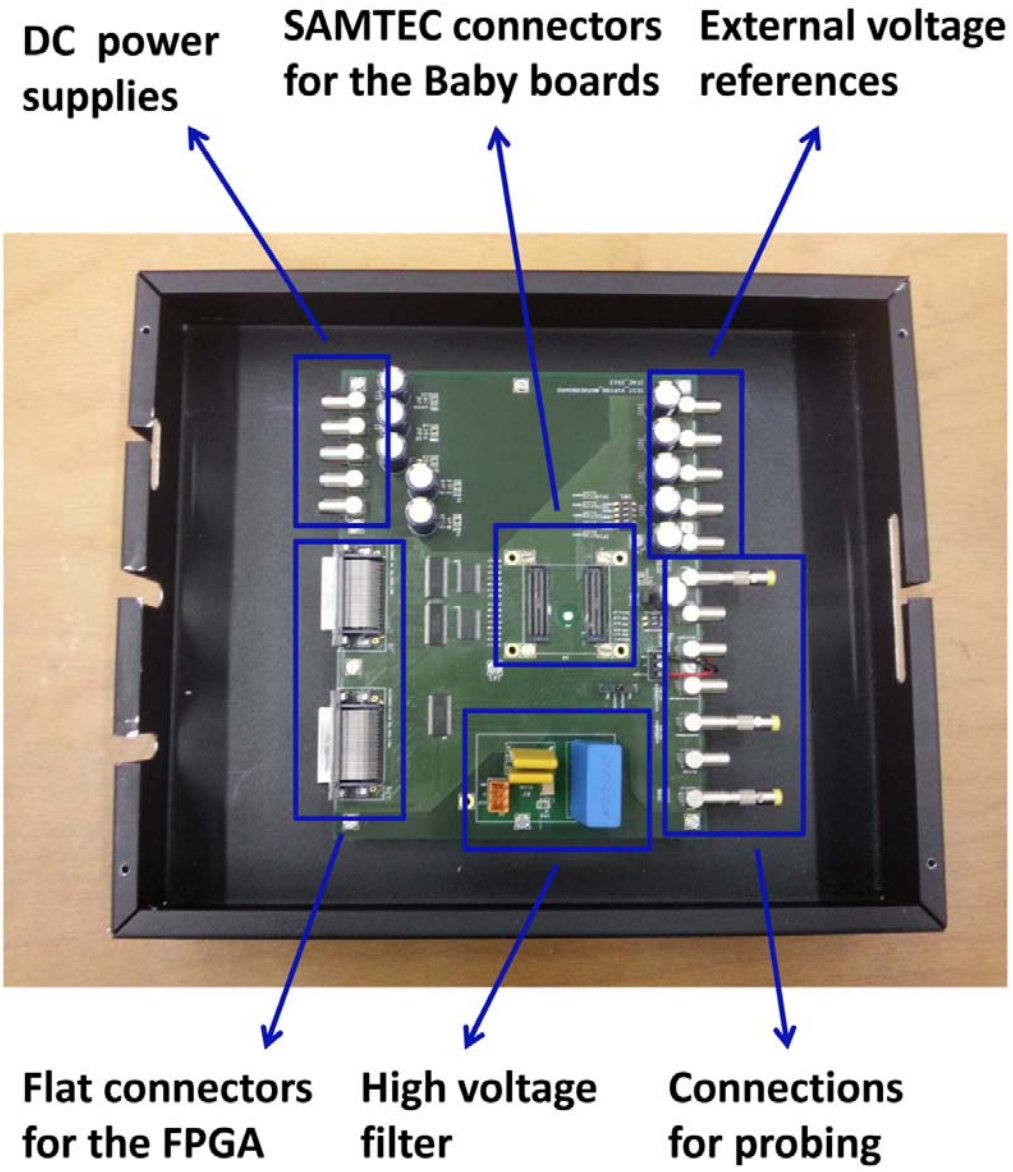

FIGURE 6.4: Motherboard PCB.

the huge size of the capacitors, they cannot be placed on the BB and have to be placed on the BB.

Some connections for external references are also placed on the MB. The VIP-PIX does not require them to operate. They are placed there as a tool for debugging. A few more connections for probing purposes are placed as well. They allow to observe signals for advanced debugging tasks of the VIP-PIX performance.

Further details on the FPGA and the GUI used for the data acquisition are explained in App. B.

6.2 Chip Probing

A total of 1584 VIP-PIX chips, from nine 8" wafers, have been probed. The probing process has been carried on before thinning and dicing the wafers. The probing of the wafers was done with customized probe card mounted on Karl-Suss probe station at CNM. The probe test checks the pixel linearity response to test pulse for both amplitude (ADC) and the time stamp (TDC). It also checks the power consumption and the electronic noise from the pedestal measurements. Then the VIP-PIX chips are classified into classes according to the probe results. The best chips are reserved to construct the VIP PET ring.

A picture of the probe station setup is shown in Fig. 6.5. The FPGA and the MB are the same that have been used for the VIP-Detector operation. An oscilloscope has been also used to monitoring the chip operating status.

A Labview routine has been used to automatize the probing process of the VIP-PIX. This application performs a variety of tests to the chip and shows a summary of the results to the user. The settings have been optimized such that the overall testing process for a single chip takes 30 s.

An example of the prompt screen after one test is shown in Fig. 6.7. It provides three pixel maps: *Trigger OK?*, *ADC OK?* and *PED OK?*. The Trigger OK? map represents the functionality of the pixel trigger. In this case the trigger of all pixels are working. The ADC OK? represents the ADC status. The ADC is considered to failure when it always delivers the same set of values or it does not show a difference response for a test pulse with different amplitude. Average 7% of the pixels have bad ADC. The PED OK? map gives a first approximation of the pedestal distribution of the pixel. If the pedestal distribution for one pixel has a spread significantly higher than what is expected or all the measurements have the same ADC value, the pedestal is taken as wrong, and the red light shows off for that pixel. The criteria to define if the pedestal is good or not can be changed, therefore it is an interpretable result. In the example shown, all the pixels with bad ADC, 8, plus another one, 9 in total, show a wrong pedestal distribution.

On the bottom left side of the panel there are two rows of indicators. These indicators show, among other features, the functionality of the reset, the chip ID, the temperature sensor, the TDC, the global register and the pixel register. The linearity of the TDC

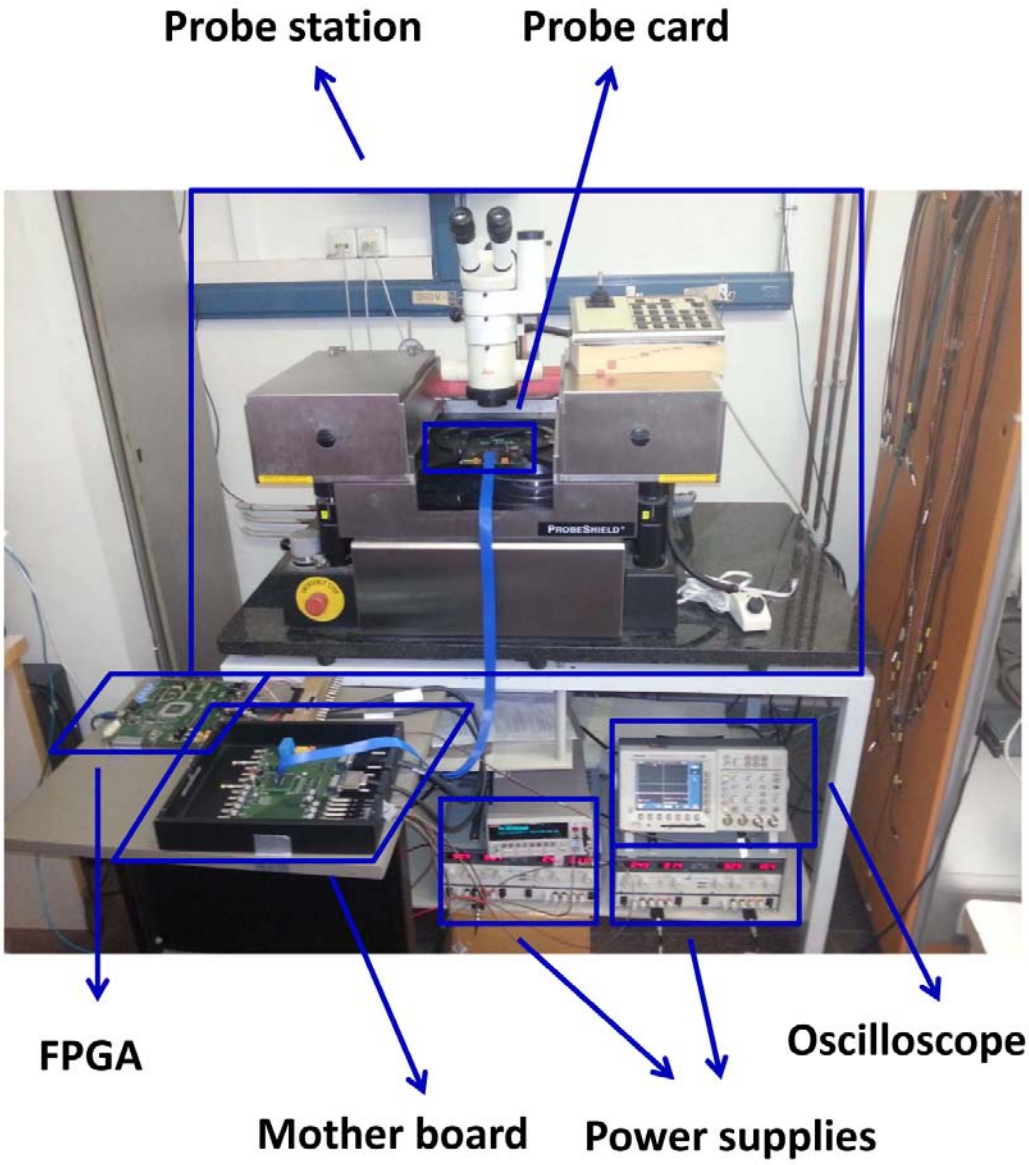

FIGURE 6.5: Picture of the setup used for the chip probing.

is also tested and shown. The criteria to decide of the TDC response is linear can be changed by the user, hence, this result is interpretable.

6.2.1 Probing Results

The chips have been classified into 6 categories according to their performance:

- Class A: # Bad ADC ≤ 7,
  (#Bad Peds + #Bad Triggers) ≤ 7 && (#Bad DTPs + #Bad Triggers) ≤ 7

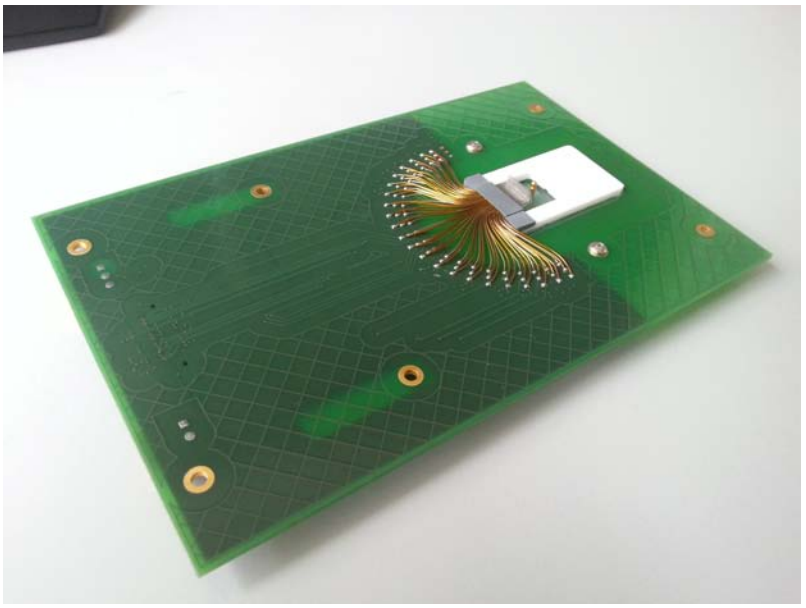

FIGURE 6.6: Probe card used for the probing of the VIP-PIX.

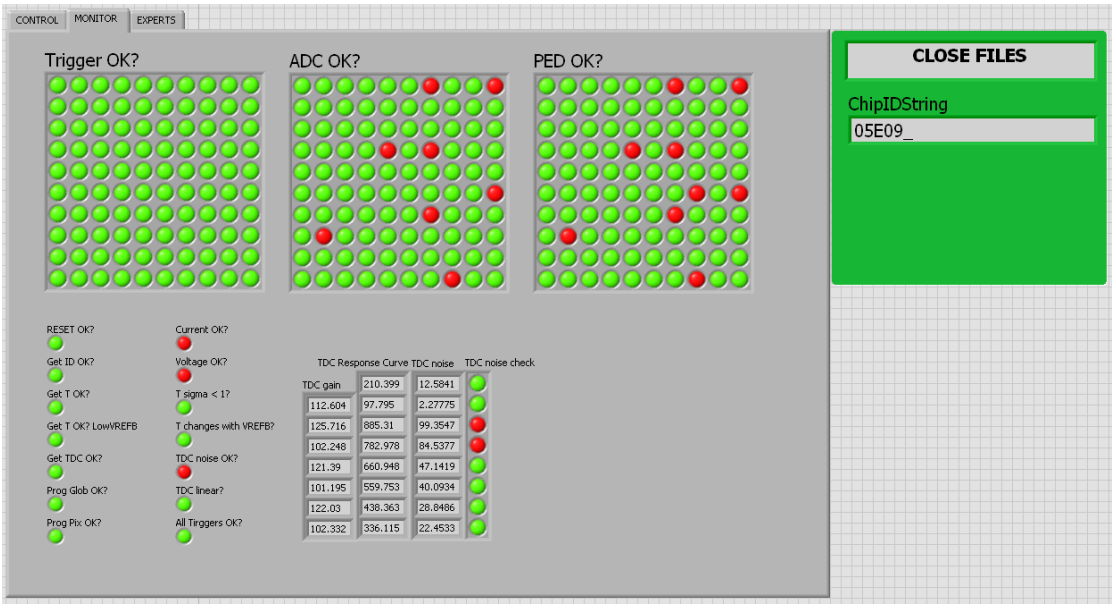

FIGURE 6.7: Example of the results shown after a probing process.

- Class B: $7 <$ # Bad ADC ≤ 10,

  $7 <$ #Bad Peds ≤ 10 && $7 <$ #Bad DTPs ≤ 10 && $7 <$ #Bad Triggers ≤ 10

- Class C: $10 <$ # Bad ADC ≤ 15

- Class D: # Bad ADC > 15

- Class E: Status TDC $\neq 1$

- Class F: Chip not probed

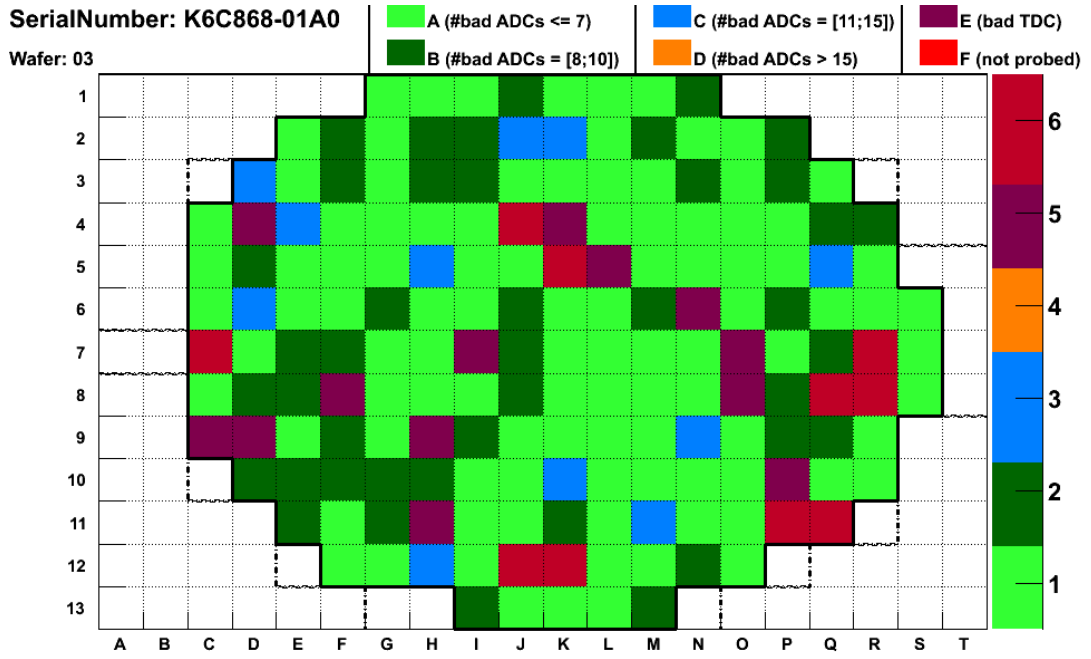

FIGURE 6.8: Classification of the chips in one wafer.

Wafer	Class A	Class B	Class C	Class D	Class E	Class F
3	100	42	11	0	13	10
4	102	49	8	0	15	2
5	93	56	16	0	8	3
6	109	43	11	0	9	4
7	96	53	15	0	10	2
8	97	44	17	0	16	2
9	96	55	10	2	10	3
10	93	51	18	1	11	2
11	94	47	16	0	16	3
Total	880 (55.6%)	440 (27.8%)	118 (7.7%)	3 (0.2%)	108 (6.8%)	31 (2.0%)

TABLE 6.1: Classification of chips per wafer and total.

A total of 9 wafers have been probed with 176 chips each. An example of the classification of the chips in one wafer is shown in Fig. 6.8. The details of the pixel classification per each wafer is shown in Tab. 6.1. Most of the chips are either class A or B (83.4%). Chips of type A or B have been chosen to build the VIP-Detector assemblies. Chips from other categories have been used as mechanical samples to test the process of assembling the VIP-Detector.

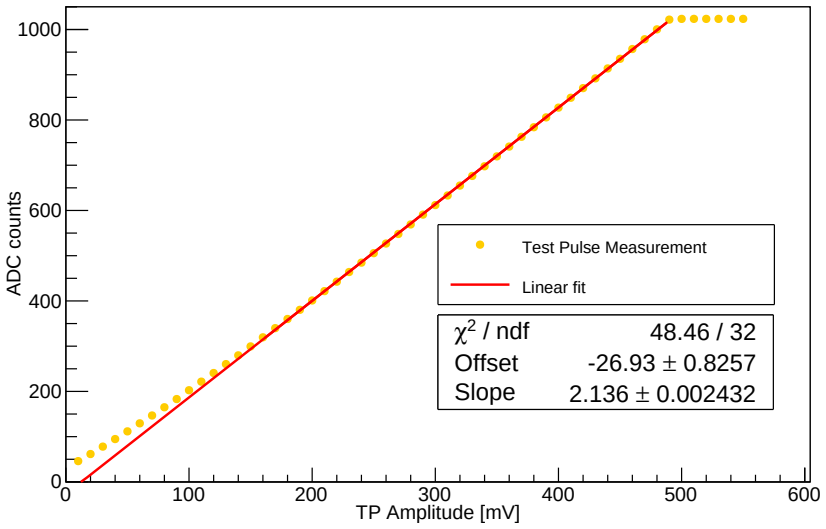

FIGURE 6.9: ADC response for test pulse with amplitudes from 10 mV up to 540 mV.

6.3 Results with VIP-Detector

6.3.1 VIP-PIX Response Characterization

The response of the VIP-PIX ADC for energy measurements has been characterized using an external test pulse with varying amplitude from 10 mV up to 550 mV in steps of 10 mV. The test pulse has been sent to the input of the pixel via the CdTe detector which acts, for such test, as simple capacitor. The advantage of using this method is to check the bump-bonding connection between every pixel electrode and the corresponding pixel channel. At the same time this scheme of test pulse injects the same pulse in all the pixels since each pixel has the same capacitance like the other ones.

Fig. 6.9 shows the ADC measurement for different test pulse amplitudes. One can see that the setup saturates for an amplitude of 490 mV. The response is linear in the range between 150 mV and 490 mV. The behavior of the pixel response below 150 mV deviates from linearity. This sort of intrinsic limitation is due to the fact of using active feedback resistor in the shaper. The VIP-PIX allows to set different gains with maximum input signal equivalent to 120 fC. In order to optimize the full dynamic range for the use of PET, the gain will be set such that the 511 keV peak is placed slightly below the 490 mV input.

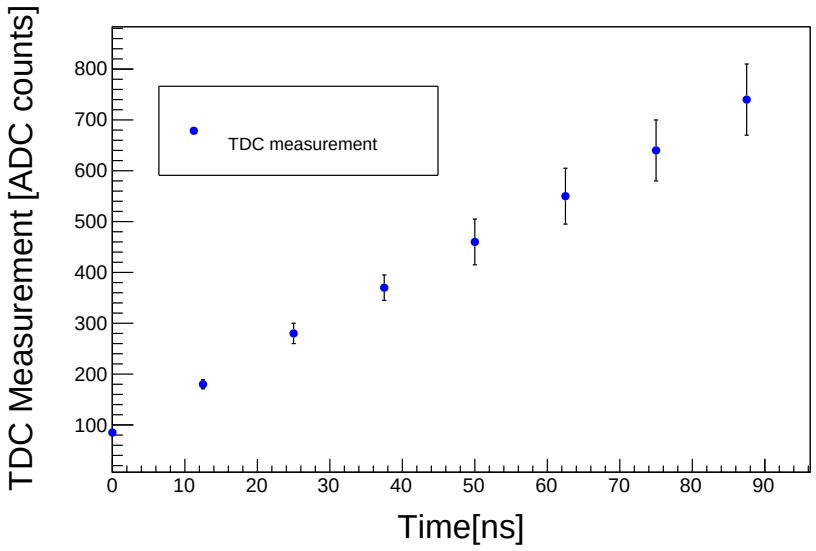

FIGURE 6.10: TDC response for signals sent after delays of 0 ns, 12.5 ns, 25 ns, 37.5 ns, 50 ns, 62.5 ns, 75 ns and 87.5 ns. The error bars grow when the value of the measurements is higher.

The rise and fall edges of the 40 MHz clock of the FPGA have been used to calibrate the response of the TDC. This allows to send pulses separated by 12.5 ns. Since the dynamic range of the TDC is 100 ns, 8 different points can be obtain for the calibration. Fig. 6.10 shows the TDC measurement for the aforementioned 8 points. The distribution of the measured value for the same time window, shows large variance. The spread on the distribution for each measurement should be comparable in all the measurements. This effect is attributed to an error in the layout of the chip.

The effect is regular and related to a 1 MHz counter, therefore, a strategy has been found to correct it. The calibration of the TDC after applying the correction is shown in Fig. 6.11. One can see that, after the correction, the variance in the measurements are smaller and compatible to each other. The behavior observed is linear and the slope is 7.348 ADC counts per nanosecond, which is a precision of 136 ps.

6.3.2 VIP-Detector Spectroscopy with ^{57}Co

The spectroscopy of ^{57}Co has been acquired with the VIP-Detector at 500 V/mm and at room temperature. Fig. 6.12 shows the spectroscopy after calibration for one pixel. The FWHM of the 122 keV peak is 3.43 keV, which represents an energy resolution of 2.81%. One should notice that no cut was applied to the data sample. From chapter

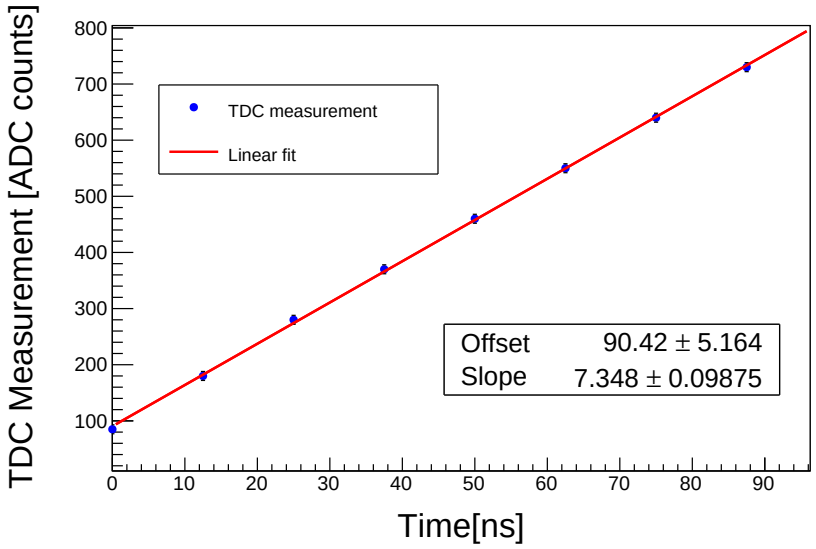

FIGURE 6.11: TDC measurement for pulses sent after 0 ns, 12.5 ns, 25 ns, 37.5 ns, 50 ns, 62.5 ns, 75 ns and 82.5 ns. 100 measurements have been taken for each point. The error bars are inside the markers.

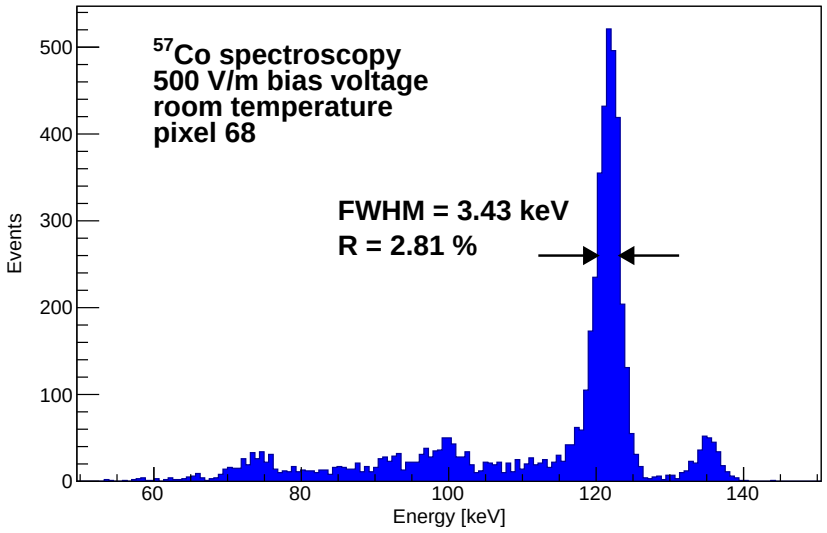

FIGURE 6.12: ^{57}Co spectroscopy for pixel 68 of the VIP-Detector 02E03 at 500 V/mm and at room temperature.

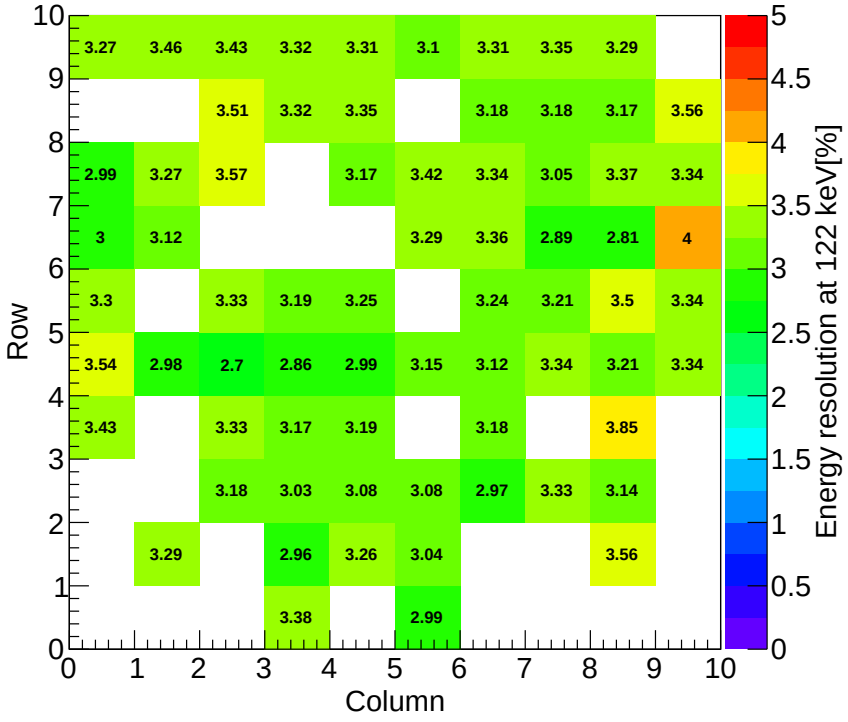

FIGURE 6.13: Energy resolution in %, at 122 keV for every pixel of the sample detector with ID 02E03. The pixels have been placed according to their position in the detector matrix. Pixels with no results are switched off either because of bad ADC or high leakage current. A white pixels means a none operational pixel due to bad ADC, or high leakage current, or bad contact with the BiSn solder bump.

5, it is known that for a pixel of 1 mm × 1 mm and for 122 keV photon, one should expect around 23.1% to have suffered from charge sharing. By removing fraction of those events, one would expect to get better results for the FWHM.

Fig. 6.13 shows the energy resolution for all the pixels of the sample 02E03. The same set of values is shown in a graph in Fig. 6.14. The average energy resolution of all the pixels is of 3.24% with a dispersion of 0.15%. These results are comparable to those acquired in Chap. 4 and better than those obtained in Chap. 5 for an energy of 122 keV.

Due to such pixel pitch, 22.5% of the events will undergo charge sharing. Charge sharing deteriorates the energy resolution and this means that the energy resolution with VIP-PIX can be improved. Unfortunately due to X-talk it is not possible to detect small energy deposition. Hopefully in the future upgrade of VIP-PIX chip this can be achieved.

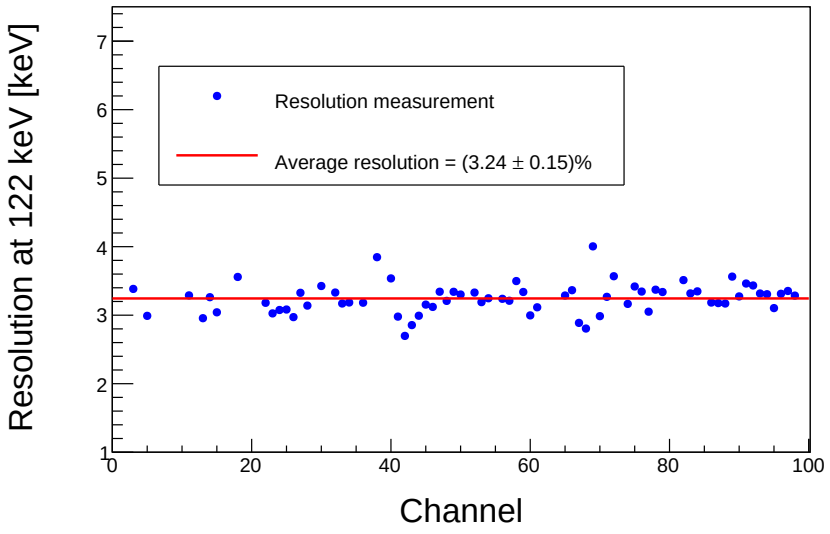

FIGURE 6.14: The energy resolution presented as FWHM normalized to the peak energy of 122 keV for all the pixels in the sample 02E03. The average of all the pixels is shown with a straight line.

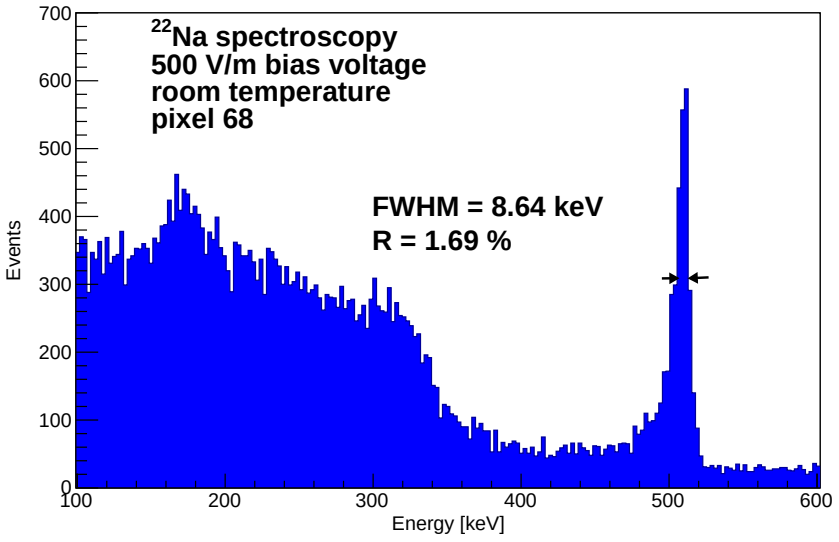

FIGURE 6.15: Spectroscopy of ^{22}Na for pixel 68 acquired at 500 V/mm bias voltage and at room temperature.

6.3.2.1 VIP-Detector Spectroscopy with ^{22}Na

The spectroscopy of the ^{22}Na has been acquired with the same detector, used for ^{57}Co, and under same conditions. Fig. 6.15 shows the spectroscopy of ^{22}Na for data collected by pixel 68. One can see that the Compton edge is at 340 keV and this shows that the calibration of ADC counts to keV has been done correctly. The FWHM at the 511 keV

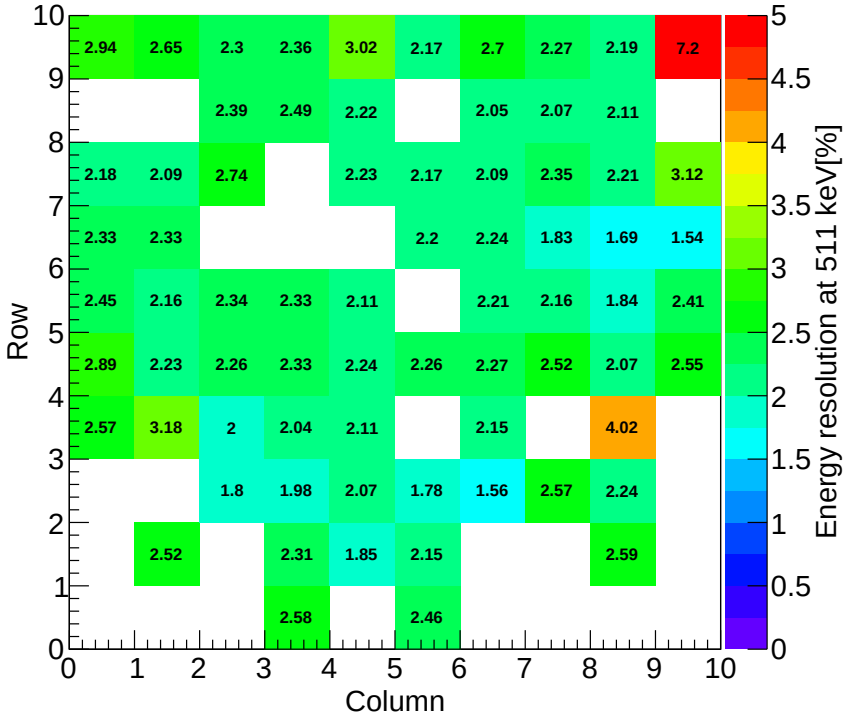

FIGURE 6.16: Energy resolution [%] of the pixels in sample 02E03 at 511 keV at 500 V/mm bias voltage and at room temperature. A white pixels means a none operational pixel due to bad ADC, or high leakage current, or bad contact with the BiSn solder bump.

peak is of 8.64 keV, which represents a resolution of 1.69%.

The energy resolution of all the pixels of sample 02E03 at 511 keV energy is shown in Fig. 6.16. The same set of data is shown in Fig. 6.17 as a scatter plot. The average energy resolution of the pixels is 2.37% with a spread of 0.69%.

As it has been mentioned in the previous section, with the current version of the VIP-PIX it is not possible to veto events that have suffered charge sharing and therefore one should compare the results in this chapter with the raw data results reported in Chap. 5.

6.4 Discussion

The VIP-PIX, an ASIC for the readout of pixelated semiconductor diodes with smart pixel readout, has been developed. It includes the full readout circuitry and delivers the

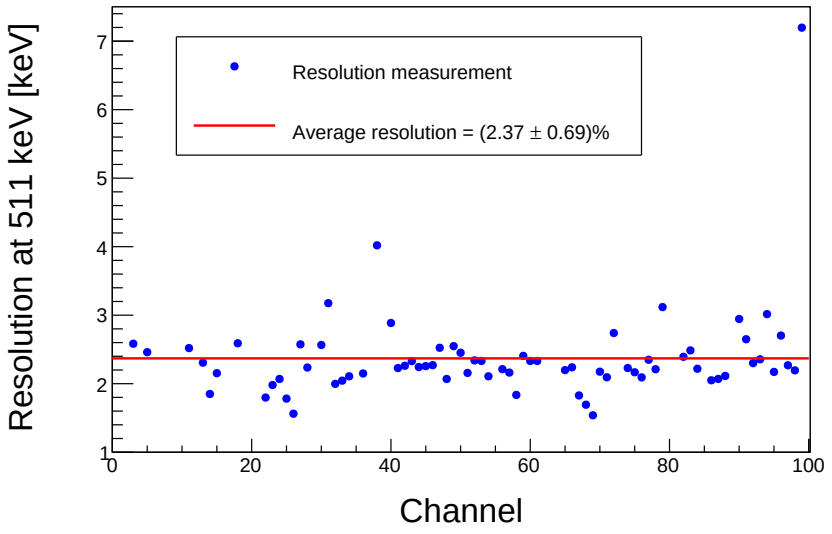

FIGURE 6.17: The energy resolution presented as FWHM normalized to the peak energy of 511keV for all the pixels in the sample 02E03. The average of all the pixels is shown with a straight line.

energy for each pixel and the timestamp of the detection. ASICs with similar properties have been developed and their performance has been reported [164–167].

The first full VIP-customized detector unit, the VIP-Detector, has been built. The VIP-Detector consists of a CdTe diode of 10 mm × 10 mm dimensions and 2 mm thickness mounted on a VIP-PIX ASIC. The diode is segmented into pixels of 1 mm pitch. The energy resolution of the VIP-Detector have been evaluated at 500 V/mm bias voltage and at room temperature. The resolution at 511 keV is of 3.24% whereas for 122 keV is of 2.37%. These results correspond to the raw data because neither the events undergoing charge sharing nor those dominated by holes can be rejected. In a further upgrade of the VIP-PIX chip, where events undergoing charge sharing can be rejected, this results are expected to improve.

Results with customized detector devices using CdTe or CdZnTe have been reported [39, 73, 148, 168–176]. The VIP-Detector is a compact detector for gamma ray spectroscopy. It offers a high performance and a relatively easy readout setup due to the digital part included in the back-end. The VIP-Detector is the first step to reach the main aim of the VIP Project, to build and characterize the VIP-Module.

Chapter 7

Conclusions

The performance of the VIP design has been evaluated by using a single pixel diode, then an array of pixels, and finally with a 100 pixel detector assembly bump bonded to VIP-PIX ASIC. For each of the three stages, an independent process of characterization has been carried out. A dedicated setup, hardware and software, has been developed.

The single pixel diode has been used to measure the energy resolution and the coincidence time resolution of a CdTe diode with 2 mm thickness. The energy resolution measured at -500 V/mm and at room temperature at 511 keV and 122 keV is 1.57% and 3.03%, respectively. By decreasing the temperature down to -8°C and doubling the bias voltage to -1000 V/mm, the energy resolution at 511 keV is of 1.2%.

The coincidence time resolution measured at -1000 V/mm and at -8°C is of 12.5 ns FWHM for events with energy above 25 keV. At such minimum acceptance energy, 70% of the events are acquired within 20.5 ns. For events with minimum energy of 500 keV, the FWHM is reduced up to 6 ns.

The charge sharing effect has been measured for pixels with size 2 mm $\times$ 1 mm using the radioactive sources ^{22}Na and ^{57}Co. The fraction of events undergoing charge sharing for inner pixels is 21.19% for ^{22}Na, and 17.32% for ^{57}Co.

The energy resolution for the raw data at 511 keV and 122 keV is of 3.62% and 5.76%, respectively. A slight improvement on the energy resolution is achieved by rejecting the events undergoing charge sharing. A significant improvement of the energy resolution is

achieved by rejecting the events with a dominant contribution of holes. A resolution of 1.28% at 511 keV and of 4.63% at 122 keV is obtained.

The characterization of the VIP-PIX shows a precision of ∼0.6 keV per ADC count for an optimized dynamic range and of 136 ps for the TDC. The average energy resolution of the pixels at 511 keV and 122 keV is of, 2.37% and 3.24%, respectively.

This work has been of great value in defining the specifications of the VIP-PIX ASIC. The obtained values for the energy resolution at 511 KeV and the coincidence window have been used to tune the simulation of the full VIP-PET detector as well for the VIP-PEM and VIP-CC. This led to a precise modeling of the final devices.

Based on the energy resolution measured at -500 V/mm and at room temperature, the simulation of the VIP-PET shows a fraction of scattered events of 3.95%, which is an order of magnitude less than the 37.9% of state-of-the-art PET scanners. The little presence of scattered events in the sample reduces significantly the background noise of the final image, and therefore, shows a better contrast. Moreover, the excellent energy resolution allows to use the VIP-module to build a Compton camera scanner.

Based on the 12.5 ns FWHM of the coincidence time resolution, the coincidence time window has been set to 20 ns in the VIP-PET simulations. The peak NEC value is obtained, for the NEMA NU2-2001 test, at 5.3 kBq/mL and is 122 kcps. For the same test, state-of-the-art scanners measure a maximum of 692 kcps for an activity concentration of 23.1 kBq/mL. The lower amplitude and position of the NEC peak for the VIP-PET compared to other PET scanners is compensated by the extremely higher purity of the events in the data sample.

Less than 30% of the events in the data sample are expected to undergo charge sharing in the VIP design. The strategy to deal with the charge sharing events will be applied offline in the data processing. A rejection of the charge sharing events will increase the signal purity but reduce the detection sensitivity. Conversely, keeping the charge sharing events, will increase the detection efficiency but reduce the purity of the sampled events. The trade-off between signal purity and efficiency must be set according to the priority of the system.

The VIP-PIX performs most part of the signal processing in each pixel independently and to work with a big amount of channels. The size of the voxel of the VIP-Detector is 1 mm $\times$ 1 mm $\times$ 2 mm.

With a segmentation of 1 mm in the radial direction an excellent measurement of the DOI is obtained. Hence, the parallax error is significantly reduced and the final image is sharper.

The work that has been done over the past 4 years, detailed in this thesis, has validated the viability of achieving superb PET images with a scanner a la VIP. The first image of Derenzo phantom is expected to be done in June 2015.

Appendix A

JB-2N Power Supply Specifications

JB / JBE Series

hivolt.de

0.3kV – 2kV, 1.8W - 2.5W
ULTRA LOW RIPPLE,
HIGH VOLTAGE POWER SUPPLIES FOR PMT

Matsusada Precision

- Exeptional low ripple and high stability
- Remote voltage and resistance programmable
- Voltage and current monitor
- Protected against arc and short circuit
- Optional output connector
- EN60950-1 and CE approved
- TÜV approved (0.6kV – 2kV models)

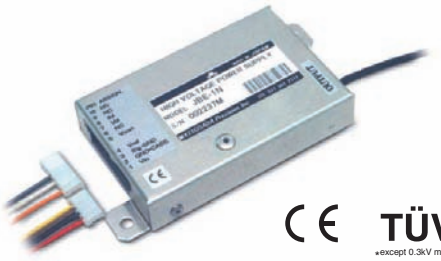

CE TÜV *except 0.3kV model

• APPLICATIONS

- Photomultipliers, Phototubes
- GM tubes, Radiation counters tubes
- MASS spectrometry, Electron beam / Ion beam

JB and JBE Series are ultra low ripple, high voltage, high performance power supplies for PMT. Remote programming as well as protection against arc and short circuit is integrated. The two series differ in the type of input connectors.

Output Voltage	Output Current	Model				Ripple	
		Positive Polarity		Negative Polarity		HF	LF
0 – 0.3 kV_{DC}	8 mA	JB-0.3P	JBE-0.3P	JB-0.3N	JBE-0.3N	1mVp-p (>5kHz)	4mVp-p (≦5kHz)
0 – 0.6 kV_{DC}	3 mA	JB-0.6P	JBE-0.6P	JB-0.6N	JBE-0.6N		
0 – 1 kV_{DC}	2.5 mA	JB-1P	JBE-1P	JB-1N	JBE-1N		
0 – 1.5 kV_{DC}	1.5 mA	JB-1.5P	JBE-1.5P	JB-1.5N	JBE-1.5N		
0 – 2 kV_{DC}	1 mA	JB-2P	JBE-2P	JB-2N	JBE-2N		

• SPECIFICATIONS

Input Voltage:	+24V ±10% @300mA typ
Output Control:	An external 5kΩ potentiometer or a remote 0 to +10V source (input imped. 100kΩ typ)
Regulation:	Line: 20ppm for ±1V input change Load: 20ppm for 0 to 100% load change
Stability:	15ppm/15min., 50ppm/8h
Temperature coeff.:	50ppm/°C max, 20ppm/°C typ.
Vref out:	10V ±2%, 50ppm/°C
Monitor Output:	Voltage & Current, 0 to +10V ±2.5% accuracy (output impedance 10kΩ typ)
Current limit:	120% of maximum output current
Protection:	Short circuit and arc protected
I/O terminal:	Input JB: Connector Connector housing (MOLEX) 4 PIN 22-01-2045 5 PIN 22-01-2055 CRIMP PIN: 08-50-0032 Input JBE: Connector (mating connector with 30cm leads assorted) Connector is EHR(JST) Output: 50cm cable
Temperature range:	Operating: -10°C to +50°C Storage: -20°C to +70°C
Humidity:	20% to 80%RH (no condensation)

*Specifications are at the maximum rated output after a 1h warm-up period unless otherwise specified.

• DIMENSIONS mm (inch)

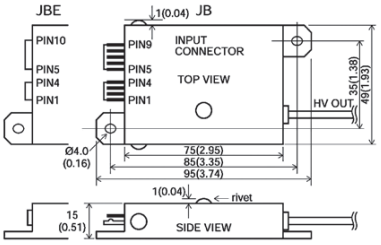

• CONNECTION DIAGRAM

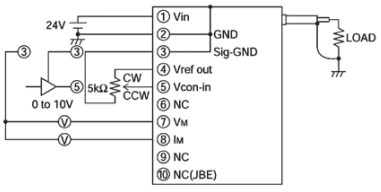

• OPTIONS

-LMH	MHV Output Connector
-LSH	SHV Output Connector
CN4-JB, CN5-JB	Accessory: Input Connector assembled with 25cm flying leads
CN4-JBE, CN5-JBE	Accessory: Input Connector assembled with 30cm flying leads

hivolt.de GmbH & Co. KG
Tarpen 40 • Geb. 2 • D-22419 Hamburg • Germany • ✆ +49 40 537122-0 • 🖷 +49 40 537122-99 • info@hivolt.de • www.hivolt.de

FIGURE A.1: Datasheet of the JB-2N power supply from Hivolt.

Appendix B

Software Used in the VIP-PIX Setup

B.1 FPGA

The FPGA used in this setup is a *Cyclone II* from Altera[1]. The FPGA has been used to handle the read/write process of the VIP-PIX. The conceptual scheme of the processes that the FPGA performs in the VIP-PIX is shown in Fig. B.1.

In the *Global reset* the complete configuration of the chip is set to the default mode, the counters are reset, and the FIFO memory is cleaned.

The *FIFO reset* cleans the FIFO buffer memory of the VIP-PIX. The FIFO memory is used to store the data acquired in the acquisition mode. The FIFO memory has a capacity of 12 words, which is 1 event. This function is used to reject any event already loaded in the memory.

Get chip ID returns the chip ID of the chip. The chip ID consists of 16 bits and contains the information of the *wafer, row and column*. The wafer is the label of the wafer in which the chip has been manufactured. Row and column tell the position of the chip within the wafer. The chip ID has to be manually set for each chip with bump depositions, see Fig. B.2.

[1] Altera®, US.

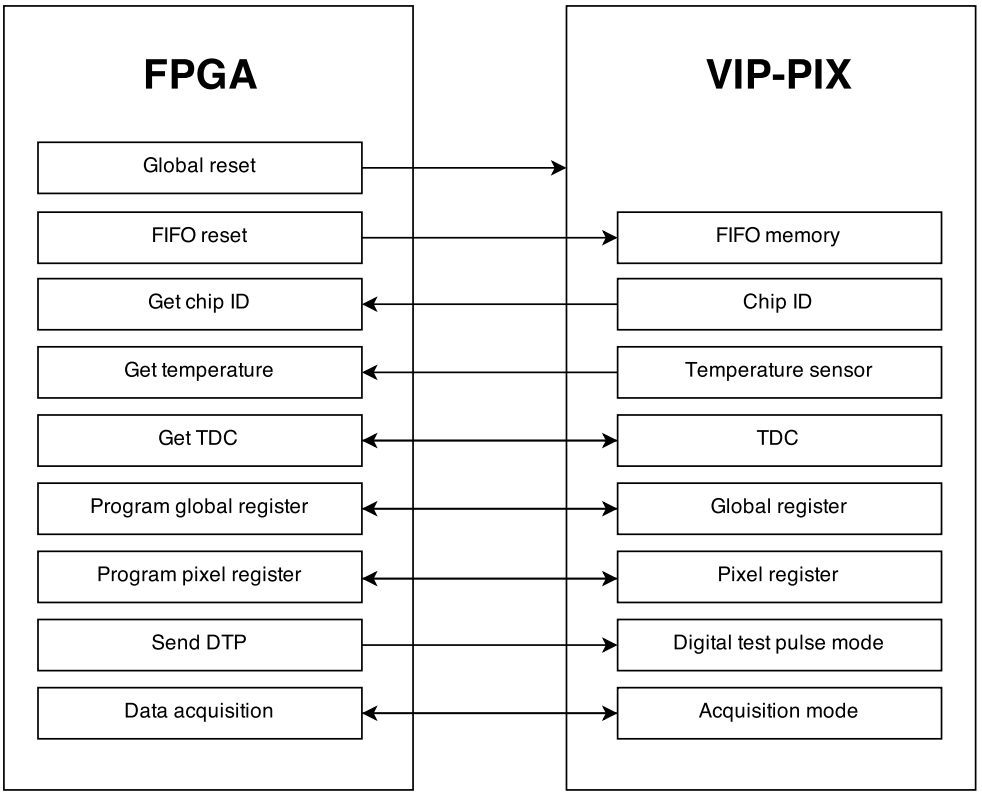

FIGURE B.1: Sketch of the processes carried out by the FPGA. The intermediate stages between the FPGA and the VIP-PIX, the MB and the BB, have been ommited for simplicity.

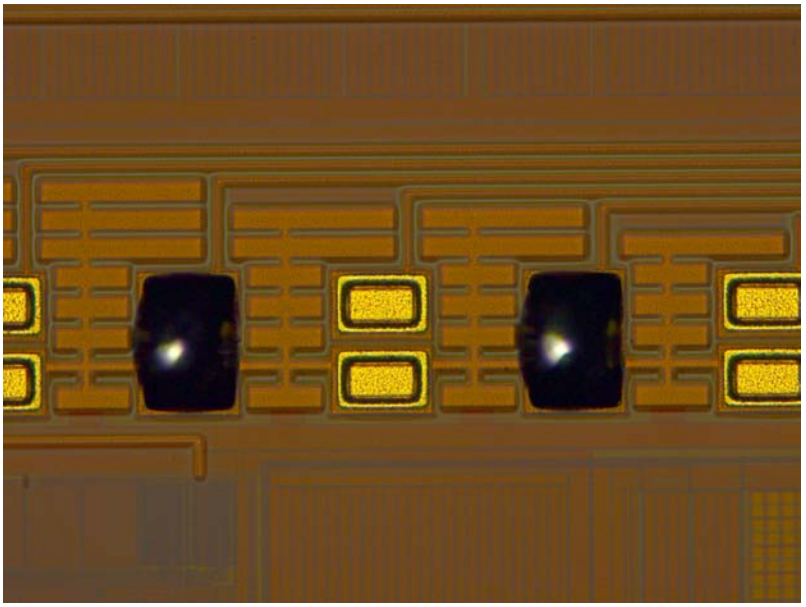

FIGURE B.2: Five of the pads of the chip ID for one VIP-PIX chip with two of the pads connected. If the two pads are not connected then this bit =0, otherwise =1.

Get temperature returns de value provided the temperature sensor in the VIP-PIX. The value obtained is in ADC counts and must be converted to Celsius degrees according to the calibration shown in Sec. 3.2.5.

Get TDC returns the TDC timestamp for a pulse sent with an offset of time with respect to a 10 MHz clock. The offset corresponds to values from 0 ns to 87.5 ns with steps of 12.5 ns. The value obtained has 10 bit precision.

Program global register sets the global register of the VIP-PIX. The process returns the global register that has been loaded into the chip to cross check if the process has been successful.

The *Program pixel register* sets the pixel register of the channels of the VIP-PIX. The process returns the pixel register as in the case of the global register and for the same purpose.

Send DTP requests the VIP-PIX to create an internal test pulse. The internal test pulse mode has to be activated previously with the global and pixel registers. The amplitude of the test pulse has to be previously defined as well.

The *Data acquisition* process sets the VIP-PIX in the data acquisition mode and returns the events acquired by the chip. The settings of the acquisition have to be defined previously in the configuration of the global and pixel registers.

B.2 GUI: VISCA

VISCA, a **V**irtual **I**nstrument **S**ystem for **C**hip **A**nalysis, is a software for data acquisition developed with Labview. VISCA has been designed to characterize the performance of the VIP-PIX and the VIP-Detector.

VISCA handles the FPGA to control the VIP-PIX, power supplies, a pulse generator, a multiple-channel DAC, and a scaler. VISCA is mainly used to acquire data but it can also carry on sweeps of voltages for the chip characterization, sweep of amplitudes for analog test pulses, and leakage current monitoring among a wide list of processes.

This section explains the basic hierarchy of VISCA with the devices in the setup and shows its basic graphic appearance.

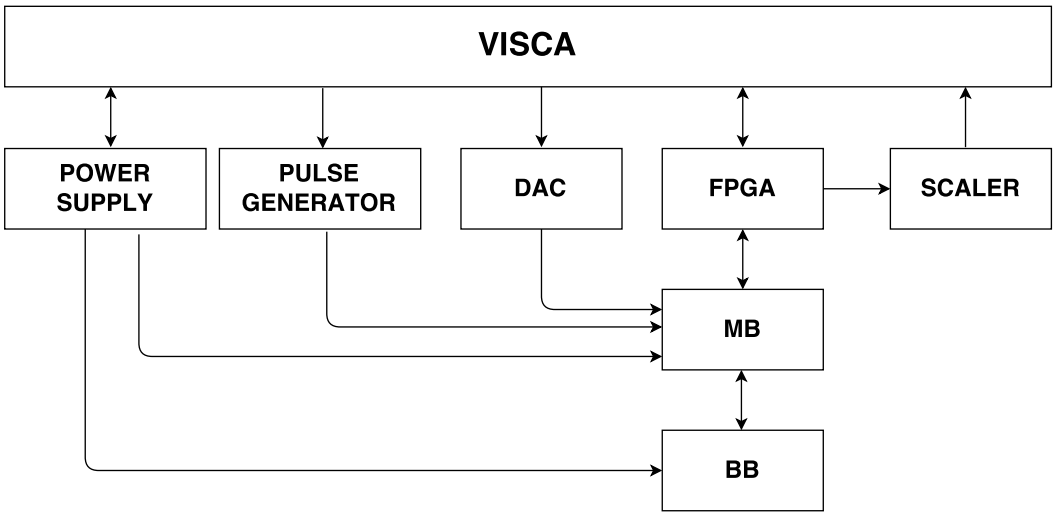

FIGURE B.3: Hierarchy of the devices included in the setup and VISCA.

B.2.1 Software Flow Diagram

Fig. B.3 shows a conceptual scheme of the hierarchy of the VISCA software and the rest of the devices involved in the setup.

VISCA controls two sourcemeter power supplies model 2410 from keithley. One of them is usually employed to bias the CdTe diode and the other to monitor the leakage current going through the guard ring. These devices can be used to provide sweeps of voltage to characterize the voltage references of the chip.

The pulse generator is a waveform generator that can provide pulses with different shape with an adjustable period and amplitude. It is used to provide an external test pulse to the chip and charaterize the response as a function of the total input charge and the frequency of the signal.

The VME DAC offers 16 channel outputs. It is used to provide the voltage references of the chip externally.

The FPGA controls the chip using the processes explained in Sec. B.1. A set of functions defined in a DLL have been developed to control the FPGA and acquire the data.

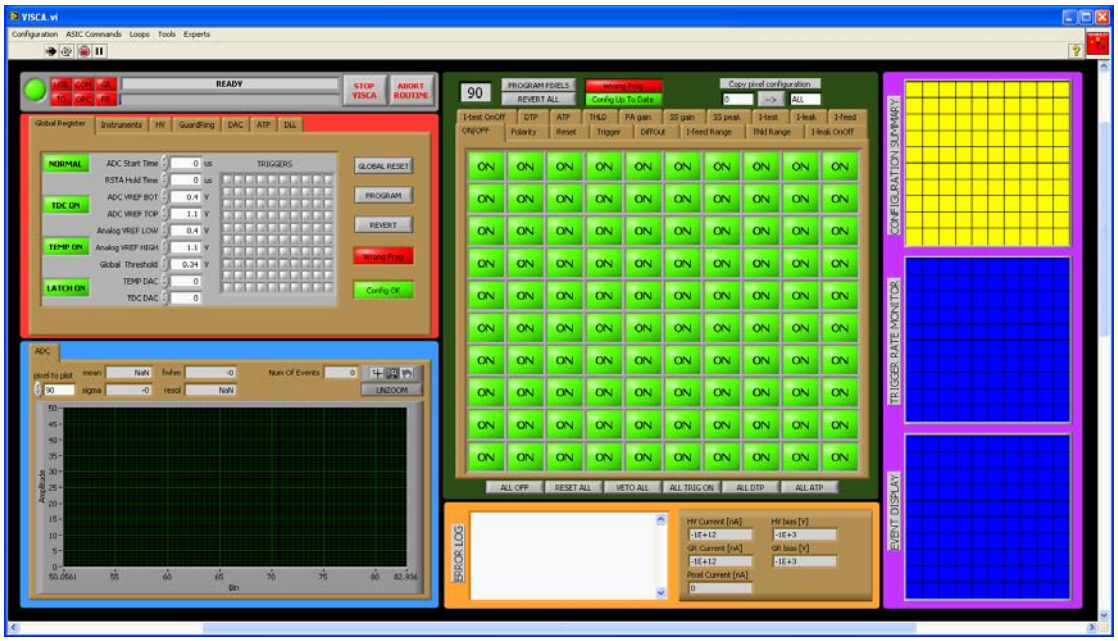

FIGURE B.4: Screenshot of VISCA front panel

The scaler measures the width of the pulses coming from the MB. A measurement of the pulse width with high precision is needed to characterize the stand-alone samples of the VIP-PIX.

A snapshot of the front panel of VISCA is shown in Fig. B.4. It provides easy and complete accessibility to the VIP-PIX chip. It consists of the status monitor section (grey), the global configuration section (red), the data monitor section (blue), the pixel register section (green), the error log and the bias monitor section (yellow) and the pixel monitor section (purple).

The status monitor section contains the main controls to stop VISCA of the background running sub-routine. It also contains a number of indicators to monitor the running status of VISCA, the USB, the FPGA, and of any sub-rountine running in background.

The global configuration section is identified by a red background. It contains a folder with seven tabs. The Global Register tab, providing control over the chip global register configuration. The Intruments tab, for defining and activating the communication with external instrments. The HV tab, providing control over the Keithely 1 instrument, meand to be employed for the HV bias. The Guard Ring tab, providing control over the Keithley 2 instrument, meant to be employed for the guard ring (GR) bias. The DAC tab, providing control for the VME DAC instrument. The ATP tab, providing control

over the BNC wave generator, meant to be used to inject an arbitrary ATP. The DLL tab, with controls and indicators to perform basic inquiries to the chip digital control.

The data monitor section contains a folder with one tab named ADC. The tab contains an histogram, one numberic control, 5 numeric indicators, the UNZOOM button and the Labview standard graph palette.

The pixel register section contains all the controls and indicators to change and program the pixel register configuration. It is divided into two different parts: a pixel register folder occupying most of the section area, and a set of buttons, LED, and numeric displays located either right above of right below the pixel register folder.

The bias monitor and error log section contains two different monitors: the error log monitor on the left side, and the bias monitor on the right side. The Error Log monitor, initially white and empty, displays all the error messages collected during the execution of VISCA and the background rountines. In case of an error, a new message is appended to the log and the background of the log window turns red. By default the window is automatic scrolling down to the last error and turn the window background back to white, the user can right-click on the window itself and choose one of the three items in the pop up menu.

The pixel monitor section contains three 10×10 matrix monitors, from top to bottom: The configuration summary monitor, that shows, for each pixel, a different color corresponding to a specific configuration. The trigger rate, that shows, for each pixel, the current trigger rate, normalized to the number of active pixels. The color is set in order to show a uniform green when all the pixels are collections data at compatible rate. A blueish color indicates a lower than average rate, while colors from yellow to red indicate a higher than average rate. The event display, that randomly shows one events per data taking cycle. For each event, the energy corresponding to the trigger pixel and the eight neighbor pixels is displayed. The color palette is set in order to have a blue for 0 ADC counts, and a red color for 1024 ADC counts.

Bibliography

[1] James E. Turner. *Atoms, Radiation, and Radiation Protection*. Wiley-VCH, third edition, 2009.

[2] Nist xcom: Photon cross sections database. URL http://www.nist.gov/pml/data/xcom/.

[3] Glenn F. Knoll. *Radiation Detection and Measurement*. Wiley, third edition, 2000.

[4] Roger Lecomte. Novel detector technology for clinical PET. *European Journal of Nuclear Medicine and Molecular Imaging*, 36(1):69–85, 2009. ISSN 1619-7070.

[5] Virginia Ch. Spanoudaki and Craig S. Levin. Photo-detectors for time of flight positron emission tomography (ToF-PET). *Sensors*, 10(11):10484–10505, 2010.

[6] I.F. Castro, A.J. Soares, and J.F. Veloso. Impact of dark counts in low-light level silicon photomultiplier multi-readout applications. In *Nuclear Science Symposium Conference Record (NSS/MIC), 2009 IEEE*, pages 1592–1596, Oct 2009.

[7] S. Gundacker, E. Auffray, B. Frisch, H. Hillemanns, P. Jarron, T. Meyer, K. Pauwels, and P. Lecoq. A systematic study to optimize sipm photo-detectors for highest time resolution in PET. *Nuclear Science, IEEE Transactions on*, 59 (5):1798–1804, Oct 2012.

[8] M. Grodzicka, M. Moszynski, T. Szczesniak, M. Kapusta, M. Szawlowski, and D. Wolski. Energy resolution of scintillation detectors with sipm light readout. In *Nuclear Science Symposium Conference Record (NSS/MIC), 2010 IEEE*, pages 1940–1948, Oct 2010.

[9] Gopal B. Saha. *Basics of PET Imaging. Physics, chemistry, and regulations*. Springer Science Business Media, Inc. New York, 2005.

[10] Valk P E, Delbeke D, Bailey D L, Townsend D W, and Maisey M N (Eds). *Positron Emission Tomography. Clinical practice*. Lexington KY 2011, 2010.

[11] K. Shiling. The role of positron emission mammography in breast cancer imaging and management. *Applied Radiology*, pages 26–36, 2008.

[12] Weidong Luo, E. Anashkin, and C.G. Matthews. Performance evaluation of a PEM scanner using the nema nu 4-2008 small animal PET standards. *Nuclear Science, IEEE Transactions on*, 57(1):94–103, Feb 2010.

[13] Yónatan Calderón, dir. Chmeissani, Mokhtar, dir. Kolstein, Machiel, and Pilar Casado. Design, development, and modeling of a compton camera tomographer based on room temperature solid state pixel detector. *PhD Thesis, Universitat Autònoma de Barcelona. Departament de Física*, 2014.

[14] Ca nadas Castro M. Aspectos metodológicos para la evaluación de sistemas de tomografía por emisión de positrones empleando técnicas montecarlo, protocolos estandarizados y diferentes trazadores. *Ph. D. thesis, Universidad Politécnica de Madrid*, 2012.

[15] J.A. Sorenson S.R. Cherry and M.E. Phelps. *Physics in nuclear medicine*. Saunders, third edition, Philadelphia U.S.A. 2003.

[16] Ekaterina Mikhaylova, dir. Chmeissani, Mokhtar, dir. De Lorenzo, Gianluca, and Enrique Fernández. Voxel imaging pet pathfinder: A novel approach to positron emission tomography based on room temperature pixelated solid state detectors. *PhD Thesis, Universitat Autònoma de Barcelona. Departament de Física*, 2014.

[17] J.-G. Macias-Montero, M. Sarraj, M. Chmeissani, C. Puigdengoles, G. De Lorenzo, and R. Martinez. Toward VIP-PIX: A low noise readout ASIC for pixelated cdte gamma-ray detectors for use in the next generation of PET scanners. *Nuclear Science, IEEE Transactions on*, 60(4):2898–2904, Aug 2013.

[18] J.-G. Macias-Montero, M. Sarraj, M. Chmeissani, G. De Lorenzo, C. Puigdengoles, and R. Martinez. A 2d 4x4 channel readout asic for pixelated cdte detectors for medical imaging applications. In *Nuclear Science Symposium and Medical Imaging Conference (NSS/MIC), 2013 IEEE*, pages 1–7, Oct 2013.

[19] E. Mikhaylova, G. De Lorenzo, M. Chmeissani, M. Kolstein, M. Canadas, P. Arce, Y. Calderon, D. Uzun, G. Arino, J.G. Macias-Montero, R. Martinez, C. Puigdengoles, and E. Cabruja. Simulation of the expected performance of a seamless scanner for brain PET based on highly pixelated CdTe detectors. *Medical Imaging, IEEE Transactions on*, 33(2):332–339, Feb 2014.

[20] D Uzun, G De Lorenzo, M Kolstein, and M Chmeissani. Simulation and evaluation of a high resolution VIP PEM system with a dedicated lm-osem algorithm. *Journal of Instrumentation*, 9(05):C05011, 2014.

[21] G De Lorenzo, M Chmeissani, D Uzun, M Kolstein, I Ozsahin, E Mikhaylova, P Arce, M Ca nadas, G Ari no, and Y. Calderón. Pixelated CdTe detectors to overcome intrinsic limitations of crystal based positron emission mammographs. *Journal of Instrumentation*, 8(01):C01030, 2013.

[22] "NEMA Standards Publication NU 4-2008". Performance measurements for small animal positron emission tomographs (PETs). *National Electrical Manufacturers Association*, 2008.

[23] Y. Calderon, M. Kolstein, D. Uzun, G. De Lorenzo, M. Chmeissani, P. Arce, G. Arino, E. Cabruja, M. Canadas, J.G. Macias-Montero, R. Martinez, E. Mikhaylova, I. Ozsahin, and C. Puigdengoles. Modeling, simulation, and evaluation of a compton camera based on a pixelated solid-state detector. In *Nuclear Science Symposium and Medical Imaging Conference (NSS/MIC), 2011 IEEE*, pages 2708–2715, Oct 2011. doi: 10.1109/NSSMIC.2011.6152954.

[24] Charles L. Melcher. Scintillation crystals for PET. *Journal of Nuclear Medicine*, 41(6):1051–1055, 2000.

[25] R.A. Yotter and D.M. Wilson. A review of photodetectors for sensing light-emitting reporters in biological systems. *Sensors Journal, IEEE*, 3(3):288–303, June 2003.

[26] A. Osovizky, Udi Wengrowicz, M. Ghelman, Ilan Cohenzada, V. Pushkarsky, D. Ginzburg, Yehuda Gabay, Asaf Algom, R. Seif, A. Manor, Arie Beck, Eli Vulaski, Michael Ellenbogen, and Danny Tirosh. Scintillation light readout using silicon photomultiplier - review and experimental results. In *Nuclear Science Symposium Conference Record, 2008. NSS '08. IEEE*, pages 2482–2483, Oct 2008.

[27] H. Kume. *Photomultiplier Tube: Principle to Application.* Toyooka, Japan: Hamamatsu Photonics, K. K., 1994.

[28] C.M. Pepin, P. Berard, A.-L. Perrot, C. Pepin, D. Houde, R. Lecomte, C.L. Melcher, and H. Dautet. Properties of LYSO and recent LSO scintillators for phoswich PET detectors. *Nuclear Science, IEEE Transactions on*, 51(3):789–795, June 2004.

[29] J. Fink, H. Krüger, P. Lodomez, and N. Wermes. Characterization of charge collection in CdTe and CZT using the transient current technique. *Nuclear Instruments and Methods in Physics Research Section A: Accelerators, Spectrometers, Detectors and Associated Equipment*, 560(2):435 – 443, 2006.

[30] R. Devanathan, L.R. Corrales, F. Gao, and W.J. Weber. Signal variance in gamma-ray detectors—a review. *Nuclear Instruments and Methods in Physics Research Section A: Accelerators, Spectrometers, Detectors and Associated Equipment*, 565 (2):637 – 649, 2006.

[31] Egesta Lopci, Cristina Nanni, Paolo Castellucci, Gian Carlo Montini, Vincenzo Allegri, Domenico Rubello, Franca Chierichetti, Valentina Ambrosini, and Stefano Fanti. Imaging with non-FDG PET tracers: outlook for current clinical applications. *Insights Into Imaging*, 1:373–385, 2010.

[32] Biersack HJ Ruhlmann J, Oehr P. *PET in oncology: Basics and clinical application.* New York, NY:Springer, 1999.

[33] Yusuf E. Erdi, Homer Macapinlac, Kenneth E. Rosenzweig, John L. Humm, Steven M. Larson, Alev K. Erdi, and Ellen D. Yorke. Use of PET to monitor the response of lung cancer to radiation treatment. *European Journal of Nuclear Medicine*, 27(7):861–866, 2000. ISSN 0340-6997.

[34] H. Shinotoh and D.B. Calne. The use of pet in parkinsons-disease. *Brain and Cognition*, 28(3):297 – 310, 1995.

[35] Suleman Surti, Austin Kuhn, Matthew E. Werner, Amy E. Perkins, Jeffrey Kolthammer, and Joel S. Karp. Performance of philips gemini TF PET/CT scanner with special consideration for its time-of-flight imaging capabilities. *Journal of Nuclear Medicine*, 48(3):471–480, 2007.

[36] B W Jakoby, Y Bercier, M Conti, M E Casey, B Bendriem, and D W Townsend. Physical and clinical performance of the mCT time-of-flight PET/CT scanner. *Physics in Medicine and Biology*, 56(8):2375, 2011.

[37] M. Teräs, T. Tolvanen, J.J. Johansson, J.J. Williams, and J. Knuuti. Performance of the new generation of whole-body PET/CT scanners: Discovery STE and discovery VCT. *European Journal of Nuclear Medicine and Molecular Imaging*, 34 (10):1683–1692, 2007. ISSN 1619-7070.

[38] E.P. Delfino, S. Majewski, R.R. Raylman, and A. Stolin. Towards 1mm PET resolution using DOI modules based on dual-sided sipm readout. In *Nuclear Science Symposium Conference Record (NSS/MIC), 2010 IEEE*, pages 3442–3449, Oct 2010.

[39] Y. Morimoto, Y. Ueno, W. Takeuchi, S. Kojima, K. Matsuzaki, T. Ishitsu, K. Umegaki, Y. Kiyanagi, N. Kubo, C. Katoh, T. Shiga, H. Shirato, and N. Tamaki. Development of a 3D brain PET scanner using CdTe semiconductor detectors and its first clinical application. *Nuclear Science, IEEE Transactions on*, 58(5):2181–2189, Oct 2011.

[40] P. Vaska, A. Dragone, W. Lee, D.-H. Kim, J.-F. Pratte, Y.-G. Cui, J. Fried, S. Krishnamoorthy, A. Bolotnikov, S.-J. Park, P. O'Connor, F.A. Dilmanian, and R.B. James. A prototype czt-based pet scanner for high resolution mouse brain imaging. In *Nuclear Science Symposium Conference Record, 2007. NSS '07. IEEE*, volume 5, pages 3816–3819, Oct 2007.

[41] M. Chmeissani, P. Arce, and M. Canadas. Modeling and simulation of PET scanner based on pixelated solid-state detector. In *Nuclear Science Symposium Conference Record (NSS/MIC), 2009 IEEE*, pages 3496–3502, Oct 2009.

[42] A. Lempicki, A.J. Wojtowicz, and E. Berman. Fundamental limits of scintillator performance. *Nuclear Instruments and Methods in Physics Research Section A: Accelerators, Spectrometers, Detectors and Associated Equipment*, 333(2–3):304 – 311, 1993.

[43] P.F. Bloser, J.S. Legere, C.M. Bancroft, M.L. McConnell, and J.M. Ryan. Silicon photo-multiplier readouts for scintillators in high-energy astronomy. In *Nuclear*

Science Symposium Conference Record, 2008. NSS '08. IEEE, pages 727–731, Oct 2008.

[44] M. Gierlik, J. Iwanowska, T. Kozlowski, M. Moszynski, L. Swiderski, and T. Szczesniak. Investigation of the properties of 3"× 3" different scintillation detectors for neutron activation analysis techniques. *Nuclear Science, IEEE Transactions on*, 59(1):230–235, Feb 2012.

[45] T. Szczesniak, M. Moszynski, Lukasz Swiderski, A. Nassalski, P. Lavoute, and M. Kapusta. Fast photomultipliers for TOF PET. *Nuclear Science, IEEE Transactions on*, 56(1):173–181, Feb 2009.

[46] T. Szczesniak, M. Moszynski, A. Syntfeld-Kazuch, L. Swiderski, M.A.S. Koschan, and C.L. Melcher. Timing resolution and decay time of LSO crystals Co-doped with calcium. *Nuclear Science, IEEE Transactions on*, 57(3):1329–1334, June 2010.

[47] Dennis R Schaart, Stefan Seifert, Ruud Vinke, Herman T van Dam, Peter Dendooven, Herbert Löhner, and Freek J Beekman. LaBr 3 :ce and sipms for time-of-flight PET: achieving 100 ps coincidence resolving time. *Physics in Medicine and Biology*, 55(7):N179, 2010.

[48] M. Moszynski, M. Kapusta, A. Nassalski, T. Szczesniak, D. Wolski, L. Eriksson, and C.L. Melcher. New prospects for time-of-flight PET with LSO scintillators. *Nuclear Science, IEEE Transactions on*, 53(5):2484–2488, Oct 2006.

[49] A. Karar, Y. Musienko, and J.Ch. Vanel. Characterization of avalanche photodiodes for calorimetry applications. *Nuclear Instruments and Methods in Physics Research Section A: Accelerators, Spectrometers, Detectors and Associated Equipment*, 428(2–3):413 – 431, 1999. ISSN 0168-9002.

[50] L M P Fernandes, F D Amaro, A Antognini, J M R Cardoso, C A N Conde, O Huot, P E Knowles, F Kottmann, J A M Lopes, L Ludhova, C M B Monteiro, F Mulhauser, R Pohl, J M F dos Santos, L A Schaller, D Taqqu, and J F C A Veloso. Characterization of large area avalanche photodiodes in x-ray and vuv-light detection. *Journal of Instrumentation*, 2(08):P08005, 2007.

[51] Katsuhiko Nishida. Avalanche-noise dependence on avalanche-photodiode structures. *Electronics Letters*, 13(14):419–421, July 1977.

[52] M.C. Brain. Absolute noise characterisation of avalanche photodiodes. *Electronics Letters*, 14(15):485–487, July 1978. ISSN 0013-5194.

[53] F. Zappa, A. Gulinatti, P. Maccagnani, S. Tisa, and S. Cova. Spada: single-photon avalanche diode arrays. *Photonics Technology Letters, IEEE*, 17(3):657–659, March 2005.

[54] A. Lacaita, M. Ghioni, and S. Cova. Double epitaxy improves single-photon avalanche diode performance. *Electronics Letters*, 25(13):841–843, June 1989.

[55] Alexis Rochas, Gregoire Ribordy, B. Furrer, P. A. Besse, and R. S. Popovic. First passively-quenched single photon counting avalanche photodiode element integrated in a conventional cmos process with 32ns dead time. In *Proc. SPIE*, volume 4833, pages 107–115, 2003.

[56] Karl Hecht. Zum mechanismus des lichtelektrischen primärstromes in isolierenden kristallen. *Zeitschrift für Physik*, 77(3-4):235–245, 1932. ISSN 0044-3328.

[57] W. Akutagawa and K. Zanio. Gamma response of Semi-insulating material in the presence of trapping and detrapping. *Journal of Applied Physics*, 40(9):3838–3854, 1969.

[58] G.F. Knoll and D.S. Mcgregor. Fundamentals of semiconductor detectors for ionizing radiation. In *Symposium F – Semiconductors for Room-Temperature Radiation Detector Applications*, volume 302 of *MRS Proceedings*, 1 1993.

[59] T. Takahashi, T. Mitani, Y. Kobayashi, M. Kouda, G. Sato, S. Watanabe, K. Nakazawa, Y. Okada, M. Funaki, R. Ohno, and K. Mori. High-resolution schottky cdte diode detector. *Nuclear Science, IEEE Transactions on*, 49(3):1297–1303, Jun 2002.

[60] W. Shockley. Currents to conductors induced by a moving point charge. *Journal of Applied Physics*, 9(10):635–636, 1938.

[61] Simon Ramo. Currents induced by electron motion. *Proceedings of the IRE*, 27 (9):584–585, Sept 1939.

[62] U. Lachish. Driving spectral resolution to the noise limit in semiconductor gamma detector arrays. *Nuclear Science, IEEE Transactions on*, 48(3):520–523, Jun 2001.

[63] P. Maj, A. Baumbaugh, G. Deptuch, P. Grybos, and R. Szczygiel. Minimization of charge sharing effect in silicon hybrid pixel x-ray detectors based on pattern recognition algorithm. In *Industrial Technology (ICIT), 2012 IEEE International Conference on*, pages 551–556, March 2012.

[64] S. Pagliarini, F. Kastensmidt, L. Entrena, A. Lindoso, and E. San Millan. Analyzing the impact of single-event-induced charge sharing in complex circuits. *Nuclear Science, IEEE Transactions on*, 58(6):2768–2775, Dec 2011. ISSN 0018-9499. doi: 10.1109/TNS.2011.2168239.

[65] Mikiko Ito, Jae Sung Lee, Sun Il Kwon, Geon Song Lee, Byungsik Hong, Kyong Sei Lee, Kwang-Souk Sim, Seok Jae Lee, June Tak Rhee, and Seong Jong Hong. A four-layer DOI detector with a relative offset for use in an animal PET system. *Nuclear Science, IEEE Transactions on*, 57(3):976–981, June 2010.

[66] Fumihiko Nishikido, Naoko Inadama, Ichiro Oda, Kengo Shibuya, Eiji Yoshida, Taiga Yamaya, Keishi Kitamura, and Hideo Murayama. Four-layer depth-of-interaction PET detector for high resolution PET using a multi-pixel S8550 avalanche photodiode. *Nuclear Instruments and Methods in Physics Research Section A: Accelerators, Spectrometers, Detectors and Associated Equipment*, 621 (1–3):570 – 575, 2010. ISSN 0168-9002.

[67] R.S. Miyaoka, Xiaoli Li, C. Lockhart, and T.K. Lewellen. Comparison of detector intrinsic spatial resolution characteristics for sensor on the entrance surface and conventional readout designs. *Nuclear Science, IEEE Transactions on*, 57(3):990–997, June 2010.

[68] Marnix C Maas, Dennis R Schaart, D J (Jan) van der Laan, Peter Bruyndonckx, Cedric Lemaître, Freek J Beekman, and Carel W E van Eijk. Monolithic scintillator PET detectors with intrinsic depth-of-interaction correction. *Physics in Medicine and Biology*, 54(7):1893, 2009.

[69] A Vandenbroucke, A M K Foudray, P D Olcott, and C S Levin. Performance characterization of a new high resolution PET scintillation detector. *Physics in Medicine and Biology*, 55(19):5895, 2010.

[70] W.W. Moses and S.E. Derenzo. Design studies for a PET detector module using a pin photodiode to measure depth of interaction. *Nuclear Science, IEEE Transactions on*, 41(4):1441–1445, Aug 1994.

[71] Yiping Shao, Hongrui Li, and Kanke Gao. Initial experimental studies of using solid-state photomultiplier for PET applications. *Nuclear Instruments and Methods in Physics Research Section A: Accelerators, Spectrometers, Detectors and Associated Equipment*, 580(2):944 – 950, 2007. Imaging 2006 Proceedings of the 3rd International Conference on Imaging Techniques in Subatomic Physics, Astrophysics, Medicine, Biology and Industry.

[72] Yongfeng Yang, Purushottam A Dokhale, Robert W Silverman, Kanai S Shah, Mickel A McClish, Richard Farrell, Gerald Entine, and Simon R Cherry. Depth of interaction resolution measurements for a high resolution PET detector using position sensitive avalanche photodiodes. *Physics in Medicine and Biology*, 51(9): 2131, 2006.

[73] G.S. Mitchell, S. Sinha, J.R. Stickel, Spencer L. Bowen, L.J. Cirignano, P. Dokhale, Hadong Kim, K.S. Shah, and S.R. Cherry. Cdte strip detector characterization for high resolution small animal PET. *Nuclear Science, IEEE Transactions on*, 55 (3):870–876, June 2008.

[74] Paul Vaska, Do Hyun Kim, Sudeepti Southekal, Jean-Francois Pratte, Jack Fried, Srilalan Krishnamoorthy, Sean Stoll, and Aleksey Bolotnikov. Ultra-high resolution PET: A CZT-based scanner for the mouse brain. *J. Nucl. Med.*, 50(2 MeetingAbstracts):293, 2009.

[75] Y Gu, J L Matteson, R T Skelton, A C Deal, E A Stephan, F Duttweiler, T M Gasaway, and C S Levin. Study of a high-resolution, 3D positioning cadmium zinc telluride detector for PET. *Physics in Medicine and Biology*, 56(6):1563, 2011.

[76] Wai-Hoi Wong, J. Uribe, K. Hicks, and Guoji Hu. An analog decoding BGO block detector using circular photomultipliers. *Nuclear Science, IEEE Transactions on*, 42(4):1095–1101, Aug 1995. ISSN 0018-9499.

[77] R. Lecomte, J. Cadorette, P. Richard, S. Rodrigue, and D. Rouleau. Design and engineering aspects of a high resolution positron tomograph for small animal

imaging. *Nuclear Science, IEEE Transactions on*, 41(4):1446–1452, Aug 1994. ISSN 0018-9499.

[78] SibylleI. Ziegler, BerndJ. Pichler, Guido Boening, Magdalena Rafecas, Wendelin Pimpl, Eckart Lorenz, Norbert Schmitz, and Markus Schwaiger. A prototype high-resolution animal positron tomograph with avalanche photodiode arrays and lso crystals. *European Journal of Nuclear Medicine*, 28(2):136–143, 2001. ISSN 0340-6997.

[79] Martin S Judenhofer, Hans F Wehrl, Danny F Newport, Ciprian Catana, Stefan B Siegel, Markus Becker, Axel Thielscher, Manfred Kneilling, Matthias P Lichy, Martin Eichner, Karin Klingel, Gerald Reischl, Stefan Widmaier, Martin Rocken, Robert E Nutt, Hans-Jurgen Machulla, Kamil Uludag, Simon R Cherry, Claus D Claussen, and Bernd J Pichler. Simultaneous PET-MRI: a new approach for functional and morphological imaging. *Nat Med*, 14:459–465, 2008.

[80] A. N. Otte, J. Barral, B. Dolgoshein, J. Hose, S. Klemin, E. Lorenz, R. Mirzoyan, E. Popova, and M. Teshima. A test of silicon photomultipliers as readout for PET. *Nuclear Instruments and Methods in Physics Research A*, 545:705–715, June 2005. doi: 10.1016/j.nima.2005.02.014.

[81] Samuel Espana, Gustavo Tapias, Luis M. Fraile, Joaquin L. Herraiz, E. Vicente, Jose Udias, M. Desco, and Juan J. Vaquero. Performance evaluation of SiPM detectors for PET imaging in the presence of magnetic fields. In *Nuclear Science Symposium Conference Record, 2008. NSS '08. IEEE*, pages 3591–3595, Oct 2008.

[82] P H Jarritt, K J Carson, A R Hounsell, and D Visvikis. The role of PET/CT scanning in radiotherapy planning. *The British Journal of Radiology*, 79 (special_issue_1):S27–S35, 2006.

[83] Vincent Grégoire, Karin Haustermans, Xavier Geets, Sarah Roels, and Max Lonneux. PET-based treatment planning in radiotherapy: A new standard? *Journal of Nuclear Medicine*, 48(1 suppl):68S–77S, 2007.

[84] Søren M. Bentzen. Radiation therapy: Intensity modulated, image guided, biologically optimized and evidence based. *Radiotherapy and Oncology*, 77(3):227 – 230, 2005. ISSN 0167-8140.

[85] Habib Zaidi, Hansjörg Vees, and Michael Wissmeyer. Molecular PET/CT imaging-guided radiation therapy treatment planning. *Academic Radiology*, 16(9):1108 – 1133, 2009. ISSN 1076-6332.

[86] Eric C. Ford, Joseph Herman, Ellen Yorke, and Richard L. Wahl. 18F-FDG PET/CT for image-guided and intensity-modulated radiotherapy. *Journal of Nuclear Medicine*, 50(10):1655–1665, 2009.

[87] Leiderman DB, Albert P, Balish M, Bromfield E, and Theodore WH. The dynamics of metabolic change following seizures as measured by positron emission tomography with fludeoxyglucose F18. *Archives of Neurology*, 51(9):932–936, 1994.

[88] Paola A. Erba, Martina Sollini, Elena Lazzeri, and Giuliano Mariani. Fdg-pet in cardiac infections. *Seminars in Nuclear Medicine*, 43(5):377 – 395, 2013. Non-Oncology PET (Part I).

[89] Olga G. James, Jared D. Christensen, Terence Z. Wong, Salvador Borges-Neto, and Lynne M. Koweek. Utility of FDG PET/CT in inflammatory cardiovascular disease. *RadioGraphics*, 31(5):1271–1286, 2011.

[90] Thomas H Marwick MD, PhD, Kesavan Shan MD, Sanjiv Patel MD, Raymundo T Go MD, and Michael S Lauer MD. Incremental value of rubidium-82 positron emission tomography for prognostic assessment of known or suspected coronary artery disease. *The American Journal of Cardiology*, 80(7):865 – 870, 1997.

[91] U. Amaldi and B. Larsson (Eds). *Hadrontherapy in oncology.* Elsevier Science, 1994. ISBN 0-444-81918-5.

[92] Ugo Amaldi and Gerhard Kraft. Hadrontherapy: Cancer treatment with proton and carbon beams. In Yves Lemoigne and Alessandra Caner, editors, *Radiotherapy and Brachytherapy*, NATO Science for Peace and Security Series B: Physics and Biophysics, pages 165–171. Springer Netherlands, 2009. ISBN 978-90-481-3095-5.

[93] Zhu X and Fakhri GE. Proton therapy verification with PET imaging. *Theranostics*, 3:731–40, 2013.

[94] F. Diblen, H. Rohling, I. Torres-Espallardo, P. Solevi, J. Gillam, D. Watts, S. Espana, S. Vandenberghe, F. Fiedler, and M. Rafecas. Comparison study of RPC

and crystal based PET systems for hadron therapy monitoring. In *Nuclear Science Symposium and Medical Imaging Conference (NSS/MIC), 2012 IEEE*, pages 2212–2217, Oct 2012.

[95] J. Cabello, I. Torres-Espallardo, J.E. Gillam, and M. Rafecas. PET reconstruction from truncated projections using total-variation regularization for hadron therapy monitoring. *Nuclear Science, IEEE Transactions on*, 60(5):3364–3372, Oct 2013.

[96] Maurizio Conti. Focus on time-of-flight PET: the benefits of improved time resolution. *European Journal of Nuclear Medicine and Molecular Imaging*, 38(6): 1147–1157, 2011. ISSN 1619-7070.

[97] Nizar A. Mullani, David C. Ficke, Ross Hartz, Joanne Markham, and Gary Wong. System design of fast pet scanners utilizing time-of-flight. *Nuclear Science, IEEE Transactions on*, 28(1):104–108, Feb 1981.

[98] R. Allemand, C. Gresset, and J. Vacher. Potential advantages of a cesium fluoride scintillator for a time-of-flight positron camera. *Journal of Nuclear Medicine*, 21 (2):153–155, 1980.

[99] M. Moszynski, M. Kapusta, A. Nassalski, T. Szczesniak, D. Wolski, L. Eriksson, and C.L. Melcher. New prospects for time-of-flight PET with LSO scintillators. *Nuclear Science, IEEE Transactions on*, 53(5):2484–2488, Oct 2006.

[100] Maurizio Conti, Bernard Bendriem, Mike Casey, Mu Chen, Frank Kehren, Christian Michel, and Vladimir Panin. First experimental results of time-of-flight reconstruction on an LSO PET scanner. *Physics in Medicine and Biology*, 50(19): 4507, 2005.

[101] Einat Even-Sapir, Zohar Keidar, and Rachel Bar-Shalom. Hybrid imaging (SPECT/CT and PET/CT)—improving the diagnostic accuracy of functional/metabolic and anatomic imaging. *Seminars in Nuclear Medicine*, 39(4):264 – 275, 2009. Hybrid Imaging Anniversary Issue (Part I).

[102] Dominique Delbeke, Heiko Schöder, William H. Martin, and Richard L. Wahl. Hybrid imaging (SPECT/CT and PET/CT): Improving therapeutic decisions. *Seminars in Nuclear Medicine*, 39(5):308 – 340, 2009. Hybrid Imaging Anniversary Issue (Part II).

[103] D W Townsend and T Beyer. A combined PET/CT scanner: the path to true image fusion. *The British Journal of Radiology*, 75(suppl_9):S24–S30, 2002.

[104] Wolf-Dieter Heiss. The potential of PET/MR for brain imaging. *European Journal of Nuclear Medicine and Molecular Imaging*, 36(1):105–112, 2009.

[105] Gerald Antoch and Andreas Bockisch. Combined PET/MRI: a new dimension in whole-body oncology imaging? *European Journal of Nuclear Medicine and Molecular Imaging*, 36(1):113–120, 2009.

[106] StephanG. Nekolla, Axel Martinez-Moeller, and Antti Saraste. PET and MRI in cardiac imaging: from validation studies to integrated applications. *European Journal of Nuclear Medicine and Molecular Imaging*, 36(1):121–130, 2009.

[107] Yiping Shao, Simon R Cherry, Keyvan Farahani, Ken Meadors, Stefan Siegel, Robert W Silverman, and Paul K Marsden. Simultaneous PET and MR imaging. *Physics in Medicine and Biology*, 42(10):1965, 1997.

[108] Keyvan Farahani, Randal Slates, Yiping Shao, Robert Silverman, and Simon Cherry. Contemporaneous positron emission tomography and MR imaging at 1.5 t. *Journal of Magnetic Resonance Imaging*, 9(3):497–500, 1999. ISSN 1522-2586.

[109] P K Marsden, D Strul, S F Keevil, S C R Williams, and D Cash. Simultaneous PET and NMR. *The British Journal of Radiology*, 75(suppl_9):S53–S59, 2002.

[110] Bernd Pichler, Hans F Wehrl, Armin Kolb, and Martin S Judenhofer. PET/MRI: The next generation of multi-modality imaging? *Seminars in nuclear medicine*, 38:199–208, 2009.

[111] Tohru Shiga, Yuichi Morimoto, Naoki Kubo, Norio Katoh, Chietsugu Katoh, Wataru Takeuchi, Reiko Usui, Kenji Hirata, Shinichi Kojima, Kikuo Umegaki, Hiroki Shirato, and Nagara Tamaki. A new PET scanner with semiconductor detectors enables better identification of intratumoral inhomogeneity. *Journal of Nuclear Medicine*, 50(1):148–155, 2009.

[112] C.J. Thompson, K. Murthy, Y. Picard, I.N. Weinberg, and R. Mako. Positron emission mammography (PEM): a promising technique for detecting breast cancer. In *Nuclear Science Symposium and Medical Imaging Conference, 1994., 1994 IEEE Conference Record*, volume 4, pages 1893–1897 vol.4, Oct 1994.

[113] A. Del Guerra, N. Belcari, W. Bencivelli, A. Motta, S. Righi, A. Vaiano, G. Di Domenico, E. Moretti, N. Sabba, G. Zavattini, R. Campanini, N. Lanconelli, A. Riccardi, M.N. Cinti, R. Pani, and R. Pellegrini. Monte carlo study and experimental measurements of breast tumor detectability with the YAP-PEM prototype. In *Nuclear Science Symposium Conference Record, 2002 IEEE*, volume 3, pages 1887–1891 vol.3, Nov 2002.

[114] Lawrence MacDonald, John Edwards, Thomas Lewellen, David Haseley, James Rogers, and Paul Kinahan. Clinical imaging characteristics of the positron emission mammography camera: PEM flex solo II. *Journal of Nuclear Medicine*, 50 (10):1666–1675, 2009.

[115] Mami Iima, Yuji Nakamoto, Shotaro Kanao, Tomoharu Sugie, Takayuki Ueno, Mayumi Kawada, Yoshiki Mikami, Masakazu Toi, and Kaori Togashi. Clinical performance of 2 dedicated PET scanners for breast imaging: Initial evaluation. *Journal of Nuclear Medicine*, 53(10):1534–1542, 2012.

[116] Y. Yamada, K. Kitamura, Nobuya Hashizume, Y. Yamakawa, and Y. Kumazawa. Reconstruction of 4-layer DOI detector equipped c-shaped PEM via list-mode iterative algorithm. In *Nuclear Science Symposium Conference Record, 2007. NSS '07. IEEE*, volume 6, pages 4397–4400, Oct 2007.

[117] L. Moliner, A. J. González, A. Soriano, F. Sánchez, C. Correcher, A. Orero, M. Carles, L. F. Vidal, J. Barberá, L. Caballero, M. Seimetz, C. Vázquez, and J. M. Benlloch. Design and evaluation of the mammi dedicated breast PET. *Medical Physics*, 39(9):5393–5404, 2012.

[118] R. Freifelder, C. Cardi, I. Grigoras, J.R. Saffer, and J.S. Karp. First results of a dedicated breast PET imager, BPET, using NaI(Tl) curve plate detectors. In *Nuclear Science Symposium Conference Record, 2001 IEEE*, volume 3, pages 1241–1245 vol.3, Nov 2001.

[119] N.K. Doshi, R.W. Silverman, Y. Shao, and S.R. Cherry. maxPET, a dedicated mammary and axillary region PET imaging system for breast cancer. *Nuclear Science, IEEE Transactions on*, 48(3):811–815, Jun 2001.

[120] G-C Wang, J.S. Huber, W.W. Moses, J. Qi, and W.-S. Choong. Characterization of the LBNL PEM camera. *Nuclear Science, IEEE Transactions on*, 53(3):1129–1135, June 2006.

[121] P Lecoq and J Varela. Clear-PEM, a dedicated PET camera for mammography. *Nuclear Instruments and Methods in Physics Research Section A: Accelerators, Spectrometers, Detectors and Associated Equipment*, 486(1–2):1 – 6, 2002. Proceedings of the 6th International Conference on Inorganic Scin tillators and their Use in Scientific and Industrial Applications.

[122] Yuxuan Zhang, R.A. Ramirez, Hongdi Li, Shitao Liu, Shaohui An, Chao Wang, H. Baghaei, and Wai-Hoi Wong. The system design, engineering architecture, and preliminary results of a lower-cost high-sensitivity high-resolution positron emission mammography camera. *Nuclear Science, IEEE Transactions on*, 57(1): 104–110, Feb 2010.

[123] Raymond R. Raylman, Stan Majewski, Randy Wojcik, Andrew G. Weisenberger, Brian Kross, Vladimir Popov, and Harry A. Bishop. The potential role of positron emission mammography for detection of breast cancer. a phantom study. *Medical Physics*, 27(8):1943–1954, 2000.

[124] R. W. Todd, J. M. Nightingale, and D. B. Everett. A proposed γ camera. *Nature*, 251:132–134, September 1974.

[125] B. Plimley, D. Chivers, A. Coffer, and K. Vetter. Experimental benchmark of electron trajectory reconstruction algorithm for advanced compton imaging. *Nuclear Science, IEEE Transactions on*, 60(3):2308–2313, June 2013.

[126] Y. Ichinohe, S. Takeda, H. Odaka, S. Watanabe, T. Fukuyama, M. Ohta, T. Takahashi, K. Nakazawa, H. Tajima, Y. Fukazawa, and T. Tanaka. Study of event reconstruction algorithm for a large-scale si/cdte multilayer compton camera. In *Nuclear Science Symposium and Medical Imaging Conference (NSS/MIC), 2013 IEEE*, pages 1–4, Oct 2013.

[127] A. Andreyev, A. Sitek, and A. Celler. Stochastic image reconstruction method for compton camera. In *Nuclear Science Symposium Conference Record (NSS/MIC), 2009 IEEE*, pages 2985–2988, Oct 2009.

[128] Philippe P. Bruyant. Analytic and iterative reconstruction algorithms in spect. *Journal of Nuclear Medicine*, 43(10):1343–1358, 2002.

[129] L.A. Shepp and Y. Vardi. Maximum likelihood reconstruction for emission tomography. *Medical Imaging, IEEE Transactions on*, 1(2):113–122, Oct 1982.

[130] H.M. Hudson and R.S. Larkin. Accelerated image reconstruction using ordered subsets of projection data. *Medical Imaging, IEEE Transactions on*, 13(4):601–609, Dec 1994.

[131] S.J. Wilderman, J.A. Fessler, N.H. Clinthorne, J.W. LeBlanc, and W.L. Rogers. Improved modeling of system response in list mode em reconstruction of compton scatter camera images. *Nuclear Science, IEEE Transactions on*, 48(1):111–116, Feb 2001.

[132] A Sitek. Representation of photon limited data in emission tomography using origin ensembles. *Physics in Medicine and Biology*, 53(12):3201, 2008.

[133] Pedro Arce, Juan Ignacio Lagares, Laura Harkness, Daniel Pérez-Astudillo, Mario Cañadas, Pedro Rato, María de Prado, Yamiel Abreu, Gianluca de Lorenzo, Machiel Kolstein, and Angelina Díaz. Gamos: A framework to do Geant4 simulations in different physics fields with an user-friendly interface. *Nuclear Instruments and Methods in Physics Research Section A: Accelerators, Spectrometers, Detectors and Associated Equipment*, 735(0):304 – 313, 2014.

[134] "NEMA Standards Publication NU 2-2001". Performance measurements of positron emission tomographs. *National Electrical Manufacturers Association*, 2001.

[135] Jennifer R Stickel and Simon R Cherry. High-resolution PET detector design: modelling components of intrinsic spatial resolution. *Physics in Medicine and Biology*, 50(2):179, 2005.

[136] "NEMA Stanards Publication NU 1-2007". Performance measurements of gamma cameras. *Rosslyn, VA: National Electrical Manufacturers Association*, 2007.

[137] T.F Budinger, S.E. Derenzo, G.T. Gullberg, W.L. Greenberg, and R.H. Huesman. Emission computer assisted tomography with single-photon and positron annihilation photon emitters. *J Comput Assist Tomogr.*, 1:131–45, 1977.

[138] M Kolstein, G De Lorenzo, E Mikhaylova, M Chmeissani, G Ariño, Y Calderón, I Ozsahin, and D Uzun. Evaluation of origin ensemble algorithm for image reconstruction for pixelated solid-state detectors with large number of channels. *Journal of Instrumentation*, 8(04):P04030, 2013.

[139] M Kolstein, G De Lorenzo, and M Chmeissani. Evaluation of list-mode ordered subset expectation maximization image reconstruction for pixelated solid-state compton gamma camera with large number of channels. *Journal of Instrumentation*, 9(04):C04034, 2014.

[140] Sanjiv S. Gambhir, Daniel S. Berman, Jack Ziffer, Michael Nagler, Martin Sandler, Jim Patton, Brian Hutton, Tali Sharir, Shlomo Ben Haim, and Simona Ben Haim. A novel high-sensitivity rapid-acquisition single-photon cardiac imaging camera. *Journal of Nuclear Medicine*, 50(4):635–643, 2009.

[141] Tsunemasa Taguchi, Junji Shirafuji, and Yoshio Inuishi. Growth by travelling heater method and chracteristic of undoped high-resistivity cdte. *Japanese Journal of Applied Physics*, 17(8):1331, 1978.

[142] K. Suzuki, Satoru Seto, T. Sawada, and K. Imai. Carrier transport properties of HPB CdZnTe and THM CdTe:Cl. *Nuclear Science, IEEE Transactions on*, 49(3): 1287–1291, Jun 2002.

[143] Y. Okada, T. Takahashi, G. Sato, S. Watanabe, K. Nakazawa, K. Mori, and K. Makishima. CdTe and CdZnTe detectors for timing measurements. *Nuclear Science, IEEE Transactions on*, 49(4):1986–1992, Aug 2002.

[144] A. Koike, T. Okunoyama, T. Ito, H. Morii, Yoichiro Neo, Hidenori Mimura, and T. Aoki. Carrier transportation and polarization properties in CdTe diode detectors. In *Nuclear Science Symposium Conference Record (NSS/MIC), 2010 IEEE*, pages 3797–3803, Oct 2010.

[145] V. Stankova, E. Chesi, V. Cindro, N.H. Clinthorne, E. Cochran, A. Gil, B. Grosicar, K. Honscheid, H. Kagan, C. Lacasta, V. Linhart, M. Mikuz, C. Solaz, A. Studen, P. Weilhammer, D. Zontar, and G. Llosa. Characterization and performance of a DAQ system for the readout of silicon pixel detectors. In *Nuclear Science Symposium and Medical Imaging Conference (NSS/MIC), 2011 IEEE*, pages 841–844, Oct 2011.

[146] J Franc, P Höschl, E Belas, R Grill, P Hlídek, P Moravec, and J Bok. CdTe and CdZnTe crystals for room temperature gamma-ray detectors. *Nuclear Instruments and Methods in Physics Research Section A: Accelerators, Spectrometers, Detectors and Associated Equipment*, 434(1):146 – 151, 1999.

[147] Y. Eisen, A. Shor, and I. Mardor. CdTe and CdZnTe gamma ray detectors for medical and industrial imaging systems. *Nuclear Instruments and Methods in Physics Research Section A: Accelerators, Spectrometers, Detectors and Associated Equipment*, 428(1):158 – 170, 1999.

[148] J.R. Macri, B.A. Apotovsky, J.F. Butler, M.L. Cherry, B.K. Dann, A. Drake, F.P. Doty, T.G. Guzik, K. Larson, M. Mayer, M.L. McConnell, and J.M. Ryan. Development of an orthogonal-stripe CdZnTe gamma radiation imaging spectrometer. *Nuclear Science, IEEE Transactions on*, 43(3):1458–1462, Jun 1996.

[149] C Scheiber. CdTe and CdZnTe detectors in nuclear medicine. *Nuclear Instruments and Methods in Physics Research Section A: Accelerators, Spectrometers, Detectors and Associated Equipment*, 448(3):513 – 524, 2000.

[150] C. Matsumoto, T. Takahashi, K. Takizawa, R. Ohno, T. Ozaki, and K. Mori. Performance of a new Schottky CdTe detector for hard x-ray spectroscopy. In *Nuclear Science Symposium, 1997. IEEE*, pages 569–573 vol.1, Nov 1997.

[151] Tadayuki Takahashi, Biswajit Paul, Kazuyuki Hirose, Chiho Matsumoto, Ryouichi Ohno, Tsutomu Ozaki, Kunishiro Mori, and Yoshihiro Tomita. High-resolution Schottky CdTe diode for hard x-ray and gamma-ray astronomy. *Nuclear Instruments and Methods in Physics Research Section A: Accelerators, Spectrometers, Detectors and Associated Equipment*, 436(1–2):111 – 119, 1999.

[152] J.J. Griesmer, B. Kline, J. Grosholz, K. Parnham, and D. Gagnon. Performance evaluation of a new CZT detector for nuclear medicine: Soltice. In *Nuclear Science Symposium Conference Record, 2001 IEEE*, volume 2, pages 1050–1054 vol.2, Nov 2001.

[153] S. Watanabe, T. Takahashi, Y. Okada, G. Sato, M. Kouda, T. Mitani, Y. Kobavashi, K. Nakazawa, Y. Kuroda, and M. Onishi. CdTe stacked detectors for gamma-ray detection. In *Nuclear Science Symposium Conference Record, 2001 IEEE*, volume 4, pages 2434–2438, 2001.

[154] Karl-Ludwig Giboni, Elena Aprile, Tadayoshi Doke, Masahiko Hirasawa, and Mikio Yamamoto. Coincidence timing of Schottky CdTe detectors for tomographic imaging. *Nuclear Instruments and Methods in Physics Research Section A: Accelerators, Spectrometers, Detectors and Associated Equipment*, 450(2–3):307 – 312, 2000.

[155] Gaspar Delso, Sebastian Fürst, Björn Jakoby, Ralf Ladebeck, Carl Ganter, Stephan G. Nekolla, Markus Schwaiger, and Sibylle I. Ziegler. Performance measurements of the siemens mMR integrated whole-body PET/MR scanner. *Journal of Nuclear Medicine*, 52(12):1914–1922, 2011.

[156] J. D. Eskin, H. H. Barrett, and H. B. Barber. Signals induced in semiconductor gamma-ray imaging detectors. *Journal of Applied Physics*, 85(2), 1999.

[157] M Kolstein, G Ariño, M Chmeissani, and G De Lorenzo. Simulation of charge transport in pixelated CdTe. *Journal of Instrumentation*, 9(12):C12027, 2014.

[158] A. Studen, K. Brzezinski, E. Chesi, V. Cindro, N.H. Clinthorne, M. Grkovski, B. Grosicar, K. Honscheid, S.S. Huh, H. Kagan, C. Lacasta, G. Llosa, M. Mikuz, A. Rudge, S. Smith, V. Stankova, P. Weilhammer, and D. Zontar. A laboratory PET scanner with silicon detectors segmented to 1 mm3 detection cells. In *Nuclear Science Symposium and Medical Imaging Conference (NSS/MIC), 2012 IEEE*, pages 1305–1310, Oct 2012.

[159] Yuefeng Zhu, S.E. Anderson, and Zhong He. Sub-pixel position sensing for pixelated, 3-D position sensitive, wide band-gap, semiconductor, gamma-ray detectors. *Nuclear Science, IEEE Transactions on*, 58(3):1400–1409, June 2011. ISSN 0018-9499.

[160] D.G. Marks, H.B. Barber, H.H. Barrett, E.L. Dereniak, J.D. Eskin, K.J. Matherson, J.M. Woolfenden, E.T. Young, F.L. Augustine, W.J. Hamilton, J.E. Venzon, B.A. Apotovsky, and F.P. Doty. A 48x48 CdZnTe array with multiplexer readout. In *Nuclear Science Symposium and Medical Imaging Conference Record, 1995., 1995 IEEE*, volume 2, pages 752–756 vol.2, Oct 1995.

[161] Jae Cheon Kim, Stephen E. Anderson, Willy Kaye, Feng Zhang, Yuefeng Zhu, Sonal Joshi Kaye, and Zhong He. Charge sharing in common-grid pixelated

CdZnTe detectors. *Nuclear Instruments and Methods in Physics Research Section A: Accelerators, Spectrometers, Detectors and Associated Equipment*, 654(1): 233 – 243, 2011.

[162] Feng Zhang, Zhong He, and Dan Xu. Analysis of detector response using 3-D position-sensitive CZT gamma-ray spectrometers. *Nuclear Science, IEEE Transactions on*, 51(6):3098–3104, Dec 2004.

[163] V. Stankova, J. Barrio, K. Brzezinski, E. Chesi, V. Cindro, N.H. Clinthorne, E. Cochran, B. Grosicar, G. Llosa, H. Kagan, K. Honscheid, V. Linhart, M. Mikuz, C. Solaz, A. Studen, P. Weilhammer, D. Zontar, and C. Lacasta. DAQ system for the readout of silicon pixel detectors based on VataGP7 front-end ASIC. In *Nuclear Science Symposium and Medical Imaging Conference (NSS/MIC), 2012 IEEE*, pages 1084–1086, Oct 2012.

[164] A. Michalowska, O. Gevin, O. Lemaire, F. Lugiez, P. Baron, H. Grabas, F. Pinsard, O. Limousin, and E. Delagnes. IDeF-X HD: A low power multi-gain CMOS ASIC for the readout of Cd(Zn)Te detectors. In *Nuclear Science Symposium Conference Record (NSS/MIC), 2010 IEEE*, pages 1556–1559, Oct 2010.

[165] Mario Locker, P. Fischer, S. Krimmel, H. Kruger, M. Lindner, K. Nakazawa, T. Takahashi, and N. Wermes. Single photon counting x-ray imaging with Si and CdTe single chip pixel detectors and multichip pixel modules. *Nuclear Science, IEEE Transactions on*, 51(4):1717–1723, Aug 2004. ISSN 0018-9499.

[166] S. Basolo, J.-F. Berar, N. Boudet, P. Breugnon, B. Caillot, J.-C. Clemens, P. Delpierre, B. Dinkespiler, I. Koudobine, C. Meessen, M. Menouni, C. Mouget, P. Pangaud, R. Potheau, and E. Vigeolas. Xpad: pixel detector for material sciences. *Nuclear Science, IEEE Transactions on*, 52(5):1994–1998, Oct 2005. ISSN 0018-9499.

[167] M.D. Wilson, S.J. Bell, R.J. Cernik, C. Christodoulou, C.K. Egan, D. O'Flynn, S. Jacques, S. Pani, J. Scuffham, P. Seller, P.J. Sellin, R. Speller, and M.C. Veale. Multiple module pixellated CdTe spectroscopic x-ray detector. *Nuclear Science, IEEE Transactions on*, 60(2):1197–1200, April 2013. ISSN 0018-9499.

[168] Feng Zhang, W.R. Kaye, and Zhong He. Performance of 3-D position sensitive CdZnTe detectors for gamma-ray energies above 1 MeV. In *Nuclear Science Symposium Conference Record (NSS/MIC), 2009 IEEE*, pages 2012–2016, Oct 2009. doi: 10.1109/NSSMIC.2009.5402137.

[169] T. Takahashi, S. Watanabe, M. Kouda, G. Sato, Y. Okada, S. Kubo, Y. Kuroda, M. Onishi, and R. Ohno. High-resolution CdTe detector and applications to imaging devices. *Nuclear Science, IEEE Transactions on*, 48(3):287–291, Jun 2001. ISSN 0018-9499.

[170] J.J. Griesmer, B. Kline, J. Grosholz, K. Parnham, and D. Gagnon. Performance evaluation of a new CZT detector for nuclear medicine: Soltice. In *Nuclear Science Symposium Conference Record, 2001 IEEE*, volume 2, pages 1050–1054 vol.2, Nov 2001. doi: 10.1109/NSSMIC.2001.1009733.

[171] C.M Stahle, B.H Parker, A.M Parsons, L.M Barbier, S.D Barthelmy, N.A Gehrels, D.M Palmer, S.J Snodgrass, and J Tueller. CdZnTe and CdTe detector arrays for hard x-ray and gamma-ray astronomy. *Nuclear Instruments and Methods in Physics Research Section A: Accelerators, Spectrometers, Detectors and Associated Equipment*, 436(1–2):138 – 145, 1999. ISSN 0168-9002.

[172] A. Meuris, O. Limousin, O. Gevin, F. Lugiez, I. Le Mer, F. Pinsard, M. Donati, C. Blondel, A. Michalowska, E. Delagnes, M.-C. Vassal, and F. Soufflet. Caliste HD: A new fine pitch Cd(Zn)Te imaging spectrometer from 2 keV up to 1 MeV. In *Nuclear Science Symposium and Medical Imaging Conference (NSS/MIC), 2011 IEEE*, pages 4485–4488, Oct 2011. doi: 10.1109/NSSMIC.2011.6154695.

[173] M. Porro, L. Andricek, S. Aschauer, M. Bayer, J. Becker, L. Bombelli, A. Castoldi, G. De Vita, I. Diehl, F. Erdinger, S. Facchinetti, C. Fiorini, P. Fischer, T. Gerlach, H. Graafsma, C. Guazzoni, K. Hansen, P. Kalavakuru, H. Klar, A. Kugel, P. Lechner, M. Lemke, G. Lutz, M. Manghisoni, D. Mezza, D. Muntefering, U. Pietsch, E. Quartieri, M. Randall, V. Re, C. Reckleben, C. Sandow, J. Soldat, L. Struder, J. Szymanski, G. Weidenspointner, and C.B. Wunderer. Development of the depfet sensor with signal compression: A large format x-ray imager with mega-frame readout capability for the european xfel. *Nuclear Science, IEEE Transactions on*, 59(6):3339–3351, Dec 2012. ISSN 0018-9499.

[174] Z. He, W. Li, G.F. Knoll, D.K. Wehe, J. Berry, and C.M. Stahle. 3-d position sensitive CdZnTe gamma-ray spectrometers. *Nuclear Instruments and Methods in Physics Research Section A: Accelerators, Spectrometers, Detectors and Associated Equipment*, 422(1–3):173 – 178, 1999.

[175] Y Gu, J L Matteson, R T Skelton, A C Deal, E A Stephan, F Duttweiler, T M Gasaway, and C S Levin. Study of a high-resolution, 3D positioning cadmium zinc telluride detector for PET. *Physics in Medicine and Biology*, 56(6):1563, 2011.

[176] J. Carrascal, J. Castilla, J.C. Oller, O. Vela, L. Romero, P. Rato, and J.M. Perez. Energy and DOI calibrations for high spatial resolution czt detectors. *Nuclear Science, IEEE Transactions on*, 61(1):518–527, Feb 2014. ISSN 0018-9499.